COMPUTATIONAL MODELING OF NANOPARTICLE DISTRIBUTION AND TOXICITY IN BIOLOGICAL SYSTEMS

By

DWAIPAYAN MUKHERJEE

A dissertation submitted to the

Graduate School—New Brunswick

Rutgers, The State University of New Jersey

In partial fulfillment of the requirements

For the degree of

Doctor of Philosophy

Graduate Program in Chemical and Biochemical Engineering

Written under the direction of

Panos G. Georgopoulos

And approved by

_____

_____

_____

_____

_____

New Brunswick, New Jersey

May, 2015

ABSTRACT OF THE DISSERTATION

COMPUTATIONAL MODELING OF NANOPARTICLE DISTRIBUTION AND TOXICITY IN BIOLOGICAL SYSTEMS

By DWAIPAYAN MUKHERJEE

Dissertation Director:

Panos G. Georgopoulos

Engineered Nanoparticles are increasingly becoming a part of our daily lives due to their presence in an overwhelming majority of consumer products. Potential health risks due to chronic exposure to such particulate matter have not been properly evaluated. A multiscale, mechanistic, toxicodynamic model was developed as part of this dissertation, for studying the impact of inhaled nanoparticles on lung function in mammalian biological systems. The biologically-based model was developed in a modular fashion, with separate consideration given to NP distribution in the entire organism as well as various mechanisms at the cell, tissue, organ, and organism levels. Specifically the effect of inhaled nanoparticles on pulmonary function is evaluated and estimated based on resultant surfactant dysfunction. Pulmonary surfactant depletion is explicitly modeled by incorporating dynamics of surfactant constituents such as phospholipids and various lipoproteins. Various nanoparticle transformation

processes such as agglomeration, dissolution, diffusion, and lipid adsorption inside biological systems, are explicitly considered and their effects on surfactant modification assessed. The model relates pulmonary mechanics at the organ level with cellular level surfactant dynamics in the lung, both of which are affected by nanoparticle inhalation. The model was evaluated with data from *in vitro* and *in vivo* measurements of surfactant levels, cell counts, and overall dynamic impedance in rodent lungs. The model was also extrapolated to adult humans and prediction of changes in pulmonary tissue resistance and elastance in humans are presented based on comparable one-time nanoparticle exposure. This is the first instance of a comprehensive modeling framework integrating research and mechanistic information regarding nanoparticle-biosystem interactions at multiple scales and linking pulmonary mechanisms and processes due to interaction with particulate matter with pulmonary function in human subjects.

Acknowledgments

I would like to express my sincerest gratitude to my advisor Dr. Panos G. Georgopoulos for his guidance and support throughout my Ph.D. research at the Computational Chemodynamics Laboratory (CCL) at Rutgers University. His encouragement during difficult times, his clarity of thought when there were research dead ends, and his unwavering spirit of hard work and perseverance has always inspired me and helped me in completing this work. His words of wisdom will remain as valuable lessons in my life.

I am also grateful to my dissertation committee members Dr. Yannis Androulakis, Dr. Henrik Pedersen, Dr. Nina Shapley, and Dr. Andrew Gow for their insightful comments and for taking time to guide me through my dissertation. I appreciate their help in always having time for me to discuss my proposal, my dissertation and my research, and their support in various capacities since I joined the Chemical & Biochemical Engineering department in 2008.

I would like to specially acknowledge the guidance and support of Dr. Sastry Isukapalli, who as a part of CCL, taught me many of the basics of programming and guided me in developing models from basic building blocks. I would like to thank Dr. Christopher Brinkerhoff, who as a post doctoral research member, has been a mentor and a close friend and taught me numerous techniques in computational modeling. I am grateful to Dr. Andrew Gow from the Department of Pharmacology and Toxicology at Rutgers University, for his time and help in understanding rodent pulmonary effects and for teaching me the intricacies of pulmonary biology.

I would like to extend my sincere gratitude to my colleagues and friends at the Rutgers School of Pharmacy, Rutgers School of Public Health, and at the Imperial College, London for sharing with me their own *in vitro* and *in vivo* data on nanotoxicological effects of nanoparticles. They have always had time for me to help me understand the data, the experimental protocols, and various other factors related to the study subjects and the chemical formulations. I would like to especially mention the assistance provided by Danielle Botelho & Dr. Christopher Massa (Rutgers School of Pharmacy), Dr. Srijata Sarkar & Dr. Stephan Schwander (Rutgers School of Public Health), Joanna Seiffert, Dr. Teresa Tetley, & Dr. Fan Chung (Imperial College, London) and Dr. Jim Zhang (Duke University). Without their help in understanding the biological mechanisms for nanotoxicology, this thesis would not have been possible.

I would also like to thank my colleagues Dr. Yong Zhang, Dr. Sagnik Mazumdar, Steven Royce, Xiaogang Tang, Zhongyuan Mi, Ting Cai, Jocelyn Alexander, Peter Koutsoupias, Shu Xu, Pamela Shade, and Yanran Wang. They have provided encouragement, inspiration, and support and made the past few years delightful and enjoyable. I would like to especially acknowledge Ms. Linda Everett and Ms. Teresa Boutillette for their help, encouragement and unwavering support. I wish to thank all my other friends here at Rutgers, who have helped me in countless ways and provided companionship and encouragement

I cannot say enough to express my gratitude for my best friend and wife, Srijita. She has been by my side all through this time, helping and supporting me in every possible way. With her artistic skills, she has helped create many of the diagrams presented in this dissertation. Her sacrifice, understanding, and immense patience has made this work possible. My deepest gratitude goes to my sister Shreyasee Mukherjee, who as a graduate student at Rutgers works harder than me, and yet finds time to manage multiple activities at home and at school. She has been an inspiration and a role model for me. Last but not the least, I want to acknowledge my beloved parents

Dipankar and Shyamosree Mukherjee. They were the ones who pushed me towards higher studies after I completed college. I could not have pursued and finished my Ph.D. studies without their selfless and unconditional support and patience and this dissertation is dedicated to them.

Financial support for this work has been primarily provided by the NIEHS funded RESAC Center (Respiratory Effects of Silver and Carbon Nanomaterials - Grant Number U19ES019536-01). Additional support has been provided by the NIEHS sponsored Center for Environmental Exposures and Disease (CEED - Grant Number NIEHS P30E5S005022) at the Environmental and Occupational Health Sciences Institute (EOHSI) at Rutgers University.

Dedication

To my parents

Dipankar & Shyamosree Mukherjee

Table of Contents

List of Tables

List of Figures

Chapter I

Background and Importance

I.1 Background

At the beginning of the last decade, nanotechnology emerged as a new paradigm, which promised new and revolutionary properties in commonly known chemicals and substances. Particles with at least one dimension ranging from 1-100 nm generally come under the purview of nanotechnology [1]. Nano-sized particles have always been present in nature as dust, pollen, or other bio-aerosols or have been produced by human activities such as combustion, mining, construction, etc. Nanotechnology has led to a different class of particles which could be called Engineered Nanomaterials (ENMs) and comprise nanospheres, wires, needles, tubes, fibres, etc. [2] in the nanometer size range which have been manufactured for diverse industrial or consumer applications. The innovations in nanotechnology were possible due to advanced precision machinery and instruments which could manipulate physical, chemical, and electrical properties at the nano-scale. ENMs have been defined in technical standards [3] as "intentionally manufactured and/or engineered" as different from naturally-produced nano-sized particles. These nano-sized metal or non-metal particles could be engineered to perform a host of functions in a far more efficient way than possible in the macro-scale. The huge promise the field offered was soon justified as newer products emerged over time and more and more manufacturers started using

innovations at the nano-scale to make their products better and more efficient. It has been amply pointed out that research into novel applications of ENMs far exceeds our ability to predict their possible risks to human health or the environment [4, 5]. There is a clear disparity between animal or cellular toxicological models for ENMs and effective safety regulations concerning use and disposal of these ENMs. While multiple toxicological studies [6, 7, 8, 9] have predicted high levels of biotoxicity from ENMs, these results could not be translated into effective safety regulations or policy concerning the use and disposal of ENMs.

I.1.1 Environmental burden and risk

Nanotechnology started offering greener alternatives for the same processes and in general made processes more efficient, requiring less energy and producing lower levels of emission to the environment. Because of their size, nanoparticles (NPs) offer a larger surface-to-volume ratio than other bulk chemicals and tend to enhance processes whose rates are a function of surface area. All physico-chemical processes involving chemicals consist of surface reactions or electrical interactions at the particle surface. By greatly enhancing the available surface area per volume of chemicals, ENMs make the reaction kinetics faster. As a result of this, ENMs have found widespread applications in the fields of catalysis, electrochemistry, food processing, medicine, and biomedical engineering. Today ENMs can be generated with relative ease and are currently used in diverse industrial applications from electronics, pharmaceuticals, biomedicine, consumer products, to environmental remediation. The Project on Emerging Nanotechnologies (formerly known as the Woodrow Wilson Center) [10] compiles a list of nanotechnology-enabled products manufactured worldwide and lists over 1300 products in commercial use today, which use ENMs in some form. Figure I.1 shows the rapid increase in the number of ENM-containing products in the US over the years. The increased use of these novel materials is resulting in an

ever-increasing environmental burden of ENMs, whose bio-degradability and environmental life-cycle is still a matter of debate [11].

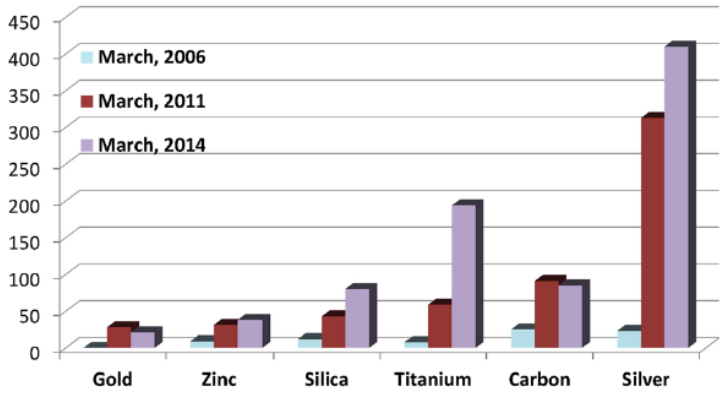

Figure I.1: Numbers of ENM containing consumer products in the US over the years as reported by the Project on Emerging Nanotechnologies [10] (Figure reproduced from Royce *et al.*, *Journal of Nanoparticle Research*, 16(11), 1-25, 2014, Figure no. 1(a), with kind permission from Springer Science and Business Media.)

The unique properties of ENMs that lead to their wonderful abilities, however, also create unpredictable scenarios once they enter the environment and living systems. This led to the emergence of a new field of study called "Nanotoxicology", to deal with specific biological toxicity mechanisms which are unique to nanoparticles [12]. It was recognized that the unique properties of these particles such as their small size, large surface area per unit mass, and the various surface modifications were key determinants in understanding nanotoxicology [13, 14, 15]. The potential impact of ENMs on the environment and on living beings was first discussed in detail by Colvin [16]. Colvin [16] highlighted the uncertainties surrounding a comprehensive environmental and biological risk assessment of these new materials. Since then, a number of researchers [17, 18, 19, 11, 20, 5] have attempted to characterize the amount and form of ENMs distributed across the environment and inside living organisms and their potential impact. The major problems faced in conducting an in-depth risk characterization of ENMs are summarized below:

- ENMs are very different in their physico-chemical properties from the same bulk

materials and hence safety regulations and safety data-sheets based on the bulk material can only provide a limited guideline to acceptable levels of exposure [16, 4, 21]

- There is an absence of comprehensive, detailed reporting on the part of manufacturers with regards to ENMs and products containing ENMs in some form, thus making accurate assessment of environmental burdens or potential exposures difficult [11, 22]

- Existing toxicological studies in animals often employ large ENM doses and involve select cell cultures, which cannot give realistic estimates of biological risk to humans based on daily low-level exposures [2]

I.1.2 Biological effect of ENMs

Interactions of various toxic chemicals have been studied within the physiological system under the purview of toxicology. However, the methodologies developed for assessing biological risk for these "traditional" toxic chemicals are seriously deficient when used for ENMs [2]. Traditional toxicological approaches are based on dose-response relations that relate the mass concentrations of a chemical in the dose to the corresponding biological effect measured by cell death, or various cellular toxicity biomarkers such as ROS, LDH, etc. [2]. However, in the case of ENMs a very small mass concentration of the original constituent material might be associated with a very high particle surface area and lead to high surface reactivity. Other properties like shape, particle number, aggregation state, and surface chemistry are all critical parameters affecting biological reactivity [19], and so traditional mass-based approaches for assessing biological effect would not be able to capture the relationship between ENM properties and resultant biological impact. There are increasing concerns that ENMs lead to adverse effects in biological systems [21, 23, 22], including cardiovascular effects. Though there has been a lot of research looking into

ENM interaction with biological systems in the last several years, a comprehensive risk assessment framework which combines dose-to-effect analysis of ENMs along with its relation to their pertinent physico-chemical properties has been seriously lacking. Maynard *et al.* [14] in a seminal publication, pointed out five "grand" challenges in the development of safe nanotechnologies through scientific research and the third challenge called for models for predicting ENM behavior in the environment and inside the body. This thesis attempts to tackle this important issue for inhaled ENMs in particular by developing a multiscale approach at understanding ENM-interactions inside the body.

I.2 Human exposure to Engineered Nanoparticles

Exposure to engineered nanomaterials (ENMs) may be classified into 2 types: intentional and non-intentional [24]. Intentional exposure results from the use of specially designed nanoparticles as drug-delivery vehicles and for imaging, which enter the human body in well-known dose and frequency. Unintentional exposure results from nanoparticles in occupational and home environments and from use of products containing ENMs. It is expected to be a function of human activity, time of day, age group, and product usage patterns across the population. Nanosilver (nAg) is the most widely used among nano materials used in various consumer products, as is evident from Figure I.1. Silver is a known anti-microbial and so silver nanoparticles (nAg) are used as anti-microbial coatings in medical devices and as anti-microbial agents in cosmetics, personal care products, and home electronics [19]. Silver nanoparticles are used extensively in fabrics and textiles of all kinds, especially those prone to sweaty conditions to prevent bacterial growth [25]. Table I.1 lists some examples of nAg based product categories and their potential exposure routes.

I.2.1 Potential exposure routes

Three possible routes of exposure to nAg are ingestion, dermal, and inhalation. Nanosilver in colloid form (also called colloidal silver) has some medicinal benefits and they are sometimes consumed in small quantities as dietary supplements [26]. Hence, ingestion exposure to nAg is mostly voluntary and, within limits, is considered a safe practice. Dermal exposure is also another significant route of exposure to silver ENMs. nAg has been incorporated into products where dermal exposure is frequent (e.g. clothing, cosmetics, appliances). The other probable route of exposure to nAg is inhalation. nAg has been used as an active ingredient in a number of spray products [27]. A consider amount of nAg is released during the product usage and remain suspended in the air, providing a direct risk of inhalation exposure to consumers [28, 27].

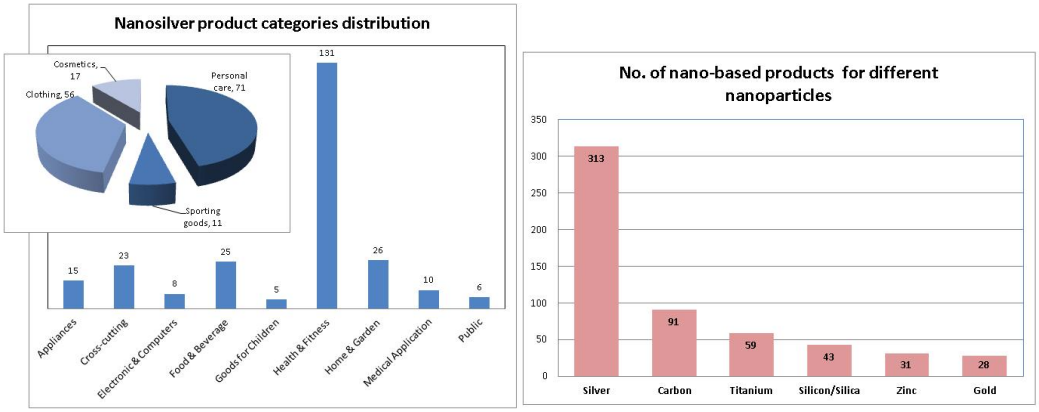

(a) (b)

Figure I.2: Nanoparticle distribution across various product categories and nanomaterials

Inhalation exposure

In this thesis, primary focus is ultimately given to modeling the risks due to inhalation exposure to ENMs. Inhalation exposure is one of the most important routes of exposure to ENMs. This is because ENMs are extremely small in size and can remain

Table I.1: Examples of nanosilver containing consumer products and concentrations

Categories	**nAg function**	**Potential exposure route(s)**	**Concentration**
Appliance	disinfectant	none	N/A
Coating	antibacterial, antibiofilm	dermal	100-2000 ppm
Clothing	antibacterial, antifungal	dermal, inhalation	14.6 ppm
Cosmetic, personal skin care	antiviral, disinfectant	dermal, inhalation	6 ppm
Dietary supplement	antiviral	ingestion	10-30 ppm
Electronic, computer	facilitate electric and thermal conduction	none	N/A
Household cleaning	disinfectant	dermal, inhalation	32-1000 ppm

airborne once they are released into the environment both during manufacturing processes and during their use in consumer products. Many of the consumer products containing ENMs are in the form of sprays and powders resulting in a considerable risk of inhalation exposure during use. Nazarenko *et al.* [27] have estimated inhalation exposure from use of consumer sprays containing ENMs, using mannequins within controlled spray chambers. Nanoparticle inhalation has been implicated as a significant cause behind a number of respiratory and cardiovascular diseases [30, 31, 32]. Moreover, people with existing lung diseases, such as asthma, bronchitis, and chronic obstructive pulmonary disease (COPD) are more susceptible to such effects. Inhalation exposure also presents one of the most direct routes for xenobiotics to reach the blood stream in the body [33, 34]. Unlike for oral exposure, where xenobiotics have to pass through the liver to reach the blood and for dermal exposure, where they have to pass through multiple layers of skin, for inhalation the pathway to circulation is significantly easier. Inhaled particles are not detoxified by the liver, nor excreted via feces, thus making inhalation exposure one of the high risk scenarios possibly leading

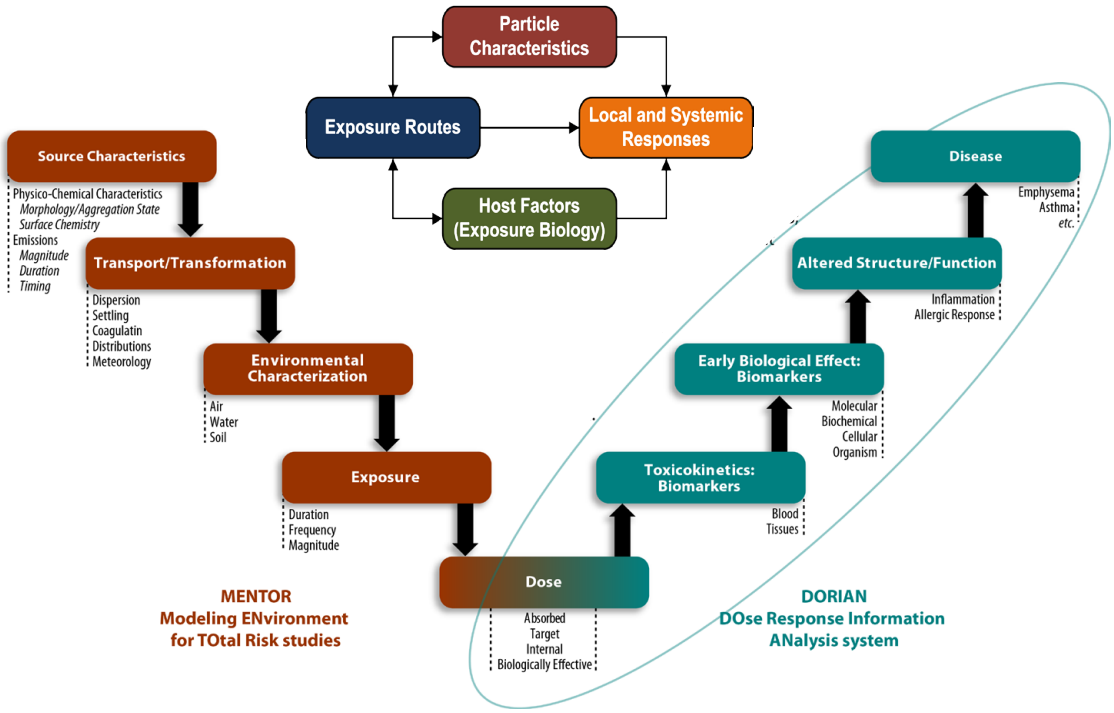

Figure I.3: Schematic representation of framework structure for comprehensive source-to-dose-to-effect analysis for environmental chemicals (adapted from Georgopoulos [29]) with the series of biological dose-to-effect steps separately identified

to disease effects in normal and susceptible populations.

I.3 Integrated Modeling of Xenobiotic Dose-to-Effects

The primary focus of this thesis is on developing an integrative multiscale computational modeling framework which integrates information and mechanisms for multiple biological scales (molecular, cellular, tissue, and organism) and data types (*in vitro* and *in vivo*) to support risk studies for inhaled ENMs in humans. This approach follows the biologically-based DOse Response INformation ANalysis system (DORIAN) developed byGeorgopoulos [29]. DORIAN (shown circled in figure I.3) is a part of the comprehensive MENTOR-DORIAN source-to-dose-to-effect framework for assessing

risk due to xenobiotics by assessing the entire gamut of processes from exposure to disease due to environmental toxicants. The proposed new biologically-based modules of DORIAN will incorporate a novel, customized, population-balance based (rather than mass balance alone) description of physiologically-based particle biokinetics and tissue toxicodynamics, explicitly accounting for particle properties such as shape, surface charge, aggregation state, etc., that critically affect particle-biosystem interactions. The biokinetic processes to be integrated in a framework similar to DORIAN will include biophysical processes such as mucociliary movement, macrophage phagocytosis, surfactant secrection, interstitial translocation, lymphatic drainage, and immune processes. It will translate and incorporate state-of-the-art knowledge regarding relevant biological mechanisms affecting particle-biology interactions and current *in vitro* and *in vivo* findings from collaborating groups. Figure I.4 represents a brief outline of the framework proposed to understand the relation between particle inhalation and disease outcomes.

I.3.1 Integration of biological information from multiple sources

The overarching aim for this thesis is to demonstrate a framework to integrate biological toxicity information form multiple sources in order to formulate a comprehensive risk framework for ENMs. As pointed out earlier, nanotoxicity mechanisms are complicated due to multiple nanoscale interactions with biomolecules and also the various tunable properties of ENMs which makes their behavior harder to predict. Unlike bulk chemicals, fate and toxicity of ENMs cannot be scaled across dose, particle-type, or species in a simple manner. Traditional dose-response based paradigms of toxicity focus on developing appropriate *in vitro* cellular models to test toxicological doses and outcomes, which are then scaled to animal models, and finally scaled to human subjects using appropriate physiological scaling. However, toxicological assessment for ENMs in *in vitro* and *in vivo* models have produced widely varying results [35, 36], which have prevented the formulation of an unifying biological risk framework for

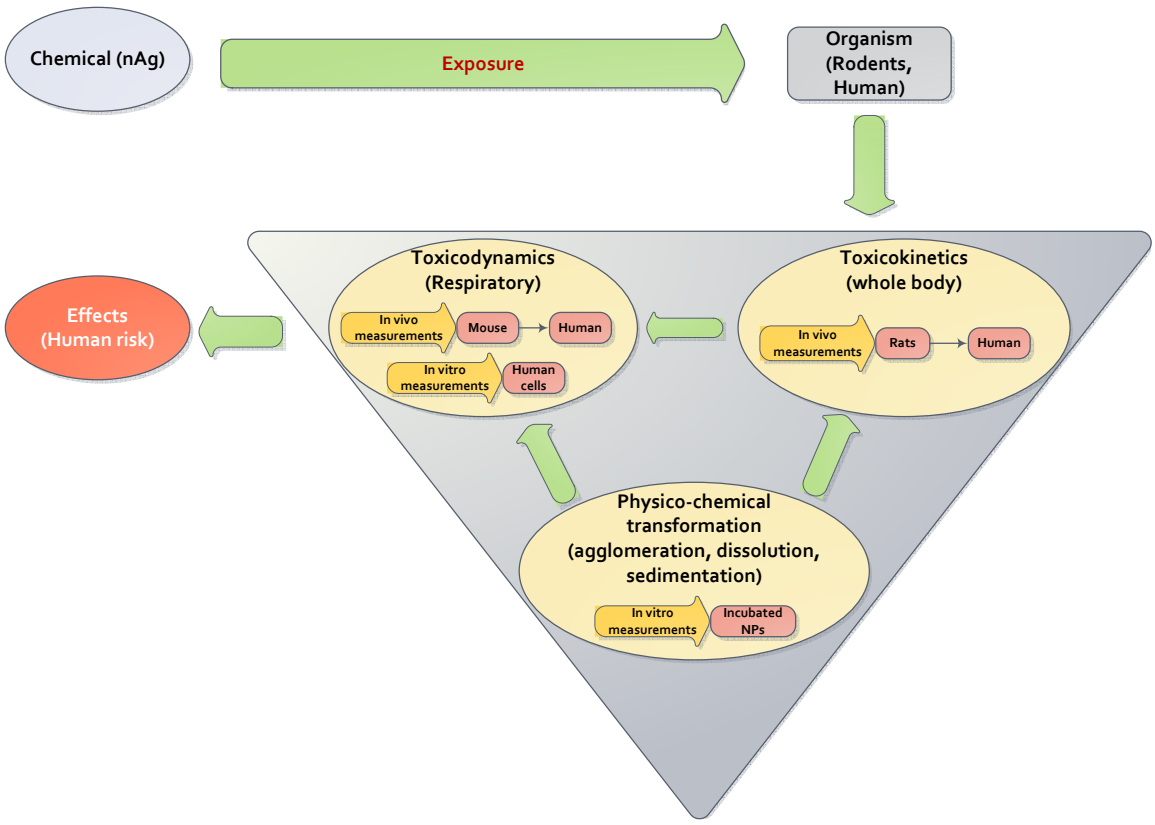

Figure I.4: Brief outline for research accomplished in the thesis, with integration of relevant *in vitro* and *in vivo* information from multiple sources and for multiple biological scales

ENMs. Both *in vitro* and *in vivo* assays have their unique advantages and are critical for understanding biointeractions of ENMs. *In vitro* systems involving mammalian cell cultures are important for understanding key cellular mechanisms such as uptake, phagocytosis, production of inflammatory markers, apoptosis, etc., all of which are induced due to ENM exposure. *In vitro* studies allow the investigation of a select pathway or few interrelated pathways without the complication of multiple cell types and biomolecules [37, 38]. *In vitro* studies also allow one to investigate NP transformation mechanisms in various chemical media in order to postulate possible transformation mechanisms in living systems [39, 40, 41, 42]. *In vivo* studies generally involve laboratory animals (mostly rodents) and allow one to study organism-level changes due to ENM exposure [43]. While all these methods provide useful information necessary for assessing biological risk from ENMs, these alone cannot provide a

comprehensive understanding necessary to formulate a biological risk framework. In addition to information from these sources, there is the need for *in silico* models comprising computational models which would provide the necessary platform in order to integrate information from diverse sources and predict biological outcomes resulting from ENM exposures [44, 45]. The 2007 report of the National Research Council (NRC) supported the increased use of high-throughput methods of toxicity screening which involved increased use of *in silico* models along with targeted *in vitro* and *in vivo* studies [45]. Figure I.5 shows the interaction between these diverse methods of investigation and how they can come together and share information in order to develop an overarching risk assessment framework.

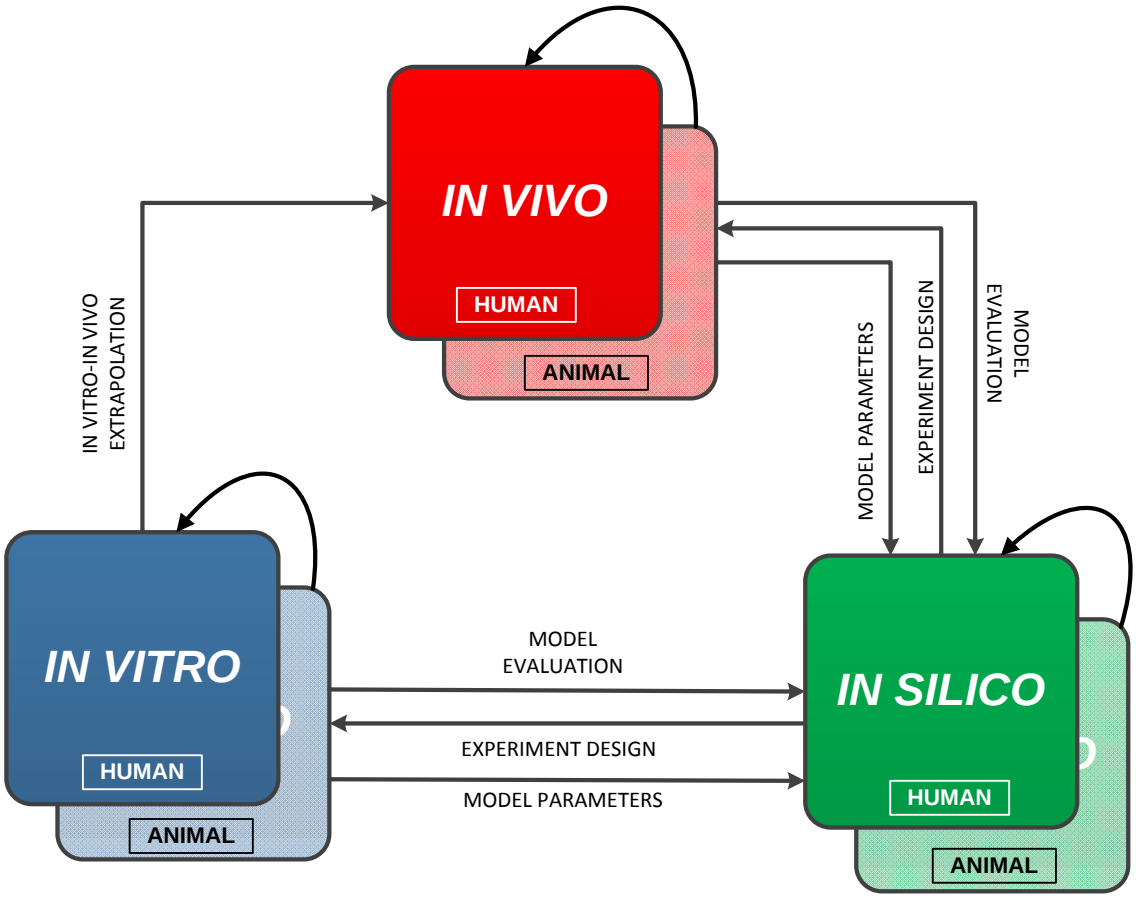

Figure I.5: Schematic representation of data integration and interaction between *in vitro*, *in vivo*, and *in silico* models, including information flow between different models (Figure reproduced from Mukherjee *et al.* [44] under Creative Commons Attribution License).

Figure I.4 shows a schematic outline of how the stated goal of utilizing diverse sources of information to produce a predictive, bio-toxicity framework has been achieved for silver ENMs in this thesis. The thesis describes a step-wise, multiscale approach to model the biological impact of inhaled silver ENMs. The thesis has also developed and demonstrated approaches that translate the knowledge of *in vitro* and *in vivo* effects of ENMs into a comprehensive risk analysis and assessment framework. The model framework considers all important properties of the ENMs explicitly and so can be extended to other types of ENMs with different surface properties. Diverse types of metals and non-metals such as gold, silica, zinc, carbon, titanium dioxide, etc., are used as ENMs in various consumer products. The modeling framework demonstrated in this thesis can be implemented for any of these ENMs, provided their physico-chemical properties are accounted for. ENMs are also used as novel drug-delivery vehicles for improving delivery of therapeutic agents to target organs, tumor cells, or pathogens [46]. The model framework demonstrated here can be used to assess pharmacokinetics of novel drug formulations and can assist in optimization of surface properties of these ENMs to enhance bioavailability. The model developed here in its entirety can be envisioned as a "hypothesis generator" that will allow formulation and preliminary testing of various hypotheses regarding the mechanisms underlying the biokinetics and toxicodynamics of ENMs, thus allowing in the future to optimize the collection of additional data and the design of further *in vitro* and *in vivo* studies for a wider range of ENMs.

I.4 Main objectives, aims, and tasks

- **Objective 1**: Understanding nanoparticle distribution in the animal body using computational models
  - **Specific aim 1**: Physiologically Based Toxicokinetic (PBTK) modeling at a whole-body scale using silver nanoparticles (nAg) in rats as an example

  - **Specific aim 2**: Implementation of the PBTK model for inhalation exposure to estimate pulmonary tissue dosimetry in rodents and humans

- **Objective 2**: Nanoscale Particokinetic modeling (ADSRM), to quantify particle-biomolecule interactions at the particle scale

  - **Specific aim 1**: Nanoparticle agglomeration, diffusion, sedimentation, reaction modeling (ADSRM) in *in vitro* media
  - **Specific aim 2**: Extension of the ADSRM framework to the pulmonary alveolar lining to quantify nanoparticle transformation after inhalation exposure

- **Objective 3**: Pulmonary Toxicodynamic (TD) modeling of NPs, considering functional interactions at both tissue and cell level in the lung

  - **Specific aim 1**: Modeling and parameterization of multiscale effects for NP-surfactant interaction and changes in surfactant dynamics at the tissue level using lung lavage measurements in mice
  - **Specific aim 2**: Scale up of the Pulmonary TD Model in mice to rats and incorporating differences in pulmonary physiology between rats and mice
  - **Specific aim 3**: Scale up of the TD Model to adult humans to estimate tissue level changes due to inhalation exposure in humans

- **Objective 4**: Alveolar mechanics model in multiple species to link surfactant dysfunction to organism-scale lung function

  - **Specific aim 1**: Modeling alveolar recruitment/derecruitment in rodents based on normal breathing pressure cycle
  - **Specific aim 2**: Aim 2: Linking bronchoalveolar factors modeled in tissue level model to organism scale alveolar R/D model

– **Specific aim 3**: Formulate human lung function changes based on inhalation exposure

Chapter II

Organism Scale Biodistribution

II.1 Background

This section focusses on developing a whole-body toxicokinetic model for silver nanoparticles (nAg) to estimate tissue and blood distribution of particles and ions for different exposure routes. The Physiologically-Based Toxicokinetic (PBTK) model has been developed for rats and compared with *in vivo* measurements available in the literature [47]. PBPK modeling of NPs in general has not received much attention, mainly due to the lack of reliable physiological and biochemical data. PBPK modeling of nanoparticles faces various challenges, some of which are summarized in Table II.1, including the lack of appropriate physiological and biochemical data. A major problem in this regard is the fact that properties of NPs are a function of their size and surface characteristics. The NPs used in various commercial applications are generally of various sizes and are endowed with unique properties. This makes physiological and pharmacokinetic modeling of NPs a function of particle properties [48] and also the ultimate application for which the NP was manufactured. The varied types of commercial applications of these NPs also make the the modes of human exposure widely varying. However, there have been a number of recent articles on the physiological modeling of NPs. Li *et al.* [24] have reviewed PBPK models of NPs which were developed prior to 2010. There have been modeling efforts for quantum dots

(QD) [49, 50], carbon NPs [51], and also nAg [47].

Table II.1: A partial list of challenges in NP toxicokinetic modeling (compared with "traditional" physiologically-based toxicokinetics)

Toxicokinetic Processes	"Traditional" PBTK Modeling	Nanoparticle PBTK Modeling
ABSORPTION (local)	diffusion and active transport	opsonization (protein binding) in the blood; cellular recognition and internalization (endocytosis, phagocytosis); physical property changes; size dependent
DISTRIBUTION (systemic)	primarily blood circulation	size dependent; distribution via blood influenced by blood vessel endothelium (more effective in fenestrated and discontinuous endothelium); increased importance of lymphatic system; role of reticuloendothelial system; olfactory nerve path to brain
METABOLISM	enzymatic transformation	enzymatic degradation processes may depend on size, shape, coating, etc.
ELIMINATION	excretion	clearance; renal and biliary (size dependent)

II.2 Modes of human exposure

Silver ENM finds its way into a large number of consumer products of daily use and consequently humans are exposed via different routes. An accurate estimate of total exposure to nAg would entail a detailed analysis of the daily activities of an individual. The current work focusses on developing a comprehensive PBPK model for nAg considering all possible modes of exposure and different exposure scenarios. Each mode of exposure requires focus on a specific mechanism in the physiological system.

II.2.1 Dermal exposure

The most common mode of exposure to nAg appears to be dermal exposure [19], due to the wide array of textiles, cosmetics and medical products that contain nAg, that remains in contact with the individual's skin for varying durations of time. A number of different varieties of branded socks have nAg in their fabric to prevent the growth of odor-causing bacteria [25]. For this mode of exposure, the required parameters are the duration of contact with the particular product, the concentration of nAg in the product and the rate of transport of nAg into the skin from the product. Absorption of nAg through burnt skin has been studied for nAg coated wound dressings [52, 53]. However, it is unclear from these studies whether silver ions or silver nanoparticles were actually absorbed into the body. After dermal absorption, particles are generally collected in the lymphatic system and the regional lymph nodes [54]. Kohli and Alpar [54] have tested latex particles of various sizes permeating through pig skin. Larese *et al.* [55] have estimated sub-cutaneous delivery of nAg, measuring Ag concentrations in various sub-cutaneous layers of human skin. Schneider *et al.* [56] have estimated various rates of dermal penetration of particles of various sizes. Kreuter *et al.* [57] investigated the systemic distribution of PMMA NPs in rats, after sub-cutaneous ingestion.

II.2.2 Oral exposure

Silver ENM formulations are used in toothpastes, food-storage containers, and utensils, leading to the possibility of oral ingestion [19]. For oral exposure, the most important phenomena is the absorption, metabolism and excretion of the particles in the gut, followed by hepatic metabolism. Gut absorption of colloidal silver has been studied by Mirsattari *et al.* [58] and Chang *et al.* [59]. Mirsattari *et al.* [58] reported a case of regular daily ingestion of a colloidal silver suspension by a subject which finally proved to be fatal. They analyzed tissue and plasma accumulation of Ag in

the subject post-mortem [58]. Kim *et al.* [60] did an oral toxicity study in Sprague-Dawley rats with 60 nm nAg, in which they quantified the total accumulation of Ag in various tissues and blood 28 days after oral dosage. The *in vivo* tissue accumulation data from Kim *et al.* [60], as well as the data from Mirsattari *et al.* [58] may be used to find values of parameters like gut absorption, fecal excretion, and urinary filtration, by optimization and parameter estimation. However, direct investigation of the rate constants of gut clearance or fecal excretion has not been carried out till date. Since it is known that nAg is not metabolized to any appreciable extent in the gut [61], the intestinal kinetics are functions of particle size rather than the functional properties of the particles. So intestinal transport rates of other similarly sized NPs can be used to provide a rough estimate of these parameters. Hillyer and Albrecht [62] performed a study in mice with gold NPs and evaluated amounts of NPs in various tissues including stomach, and small intestine. The study also involved a range of sizes which can help in formulating size-dependant parameter functions for the various intestinal processes. It is also known that some substances are absorbed from the intestine into the lymphatic system. Hussain *et al.* [63] have reviewed the uptake of particles of various sizes across gastro-intestinal lymphatics.

II.2.3 Inhalation exposure

Humans are unintentionally exposed to nanomaterials produced by industrial and mechanical activities as well as ENMs present in various consumer products in aerosol form, which are primarily taken up by the inhalation route. Inhalation exposure to ENMs results from the use of products such as cleaning sprays, cosmetic sprays (e.g. sunscreen), and coatings in surgical masks and artificial breathing devices. Cosmetics in powder form can also lead to potential inhalation exposures depending on the point of application. There are a number of nAg sprays in the market which are used as disinfectants or room-fresheners. Exposure to environmental airborne NPs also occurs primarily through inhalation. This route of exposure also presents the

easiest route for NP entry into the body due to the large lung surface area and the minimal anatomical barriers limiting access to the body [64]. As opposed to other routes of exposure, inhalation of nanoparticles has been considered as a potential cause of adverse health effects and may have a strong influence on the pulmonary and cardiovascular systems, leading to increased cardiovascular morbidity and mortality [65]. MacCalman *et al.* [34] have developed a detailed PBPK model for NPs with inhalation exposure, validating the model with data for iridium and nAg. For the case of inhalation exposure, deposition in various regions of the airway and dynamics of blood-alveoli distribution is important. The particles are carried along with inspired air along the airway before they reach the alveoli. A fraction of particles are deposited at various locations along the airway and are trapped by the muco-ciliary apparatus. Particles trapped in the mucus layer are transported by the muco-ciliary elevator to the pharynx where a fraction goes to the gut through the GI tract. The rest of the particles in the pharynx are excreted as various mucus secretions during coughing and sneezing. A fraction of the particles reaching the alveoli are taken up by alveolar macrophages by phagocytosis and the rest end up in the pulmonary interstitial space. Many of the inhaled substances are absorbed through the alveoli into blood and also end up in lymph nodes as the lung is conspicuously supplied with lymphatic vessels. Data for systemic absorption of nAg from lungs in rats have been collected by Takenaka *et al.* [33], and Ji *et al.* [66]. *In vivo* data from Takenaka *et al.* [33] were used by MacCalman *et al.* [34] for their PBPK model. There is an additional pathway by which inhaled NPs reach the brain directly. The presence of this olfactory-nervous pathway has been confirmed by Takenaka *et al.* [33], who found inhaled nAg in the olfactory nerve and brain of rats, thus presenting a route bypassing the blood-brain barrier. Takenaka *et al.* [33] have also evaluated Ag concentrations in various tissue compartments: lung, liver, blood, lymph nodes and brain. However, MacCalman *et al.* [34] have not considered pulmonary airway deposition in detail. For an inhalation exposure model, the rates of NP deposition in various parts of the airway

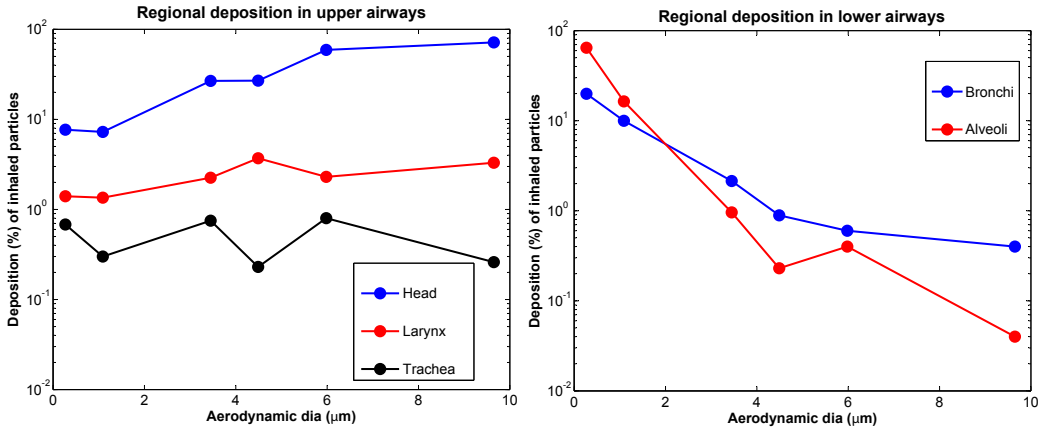

(a) Upper airway (b) Lower airway

Figure II.1: Regional ultrafine particle deposition in mice (based on data from Raabe *et al.* [72]).

for various sizes of particles is a critical determinant [67, 68, 69]. Inhalation dosimetry is well studied in humans, mice, and rats ([70], [71], [72]). The Multiple-Path Particle Dosimetry (MPPD) model [71], originally developed jointly by the Chemical Industry Institute of Toxicology (CIIT, currently The Hamner Institutes for Health Sciences) and the Dutch National Institute for Public Health and the Environment (RIVM), provides estimates of fractional deposition of inhaled sub-micrometer particles at different sections of the airway in rats and in humans. The MPPD software [71] is used to estimate inhalation dosimetry in rats and humans. For mouse, the fractions calculated by [72] for ultrafine particle deposition in the airway are taken (shown in figure II.1). Figure II.2 compares fractional pulmonary deposition in mice, rat, and humans. It can be observed that larger animals have more efficient pulmonary clearance mechanisms and have comparatively smaller fraction of inhaled particles reaching the critical alveolar region.

II.2.4 Injected dosage

Injected dosage is not a common mode of exposure unless the exposure is intentional and the nanoparticles are injected as drug-delivery vehicles or as sensors for imaging.

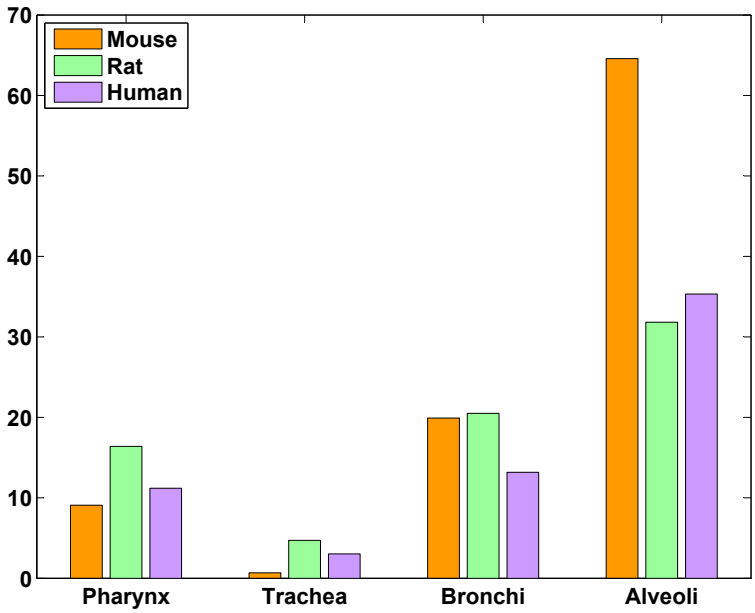

Figure II.2: Comparison of percentage deposition of ultrafine (1 - 20 nm) particles for four different sections of the pulmonary airway in three different species (Data for mice from Raabe *et al.* [72]; for rats and humans from MPPD [71]).

However, it is a common mode of dosage for *in vivo* bio-distribution studies, as it removes the complications of the other modes of exposure described above. Such dosage is important primarily to estimate blood-tissue distribution of nanoparticles and is frequently used in *in vivo* studies involving laboratory animals. The PBPK model by Lankveld *et al.* [47] considers injected dosage regimens in rats and estimates blood-tissue partition coefficients for various tissue compartments. The model by Lankveld *et al.* [47] was first successfully implemented in this thesis and the partition coefficients were incorporated for the detailed PBPK model developed later.

II.2.5 Metabolism

Despite the fact that there exists ample evidence of NP distribution to the liver, there is no data on the metabolism of the NPs in the liver or elsewhere in the body. It can be assumed that nanoparticles would be taken up by macrophages like the Kupffer cells [24] in the liver and then metabolized. However, not much information is present in the literature on the rates of metabolism. Colloidal silver is known to

be metabolized in the human body [73]. Other than biochemical transformations, we also need to consider any other physical change which can transform particle size and charge of the nanoparticles. The ADME (Absorption, Distribution, Metabolism, and Elimination) of silver nanoparticles is a strong function of their size, charge, and level of aggregation. Recently, Stebounova *et al.* [74], studied nanoparticle transformations in simulated biological media and their data may be used to estimate conversion of nAg to silver ions. Ho *et al.* [75], have estimated the oxidative dissolution of silver nanoparticles in biological fluids. Such oxidative processes are known to take place in the hepatocyte.

II.2.6 Excretion

Fecal and biliary excretion are both predicted to be important routes of nanoparticle elimination from the body [19], however definite rates have not yet been measured in animal studies. It was reported that treatment of burn wounds with nAg containing wound dressings (Acticoat) lead to detectable levels of silver in urine of the patient [52]. However, it is plausible to conclude that a large portion of the silver in urine might be due to silver ions rather than nAg since nAg are not known to be soluble in water and also because the glomerular endothelial cells have fenestrations which are 70-90 nm in diameter. Choi *et al.* [76], showed that a cut-off size of < 5.5 nm exists for Qdots, with respect to glomerular filtration, which ensures efficient and complete renal clearance. Kim *et al.* [60], showed that in rats after an oral dosage of 60 nm nAg, there is an appreciable and dose-dependent accumulation of silver in the kidney which is more than the accumulation noted in other tissues. This might be due to insufficient renal excretion of the particles. Renal clearance of larger-sized nanoparticles could thus be very slow but still possible [77]. So the renal excretion of silver nanoparticle would depend on the size of the particles, unless the particles are metabolized to silver ions, which are readily soluble and may be excreted, again showing that the rate of transformation of nAg to silver ions is very important and

needs to be estimated in any toxicokinetic model. Biliary excretion of nAg has not been studied, however Furumoto *et al.* [78], studied biliary excretion for polystyrene microspheres in rats, and in the absence of data specific to nAg, such data can be used to estimate the biliary excretion rates.

Table II.2: Summary of information available for PBPK modeling of silver nanoparticles (white - data available for nAg, yellow - data available for NPs similar to nAg, orange - data available for other NPs, red - no data available)

Types of parameters		Parameter to be estimated	References	Species tested	NP type	NP sizes evaluated (in nm)
Parameters based on exposure routes	Oral	Stomach transport	Hillyer and Albrecht [62]	Mice	Gold NP	4,10,28,58
		Intestinal absorption(blood)	Hillyer and Albrecht [62]	Mice	Gold NP	4,10,28,58
		Intestinal absorption(lymph)	Hussain *et al.* [63]	Various species	Various NPs	Various sizes
	Inhalation	Airway deposition	MPPD[1] [71]	General	Any particle	All sizes
		Alveolar exchange	MacCalman *et al.* [34]	Rat	Silver & iridium NP	15 - 20
		Olfactory transport	Takenaka *et al.* [33]	Rat	Silver NP	15 - 20
		Lymphatic absorption	Takenaka *et al.* [33]	Rat	Silver NP	15 - 20
	Dermal	Dermal permeation	Larese *et al.* [55]	Human	Silver NP	9.8 - 48.8
		Lymphatic accumulation	Kohli and Alpar [54]	Pig	Latex particles	50,100,200,500
		Subcutaneous blood uptake	Kreuter *et al.* [57]	Rat	PMMA[2] NP	10 - 60
Other physiological parameters	Excretion	Renal excretion	Choi *et al.* [76]	Rat	Quantum dots	4.4 - 8.7
		Fecal excretion	-	-	-	-
		Biliary excretion	Furumoto *et al.* [78]	Rat	Polystyrene NP	50
	Tissue uptake	Partition coefficients	Lankveld *et al.* [47]	Rat	Silver NP	20,80,110
Biochemical parameters	Metabolism rates	Hepatocyte metabolism	-	-	-	-
		Macrophage metabolism	-	-	-	-
	Physical deformation	Agglomeration/ Disintegration	Stebounova *et al.* [74]	Biological fluid	Silver NP	10
		Dissolution	Stebounova *et al.* [74]	Biological fluid	Silver NP	10

1:Multiple-Path Particle Dosimetry, 2:Poly methyl-methacrylate

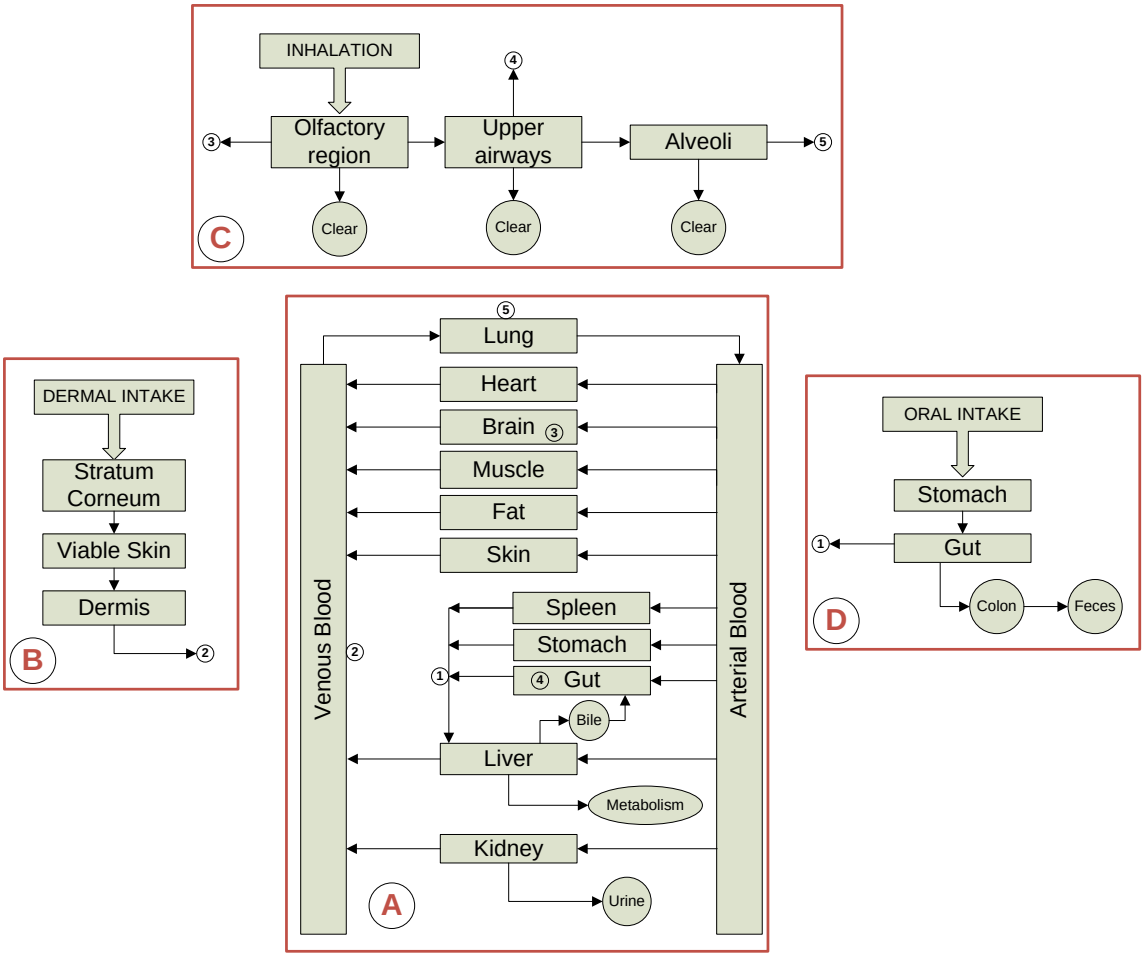

Figure II.3: Steps in the development of a multi-exposure silver nanoparticle PBPK model, block A being the core part, with blocks B,C, and D adding on in the case of dermal, inhalation, and oral exposures respectively

II.3 PBPK modeling approach for nanosilver

PBPK models for silver nanoparticles were developed in the recent past by Lankveld *et al.* [47] and by Bachler *et al.* [79]. The model by Lankveld *et al.* [47] is a simple model using 5 tissue compartments: liver, kidney, spleen, blood, and remaining tissues in rats. It considers elimination as a lumped process including renal and fecal elimination and metabolic processes. Bachler *et al.* [79] has developed a detailed PBPK model for nAg and ionic silver, considering dermal, oral, and inhalation exposure routes. However, the uptake of nAg from each of the exposure routes was

approximated using a single absorption fraction. For NPs, size, shape, and coating chemistry affect the rates of these processes and they need to be separately considered to understand the risk from different particle sizes. Considering individual elimination processes also allows one to utilize biomarker measurements. Processes of agglomeration, disintegration and dissolution also need to be considered in the case of nAg.

II.4 Development of a multi-chemical, multi-exposure PBPK model for silver nanoparticles and ionic silver

As summarized in section II.1, exposure to nAg can occur from a wide array of consumer products which can result in oral, inhalation, and dermal exposure. Prediction of tissue biodistribution of nAg requires simulation of realistic exposure scenarios. A multiscale, multi-route PBPK model has been developed which considers NPs of multiple sizes and also ionic silver for a complete understanding of the fate of the material inside the animal body. The model has been developed using published mechanistic data and information from literature concerning tissue and cellular distribution and metabolic reactions within them. PBPK models traditionally assume tissue:blood equilibrium and estimate chemical biodistribution by equilibrium partition coefficients (PC). However, for NPs which are 1-2 orders of magnitude larger in size than traditional chemicals, assumption of equilibrium might not be correct. Besides, cellular uptake, there are other important particle-specific mechanistic processes (particle adhesion, phagocytosis, etc.) which need to be considered for nanoparticles [48]. The PBPK model developed here considers the major partico-kinetic processes which are considered important over multiple scales of the whole body, tissue and the cells.

The development of the PBPK model has been accomplished in modular fashion, due to the multitude of mechanisms occurring at every level. Figure II.3 shows the

essential parts of the multi-route PBPK model. Block A represents the biodistribution of chemicals among tissues and blood. This module helps analyze the blood-tissue exchange without the complications created by gut absorption or inhalation. Block A is also used to compare and parametrize the model with *in vivo* measurements, in most of which the dosage form is intra-venous injection. Blocks B, C, and D represent the various complications due to multiple routes of exposures. Block A is the core of the PBPK model, with the other blocks adding on various complexities depending on the mode of exposure.

II.4.1 Tissue-blood particokinetics

The assumptions and mechanisms true for small molecules cannot be used for nanoparticles. Their size and nature make them unique with respect to transport, absorption and metabolism. With respect to size, they are similar to biomolecules or drug molecules, which are delivered to target tissues. However, with respect to chemical characteristics they behave like xenobiotics and are attacked and phagocytosed by macrophages in the blood and tissues. Unlike large macromolecules such as proteins and carbohydrates, they are not recognized by cell receptors which are responsible for internalizing essential macromolecules. So their tissue uptake depends on many possibilities and cannot be described by simple flow-limited or diffusion-limited approaches. Table II.3 shows the various modeling approaches in the current literature regarding cellular uptake of particles circulating in blood. The various particle-specific processes which affect tissue distribution of nanoparticles are summarized below. The individual processes have been discussed in detail in subsequent sections.

- Lympho-osmotic exchange between vascular and interstitial compartment of tissues
- Cellular endocytosis of particles
- Particle adhesion and dissociation at blood vessel walls

Table II.3: Various approaches to modeling the blood-tissue exchange of chemicals

Modeling methodology	Mechanism considered	Critical factors & processes	Particle type	References
Vascular transport	Theoretical modeling	Depletion layer, binding to vascular wall	General particles	Shah [80]
Flow-limited model	*In vivo* measurements	Partition coefficients	Qdots	Lee *et al.* [50]
Diffusion-limited model	Data-fitting	Zero-order coefficient	silver nanoparticles	Lankveld *et al.* [47]
	Molecular dynamics	Diffusion coefficient	General particles	Li *et al.* [24]
	Hill equation	Distribution coefficient	Qdots	Lin *et al.* [49]
Two-pore model	Data-fitting	Fluid filtration, lymph flow rate	Monoclonal antibodies	Davda *et al.* [81]
Active transport	Experiment and modeling	Positive charge, cellular motors	Silica particles	Orr *et al.* [82]
Particle adhesion	Deterministic & Stochastic	Darcy's Law, Force balance, Brownian motion	General particles	Su *et al.* [83]
Particle internalization	Endocytosis	Aspect ratio, critical radius	General particles	Decuzzi and Ferrari [84]
	Phagocytosis	Clathrin mediation	Xenobiotics, virus	Conner and Schmid [85]

- Phagocytosis of particles in tissues, blood, and lymph
- Dissolution of silver nanoparticles into ionic silver

Tissue uptake of nanoparticles

PBPK models traditionally use flow-limited or diffusion-limited tissue uptake models for small chemical molecules. The transport of molecules from the blood stream in capillaries to the cells in tissues takes place through the lipid-bilayer of cell membranes through passive diffusion through the pores or by active transport which is generally receptor-mediated. Generally, the pore-size of cell membranes is of the order of 0.3-0.5

nm [86]. Lipid soluble molecules of larger sizes can enter cells simply by dissolving in the lipid bilayer. Small chemical molecules such as metals, or other inorganic chemicals can enter cells by passive diffusion through the pores. Bio-molecules which are generally larger in size are transported into the cells with the help of active transporters or receptors. The uptake of nanoparticles, which are mostly bigger than 1 nm is not clearly understood. However, it is clear that their transport cannot be described by flow-limited passive diffusion. To elucidate the mechanisms of particle permeation in cells and the effect of size, shape and charge, various macro and micro-scale approaches have been described in the literature.

Transport from vascular to interstitial space

Flow-limited models have traditionally been successful for small chemicals but their application to nanoparticles is problematic. Flow-limited models assume a fast equilibrium to be attained between blood in the capillary endothelium and tissue interstitial space. The equilibrium concentrations are given by partition coefficients (PC) which are generally estimated based on the lipophilicity of the chemical and that of the tissue [87]. Lee *et al.* [50], applied the flow-limited assumption with limited success for a PBPK model for Qdots of various sizes. However, the model predictions did not match the measured levels in many tissues, mostly for the early time points. More recently, Lankveld *et al.* [47], used flow-limited assumptions but to match the observed slower *in vivo* kinetics, they used a parameter called flow-limiter to make the tissue blood flows limiting. This assumption seems very artificial and is similar to using a diffusion-limited approach with a first-order diffusion constant. So, despite the fact that partition coefficients are used, this model actually uses a diffusion-limited approach. It is also difficult to capture the effects of size, shape and other physical characteristics of NPs, in a single parameter, i.e. the partition coefficient. So, a diffusion-limited approach has been replicated here. Lin *et al.* [49] have

argued that particle transfer processes might be saturable and have used a time dependent, saturable, distribution coefficient (DC) modeled based on the Hill equation. Nanoparticle extravasation is dependent on capillary fenestrations which are different for different tissues. Capillaries may be relatively continuous (as in brain, muscle, lung, etc.) or fenestrated (as in kidney) or discontinuous (as in liver and spleen) [49]. Lin *et al.* [49], considered these factors when designing distribution coefficients. All these models have considered the transport of the chemicals from the vascular blood supply to the interstitial space, but have not included the flow inside the interstitial space, which is regularly drained by lymphatic circulation. Davda *et al.* [81], considered a two-pore model for simulating the delivery of monoclonal antibodies in rats and also combined lymphatic circulation draining the interstitial space between cells in their model. They considered capillary fenestrations of 2 sizes and different flux rates through the fenestrations. In this model, the two-pore model of Davda *et al.* [81] has been used to simulate the transport of particles from the vascular to the interstitial space. The model takes into account the different sizes of capillary fenestrations in different tissues which can be a limiting factor in particle transport. It considers both convective and diffusive transfer through large and small pores and also osmotic recirculation between blood and interstitium. The relevant equations for this section are described in Appendix A.

Cellular uptake from the interstitial space

All published models described in the previous section, have considered transport from vascular to interstitial space and have assumed the intracellular space to be in equilibrium with the interstitial space. However, for uptake of NPs, the pores in the cell membrane might be a limiting factor. Cells have active transport mechanisms to deliver various substances into the cell. Sometimes NPs based on their shape, size or charge mimic the characteristics of these substances [88] and might be actively transported into cells. Some cells, especially alveolar cells have been suggested to have

active transport mechanisms for uptake of inhaled NPs using the actin machinery [82]. The process of cellular uptake might be considered as composed of two processes: the adhesion of the particles to the cells and the ultimate internalization by the cell. Due to the cell being a biological entity with its own mechanisms, the latter process seems to be a biological process which depends on the type of cell. However, the first process of adhesion to a cell surface is largely a physical process depending on the mutual surface properties of particle and cell and also on the rate of fluid flow around the cell. Nanoparticles are large enough to be considered as discrete particles, rather than a homogenous solution and hence the mechanism of particle adhesion to cells from the surrounding interstitial fluid may be considered as a physical problem described by physical theories concerning particle dynamics immersed in a fluid. It might be modeled as a deterministic problem considering all the forces acting on a particle immersed in a flowing fluid [83] or as a stochastic problem considering probabilities based on binding kinetics and Brownian motion [80]. Such models have been developed but not applied in the context of a PBPK model because of the multiple scales involved. Particle internalization by cells happens generally by endocytosis or phagocytosis depending on the type of cell. Phagocytosis would be considered for macrophages like the Kupffer cell of the liver or WBCs in blood, which are known to treat nanoparticles as foreign agents and capture them for removal from the body [85].

II.5 Results of the PBTK model

Figure II.4 shows the comparison of model prediction and *in vivo* measurements for injected doses of 23.8 g of 20nm nAg in rats on the 1st, 3rd, and 5th days (*In vivo* measurements in rats from Lankveld *et al.* [47]). Figures II.5 shows the comparison between model prediction and measurements for nAg amounts in liver, kidney, lung, and spleen for the same multiple dose at the 1st, 3rd, and 5th days. The figures show

good comparison between model predictions and observed results.

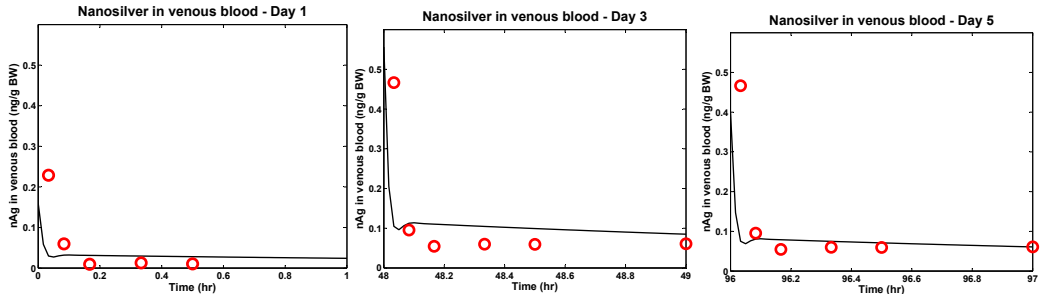

(a) Blood (Day 1) (b) Blood (Day 3) (c) Blood (Day 5)

Figure II.4: Blood concentrations of 20nm nAg, for 1, 3, and 5 day after bolus injection doses at the beginning of 1st, 3rd, and 5th day. Comparison of model prediction (black line) and measurements from Lankveld *et al.* [47] (in red)

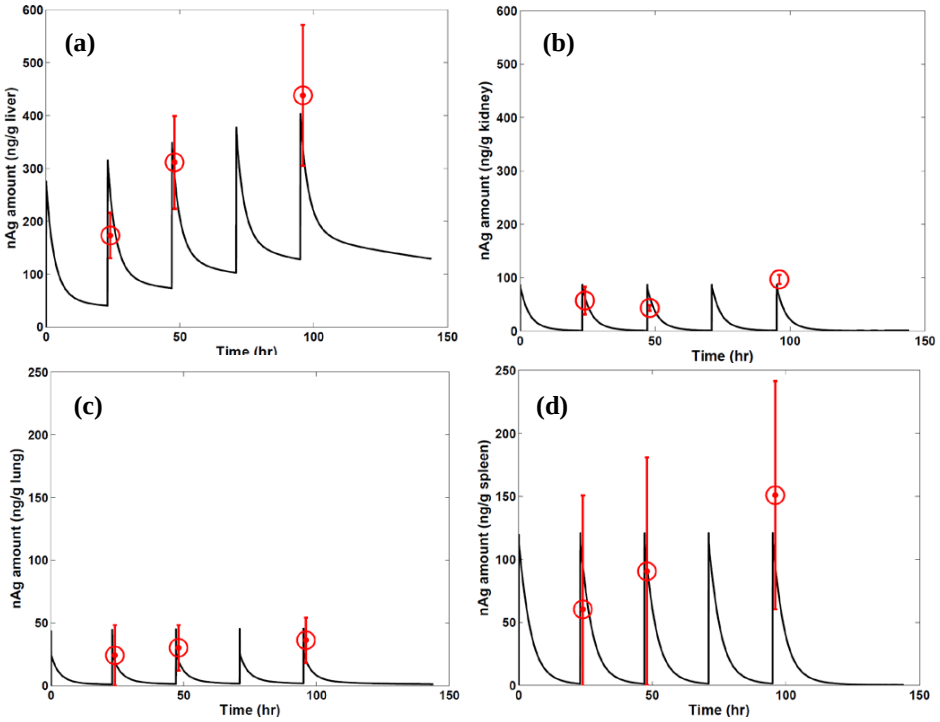

Figure II.5: Concentrations of 20nm nAg in (a) liver, (b) kidney, (c) lung and (d) spleen after multiple bolus injection doses at the beginning of 1st, 3rd, and 5th day; comparison between model predictions and measurements from Lankveld *et al.*, 2010 [47] (in red)

Chapter III

Nano Scale Transformation

III.1 Background

Engineered Nanomaterials (ENMs) differ from other conventional chemicals in the number of independent nanoscale properties, which results in complex particle-particle and particle-media interactions with all chemical and biological media. Properties of ENMs (such as size, shape, chemical composition, surface area, zeta potential, nature of coating) and media properties (such as density, viscosity, pH, etc.) affect the dynamic transformation of the ENMs involving agglomeration, dissolution, diffusion, and sedimentation. All of these processes lead to a change in size, shape, and chemical composition of the ENMs and are liable to affect their dispersion and toxicity in biological and ecological systems. Hinderliter *et al.* [41] showed that the actual amount and form of the NPs reaching the cells over time are markedly different when NP diffusion and settling area are taken into account. Limbach *et al.* [89] studied the effects of NP transformation on cellular uptake *in vitro* and found agglomeration to be a key mechanism controlling cellular uptake.

Physicochemical transformation of micro and nano-sized particles has been studied widely in relation to both environmental exposure and biological toxicity. Mathematical modeling of dynamics of particles in fluids has been studied widely [90]. Researchers have employed the aerosol general dynamic equation (GDE) to model

transformation of particulate matter in environmental and biological systems [67, 91]. Models like the Aerosol GDE are very complex equations and can be solved using suitable simplifying assumptions and with the help of computational techniques. The ISDD (*In vitro* Sedimentation, Diffusion and Dosimetry) model developed by Hinderliter *et al.* [41] models the major particokinetic processes for nanoparticles in a differential equation-based framework for use in *in vitro* dosimetry. However, the ISDD model only considers non-interacting particles and does not include dynamic agglomeration or dissolution which would be expected to occur simultaneously for nAg, along with the other processes. Further, the use of event-based stochastic models is more amenable for modeling event-based phenomena like agglomeration [92]. More recently, Liu *et al.* [93] developed a direct simulation Monte Carlo (DSMC) model which included dynamic agglomeration along with the other processes included in the ISDD model in a stochastic framework. However, like the ISDD model, it also did not consider NP dissolution. Prediction of biological toxicity will be rendered incomplete without a simultaneous quantification of silver ion production by dissolution as the "Trojan-horse mechanism" is widely known to play a critical role in cellular toxicity due to nAg [94].

Particle size, shape, and surface properties which change dynamically in any media also affect *in vitro* cell cultures differently [95]. The model developed in this section mechanistically describes the complete set of processes involved in the interaction between ENMs and their environment and includes the entire gamut of transformational processes important for nanoparticles, including aggregation, diffusion, sedimentation, and dissolution of nanoparticles in a predictive and mechanistic framework, which is applicable to environmental as well as biological systems. The model is first implemented in an *in vitro* medium for comparison with *in vitro* measurements, and then later extended to an *in vivo* system to predict nAg particokinetics in the alveolar lining fluid.

III.2 Modeling transport of particles in medium

Mathematical description of particle transport in fluids (diffusion, advection, and gravitational settling) has been available for almost a century [96]. In biological and environmental media, the processes of gravitational sedimentation, diffusion, agglomeration, and dissolution occur simultaneously. Each process has been separately modeled using well-known mechanistic rate equations and each rate has been incorporated in a stochastic framework utilizing a Direct Simulation Monte Carlo (DSMC) scheme.

Gravitational sedimentation of NPs can be described mathematically by Stokes' Law [97], which describes the sedimentation rate (V) of particles in a solution, as a function of medium viscosity (μ), the densities of particles and media (ρ_{p}, ρ_{f}), diameter of the particles (d), and the acceleration due to gravity (g). The ISDD model of Hinderliter *et al.* [41] modeled gravitational settling using Stokes' Law and Sterling's modification of Stokes' Law for agglomerates. For single particles, Stokes' Law is given by:

$$V = \frac{g(\rho_{\mathrm{p}} - \rho_{\mathrm{f}})d^2}{18\mu} \tag{III.1}$$

Equation III.1 defines the sedimentation velocity for single particles. The agglomerate sedimentation velocity can be described by Sterling's equation [98] as:

$$V_{\mathrm{agg}} = \frac{g(\rho_{\mathrm{agg}} - \rho_{\mathrm{f}})}{18\mu} d^{3-F_D} d_{\mathrm{agg}}^{F_D-1} \tag{III.2}$$

Here, effective agglomerate density, ρ_{agg} and effective agglomerate diameter, d_{agg} are properties of agglomerates which can be estimated from individual particle properties

according to Sterling [98] as:

$$\begin{aligned} &\text{i. } d_{\text{agg}} = d\left(\frac{n}{F_{\text{P}}}\right)^{1/F_D} \\ &\text{ii. } \varepsilon_{\text{agg}} = 1 - \left(\frac{d_{\text{agg}}}{d}\right)^{F_D-3} \\ &\text{iii. } \rho_{\text{agg}} = (1-\varepsilon_{\text{agg}})\rho_{\text{p}} + \varepsilon_{\text{agg}}\rho_{\text{f}} \end{aligned} \tag{III.3}$$

In equations III.2 and III.3, the parameters F_{P} and F_{D} stand for packing factor and fractal dimension respectively. Agglomerates are not homogenously packed units but have a fractal structure [98]. The fractal dimension, F_{D} generally varies between 1 and 3, with a F_{D} of 3 representing a perfect sphere with no fractal structure. Packing factor, F_{P} varies between 0 and 1, and reflects the ratio of solid volume and total volume of an agglomerate, with a F_{P} of 1 reflecting total absence of pore space in the agglomerate. ε_{agg} is the effective porosity of the agglomerate and n is the number of primary NPs in the agglomerate.

The Stokes-Einstein equation describes the rate of diffusion (D) as a function of particle diameter (d), medium viscosity (μ), and temperature (T), as:

$$D = \frac{k_{\text{B}}T}{3d\pi\mu} \tag{III.4}$$

Here k_{B} is Boltzmann's constant.

Advection (transport due to fluid motion) has not been considered here, as it is negligible in most *in vitro* and *in vivo* toxicological systems. However, advection needs to be included for most environmental media and biological fluids such as blood.

III.3 Modeling dynamic agglomeration of NPs

Aggregation of NPs in solution is a complex phenomenon because it is affected by diffusion of the individual particles and agglomerates and by the attractive and repulsive

forces acting between each other. Aggregation of NPs in a medium can be modeled using the Smoluchowski equation [99]. Smoluchowski modeled the fast coagulation of non-interacting particles using a convection-diffusion equation and developed a population-balance equation (PBE) for the development of aggregates of k particles by the collision of aggregates with i and j particles (where $i + j = k$). The PBE developed by Smoluchowski can be described as:

$$\frac{dn_{\mathrm{k}}}{dt} = \frac{1}{2}\sum_{i=1;j=k-i}^{j=k-1} \beta_{\mathrm{ij}} n_{\mathrm{i}} n_{\mathrm{j}} - n_{\mathrm{k}} \sum_{i=1}^{\infty} \beta_{\mathrm{ik}} n_{\mathrm{i}} \tag{III.5}$$

Here n_{i} is the particle number concentration of the i^{th} agglomerate, and β_{ij} is the agglomeration rate constant between the i^{th} and the j^{th} agglomerates. The agglomeration rate constant β_{ij} is given by:

$$\beta_{\mathrm{ij}} = \frac{2k_{\mathrm{B}}T}{3\mu}(r_{\mathrm{i}} + r_{\mathrm{j}})(\frac{1}{r_{\mathrm{i}}} + \frac{1}{r_{\mathrm{j}}}) \tag{III.6}$$

Here, r_{i} and r_{j} are the effective radii of the 2 colliding agglomerates, the effective radii being calculated from equation III.3 based on the number of primary particles constituting them. Smoluchowski's equation does not consider inter-particle attractive or repulsive interactions. The PBE equation developed by Smoluchowski can be modified to include such inter-particle interactions using the DLVO (Derjaguin-Landau-Verwey-Overbeek) theory. This involves replacing the agglomeration rate constant, β in equation III.5 by the modified agglomeration rate constant, k, where $k = \beta/W$, W being the stability ratio. The stability ratio is defined by the ratio of the total number of collisions between particles and the number of collisions that result in agglomeration [99] and is a measure of the stability of the particle dispersion. McGown and Parfitt [100] used the DLVO theory to formulate an expression for W_{ij},

the stability ration for the i^{th} and j^{th} agglomerate pairs, as follows:

$$W_{\text{ij}} = \frac{\int_2^\infty \frac{\beta(s)}{(s+2)^2}.a.\exp(\phi_{\text{T,ij}}/kT).ds}{\int_2^\infty \frac{\beta(s)}{(s+2)^2}.a.\exp(\phi_{\text{A,ij}}/kT).ds} \tag{III.7}$$

The denominator numerator in equation III.7 represents the number of collisions that result in agglomeration and is a function of $\phi_{\text{A,ij}}$, the attractive Van der Waal's electric potential while the numerator represents the total number of collisions and is a function of $\phi_{\text{T,ij}}$. The total interaction potential, $\phi_{\text{T,ij}}$ is the sum of the attraction potential, $\phi_{\text{A,ij}}$ and the electric repulsion potential, $\phi_{\text{R,ij}}$ for the pairs of agglomerates. s is a dimensionless distance between the pair of agglomerates given by: $s = 2R/(r_{\text{i}}+r_{\text{j}})$, where R is the distance between the centers of the 2 agglomerates, and $r_{\text{i}}, r_{\text{j}}$ are the radii of the agglomerates estimated by equation III.3. The stability equation (equation III.7) integrates the interaction potential over the entire range of distance from infinite distance of approach to collision, which is represented by $s = 2$. The attractive Van der Waal interaction potential is given by the expression proposed by Gregory [101] that accounts for the electromagnetic retardation effect:

$$\phi_{\text{A}}(h) = -\frac{Ar_{\text{i}}r_{\text{j}}}{6h(r_{\text{i}}+r_{\text{j}})}\left[1 - \frac{bh}{\lambda}ln\left(1+\frac{\lambda}{bh}\right)\right] \tag{III.8}$$

Here, h is the distance between the surfaces of the agglomerates, A is the Hamaker constant, b is a constant with a value of 5.32, and λ is the characteristic wavelength for the reaction = 100 nm.

The repulsive interaction potential between the agglomerates can be expressed by the electric double layer (EDL) interaction potential, the expression for which was developed using the Linear Superposition Principle by Gregory [102] as:

$$\phi_{\text{R}}(h) = 128\epsilon\pi\left(\frac{kT}{Ze}\right)^2\left(\frac{r_{\text{i}}r_{\text{j}}}{r_{\text{i}}+r_{\text{j}}}\right)\gamma^2\exp(-\kappa h) \tag{III.9}$$

Here, ϵ is the permittivity of the medium, Z is the valence of ions in the medium,

e is the elementary charge, κ is the Debye-Hückel parameter, and γ is the reduced surface potential which is a function of the surface zeta potential ζ of the particles and is given by:

$$\gamma = tanh\left(\frac{Ze\zeta}{4k_{\mathrm{B}}T}\right) \tag{III.10}$$

The Debye-Hückel parameter, κ is expressed in terms of the ionic strength, I of the medium as:

$$\kappa = \sqrt{\frac{2N_{\mathrm{A}}Ie^2}{\epsilon k_{\mathrm{B}}T}} \tag{III.11}$$

where, N_{A} is the Avogadro's number. Then the agglomeration rate constant, $k_{\mathrm{agg,ij}}$ can be calculated as:

$$k_{\mathrm{agg,ij}} = \beta_{\mathrm{ij}}/W_{\mathrm{ij}} \tag{III.12}$$

III.4 Modeling nanoparticle dissolution

NP dissolution processes depend on the particular chemistry of the NP and the ions present in the media. The model developed here has been demonstrated for citrate-stabilized silver NPs (nAg) and so the chemical equations described here are based on the particular chemistry of nAg and citrate. However, the model development is generic and any other NP-media combination can be modeled, provided the details of the particular chemistry are available. nAg is oxidized by dissolved oxygen (DO) in the media and the reaction is also influenced by the protons (H^+) in the media. The chemical reaction for the oxidation of Ag in solution can be expressed as [103]:

$$Ag_{(s)} + \frac{1}{4}O_{2(aq)} + H^+_{(aq)} \longleftrightarrow Ag^+_{(aq)} + \frac{1}{2}H_2O_l \tag{III.13}$$

III.4.1 Chemical equilibrium

The chemical equilibrium for the reaction can be assessed using Nernst equation, as:

$$E_{\text{net}} = E^{\circ} - \frac{RT}{nF}\log\left(\frac{[Ag^{+}]}{[H^{+}][O_2]^{1/4}}\right) \tag{III.14}$$

Here, R is the Universal Gas constant, T is the temperature of the reaction media, F is Faraday's constant, and n is the difference in the number of molecules between reactants and products based on reaction stoichiometry. $E_{\circ}$ is the standard reaction potential (at $25^{\circ}C$) for the reaction whose value is 0.47 volts [104]. E_{net} is the net free energy released by the reaction and needs to be negative for the reaction to proceed. The forward reaction given by equation III.13 stops when chemical equilibrium is reached, i.e., when E_{net} becomes positive. Anions present in the media, like phosphate or sulfide ions, would increase the rate of silver oxidation by precipitating the produced Ag^{+} ions as their respective salts and shifting the equilibrium to the rightward in equation III.13.

III.4.2 Nanoparticle surface reaction

According to the stoichiometric equation, the release rate of Ag^{+} ions can be expressed by an ordinary differential equation as:

$$\frac{d[Ag^{+}]}{dt} = k[Ag][O_2]^{0.25}[H^{+}] \tag{III.15}$$

Here, $[Ag^{+}]$, $[Ag]$, $[O_2]$, and $[H^{+}]$ represent the concentrations (in mol/L) of Ag ions, solid Ag, DO, and protons respectively and k is the reaction rate constant. For reactions involving NPs, the size and surface area of the NPs becomes a limiting criteria, as the reactions would depend on mutual collisions with the other chemical agents in the system [105]. Thus the reaction rate would be limited by the surface area of the NPs in the solution rather than by the concentration of solid Ag. So $[Ag]$

in equation III.15 would be replaced by $\pi d^2.[AgNP]$, where, $[AgNP]$ represents the number concentration of AgNPs. The reaction rate constant k would also depend on the temperature (T), and the activation energy (E_a) of the chemical reaction. Based on the hard sphere collision theory, the rate constant can be expressed as [105]:

$$k = A_o f_A (\pi d^2)[AgNP]\left(\frac{8k_B T}{\pi m}\right)^{1/2}[O_2]^{0.25}[H^+]\exp\left(\frac{-E_A}{RT}\right) \quad \text{(III.16)}$$

Here, R is the Universal Gas Constant and A_o is a scaling factor. f_A is the fraction of the NP surface area that is exposed and available for reaction. Due to the presence of coatings and stabilizing agents, the entire surface area of the NPs might not be exposed to reaction. Estimation of the available surface area is dealt with in the next section. $[H^+]$, the concentration of hydrogen ions in the solution, can be related to the pH of the solution as: $[H^+] = 10^{-pH}$. $[O_2]$ represents the concentration of dissolved oxygen (DO) in the solution which is the primary oxidizing agent. DO is responsible for the oxidation of ENMs and their coatings in solution. Presence of DO needs to dynamically accounted for not only in *in vitro* systems but also in *in vivo* and ecological systems, for modeling the dynamics of ENMs.

III.4.3 Citrate stabilization

The oxidation of Ag to Ag^+ is also affected by other chemicals present in the media. ENMs are usually coated or stabilized by a chemical which acts as a reducing agent and prevents the oxidation of Ag. In this study, a specific example of citrate-stabilized nAg has been demonstrated, where the citrate ions act as a reducing agent. Citrate ions are oxidized by DO in the media and the reaction can be formulated as:

$$\frac{1}{18}CA^{3-}(aq) + \frac{1}{4}O_2(aq) \longleftrightarrow \frac{1}{6}CO_2(aq) + \frac{1}{6}HCO_3^-(aq) + \frac{1}{18}H_2O_l \quad \text{(III.17)}$$

where, CA^{3-} represents the trivalent citrate ion $C_6H_5O_7^{3-}$. The rate constant for the oxidation of citrate ions can be estimated from the average ion release rates measured

by Zhang *et al.* [103]. Presence of citrate ions as a stabilizing agent around the NPs protects them from oxidation and dissolution in the medium. To quantify the extent of the protection, a variable F_{coat} can be defined as the ratio of the total moles of citrate adhered to the NPs to the total surface area of the NPs.

$$F_{\text{coat}} = \frac{\text{Total moles Citrate adhered to NPs}}{\text{Total SA of NPs in medium}} = \frac{n_{\text{Cit}}}{SA_{\text{T}}} \tag{III.18}$$

The fraction of NP surface area that is available for reaction, f_{A} can be estimated as:

$$f_{\text{A}} = f_{\text{Ao}} . \frac{C_{\text{Cit}}/SA_{\text{T}}}{C^{\text{o}}_{\text{Cit}}/SA^{\text{o}}_{\text{T}}} = f_{\text{Ao}} . \frac{C_{\text{Cit}}}{SA_{\text{T}}} . \frac{1}{F^{\text{o}}_{\text{coat}}} \tag{III.19}$$

Here, C_{Cit} is the concentration of citrate ions. The value of f_{A} calculated here is used in equation III.16. f_{Ao} is the value of f_{A} at the start of the reaction and is dependent on the pH of the medium. Lower pH leads to higher protonation of the citrate ions and leads to greater surface area of NPs exposed to oxidation. f_{A} changes dynamically with time as citrate ions are oxidized in the medium according to equation III.17. $F^{\text{o}}_{\text{coat}}$ is the value of F_{coat} at the start of the reaction and reflects the saturation adsorption of citrate ions on nAg. F_{coat} changes over the course of the reaction due to citrate oxidation and also due to aggregation and sedimentation of the NPs.

III.4.4 Effects of dissolved oxygen

DO is depleted from the system due to both the reactions represented by equations III.13 and III.17. Like the present system, which has been simulated here, reaction systems exposed to ambient air get dynamically replenished by oxygen from the air. The mass transfer of O_2 from the air can be represented as [103]:

$$\frac{dC_{\text{DO}}}{dt} = K_{\text{O2}}(C_{\text{S}} - C_{\text{DO}}) \tag{III.20}$$

Here, K_{O_2} is the mass transfer coefficient for oxygen from air to media and C_S is the saturation concentration of DO in the media at the ambient temperature. Zhang *et al.* [103] measured the initial DO concentration in their medium to be 7.8 mg/L and also estimated the mass transfer coefficient of oxygen K_{O_2} to be 6.01 μmol/L/hr. All relevant parameter values have been summarized in Table III.2.

III.5 Modeling NP behavior using Direct Simulation Monte Carlo (DSMC) method

Modeling dynamic phenomena in dispersed systems involving particle transport and transformation processes has been carried out in the past using the aerosol general dynamic equation (GDE) [67]. The GDE is a population-balance equation similar to the Smoluchowski equation (Eq III.5), which is in principle, an integro-differential equation and can be solved by appropriate discretization in time and space. However, the GDE is a deterministic equation, with process descriptions modeled entirely using pre-determined rate laws. In contrast, stochastic methods such as Monte Carlo (MC) capture the underlying probabilistic nature of the processes and simplifies the programming effort considerably [106]. Event-based processes like agglomeration are generally well suited to be modeled using MC schemes. MC methods enable the inclusion of multiple particle transformation mechanisms in a straightforward manner [92] and also records the history of particle populations, thus providing for a way to visualize the evolution of a particular nanoparticle population in media. Particle transport processes can also be treated in a stochastic manner and included seamlessly into the MC simulation scheme [107].

III.5.1 System geometry

The modeling scheme used here employs a Direct Simulation Monte Carlo (DSMC) method which is a time-driven algorithm [92]. Liu *et al.* [93] used the DSMC method

to model nanoparticle agglomeration and diffusion where they used a constant-number MC method. The constant number DSMC has been used here according to Liu *et al.* [93], but critical modifications have been made to capture the realistic nanoparticle scenarios *in vitro* and *in vivo*. Unlike a cubical control volume used in Liu *et al.*, the control volume used here (shown in figure III.1) reflects the geometry of the Eppendorf® tubes used for the *in vitro* measurements [39]. The model can also be modified for other geometries based on the particular system it simulates. Also, a critical requirement for dosimetry assessment for *in vitro* studies, is to quantify the fraction of NPs settling at the bottom of the system with time. Tracking the amount of NPs settled with time necessitates replication of the exact geometry of the system as settling is affected by shape and size of the vessel and also by the height of the fluid. Dissolution is a critical aspect of toxicological studies with nAg because of the importance of ionic silver in cellular toxicity [19]. The model described here includes dissolution using a particle-based surface area limited reaction mechanism, involving all chemicals and ions in the system.

III.5.2 Steps in the Monte Carlo process

The modeling scheme represented in Figure III.1 shows the control volume (CV) (shown as 1 in Figure III.1) and the actual tube (shown as 2 in Figure III.1), with the actual tube used for measurements shown inset. The CV has been selected to contain 10000 particles, initially all being monomers and uniformly dispersed in the medium. The diameters of the particle population are randomly selected from the Particle Size Distribution (PSD) corresponding to the study. The steps in the MC process are schematically expressed in Figure III.2. The 10000 NPs in the CV are randomly distributed along the vertical height of the CV such that the position z_{i} of the i^{th} NP is randomly selected from the uniform distribution, $U(0, L)$, where L is the height of the CV. The agglomeration rates (K_{agg}) and transport rates (Diffusivity, D, and sedimentation velocity, V) for the NPs in the CV are computed using equation III.1

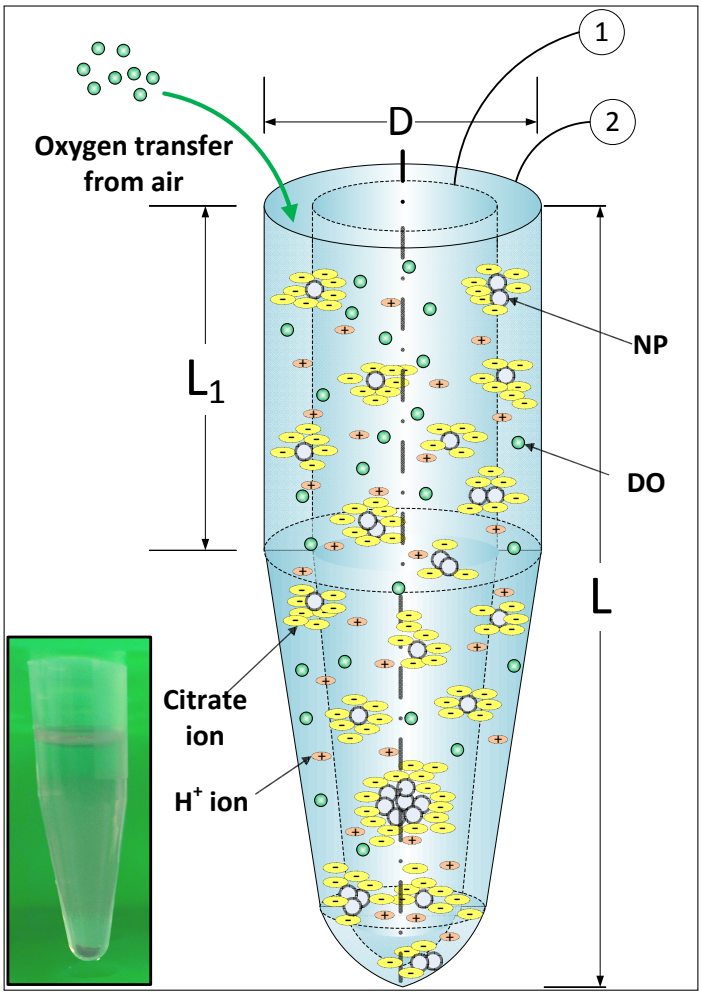

Figure III.1: Schematic diagram showing the implementation of the DSMC method in the *in vitro* system from Leo *et al.* [39], with the control volume (CV)and the actual tube labelled as 1 and 2 respectively along with an image of the actual Eppendorf tube used for the *in vitro* measurements. Nanoparticles, dissolved oxygen (DO), hydrogen and citrate ions are represented in the system. Total length, L and diameter, D are 4 cm and 1.4 cm respectively based on the actual Eppendorf tube used for measurements. L_1, the length of the cylindrical portion of the tube is 0.47 of the total length of the tube. (Diagram not drawn to scale and is representative only) (Figure reproduced from Mukherjee *et al.*, *Journal of Nanoparticle Research*, 16(10), 1-16, 2014, Figure no. 1, with kind permission from Springer Science and Business Media.)

and III.12. In this implementation of the model, 100 agglomeration events have been considered ($N_{\mathrm{t}} = 100$) at every time step. Then the time interval to the next step is calculated using the formula: $\Delta t = \frac{2N_{\mathrm{t}}V_{\mathrm{o}}}{\sum K_{\mathrm{agg}}}$. In the next step, the NPs participating in the 100 agglomeration events are selected by MC selection based on their mutual rates of agglomeration. The method employed is a sampling procedure proposed by Kruis *et al.* [106]. In this procedure, the agglomeration rates for all possible pairs of NPs in the CV are sequentially added, until the sum exceeds the value of a randomly sampled number. The mass of the newly formed agglomerate is the sum of the masses of the pair of NPs undergoing agglomeration and the agglomerate diameter is calculated using equation III.3. Subsequently, the diffusion and settling distances, $z_{\mathrm{D,i}}$ and $z_{\mathrm{S,i}}$ respectively are calculated based on respective transport equations. $z_{\mathrm{S,i}}$ is given by $z_{\mathrm{S,i}} = -v_{\mathrm{S,i}}.\Delta t$, where $v_{\mathrm{S,i}}$ is the particle's Stokes' settling velocity given by equation III.2. The distance travelled due to diffusion, $z_{\mathrm{D,i}}$ is estimated using the approach of Liu *et al.* [93], based on a random number sampled from a normal distribution such that $z_{\mathrm{D,i}} \sim N(0, 2D_{\mathrm{i}}\Delta t)$, where D_{i} is the Brownian diffusivity for the particle calculated from equation III.4. Thus the total vertical distance travelled by the i^{th} particle would be given by: $\Delta Z_{\mathrm{i}} = z_{\mathrm{D,i}} + z_{\mathrm{S,i}}$. NPs which attain a vertical position $z_{\mathrm{i}} \leq 0$ are considered to have settled.

III.5.3 Replacement of particles in the control volume

The DSMC modeling scheme implemented here is a constant number Monte Carlo method and the number of NPs in the CV have to be maintained constant. Accordingly, the particles lost due to settling or agglomeration with other particles need to be replaced continuously. Liu *et al.* [93] used the initial PSD to replace particles in the CV. However, since the particles outside the CV have also been incubated for the same time as the particles inside the CV, the external particles would be expected to be in a similar state of aggregation. Replacing particles from the original PSD would

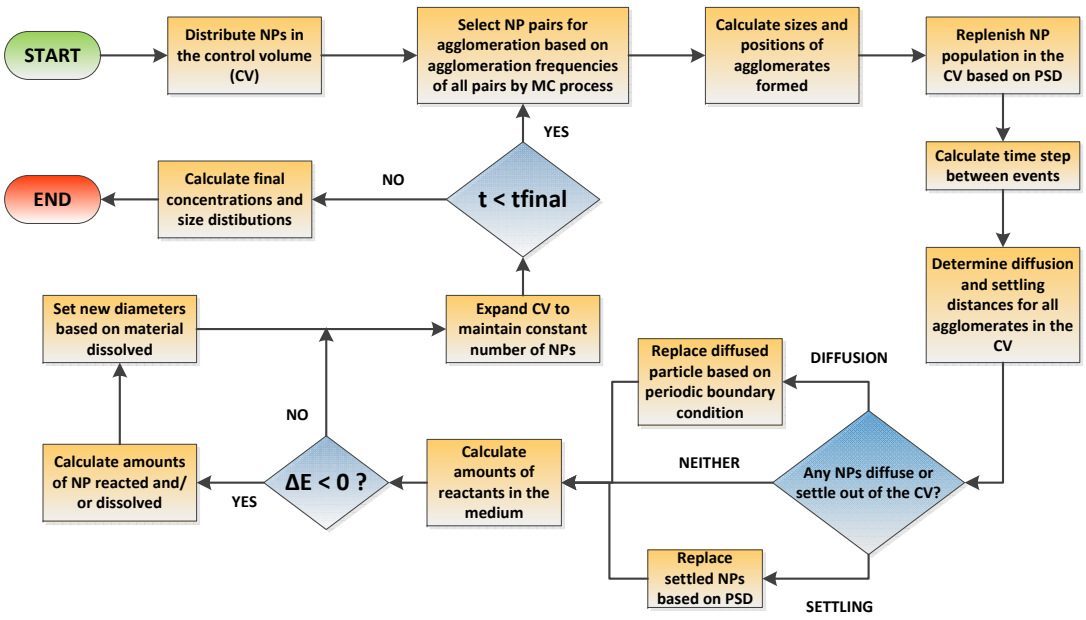

Figure III.2: Schematic showing the steps of the Direct Simulation Monte Carlo method implemented in this study (Figure reproduced from Mukherjee *et al.*, *Journal of Nanoparticle Research*, 16(10), 1-16, 2014, Figure no. 3, with kind permission from Springer Science and Business Media.)

undermine the time evolution of the system as a whole and will introduce virgin particles into the CV. Accordingly, in this DSMC scheme, replacement of particles has been carried out from the PSD of particles within the CV, based on the assumption that the PSD of particles within and external to the CV would be similar because of them being part of the same continuous system.

III.5.4 Inclusion of reaction within the DSMC scheme

The surface area based oxidation reaction mechanism has been implemented in the DSMC scheme using a particle-based approach, where each particle and agglomerate suffers oxidation based on their exposed surface area. The oxidation of citrate and the accompanying decrease in citrate-stabilization is assumed uniform over all the particles in the CV. Dissolution of Ag leads to a decrease in the diameter of the NPs. All individual component particles in an agglomerate are assumed to contribute equally to the dissolution based on their surface area. The diameter of an agglomerate

is calculated by equation III.3. Similarly, the change in diameter of an agglomerate can be calculated based on the changes in diameter of all constituting NPs as:

$$\Delta d_{\text{agg}} = \Delta d. \left(\frac{n}{F_{\text{P}}} \right)^{1/F_D} \tag{III.21}$$

Simultaneously, the reactions of all other chemicals (citrate, oxygen, and hydrogen) are calculated and their individual amounts are updated.

Table III.1: Properties of *in vitro* medium for citrate-stabilized nAg study

Property	Value	Comments
Basic medium	DI water	
Density	1000 kg/m^3	Density of water
Viscosity	0.001 Pa-s	Viscosity of water
pH	3,5,7	Maintained constant by sodium perchlorate buffer
Ionic strength	0.0463,0.0445,0.041 mol/L	Calculated for *in vitro* system
Zeta potential	-18.2,-22.5,-32.5	Estimated by Leo *et al.* [39]
Temperature	37°C	Constant temp.
Initial DO	0.28 mol/m^3	Based on satd. conc. in water
Rel. permittivity	80	Based on water at 20°C
Valence of ions	-1	Based on medium used

III.6 Results and discussion

III.6.1 Aggregation of nAg

Aggregation of citrate-stabilized AgNP was simulated using the model developed in this work, and model predictions were compared with *in vitro* measurements from Leo *et al.* [39] for citrate-stabilized AgNP incubated for 7 days in a sodium perchlorate buffer. The values of the parameters pertaining to the incubation medium are summarized in Table III.2. Values of other parameters used in the implementation of the model are also shown in Table III.2. Figures III.3(a), (b), and (c) show comparisons

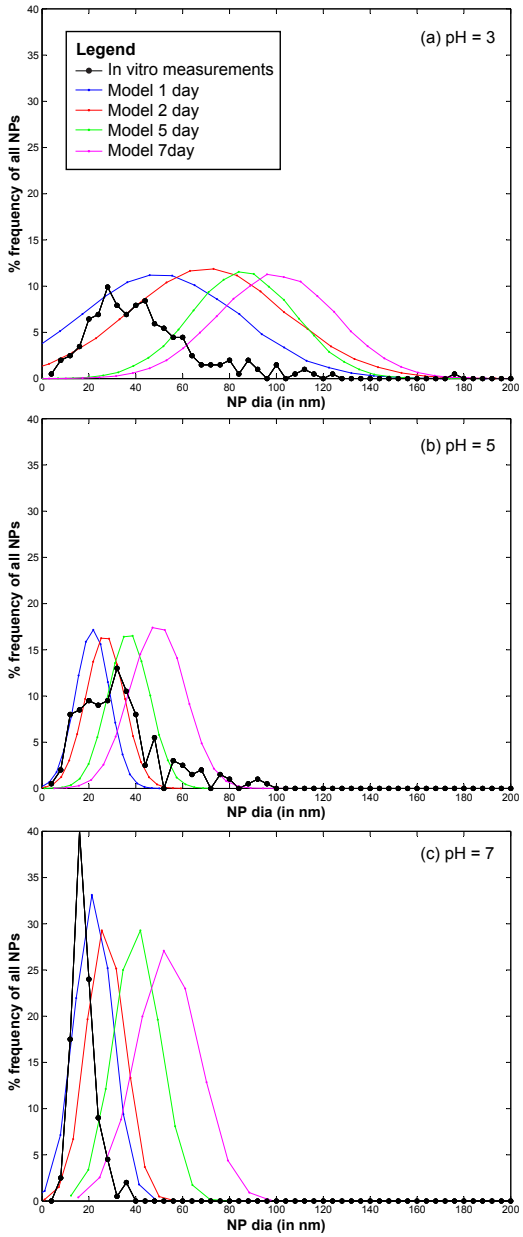

Figure III.3: Comparison of model prediction for 1, 2, 5, & 7 days and *in vitro* measurements for AgNP size distribution after 7 days of incubation at pH (a) 3, (b) 5, and (c) 7. (Figure reproduced from Mukherjee *et al.*, *Journal of Nanoparticle Research*, 16(10), 1-16, 2014, Figure no. 4, with kind permission from Springer Science and Business Media.)

Table III.2: Parameter values used in the *in vitro* nanoparticle transformation model

Parameter	Value	Reference
Hamaker Constant	37×10^{-21} J	Huynh and Chen [108]
Permittivity of vacuum	8.854×10^{-12} farad/m	
Characteristic wavelength	100 nm	Gregory [101]
Parameter b	5.32	Gregory [101]
Activation energy	33×10^{3} J	Zheludkevich *et al.* [109]
Rate constant for citrate oxidation	1.235×10^{-10} mol/m^3/sec	Estimated from Zhang *et al.* [103]
Mass transfer rate of O_2	1.67×10^{-6} mol/m^3/sec	Estimated by Zhang *et al.* [103]
Saturation conc. of O_2	8.96 mg/L	Zhang *et al.* [103]
Standard oxidation potential,E_o	0.47 V	Zhang *et al.* [103]

between the measurements from Leo *et al.* [39] (black dots) with model predictions for 1, 2, 5, & 7 days. The system with the medium at pH = 3 shows the largest increase in diameter followed by the system with medium at pH = 5. At a pH = 7, which is the same as distilled water, the agglomeration is negligible at 7 days. The model in general predicts faster agglomeration than what is observed in the *in vitro* system. This might be due to additional stabilization by the citrate ions, which prevents aggregation of NPs. There is large uncertainty in the quantification of citrate coating and surface coverage, as direct measurements were not carried out in the specific medium. The observed difference between model predictions and measurements might also be due to the difference in the estimation of agglomerate diameters between model and measurement. For the *in vitro* measurement technique, the average of two largest dimensions of NPs was recorded [39] as the estimate of diameter. The model however, estimates the effective spherical diameter (or the hydrodynamic diameter) from Equation III.3, which might be different from the measured diameter *in*

vitro employing the above technique, since NPs tend to form elongated strands due to agglomeration [39]. However, the change in diameter is comparable to that observed by Zhang *et al.* [103] in the linear growth phase. Decrease in pH is accompanied by an increase in ionic strength, as shown in Table III.2, which leads to a compression of the electric double layer, thus increasing inter-particle interaction [110], leading to increased agglomeration. Particle agglomeration is affected by the surface zeta potential, ζ, which alters with change in medium pH and ionic strength, I. The variation of ζ with pH and I is modeled using measurements from Leo *et al.* [39] and Salgin *et al.* [111]. The details of the functional modeling expressing ζ with pH and I are included in the SI. pH is known to have a stronger effect [112] on particle ζ and for values of pH higher than the isoelectric point (pI), a decrease in pH shifts the value of ζ closer to zero and leads to greater agglomeration. Figures III.4(a) and (b) show the size and number distribution respectively of the NPs in the CV at 1, 2, 5, 10, and 14 days after incubation. The figures show that the size and number distributions in the CV become progressively broader and move towards larger sizes as time progresses. Figures III.4 (c) and (d) show the changes in NP diameter mean and standard deviation of the NP population in the CV for different values of pH. A pH of 3 leads to much greater agglomeration resulting in larger mean diameter and also larger variation is diameters across the population. The difference between the plots for pH = 5 and pH = 7 is minor because the effect of higher pH is reduced due to decreased dissolution at higher pH. While a lower pH of 5 causes more agglomeration than a pH of 7, increased Ag dissolution at a pH of 5 (shown in dissolution results) causes reduction in the agglomerate diameters thus cancelling the effect due to increased agglomeration.

III.6.2 Settling of nanoparticles

Figure III.5(a) shows the fraction of NPs settled at the bottom of the tube for different values of pH. It shows the mass fraction of NPs settled and also the number fraction of

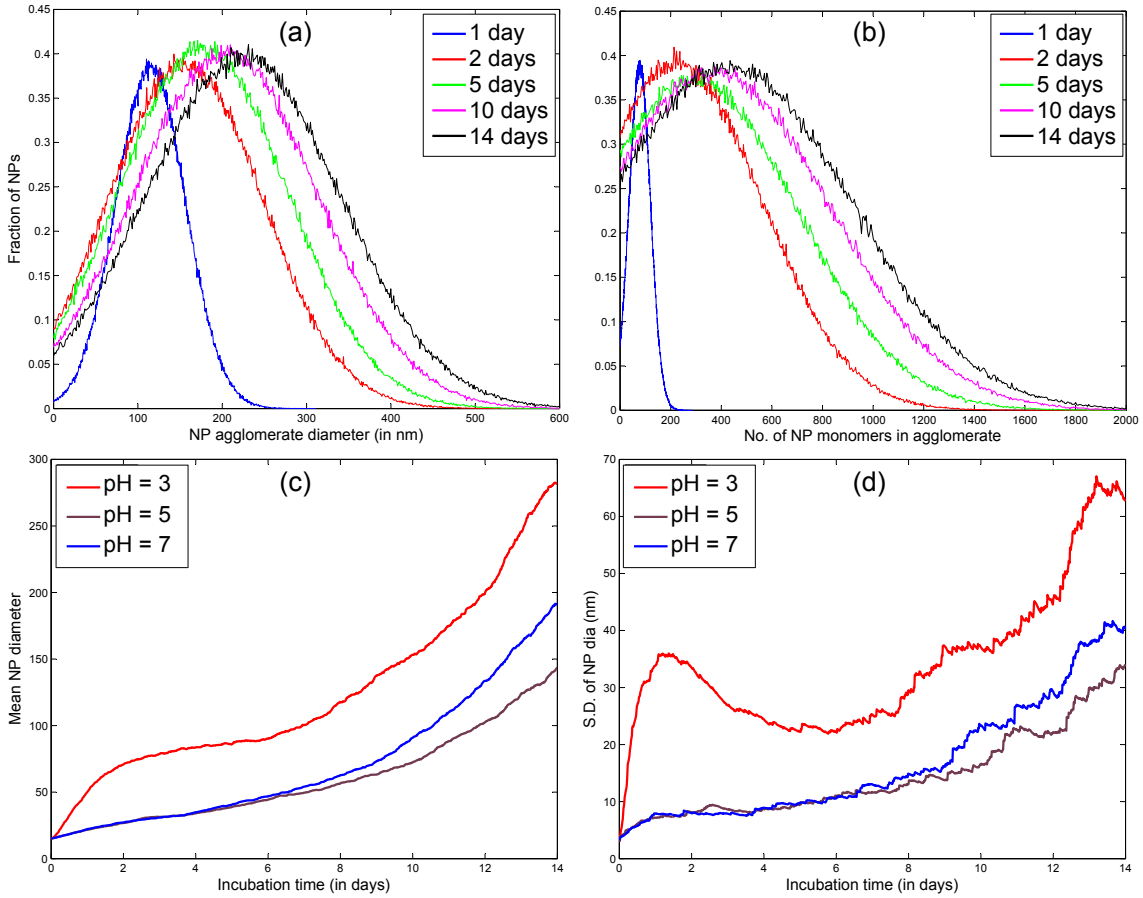

Figure III.4: Model simulation results of change in NP agglomeration state over the span of 14 days incubation time; panels (a) & (b) depict NP diameter distributions and distributions of number of primary NPs in an agglomerate in the model CV as it changes over 1, 2, 5, 10, and 14 days of incubation in a medium of pH = 3; panels (c) & (d) depict dynamic changes in NP mean diameter and SD of NP diameter in the CV over 14 days of incubation in different pH. (Figure reproduced from Mukherjee *et al.*, *Journal of Nanoparticle Research*, 16(10), 1-16, 2014, Figure nos. 5 & 6, with kind permission from Springer Science and Business Media.)

primary NPs (monomers) settled. Gravitational settling depends on the height of the liquid level above the bottom of the vessel, since the particles have to travel downwards at the Stokes' settling velocity given by Equation III.2. However, since the population of NPs inside the CV forms a representative sample of the entire population of NPs, the fractions settled would be the same for the NPs inside the CV as for the rest of the NPs. Figure III.5(a) shows that there is a difference between the mass fraction settled and number fraction settled (thick and thin lines) and that the difference increases with time. This is due to the faster settling of the higher mass aggregates, leading to a higher total mass of the settled population. Acidic pH (pH = 3) leads to higher settling due to the formation of larger agglomerates. Lower pH also promotes increased protonation of the citrate ions which are used to stabilize the AgNP. Higher rate of citrate removal shifts the NP ζ-potential closer to the isoelectric point, thus reducing the inter-particle repulsion and promoting aggregation and settling. Figure III.5(b) shows the estimated numbers of NPs settled in the CV. The thin line depicts the number of primary NP monomers settled, i.e. the total number of monomers settled irrespective of their state of aggregation. The bold line depicts the number of agglomerates settled. The increasing divergence of the 2 lines shows that the agglomerates that are settling have an increasing number of constituting monomers, i.e. the larger agglomerates tend to settle preferentially. Settling of NPs is important for estimating dosimetry for *in vitro* toxicological studies, where NPs are incubated with cell cultures generally located at the bottom of the vessel. The actual exposure of cells is to the settled population of NPs and not to the entire population [41]. Figure III.5(c) shows the change in size distribution of the settled NPs at the bottom of the vessel. The size distribution shifts to the right with time, which shows that the bigger agglomerates are preferentially settled. This also demonstrates increased spread due to the variety of particle sizes being settled. Size distribution and agglomerate status of the settled NP population can help in producing more accurate predictions of *in vitro* cellular toxicity. Smaller NPs can cross cellular membranes easily whereas larger

agglomerates tend to produce an increased immune response in phagocytic cells like macrophages.

III.6.3 Dissolution of nAg

Dissolution of citrate-stabilized AgNP was simulated using the model developed for this study and model predictions were compared with *in vitro* measurements by Leo *et al.* [39]. The properties of the medium used by Leo *et al.* are summarized in Table III.2. The model simulation was performed using DSMC for 14 days, for a population of 10,000 particles in the control volume and for 3 different pH values - 3, 5, and 7. The oxidation of Ag is dependent on the fraction of exposed surface area and is affected by the pH of the medium. Lower pH will lead to higher protonation of citrate resulting in higher exposed surface area available for oxidation. Figure III.5(d) shows a comparison between model predictions and *in vitro* measurements over 14 days for pH 3, 5, and 7. The model predictions agree well with the measurements and capture both the initial high rate of dissolution and the later steady dissolution due to the decrease in reactive surface area of the NPs, as well as the decrease in DO. The reaction kinetics are dependent on the exposed surface area of the NPs; reduction in surface area due to agglomeration and settling causes a reduction in the dissolution rate.

III.7 ADSRM implementation for alveolar lining

Nanoparticle (NP) transformation has been modeled by multiple researchers using physical theories to assess cellular dosimetry. However, most of these studies have been performed for *in vitro* systems to estimate particle dosimetry to cell cultures. The model described in this section extends the ADSRM framework developed for *in vitro* systems, to an *in vivo* setting, enabling the assessment of ENM interactions with various fractions of lipids and surfactant proteins which are present as constituents

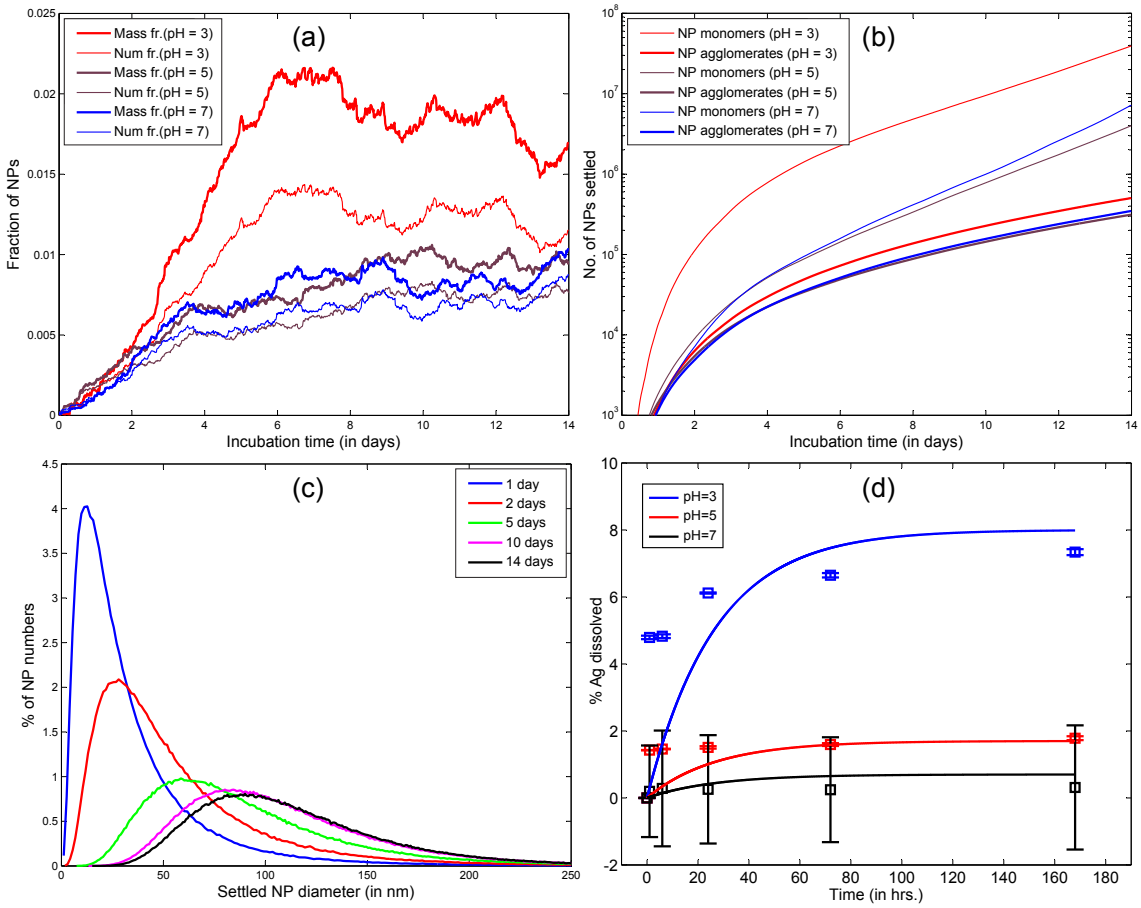

Figure III.5: (a) Model results of fraction of NPs settled with bold line representing the mass fraction and the thin line representing the number fraction of primary monomeric NPs. (b)Model results of numbers of NPs settled; bold line represents the number of NP monomers which have settled irrespective of their state of aggregation and the thin line represents the number of NP agglomerates which have settled. (c) Model results of distributions of settled NP diameter over time (pH = 3). (d) Comparison of model prediction of nAg dissolution and *in vitro* measurements over 14 days with citrate-stabilized nAg from Leo *et al.* [39] in media for 3 different pH. (Figures (a) and (b) are reproduced from Mukherjee *et al.*, *Journal of Nanoparticle Research*, 16(10), 1-16, 2014, Figure no. 8, with kind permission from Springer Science and Business Media.)

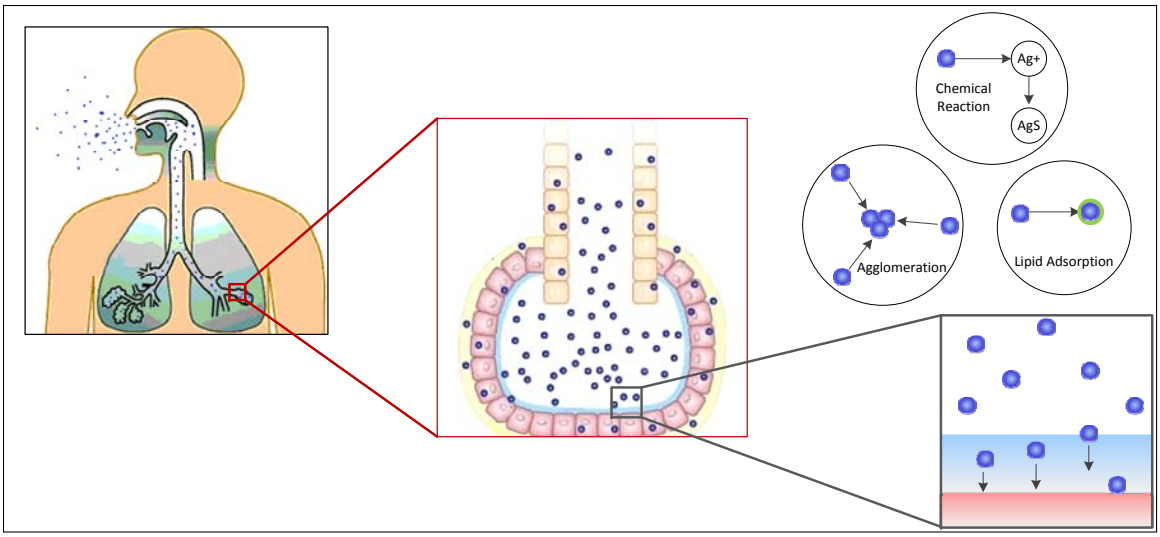

Figure III.6: Schematic representation of salient processes and mechanisms of transport and transformation of inhaled ENMs at the pulmonary alveolar lining layer. (Diagram not to scale)

of pulmonary surfactant. The alveolar fluid lining the alveolar surface is an extension of the mucus layer that covers the entire surface of the airways. However, the depth and composition of the liquid changes remarkably from the proximal airways to the more distal parts [113]. One of the most important features of the airway fluid in the alveolar region is the presence of surfactant lipids, which are responsible for reducing surface tension and preventing the collapse of the smallest airways [114]. Alveolar fluid is composed of about 80-90% lipids, primarily DPPC (Dipalmitoylphosphatidylcholine), with the remaining 10% composed of surfactant proteins [115]. Four surfactant proteins, SP-A, SP-B, SP-C, and SP-D, have been identified in the pulmonary alveolar fluid. SP-B and SP-C are known as surface-active proteins and are closely associated with surfactant lipids, assisting in the formation of lipid bilayers at the air-liquid interface [116]. SP-A and SP-D help in immune response by attaching themselves to foreign particles and identifying them for phagocytosis [115]. These critical components, i.e. phospholipids (PL) and the four surfactant proteins, have been individually considered in this model implementation, as all of them interact with inhaled particulate matter and affect their relevant toxicodynamics.

Mechanisms of toxicodynamic response at the cellular scale are affected by the form, size, and surface area of the ENMs [117]. It is well known that NP uptake by alveolar cells depends on NP size, surface area, and their surface chemistry, particularly adsorption of lipids and proteins on their surface [118]. Consequently, any analysis of the residence time distribution, clearance and biological response of NPs in any tissue system requires a detailed characterization of their form, size and surface reactivity, as these change dynamically with time. The ADSRM model developed earlier in *in vitro* systems, follows a population of ENMs over time and characterizes their dynamic transformation in chemical media, considering NP-NP and NP-media effects. Researchers have quantified NP transport, uptake, and clearance in the respiratory system [34, 38] but have not considered dynamic changes in the form and size of the NPs. Processes like lipid adsorption are known to affect NP agglomeration and dissolution [119]. Lipid adsorption and formation of protein corona on NPs is known to affect their uptake and ultimate fate in the body [120, 118], and so inclusion of these key mechanisms is essential for any toxicodynamic model for NPs. Blank *et al.* [121] attempted to recreate an alveolar air-liquid interface *in vitro* along with alveolar epithelial cells. However, to date, there have been no published models quantifying ENM transformation *in vivo*. It is almost impossible to realize the exact composition and dynamics of *in vivo* structures and functions *in vitro*. This necessitates detailed *in silico* frameworks that will aggregate and integrate relevant *in vitro* and *in vivo* information to produce estimates of *in vivo* toxicodynamic effects. The model described here extends modules from the ADSRM framework (developed earlier) to an *in vivo* setting (the pulmonary alveolar lining) by adding mechanisms of surfactant lipid and lipoprotein adsorption onto the ENMs. The model described here uses modules from the ADSRM model for diffusion, agglomeration, and reaction and introduces separate modules for adsorption of proteins and lipid vesicles, for its applicability to systems containing lipid and protein molecules, which are known to induce additional transformation mechanisms for the ENMs. The model uses a direct

simulation Monte Carlo (DSMC) scheme and estimates various critical kinetic rates pertaining to ENM transformation in the respiratory airway, which can be used to better quantify pulmonary toxicodynamics of ENMs. The approach described here is the first of its kind to include NP-lipid and NP-protein interactions, along with dynamic NP transport and transformation *in vivo*, to predict NP dosimetry in the mammalian respiratory system.

III.8 Surfactant lipid adsorption on ENMs

Inhaled particles interact with surfactant lipids from the instant they are deposited on the alveolar surface. By the time the particles arrive at the surface of alveolar cells, they have been modified by adsorption of lipids and proteins present in the alveolar fluid layer. Bakshi *et al.* [122] and Schleh and Hohlfeld [123] have reported the formation of lipid bilayers on NPs immersed in lipid emulsions, and have found the thickness of this layer to be approximately 4 nm. Detailed kinetic models for these processes are missing in the literature because it is difficult to quantify such mechanisms *in vivo*. Adsorption of lipid on to solid surfaces has been traditionally described using Langmuir kinetics [99]. However, due to the nanometer size range of ENMs, simple Langmuir kinetics of adsorption is only an approximation [99]. Mornet *et al.* [124] investigated the formation of lipid bilayers of silica NPs and found lipid "patches" on the NPs a few minutes after incubation. They also observed SUVs or liposomes adsorbed on the surface of the NPs, which later underwent deformation and rupture to form lipid bilayers on the NPs. Mornet *et al.* also found that the sizes of these SUVs were in the 10-100 nm range, which makes them comparable in size to ENMs. Interaction of these SUVs with ENMs would be influenced by their mutual surface areas of interaction, their diffusion and their surface charge distribution, thus making the process inherently heterogenous, non-uniform and affected by diffusion of the particles and lipid vesicles.

III.8.1 Monte Carlo simulation of lipid vesicle adsorption

Lipid vesicle diffusion and adsorption on solid supports has been investigated extensively, due to the wide application of "supported lipid bilayers" or SLBs in simulating cell membranes. Zhdanov and co-workers [125, 126] have used dynamic MC algorithms to simulate lipid vesicle diffusion, adsorption, deformation, and rupture on solid silica wafers immersed in lipid solutions. Their algorithm describes the solid substrate as a square grid and randomly simulates vesicle attachment to grid locations based on the vesicle size and available space on the solid grid. Zhdanov *et al.* [125] also consider inter-vesicle interaction and deformation of vesicles leading to rupture. It is not possible, computationally or otherwise, to implement all the complexities of the algorithm for multiple ENMs in solution, with each having random motion in the system. So, this model employs a simpler version of the algorithm employed by Zhdanov *et al.* [125], in which adsorption of vesicles on to ENMs is based on the sizes of the interacting vesicle and ENM and also on available area on the ENM. Lipid vesicles are also assumed to deform and rupture immediately after adsorption. The adsorption probability for a random vesicle on to a random ENM is calculated using an exponential equation based on Zhdanov *et al.* [125].

$$P_{\mathrm{ad}} = exp\left(- \alpha . \frac{d_{\mathrm{ves}}^2}{f_{\mathrm{SA}}^2 . d_{\mathrm{ENM}}^2} \right) \tag{III.22}$$

Here, d_{ves} is the lipid vesicle diameter, d_{ENM} is the ENM diameter, and f_{SA} is the fractional exposed (not covered by lipids) surface area of the ENM. The eventual likelihood of adsorption is affected by diffusion of the vesicles and ENMs and also by the probability of successful adsorption. Zhdanov *et al.* [125] characterized the probability of an ENM and a vesicle colliding due to random diffusion as $P_{\mathrm{diff}} = 0.001$ based on a diffusion coefficient of $D = 8.7 \times 10^{-10}$ m^2/sec [127]. An adsorption attempt is considered successful if a randomly selected number between 0 and 1 is less than $\frac{P_{\mathrm{ad}}}{P_{\mathrm{ad}}+P_{\mathrm{diff}}}$. The particular steps in the DSMC scheme for lipid adsorption are

implemented as follows:

1. A random ENM is selected from the population in the control volume (CV)
2. A random lipid vesicle is selected based on the size distribution of vesicles
3. P_{ad} is calculated such that if the selected ENM has zero exposed surface area, then $P_{\text{ad}} = 0$, else P_{ad} is given by Equation III.22
4. A random number p is generated between 0 and 1
5. Adsorption is considered successful if $p < \frac{P_{\text{ad}}}{P_{\text{ad}}+P_{\text{diff}}}$
6. If adsorption is successful, the relevant properties of the particular ENM are updated with the changed f_{SA} and mass
7. If the maximum number of adsorption steps has not been reached, then the steps are repeated from Step (1)

Gross and Narine [128] found mouse BAL fluid to be composed of 9% 'ultraheavy' large aggregates, 48% 'heavy' fraction with large vesicles and some tubular myelin, and 43% 'light' fraction consisting of small unilamellar vesicles (SUVs). SUVs in alveolar fluid have been reported to vary in size between 20-50 nm [115]. Large vesicles (LUVs) which constitute the heavy fraction are between 50-500 nm [115]. A size distribution is constructed for lipid vesicles by fitting a normal distribution within these reported size ranges (limits of the ranges are taken to be the upper and lower 95 percentiles of the distribution). SUVs and LUVs are randomly selected based on their relative fraction in alveolar fluid. Adsorbed lipid vesicles are assumed to rupture after adsorption, and form a lipid bilayer based on the surface area of the initial vesicles. Nordlund *et al.* [129] found only about 1% of the adsorbed vesicles to be intact at the end of adsorption on silica NPs. Various properties of surfactant and its constituent lipids are summarized in Table III.6.

III.8.2 Surfactant protein adsorption on ENMs

Adsorption of proteins on solid surfaces has been investigated for a number of practical applications. Proteins are part of all biochemical media and any foreign particle entering the body gets coated with a protein corona, thus affecting its eventual uptake and/or excretion. Uptake of silver ENMs by pulmonary cells has been shown to be affected by protein corona formation on the particles [130]. The mechanism of protein adsorption surfaces is known to be composed of the following steps [131]: (1) diffusion of proteins to the surface, (2) actual adsorption on to the surface, and (3) subsequent conformational changes in the protein structure. In the present model, the first two steps are explicitly considered. Modeling conformational changes in protein structure would require a detailed proteomics model which is beyond the scope of this work. Zhdanov and Kasemo [132] have described a Monte Carlo (MC) model for protein adsorption on solid surfaces, which has been extended here for ENMs in solution. Two separate cases are considered: Protein adsorption under (a) diffusion-controlled regime and (b) under adsorption-controlled regime. The model algorithm selects the case based on the slower or limiting process based on the conditions of the system at any given time. Under adsorption-limited regime, the adsorption probability is given by:

$$P_{\mathrm{Ad}} = 2R^2 C_{\mathrm{o}} k_{\mathrm{a}}, \tag{III.23}$$

where R is the radius of the particular protein headgroup, C_{o} is the concentration of the protein in solution, and k_{a} is the adsorption rate for the particular protein. The time step associated with the adsorption process is given by $\Delta t = \frac{1}{P_{\mathrm{Ad}}}$. Under diffusion-limited regime, the adsorption probability is given by:

$$P_{\mathrm{Ad}} = 2R^2 C_{\mathrm{o}} \sqrt{\pi D t}, \tag{III.24}$$

where D is the diffusivity of the protein in the solution and t is the system time. In this case, the time step associated with the process is given by $\Delta t = \frac{\sqrt{\pi t/D}}{C_o A}$, where A is the protein headgroup area. Adsorption of proteins is however not irreversible and is actually a net result of adsorption and desorption [126]. Furthermore, adsorption of proteins cannot be independent of adsorption of other chemical species, as the charged headgroups of proteins are liable to interact with charges already present on the ENM surface. Lipid bilayers are known to interact with proteins through electrostatic interaction and thus affect the adsorption and clustering of protein molecules [133]. Electrostatic interaction and the number of charged-groups in contact would affect adsorption and the subsequent desorption of proteins from surfaces [126]. Zhdanov and Kasemo [126] modeled protein adsorption and desorption on solid surfaces in the presence of lipid bilayers and measured adsorption rates k_{a}, and desorption rates k_{d}, for various values of surface coverage by lipid bilayers. Adsorption and desorption of surfactant proteins have been considered in this model as a function of ENM surface coverage. A power-law model was fitted to measurements by Zhdanov and Kasemo [126] to estimate k_{a} and k_{d} as:

$$k_{\mathrm{a}} = k_{\mathrm{a}}^{0}.(1 + \beta_{\mathrm{a}}.\theta^{n_a}) \tag{III.25}$$

$$k_{\mathrm{d}} = k_{\mathrm{d}}^{0}.(1 + \beta_{\mathrm{d}}.\theta^{n_d}), \tag{III.26}$$

where, k_{a}, k_{d} are the adsorption and desorption rates for the proteins on to ENMs, θ is the fractional surface coverage of ENMs by lipids, β and n are fitted parameters for adsorption and desorption. Details of the estimation of these parameters for different SPs are included in Appendix B. A net rate defined as $k'_{\mathrm{a}} = k_{\mathrm{a}}/k_{\mathrm{d}}$ was used in Equation III.23 to simulate adsorption so that the effects of both adsorption and desorption could be simultaneously taken into account in the DSMC framework. Pulmonary surfactant is composed of four types of proteins: SP-A, B, C, and D. The first three types of proteins have been investigated considerably, but relatively little information

is available for SP-D. SP-A is the most abundant protein in pulmonary surfactant, accounting for 5% by weight of surfactant, followed by SP-B and SP-C which together account for 1.5% by weight [115]. Detailed properties of the protein molecules have been summarized in Table III.7.

III.8.3 ENM transport in alveolar lining fluid

Nanoparticle diffusion and settling have been modeled by Hinderliter *et al.* [41] (ISDD model) and also recently for silver ENMs by Mukherjee *et al.* [42] (ADSRM model) for *in vitro* media. As shown in both articles, gravitational settling has a major effect on ENM settling and eventual dosimetry for *in vitro* cell cultures. However, it has been shown that, for nano-scale particles *in vivo*, the forces of surface tension exerted by the surface-active alveolar lining layer are 2-3 orders of magnitude greater than gravitational forces [134]. Accordingly, gravitational forces have been replaced by surface tension for the *in vivo* implementation of the model. For the *in vitro* implementations shown earlier, gravitational settling has been modeled using Stokes' law in a manner similar to Hinderliter *et al.* [41]. Surface forces acting on small particles in the alveolar lining were mathematically analyzed by Schurch *et al.* [134]. The net force which causes the immersion of the particles into the alveolar fluid is calculated as [134]:

$$F_s = 2\pi R\gamma.sin(\phi).sin(\theta+\phi), \tag{III.27}$$

where R is the particle radius, γ is the surface tension at the alveolar air-liquid interface, θ is the contact angle at the particle surface, and ϕ is the angle formed between the contact point and the axis of the particle. The surface force F_s can be equated to the drag force in the medium using Stokes' law to obtain:

$$v = \frac{\gamma}{3\mu}.sin(\phi).sin(\theta+\phi) \tag{III.28}$$

Schurch *et al.* [134] found that for low values of surface tension ($\gamma = 30$ dyn/cm) such as those experienced at the alveolar lining, the contact angle θ would have a value of 20° and that the value of ϕ would be about 160°.

III.8.4 ENM agglomeration

ENM agglomeration has been modeled in a fashion similar to that done earlier for *in vitro* systems, by considering modified versions of Smoluchowski's equations. However, lipid adsorption on the ENMs causes surface modification which has been found to dissuade agglomeration in silver ENMs [39]. This has been taken into account by using the values of zeta potential estimated by Leo *et al.* [39] for DPPC-adsorbed silver ENMs. Zeta potential has been considered as a weighted function of surface coverage by phospholipids as:

$$\zeta = \zeta_{\mathrm{L}}.\theta + \zeta_{\mathrm{o}}(1-\theta), \tag{III.29}$$

where ζ_{o} is the zeta potential of the ENM without lipid adsorption, ζ_{L} is the reduced zeta potential due to lipid adsorption, and θ is the fractional surface coverage of the ENM by lipids. The reduced zeta potential ζ_{L} due to lipid adsorption is estimated from the data of Leo *et al.* [39], where zeta potentials of silver NPs were measured with and without addition of DPPC. ENM agglomeration is also known to be affected by steric effects due to the presence of coating molecules. Leo *et al.* [39] reported that despite a reduction in zeta potential, addition of DPPC maintained the dispersed state of NPs and did not promote agglomeration due to steric effects of the coating molecules. There was no such effect in the results of Nordlund *et al.* [129], where addition of lipids led to increased agglomeration. This phenomenon was also observed by Kendall *et al.* [120] for particulate matter. This has been reconciled in this model by introducing steric effects for coating molecules which would produce additional repulsive interactive forces. Damodaran [135] modeled repulsive interactions due to

steric effects in proteins, by considering a repulsive energy due to steric effects, that can be represented as:

$$E_{\mathrm{st}} = (kTn_{\mathrm{m}}L/s).[(2L/d)^{2.25} - (d/2L)^{0.75}], \tag{III.30}$$

where k is the Boltzmann constant, T is the absolute temperature, n_{m} is the number of coating molecules per unit surface area of the ENM, L is the chain length of the coating molecule, $s = \sqrt{1/n_{\mathrm{m}}}$ is the mean distance between coating molecules, and d is the mean distance between interacting ENMs. The steric repulsive energy (details in Appendix B) is included in the calculation of repulsive interactions as part of Smoluchowski's equations which consider both attractive Van der Waals' forces and repulsive electrostatic forces of interaction.

III.9 Results and Discussion

The Direct Simulation Monte Carlo (DSMC) algorithm is implemented in a constant number mode. A population of 100 ENMs is selected and a control volume (CV) is defined which contains these ENMs based on the concentration of the system. At all times during the simulation, a number of internal and external coordinates of the system of ENMs are recorded. Internal coordinates of ENMs refer to various dynamic properties of the particles such as position, diameter, surface coverage by lipid, adsorbed proteins, and agglomeration state. External coordinates refer to parameters of the medium such as lipid and protein concentration, ENM number concentration, temperature, density, viscosity, *etc.* Results of the ADSRM model implementation for ENM transport and transformation are presented next, in two parts. The first part concerns model implementation *in vitro* and estimation of key parameters pertaining to ENM agglomeration and lipid adsorption. The model has been implemented for *in vitro* lipid solutions and simulation results are compared with measurements reported by Leo *et al.* [39] for silver NPs and Nordlund *et al.* [129] for silica NPs. In

the second part, the model has been implemented for the human alveolar lining layer and predictions of the model are presented for *in vivo* ENM transformation. Various critical kinetic rates are also estimated based on the *in vivo* results.

Table III.3: Properties of alveolar surfactant lipids

Lipid species	**Conc.***	**Mol.Wt.(kDa)****
PC	78	760.076
PE	3	471.609
PS	5	547.17
PG	7	787.383
SM	2	646.505
CL	5	400.637

* From *Lung Surfactants*, Notter, 2000 [115]
** From Avanti Polar Lipids, [136]

III.9.1 In vitro implementations

The ADSRM model described in the present article was implemented for an *in vitro* system based on the works by Leo *et al.* [39] and Nordlund *et al.* [129]. Some features of model implementation were exclusively applied for the *in vitro* cases as follows:

- Lipid concentration is considered to vary dynamically from their initial values in solution. Vesicle diffusivity was appropriately modified. For *in vivo* systems, levels of lipid in alveolar lining are maintained relatively constant by alveolar cells via constant secretion and removal.

- DPPC vesicle size distribution and concentration has been considered based on the commercially available formulations used in the relevant studies rather than on properties of actual biological surfactant, whose composition tends to be radically different.

- Gravitational settling has been considered rather than surface-active transport, unlike the situation in the actual alveolar lining, where surface tension aided transport far outweighs gravitational transport (discussed in Section III.8.3).

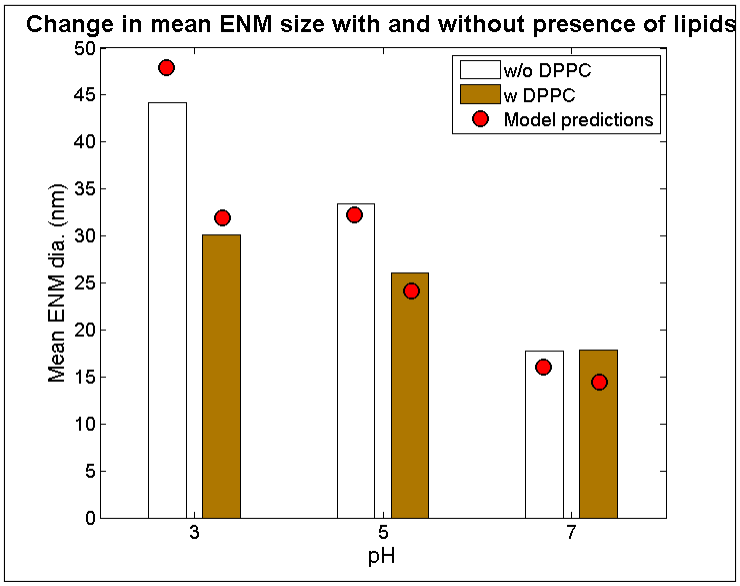

Figure III.7: Comparison of model predictions of silver ENM mean diameter (shown as stars) with *in vitro* measurements (shown by bars) from Leo *et al.*[39] for citrate-coated silver ENMs (initial mean diameter = 20 nm) incubated with and without DPPC for 7 days

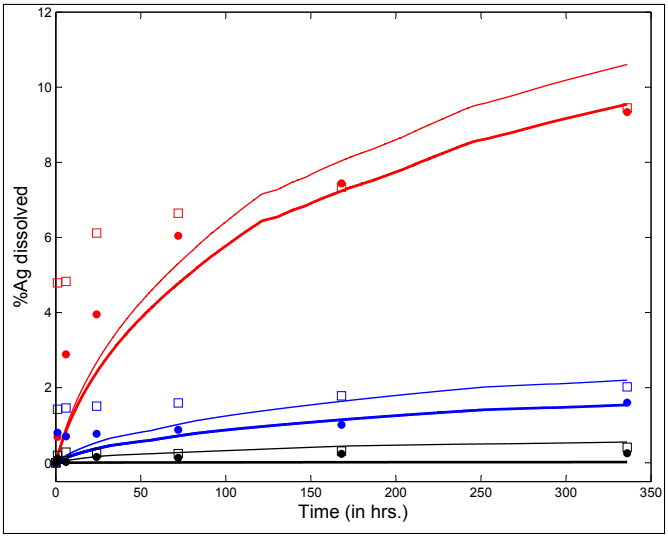

Figure III.8: Comparison of model predictions of percent Ag dissolved in solution with *in vitro* measurements from Leo *et al.*[39] for citrate-coated silver ENMs (initial mean diameter = 20 nm) incubated with and without DPPC for up to 14 days

Table III.4: Parameters used for model implementations

Parameters	**Leo *et al.*, 2013 [39]**	**Nordlund *et al.*, 2009 [129]**	***In vivo* implementation**
System	Eppendorf tube	NR	Alveolar lining
System vol.	4 ml	NR	10 ml/kg BW[137]
ENM type	Ag NP	Silica NP	Ag NP
ENM coating type	Citrate(C)	None	Citrate(C), PVP
Coating mol. wt.	258	None	258 (C), 10000 (PVP)
Initial ENM dia. (nm)	20	600	20, 110
ENM density (g/mL)	10.49	2	10.49
ENM conc. (mg/L)	25	3000	NA*
Ionic strength (mM)	0.1	100	245 [113]
pH	3, 5, 7	7.4	7.28 [113]
Initial ENM zeta potential (mV)	-18.2, -22.5, -32.5	-25 [138]	-32.5
Dissolved O_2 (mg/L)**	8.96	8.96	8.96
Temperature	37°C	22°C	37°C
Adsorption probability, α	0.004	0.001	0.004
Steric Factor, η_S	2.35	1	2.35 (C), 10.6 (PVP)

* *in vivo* dosage was simulated as inhaled aerosolized ENM present in consumer products [28].
** Saturated O_2 conc. for solutions exposed to atmospheric pressure [103].
Values unless otherwise referenced, are from the original studies.
NR = Not Reported

Leo *et al.* [39] used citrate-coated silver NPs (AgNPs) in solution (with and without DPPC) at varying values of pH and followed the change in particle size and silver dissolution over a span of 7 days. Values of various ENM and media properties were appropriately selected to mimic the *in vitro* system used by Leo *et al.* [39], and these are summarized in Table III.4. Figure III.7 shows comparisons between model predictions and *in vitro* measurements from Leo *et al.* [39] for mean diameter of AgNPs in solution after 7 days of incubation in media of different pH, with and without addition of DPPC. Mean diameter has been calculated considering the entire particle population from *in vitro* measurements reported by Leo *et al.* [39] and

taking the number-weighted mean of the particle diameters. The model captures the phenomenon of increased agglomeration due to lower values of pH reasonably well. The measurements of Leo *et al.* [39] also demonstrate decreased agglomeration due to DPPC despite the lowering of surface zeta potentials due to lipid adsorption. This has been attributed to the influence of steric factors. Accordingly, a steric factor has been included in the estimation of repulsive interaction energies for coated ENMs (Equation B.24). Appropriate modulation of values of the adsorption probability α (Equation III.22), and the steric factor, η_{S} (Equation B.24) allows the model results to match the *in vitro* measurements. The final values of the estimated parameters are summarized in Table III.4. Figure III.8 compares model predictions and *in vitro* measurements for dissolution of AgNPs in media with and without DPPC. The model shows reduced dissolution when DPPC is added due to increased surface coverage of the ENMs by DPPC molecules, which reduces the rate of silver oxidation and dissolution from the AgNP surface. Furthermore, the inhibitory effect of DPPC on Ag dissolution increases with time, as AgNP surface coverage increases. It is also seen that the effect due to lipid adsorption is much less than the effect of pH, most probably due to gravitational settling. AgNPs with large amounts of adsorbed DPPC have a greater tendency to settle and are thus removed from the solution.

Nordlund *et al.* [129] used silica NPs (SiNPs) (without coating) to study lipid adsorption from a solution of DOPC (1,2-Dioleoyl-*sn*-glycero-3-phosphocholine). DOPC has a similar zwitterionic polar headgroup as DPPC with oppositely charged amine and phosphorus groups next to each other [136]. Interactions between DOPC molecules and negatively charged SiNPs are expected to be similar to those between DPPC and citrate-stabilized AgNPs. However, as reported by Leo *et al.* [39], the presence of citrate groups might add to steric effects, which is absent in the case of SiNPs. In fact, Nordlund *et al.* [129] reported that the SiNPs have an increased tendency to agglomerate in the presence of DOPC, which suggests lesser steric effects than for

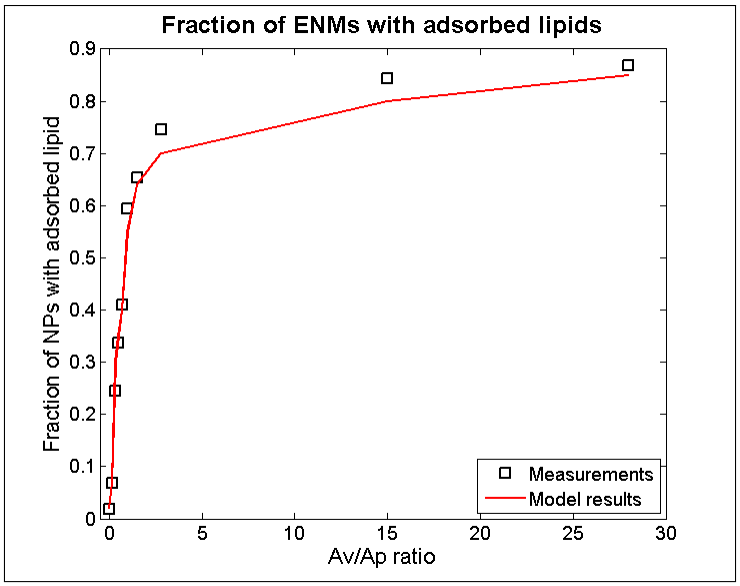

Figure III.9: Comparison of model predictions (red line) of fraction of NPs with adsorbed lipids after 1 hour of incubation, with *in vitro* measurements (black squares) from Nordlund *et al.*[129] for different values of surface area ratios of lipid vesicle to particle

NPs with coating. The ADSRM model was implemented for the *in vitro* system corresponding to the study with SiNPs, and with different values of lipid to NP ratios as performed by Nordlund *et al.* [129]. However, in that study the SiNPs were incubated with DOPC vesicles for 1 hour, accompanied by stirring. This would prevent settling of particles and, accordingly, settling was not considered here. Appropriate parameter values required for this implementation are summarized in Table III.4. In the study by Nordlund *et al.* [129], DOPC was mixed with fluorescin and the associated fluorescence on the SiNPs due to adsorbed DOPC was measured by flow cytometric analysis. Figure III.9 compares model predictions of fraction of particles with adsorbed DOPC and *in vitro* measurements from Nordlund *et al.* [129] for ten values of $A_{\mathrm{v}}/A_{\mathrm{p}}$ which represent the initial surface area ratios of vesicle to NP. Figure III.10 compares predicted average amount of DOPC adsobed on SiNPs in solution with *in vitro* measurements of average fluorescence from Nordlund *et al.* [129]. The results have been normalized by the value of mean fluorescence with no DOPC added

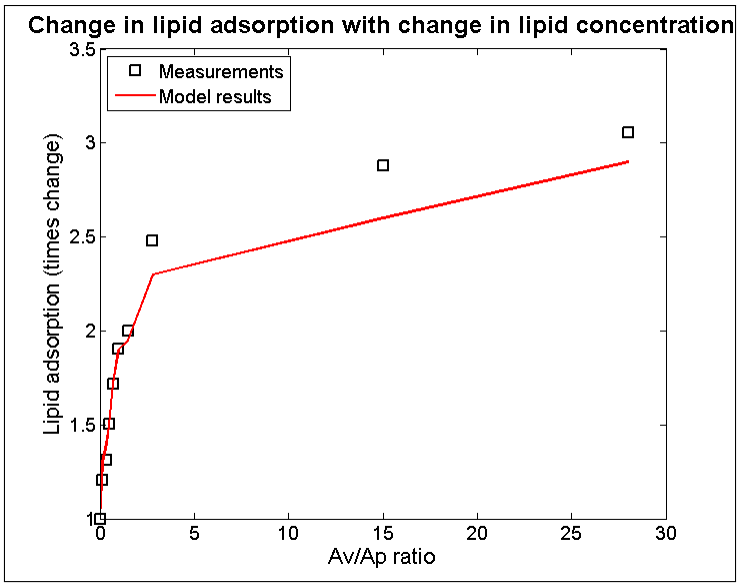

Figure III.10: Comparison of model predictions (red line) of times change in amount of adsorbed lipids with adsorbed lipids after 1 hour of incubation, with *in vitro* measurements (black squares) from Nordlund *et al.*[129] for different values of surface area ratios of lipid vesicle to particle

to correct for fluorescence produced by SiNPs themselves. This model implementation has been carried out along with appropriate selection of values for adsorption probability α (Equation III.22), and the steric factor, η_s (Equation B.24). η_s has a lower value than that in the earlier implementation due to the absence of coating on the SiNPs. Figure III.11 compares model predicted average diameter of SiNPs in solution with measurements of fluorescence with increasing vesicle to particle surface area ratios. Average diameter has been calculated by considering the entire particle population from *in vitro* measurements reported by Nordlund *et al.* and taking the number-weighted mean of the particle diameters.

III.9.2 In vivo implementation

The ADSRM system developed here is finally implemented for the human alveolar lining layer, simulating ENM dosimetry after inhalation exposure. This formulation specifically helps to estimate key kinetic parameters of ENM transformation and transport in the alveolar lining, which can inform toxicodynamic models relevant to

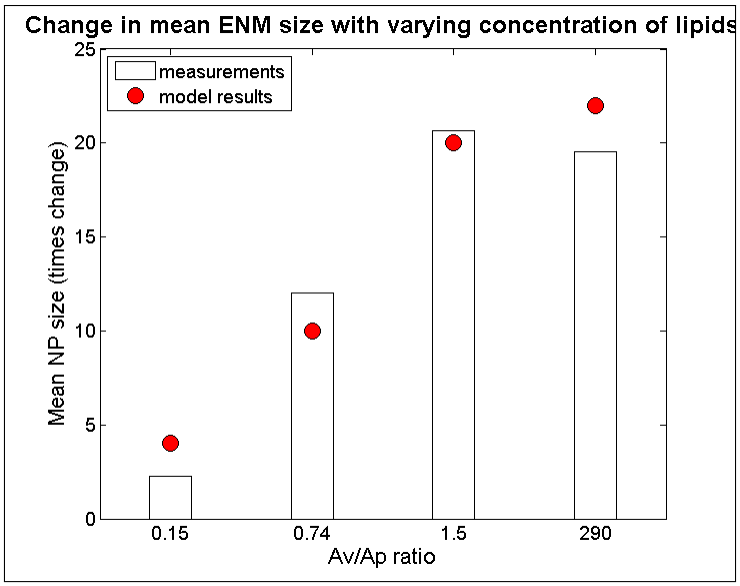

Figure III.11: Comparison of model predictions (shown as stars) of average size of silica NPs (initial mean diameter = 600 nm) after 1 hour of incubation with *in vitro* measurements (shown as bars) from Nordlund *et al.*[129] for different values of surface area ratios of lipid vesicle to particle

Table III.5: Properties of silver ENMs used in the model implementations

NP	Coating	Core material	Density (g/cm^3)	Mol.Wt.	Coating Mol.Wt	Zeta Potential (mV)
L20	Citrate	Ag	10.49	108	258	-39.2
N600	None	SiO_2	10.49	108	258	-39.2
C20	Citrate	Au	10.87	115.3	258	-44.3
P20	PVP	Au	10.87	115.3	10000	-38.2
C110	Citrate	Au	10.49	108.04	258	-45.2
P110	PVP	Au	10.49	108.04	40000	-31.6

Source: Properties for L20 from Leo *et al.*, 2013 [39]; Properties for N600 from Nordlund *et al.*, 2009 [129]; Properties for C20, P20, C110, P110 from Wang *et al.*, 2014 [43] and Mukherjee *et al.*, 2014 [42]

the human pulmonary system. The following modifications were incorporated in the model to reflect conditions relevant to the *in vivo* system:

- ENM dose to the alveolar region is based on an inhalation dose for an adult human.
- Airway dosimetry of ENMs based on alveolar deposition, is estimated by the software MPPD [139].

- Gravitational settling is replaced by surface-tension assisted transport of particles towards the cellular layer.
- Concentration of lipids and proteins are considered constant due to homeostasis maintained by constant secretion from alveolar cells.

Table III.6: Properties of the airway alveolar lining layer

Property	**Value**	**Reference**
BALF density	1.04 g/ml	Shelley, 1975 [140] (study based on male New Zealand rabbits)
Lipid conc.	328 μg/ml	Shelley, 1975 [140] (study based on male New Zealand rabbits)
Protein conc.	212 μg/ml	Shelley, 1975 [140] (study based on male New Zealand rabbits)
BALF vol.	10 ml/kg	Meyer *et al.* [137] (study based on young humans)
PL density	1.108 g/ml	Woodka *et al.* [141] (based on DPPC)
Ionic strength	245 mM	Song *et al.* [113] (study based on 6-8 week CD1 mice)
pH	7.28	Song *et al.* [113] (study based on 6-8 week CD1 mice)
Viscosity	8.79×10^{-4} kg/m-s	Stroumpoulis *et al.* [127] (based on DMPC solution)
Thickness	0.2 μm	Bastacky *et al.* [142] (based on DMPC solution)

BALF: Bronchoalveolar Lavage Fluid, PL: Phospholipid, DMPC: Dimyristoyl Phosphocholine

Various parameters of the airway and the alveolar lining layer are summarized in Table III.6. ENM dose is considered to be delivered by a single breath by an adult human, breathing in an ENM cloud with a reference concentration of 0.14 mg/m^3. The reference concentration is obtained from Royce *et al.* [28], and is based on the maximum concentration in the immediate breathing zone after spraying of a bathroom cleaner containing silver ENMs in an indoor residential microenvironment. The mass concentration is converted to number concentration based on the size distribution of the ENMs used, and the ENMs are all considered to be monomers initially. Four types of silver ENMs are used in this implementation to test the effect of ENM and coating type, specifically 20 and 110 nm silver ENMs with citrate and PVP (Poly

Vinyl Pyrrolidone) coatings. Wang *et al.* [43] used these four types of NPs to test their dosimetry in cell culture plates. The ENMs are referred to as C20, C110, P20, and P110 respectively and their properties are summarized in Table III.5. Human airway dosimetry modeling is performed using the MPPD software package [139], which considers age-dependent changes in airway morphology to calculate particle deposition based on particle size and density in different regions of the lung. The entire population of ENMs reaching the alveolar region is divided by the known air-exchange area of alveoli (70 m^2 [123]) in an adult human lung. Various parameters of the mammalian alveolar lining layer are summarized in Table III.6. The ADSRM model is implemented through a constant number DSMC algorithm consisting of the following steps:

- A constant number (N = 100) of ENMs is selected and the associated alveolar area is calculated.
- Volume of the starting control volume (CV) is calculated based on a uniform average thickness of the alveolar lining layer.
- The ENMs are initially all considered to be deposited at the top of the CV.
- ENMs are considered to be monomers as there is negligible chance for agglomeration in the airway before coming in contact with a surface.
- Diameters and all other internal coordinates of the ENMs in the CV are estimated.
- Various modules of the model - agglomeration, transport, adsorption, desorption, and reaction are successively implemented as described in detail before.
- Time is advanced by Δt based on the slowest step among all processes.
- New CV is established based on the constant number N.

- ENM and media property values are saved and the steps are run again from the fifth step described above.

Table III.7: Molecular properties of surfactant proteins present in alveolar surfactant

Protein	MW (kDa)*	Length (nm)*	Dia. (nm)*	Density (g/cm^3)+	Conc. ($\mu g/ml$)**	D (10^9 m^2/s)++
SP-A	32	20	20	1.41	132.5	0.093
SP-B	9	7.9	3	1.48	19.93	0.5474
SP-C	3.8	3.4	2	1.5	19.93	0.796
SP-D	42	92	92	1.4	39.64	0.0206

* From *Lung Surfactants*, Notter, 2000 [115]
+ From Fischer *et al.* [143]
** Based on percentage composition from Notter [115] and total protein conc. in pulmonary alveolar fluid from Shelley, 1975 [140]
++ Diffusion coefficient estimated using Svedberg equation [144] (Details in Appendix B)

The model simulation stops when the concentration of ENMs in the alveolar lining layer drops to 1% or less of its initial concentration. Since the transport of ENMs through the alveolar lining layer is a relatively fast process, compared to the earlier implementations for *in vitro* media, the model involves a relatively small number of steps to complete. The bottom of the alveolar lining and the location of the alveolar cellular surface is considered the bottom of the CV and where the ENMs settle. The current model implementation predicts the state, number, and condition (adsorbed surfactant lipids and proteins) of ENMs present at the bottom of the lining layer after inhalation, which would ultimately affect their uptake by the alveolar cells and macrophages.

Estimation of kinetic parameters

Implementation of the ADSRM model for an actual *in vivo* system allows one to test the interplay of various parameters that have been estimated from *in vitro* studies. The results allow the estimation of average kinetic rate constants, which can then be used for higher level (tissue and organism level) models. Figure III.12 shows the

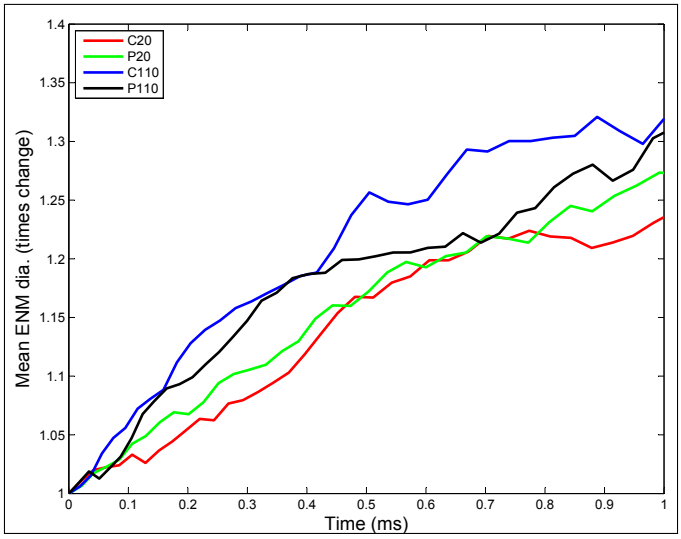

Figure III.12: ADSRM model simulation results of change in mean ENM diameter (times initial mean diameter) for four different types of silver ENMs

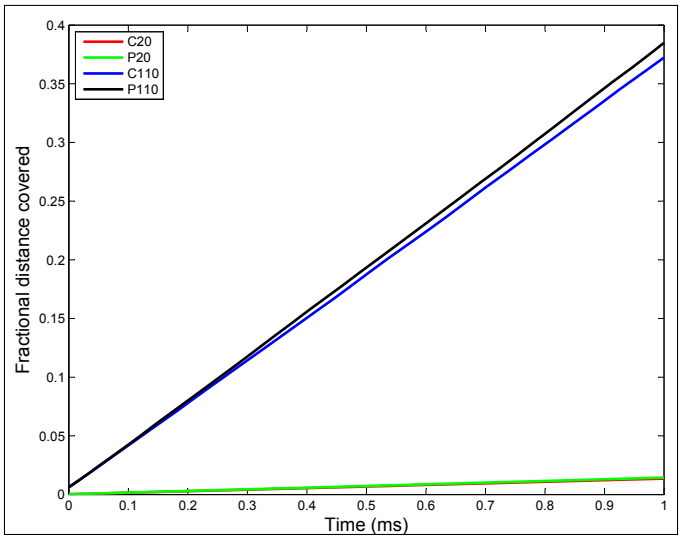

Figure III.13: ADSRM model simulation results of fractional distance covered by ENMs across the alveolar lining thickness (a value of one represents the bottom of the lining layer at the cellular surface and a value of zero represents the top of the surfactant layer)

change in ENM diameter for the different types of ENMs considered, due to agglomeration. Larger ENMs (C110 and P110) seem to have a higher rate of agglomeration than the smaller ENMs. This might be counter-intuitive since most studies [43] have demonstrated smaller particles to have a higher tendency to agglomerate than larger particles. However, such tissue-level studies compare particles based on identical mass doses of different particles. Equal mass doses of larger and smaller particles would result in significantly larger numbers of the smaller particles resulting in far higher number concentration, which would enhance the number of probable collisions between the particles per unit time. On a per particle basis, a larger ENM would have a higher van der Waals' force of attraction than a smaller ENM, which explains the observed higher rates of agglomeration for C110 and P110. Among ENMs of the same size, PVP coated ENMs have a slightly lower rate of agglomeration due to increased steric stabilization (quantified by the parameter η_{s}) by PVP molecules as compared to citrate molecules. The results shown in Figure III.12 are used to estimate an average rate of agglomeration as increase in diameter per time unit. However, the model being stochastic, there are random variations in the results. The ADSRM model is run 10 times for each ENM and various kinetic parameters are estimated for each run. The means of the estimated values are summarized in Table III.8. Due to ENM transport across the alveolar lining being driven by surface tension, there is no discernible difference in the transport rates among the different types of ENMs. So the average transport velocities for the different ENMs across the alveolar lining layer (Table III.8) are identical. Figure III.14 shows fractional surface coverage of ENM surface due to surfactant phospholipid (PL) adsorption. Smaller ENMs seem to be coated with lipids faster, due to the fact that a single interaction between a vesicle and a smaller ENM might completely cover the smaller ENM, while for a larger ENM this might require multiple interactions. Table III.8 shows the rates for PL adsorption which has been normalized by the surface area of the ENMs to cancel the effect of size. PL adsorption rate has been quantified as amount of PL adsorbed per unit

surface area per time and is estimated based on the fractional surface coverage and considering a uniform PL bilayer of 4 nm on the ENMs. Comparison of the values shows that P20 has a slightly lower value (even lower than P110) of adsorption rate which might be due to higher number of coating molecules per unit surface area (Table B.11 in Appendix B) on P20 than on P110. Figure III.15 shows the number of protein molecules adsorbed per ENM. SP-B and SP-C have a higher prevalence due to their close association with surfactant lipids. Also larger ENMs (C110 and P110) have higher tendency to attract surfactant proteins due to larger available surface area.

Table III.8: Estimated parameter values for ENM kinetics *in vivo*

Parameter	**C20**	**C110**	**P20**	**P110**
Agglomeration rate (nm/sec)	5.423×10^{-6}	3.483×10^{-5}	5.82×10^{-6}	3.986×10^{-5}
Transport rate (m/sec)	7.481×10^{-5}	7.481×10^{-5}	7.481×10^{-5}	7.481×10^{-5}
Dissolution rate (per sec)	4.25×10^{-11}	6.375×10^{-9}	5.525×10^{-14}	9.52×10^{-13}
Phospholipid (PL) adsorption rate (ng/nm^2/sec)	1.053×10^{-7}	1.304×10^{-7}	9.06×10^{-8}	1.166×10^{-7}
Surface active (SA) protein adsorption rate (nmol/nm^2/sec)	3.36×10^{-18}	1.61×10^{-19}	3.233×10^{-18}	1.29×10^{-19}
Collectin (C) adsorption rate (nmol/nm^2/sec)	2.66×10^{-18}	1.55×10^{-19}	3.737×10^{-18}	8.472×10^{-20}

III.10 Summary

The work described in this chapter, presents the development of the ADSRM framework and its extension to the pulmonary alveolar lining layer. Generally toxicokinetic or toxicodynamic models for nanoparticles [145, 34, 146] approximate various physiological compartments via well-mixed compartments and mechanisms by linear, first-order kinetic rates. However, due to the size and unique properties of ENMs, their interactions with various biochemical molecules and cells often cannot be described by simple kinetic equations. This chapter describes a stochastic, DSMC algorithm to

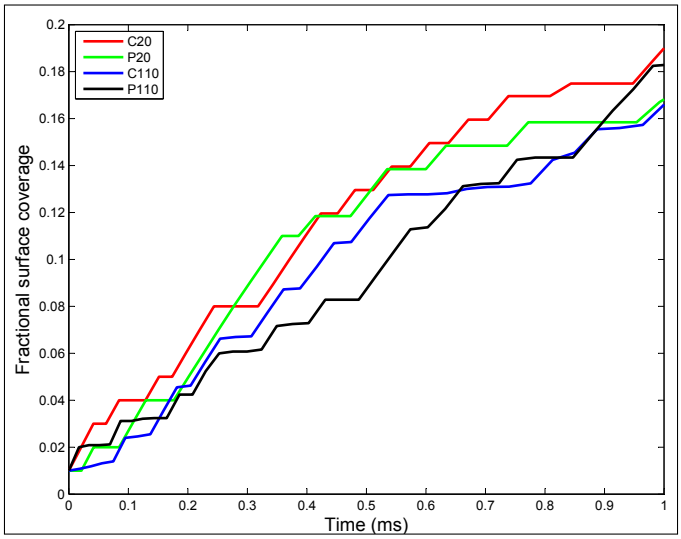

Figure III.14: ADSRM model simulation results of mean fractional surface coverage of ENMs by adsorbed surfactant phospholipids for four different types of silver ENMs.

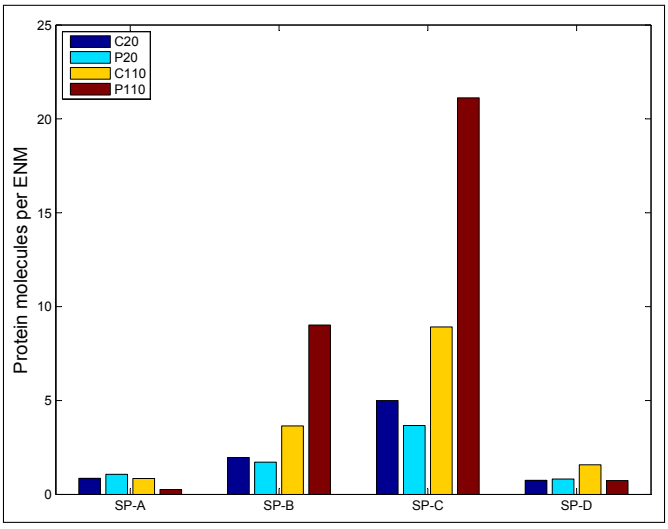

Figure III.15: ADSRM model simulation results of surfactant protein molecules adsorbed on different ENMs.

model interactions of ENMs with each other and with biological agents in the alveolar lining layer, which forms a critical first line of defense against inhaled particulate matter. The model considers agglomeration, transport, and reaction of ENMs as treated in the earlier version of the model [42], but also considers surfactant lipid and protein adsorption on ENMs. Surfactant adsorption has been identified as a critical mechanism which regulates particle toxicodynamics and affect further uptake and clearance of the ENMs. Surfactant proteins have multiple roles including promoting surface activity (SP-B, SP-C) and inducing immune response (SP-A, SP-D). All four protein types have been separately identified and their adsorption on the ENMs is modeled here using the DSMC scheme. The model was first implemented for *in vitro* systems in order to parameterize the extended formulation utilizing published data. The model was subsequently applied to the human alveolar lining layer, considering an inhalation dose of four types of ENMs, to investigate effects of size as well as surface coating type.

In vivo toxicodynamics of nanoparticles consist of multiple interactions between the particles themselves and also with cells and biochemical molecules. The model described here considers the most important interactions and mechanisms relevant to particle toxicodynamics in the alveolar lining layer. The model utilizes mechanistic information available in the scientific literature and also relevant *in vitro* studies to simulate a phenomenon for which at present, there are no *in vivo* measurements. *In vivo* characterization of particokinetics in the pulmonary regions is nearly impossible due to the small size and time scales, which prevent an accurate and quantifiable description. The model described here will be utilized, in later chapters, to inform and improve tissue-scale pulmonary toxicodynamic models involving ENMs.

Chapter IV

Tissue Scale Toxicodynamics

IV.1 Background

This chapter describes the development and evaluation of a tissue scale computational model of the toxicodynamic response of the mammalian pulmonary system due to silver nanoparticle (nAg) exposure. It has been pointed out earlier that surfactant dysfunction leading to altered pulmonary mechanics is one of the toxicodynamic responses of particulate matter inhalation [147, 148]. The tissue scale model described here utilizes nano scale information from the previous chapter and models multiple processes in the pulmonary alveolar sub-system, including surfactant dynamics, cellular processes, and surfactant regulation. The development is accomplished in two stages. First a simpler version of the model is developed and implemented for mice and model predictions compared to *in vivo* measurements of mouse lung lavage from collaborators Dr. Andrew Gow and Danielle Botelho at the School of Pharmacy, Rutgers University. The model is subsequently improved by consideration of additional biological mechanisms and the inclusion of nano scale particokinetic estimates from the previous chapter. The model is then extended and implemented for Sprague-Dawley and Brown-Norway rats followed by comparison of model predictions with *in vivo* measurements of rat lung lavage from collaborators at the National Heart and

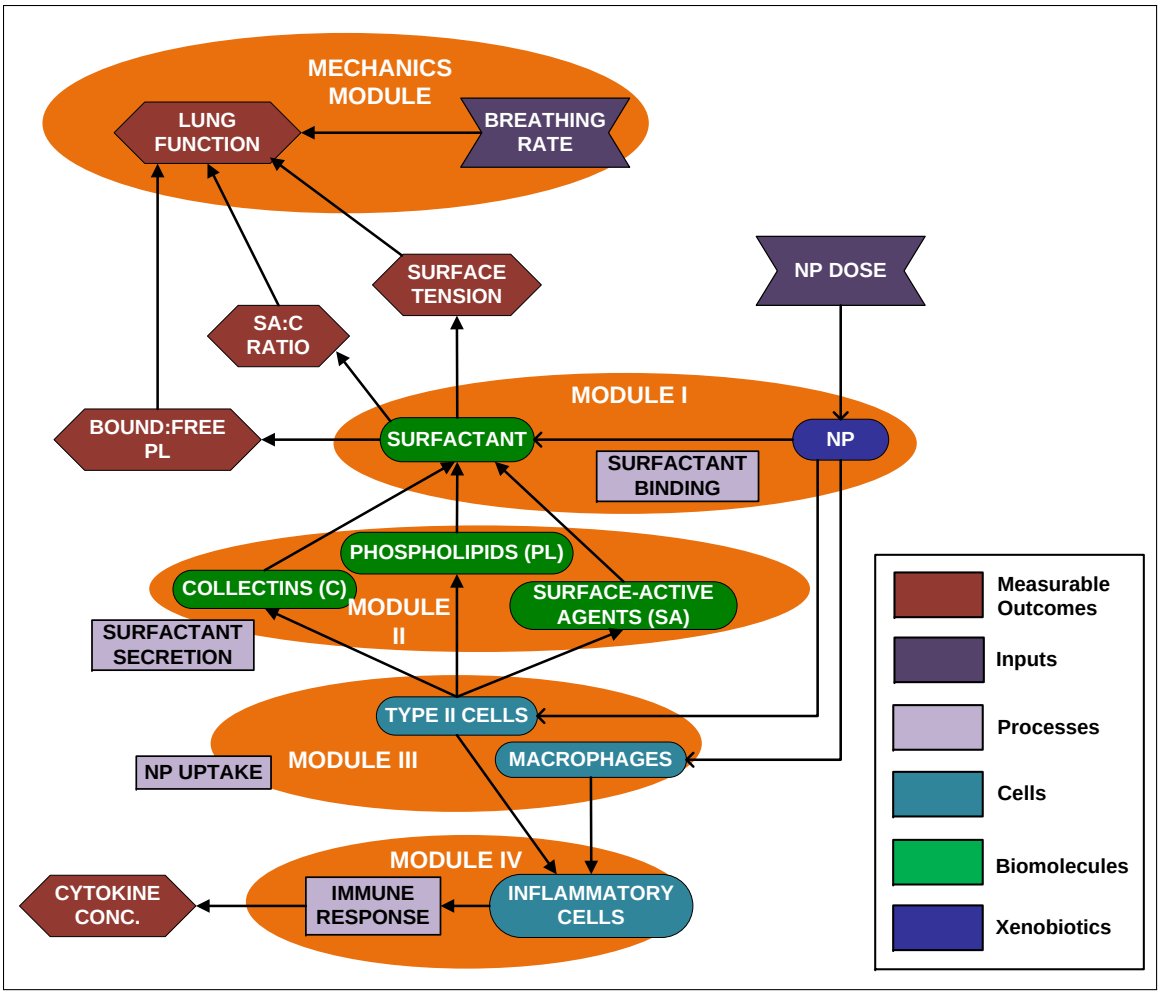

Figure IV.1: Modular decomposition of alveolar toxicodynamic processes at the tissue scale

Lung Institute of the Imperial College, London. The model is then extended to humans and model predictions are presented corresponding to nAg inhalation exposure for adult humans.

This toxicodynamic model developed here considers the effects of nanoparticle inhalation on various biochemical and biological agents in the lung. The entire alveolar system has been "separated" into functional modules and each module has been separately analyzed. Figure IV.1 shows a schematic representation of the modular decomposition of the functional modules and the interaction between various processes and variables. Module I (shown separately in Figure IV.2) considers the binding of

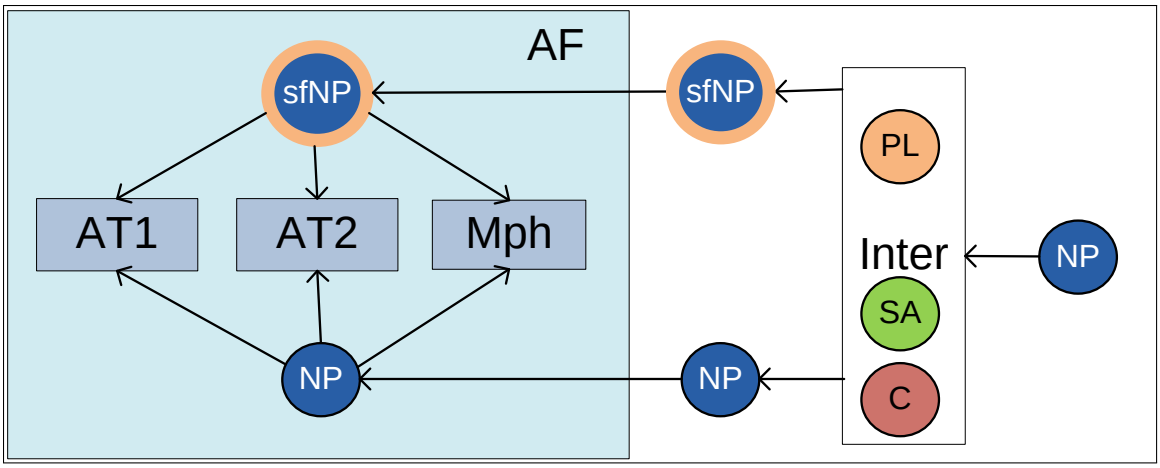

Figure IV.2: Detailed schematic of compartmental model for Modules I & III considering surfactant binding with NPs and NP uptake by alveolar Type I and Type II cells and macrophages. (Figure reproduced from Mukherjee *et al.* [145] under Creative Commons Attribution License)

surfactant to nanoparticles once they reach the alveolar surface, which results in surfactant depletion and affects lung function. Module II (Figure IV.3) considers the balance of surfactant in the system considering surfactant secretion by cells, adsorption to the interface and surfactant recycling. Module III considers particle uptake by type I and type II cells and macrophages lining the pulmonary alveolar wall.

IV.2 Model development

IV.2.1 Modeling surfactant kinetics - Module II

The compartmental model developed here, along with the various tissue compartments and cells involved in the model, are shown in Figure IV.3. Pulmonary surfactant is composed of 90% of phospholipids, and about 10% of lipoproteins [115]. The lipoproteins present in pulmonary surfactant are generally classified into 4 types: surfactant proteins (SP) A, B, C, & D. SP-B and SP-C are lipophilic proteins which are involved in modulating the surface-active function of pulmonary surfactant. They have been represented in the model as surface-active proteins, SA. SP-A and SP-D are associated with immune response of the pulmonary system to xenobiotics and have

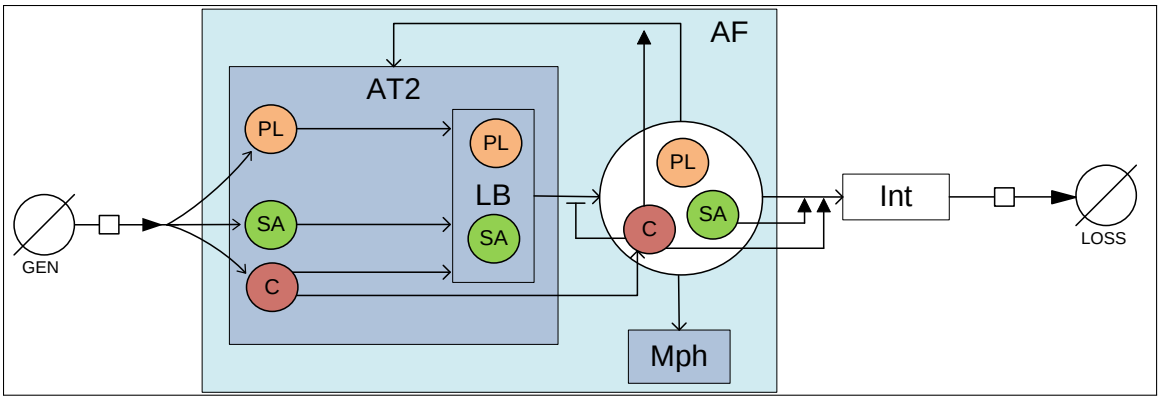

Figure IV.3: Detailed schematic of compartmental model for surfactant dynamics consisting of surfactant components phospholipids (PL), surface-active lipoprotiens (SA), and collectins (C). Physiological compartments considered are alveolar type II cells (T2), lamellar bodies (LB) within type II cells, alveolar macrophages (Mph), alveolar fluid (AF), alveolar air-liquid interface (Int), and surfactant loss to airways (Loss); (Figure reproduced from Mukherjee *et al.* [145] under Creative Commons Attribution License)

been represented as collectins, C. Pulmonary function and response to inhaled particulate matter occurs as an interplay between these various components [114]. The various steps involved in the processing of pulmonary surfactant in the mammalian lung, can be summarized as:

- Secretion of surfactant components SA, C, and PL into lamellar bodies (LB) within alveolar Type II cells [149, 114]
- Exocytosis of LB and release of surfactant into the alveolar fluid (AF)
- Processing of surfactant into tubular myelin
- Migration of tubular myelin from the AF to the alveolar air-liquid interface (Int) [150]
- Formation of the surfactant layer at the interface
- Collapse of surfactant layer at the interface
- Recycling of surfactant components into type II cells

Surfactant secretion

Surfactant components are secreted by alveolar type II cells (AT2) into lamellar bodies (LB) [151]. The process of secretion of the surfactant components is considered to occur in two steps - the secretion of the chemicals into LB and the exocytosis of LB into the AF. There is considerable debate in published literature on the exact secretory pathway of SP-A. Some researchers [152] have shown most SP-A to be secreted constitutively independent of LB. However, Fisher *et al.* [153] have shown that secretion of SP-A into LB precedes its secretion into the hypophase. But there is increasing evidence that both pathways are involved in the secretion of SP-A [154]. So, both pathways have been considered to be valid for collectins. The lamellar bodies are exocytosed from the type II cells and the secreted surfactant components released. The rate of LB exocytosis has been estimated from Martini *et al.* [151] to be 239 nmol/h/g lung. Surfactant components are also known to be recycled back into the type II cell [155, 149]. In addition to these processes of removal of surfactant components, macrophages ingest some surfactant and some amounts are lost via the airways [149]. Macrophage uptake of surfactant components has been studied by Gurel *et al.* [156] and the rate constants have been estimated from their work. Pettenazzo *et al.* [157] and others have found airway loss of surfactant to be limited to 3% over 24 hours. Accordingly, an appropriate fractional loss term is included for loss of surfactant to the airways. Details of parameter estimation are included in Appendix C.

Surfactant adsorption

The surfactant components in the alveolar fluid form concentrated film-like structures called tubular myelin [149] which are then adsorbed onto the alveolar air-liquid interface. These processes have been modeled by a single adsorption process, where the 3 surfactant components adsorb at different rates onto the alveolar surface lining. The

rate of adsorption is influenced by surfactant concentration in the sub-phase (AF) and also by the concentration in the pre-existing alveolar surface film [158]. Adsorption rate of PL, $R_{\mathrm{Ad,PL}}$ is estimated as: $R_{\mathrm{Ad,PL}} = C_{\mathrm{b}} K_{\mathrm{Ad}}(C_{\mathrm{seq}} - C_{\mathrm{s}})$, where, C_{b} is the bulk concentration of PL, C_{s} is the surface concentration, and C_{seq} is the equilibrium surface concentration estimated from the normal level of PL at the interface. The adsorption rate constant is estimated using data from Walters *et al.* [158]. Protein and lipid components of surfactant are separated during adsorption into the surface layer [149]. Since they are part of the same tubular myelin when they get adsorbed into the interface, the adsorption and depletion rates of SA and C are considered to be identical to the adsorption rate of PL but the equilibrium concentrations, C_{seq} for each component would be different. The surface film also splits during the breathing cycle and the surfactant components are returned to the hypophase [159], which is modeled by a desorption term.

Regulation of surfactant dynamics

The various components of pulmonary surfactant do not function independently. The surfactant proteins are involved in various functions in the regulation of secretion, adsorption and recycling of phospholipids in the alveolar sub-phase [149]. SP-A binds strongly to PL and promotes the formation of the tubular myelin and the interfacial surfactant film [160, 115]. SP-B and SP-C promote adsorption of PL to the alveolar surface and aid in surface tension reduction by helping spread the lipids [161]. SP-A has also been found to inhibit the secretion of PL by Type II cells [155] and to promote the recycling of PL back into Type II cells (Chapters 4 and 7 in [162]). The regulation of these processes has been quantified using results from published studies.

Model equations

The mathematical model for Module II, considers the dynamics in the alveolar lining fluid and involves five compartments, namely type II cells (AT2), lamellar bodies

(LB), alveolar fluid (AF), alveolar air-liquid interface (Int), and a purely mathematical compartment called 'Loss', which considers the net loss of surfactant from the system. The module with its constituent compartments is schematically depicted in Figure IV.3. The mass balance equations involving the five compartments are shown below. M represents the amount of a particular species in µmol, and K stands for the rate constant for a particular process in min^{-1}. The subscript 'i' represents the three surfactant components considered - PL, SA, and C.

$$\frac{dM_{\mathrm{AT2,i}}}{dt} = R_{\mathrm{Gen,i}} - (K_{\mathrm{Sec,i}} + K_{\mathrm{DSec,i}}).M_{\mathrm{AT2,i}} + K_{\mathrm{Re}}.M_{\mathrm{AF,i}} \tag{IV.1}$$

$$\frac{dM_{\mathrm{LB,i}}}{dt} = K_{\mathrm{Sec,i}}.M_{\mathrm{AT2,i}} - K_{\mathrm{LB}}.M_{\mathrm{LB,i}} \tag{IV.2}$$

$$\begin{aligned}\frac{dM_{\mathrm{AF,i}}}{dt} &= K_{\mathrm{LB}}.M_{\mathrm{LB,i}} + K_{\mathrm{DSec,i}}.M_{\mathrm{AT2,i}} + K_{\mathrm{Des}}.M_{\mathrm{Int,i}} - (K_{\mathrm{Re}} + K_{\mathrm{Deg}}).M_{\mathrm{AF,i}} \\ &\quad - K_{\mathrm{Ad,i}}M_{\mathrm{AF,i}}(M^{\mathrm{eq}}_{\mathrm{Int,i}} - M_{\mathrm{Int,i}})\end{aligned} \tag{IV.3}$$

$$\frac{dM_{\mathrm{Int,i}}}{dt} = K_{\mathrm{Ad,i}}M_{\mathrm{AF,i}}(M^{\mathrm{eq}}_{\mathrm{Int,i}} - M_{\mathrm{Int,i}}) - K_{\mathrm{Dep}}.M_{\mathrm{Int,i}} - K_{\mathrm{AW,i}}.M_{\mathrm{Int,i}} \tag{IV.4}$$

$$\frac{dM_{\mathrm{Loss,i}}}{dt} = K_{\mathrm{AW,i}}.M_{\mathrm{Int,i}} + K_{\mathrm{Deg}}.M_{\mathrm{AF,i}} - R_{\mathrm{Gen,i}} \tag{IV.5}$$

Here *Gen* stands for generation, *Sec* for secretion, *DSec* for direct secretion, *Re* for recycle, *LB* for exocytosis of lamellar bodies, *Ad* for adsorption, *Des* for desorption, *Deg* for degradation, and *AW* for airway loss. K_{DSec} is the rate constant for direct constitutive secretion into the alveolar fluid, which is known to happen for collectins [154] and does not exist for PL or SA. So K_{DSec} is zero for PL and SA. There are a total of $5 \times 3 = 15$ differential equations for the mass balance of surfactant components.

The regulatory kinetics of surfactant components on the various surfactant delivery processes as described above are mathematically described in the equations below. K^0 stands for the rate constant without the regulation effect, K stands for the rate constant with regulation, and $k^{\mathrm{j}}_{\mathrm{i}}$ represents the regulatory rate constant of species

j on process i. C represents the concentration of the particular component in the alveolar fluid in µmol/ml.

$$K_{\mathrm{Ad,PL}} = K^{0}_{\mathrm{Ad,PL}}(1 + k^{\mathrm{SA}}_{\mathrm{Ad}}.C_{\mathrm{SA}} + k^{\mathrm{C}}_{\mathrm{LB}}.C_{\mathrm{C}}) \tag{IV.6}$$

$$K_{\mathrm{LB}} = K^{0}_{\mathrm{LB}}(1 - k^{\mathrm{C}}_{\mathrm{LB}}.C_{\mathrm{C}}) \tag{IV.7}$$

$$K_{\mathrm{Re,PL}} = K^{0}_{\mathrm{Re,PL}}(1 + k^{\mathrm{C}}_{\mathrm{Re}}.C_{\mathrm{C}}) \tag{IV.8}$$

Table IV.1: Steady-state values of PL, SA, & C in various compartments (in µmol/g lung)

	Type II cell	**Lamellar Body**	**Alveolar fluid †**	**Alveolar interface**
PL	10†	1.14‡	0.0818	1.46‡
SA	0.175∗	1.995×10^{-2} ††	0.0035	0.0301 ⋄
C	1.7848 ∗∗	6.8×10^{-6} ††	0.0146	0.0151 ⋄

† Meyer *et al.* [137] (young humans)
‡ Martini *et al.* [151] (pigs)
⋄ Possmayer *et al.* [163] (Bovine surfactant)
†† Oosterlaken-Dijksterhuis *et al.* [164] (rats)
∗ Considering identical proportion of SA with respect to PL as in LB
∗∗ Considering identical proportion of C with respect to PL as in AF

Parameter estimation

The estimation of the rate constants described in the above equations has been carried out using results from published *in vitro* and *in vivo* studies. Physiological parameters for mice were estimated from the literature and, wherever unavailable, were scaled from other species using body weight (Table C.2 in Appendix C). The rate constants whose values were explicitly estimated from the literature are summarized in Table C.4 in Appendix C. Only K_{Des}, K_{Deg}, and K_{DSec} were not readily available in the literature and were estimated based on a steady-state analysis. The pulmonary surfactant sub-system maintains the levels of the various surfactant components steady at a physiological level to maintain the functions of surfactant in the lung. The steady-state values of various components in the physiological compartments are summarized in Table IV.1. The steady state in AT2 is maintained explicitly in the mathematical

model by considering the generation term as: $R_{\mathrm{Gen}} = M^{\mathrm{ss}}_{\mathrm{AT2,i}} - M_{\mathrm{AT2,i}}$. The lamellar body (LB) is a transient entity and is constantly forming and dividing and there cannot be any biological steady state for it. So the steady state analysis considers a steady state in the alveolar fluid (AF) and alveolar interface (Int). Accordingly based on Equations IV.3 and IV.4, the steady state for PL and SA ($K_{\mathrm{DSec}} = 0$) can be represented as:

$$K_{\mathrm{LB}}.M_{\mathrm{LB,i}} + K_{\mathrm{Des}}.M_{\mathrm{Int,i}} - (K_{\mathrm{Re}} + K_{\mathrm{Deg}}).M_{\mathrm{AF,i}} - K_{\mathrm{Ad,i}}M_{\mathrm{AF,i}}(M^{\mathrm{eq}}_{\mathrm{Int,i}} - M_{\mathrm{Int,i}}) = 0 \quad \text{(IV.9)}$$

$$K_{\mathrm{Ad,i}}M_{\mathrm{AF,i}}(M^{\mathrm{eq}}_{\mathrm{Int,i}} - M_{\mathrm{Int,i}}) - K_{\mathrm{Dep}}.M_{\mathrm{Int,i}} - K_{\mathrm{AW,i}}.M_{\mathrm{Int,i}} = 0 \quad \text{(IV.10)}$$

The two unknown parameters K_{Des}, and K_{Deg} are estimated for PL and SA using the steady state equations IV.9 and IV.10. For C, the equation for alveolar fluid would be different because of the direct secretion pathway of C. Equation IV.9 would be modified as:

$$K_{\mathrm{LB}}.M_{\mathrm{LB,i}}+K_{\mathrm{DSec,i}}.M_{\mathrm{AT2,i}}+K_{\mathrm{Des}}.M_{\mathrm{Int,i}}-(K_{\mathrm{Re}}+K_{\mathrm{Deg}}).M_{\mathrm{AF,i}}-K_{\mathrm{Ad,i}}M_{\mathrm{AF,i}}(M^{\mathrm{eq}}_{\mathrm{Int,i}}-M_{\mathrm{Int,i}}) = 0 \quad \text{(IV.11)}$$

K_{DSec} is estimated from Equation IV.11 assuming the value of K_{Des} for C to be equal to that of PL and SA and K_{Deg} for C estimated from [156].

The parameter values estimated from the literature are based on *in vivo* studies and hence implicitly include the regulatory effects. However, since the effects of regulation are explicitly considered in the model, the process parameters K need to be considered separate from the regulatory parameters k. The parameter values are optimized using the *fmincon* subroutine in Matlab, using the literature values of K and k as initial estimates. The final optimized parameter values (along with the initial estimates) are summarized in Table C.5 in Appendix C.

IV.2.2 Nanoparticle interaction with surfactant - Module I

Nanoparticles, like other xenobiotics, are arrested by the interfacial surfactant layer after reaching the terminal airways and are coated by a layer of surfactant. Presence of particles on the alveolar surface might cause surfactant dysfunction by two mechanisms: direct and indirect [115]. Inhaled NPs bind to a fraction of the surfactant making it unavailable for adsorption and spreading on the alveolar interface and thus limiting the capacity of the alveolar to reduce surface tension [122]. Besides the direct interaction, presence of nanoparticles in the alveolar hypophase is liable to cause increase in the production of collectins (SP-A, SP-D) to counter the xenobiotics at the cost of the secretion of phospholipid (PL) or other surface-active (SA) proteins (SP-B, SP-C). Increase in oxidative stress and lipid peroxidation leads to pulmonary inflammation, which can change the surfactant composition drastically and cause surfactant dysfunction [123]. Pulmonary inflammation is in itself a complex process and has been discussed later in this chapter. Module I, as well as Module III, are shown schematically in Figure 2. The binding of phospholipids (PL) with NP is estimated using results from [118]. The process is modeled using Michaelis-Menten kinetics which depends on the surface area A of the particles and the available amount of surfactant at the alveolar interface. The depletion of PL is given by:

$$\frac{dM_{\mathrm{PL}}}{dt} = -\frac{V_{\mathrm{A}}A}{K_{\mathrm{A}} + A}.M_{\mathrm{PL}} \tag{IV.12}$$

where M is the amount (in µmol/ml) of PL, and A denotes the surface area of nanoparticles per ml of fluid (in m^2/ml). The estimated Michaelis-Menten parameters for the NP-surfactant binding are summarized in Table C.7 of Appendix C. The loss in free PL due to binding to NPs also leads to loss in free surface area of the NPs. The loss in area and loss in PL are related as: $dm_{\mathrm{PL}} = (1000h\rho)dA$, where h is the thickness of surfactant coating formed on the surface of particles (estimated to be $\tilde{4}$nm [122]), ρ is the density of surfactant (estimated to be 1040 mg/ml by Shelley

et al. [140] = 1439.6 µmol/ml), and the factor of 1000 is included to account for the conversion between ml/m² and nm. V_{A} and K_{A} are the Michaelis-Menten parameters estimated using results from Kendall *et al.* [118]. The nanoparticle balance equations in Module 1 calculate the number of NPs in different compartments, the number bound to PL, and the number which is free of PL.

$$\frac{dN_{\mathrm{Int}}}{dt} = \left(\frac{1}{\pi d^2}\right)\frac{dA}{dt} - k_{\mathrm{NP}}.N_{\mathrm{Int}} \tag{IV.13}$$

$$\frac{dN_{\mathrm{S,AF}}}{dt} = -\left(\frac{1}{\pi d^2}\right)\frac{dA}{dt} \tag{IV.14}$$

$$\frac{dN_{\mathrm{AF}}}{dt} = k_{\mathrm{NP}}.N_{\mathrm{Int}} \tag{IV.15}$$

Here, N denotes the number density of NPs (in number per ml) in various compartments and N_{S} denotes the NPs coated with surfactant. The NPs coated with surfactant are considered to be transported into the alveolar fluid (AF) instantly because of the cyclical surfactant exchange during every breathing cycle, whereas a fraction of the naked NPs are transported to the AF, the fraction given by k_{NP}.

IV.2.3 Nanoparticle interaction with cells - Module III

NPs are taken up by alveolar cells via endocytosis or phagocytosis. This phenomenon plays a critical role in estimating exposure and fate of NPs in the biological system as the alveolar epithelial cells form the gateway to the circulatory system and hence to the entire body. Lai *et al.* [165] showed that charcoal NPs are significantly taken up by Type I cells, Type II cells, and macrophages. Cellular uptake of particles is influenced by particle type, size and surface charge [83]. The process of cellular uptake has been considered to be composed of two processes: delivery and adhesion of NPs onto the cell and uptake of NPs by the cell via endocytosis or phagocytosis. Adhesion of NPs onto cell surface is a function of particle size, surface zeta potential, and by the type of cell. Adhesion probability, k_{f} is modeled according to Su *et al.* [83] as:

$k_{f,i} = k_i \eta_o \eta_e \frac{(1-\epsilon)}{\epsilon d_c}$, where, ϵ is the tissue porosity for the particular cell type, d_c is the cell diameter, k_c is a cell type dependent parameter, η_o,η_e, are the relative affinities of particle adhesion to the cell due to their size and surface potential respectively. Details of the estimation procedures have been included in Appendix A. Values of porosity and cell diameter for the alveolar cells are summarized in Table IV.2. η_o is a function of NP diameter d_p and the relation has been obtained for alveolar Mph from Oberdorster *et al.* [38] and for other cells from Su *et al.* [83]. η_e is a function of surface zeta potential of the NPs ζ and the relation has been obtained for alveolar Mph from Tabata and Ikada [95] and for AT1 and AT2 cells from Su *et al.* [83] and Harush-Frenkel *et al.* [166]. Type I and Type II cells also differ intrinsically in their particle uptake properties due to different distribution of cationic and anionic binding sites on their surfaces [167]. Kemp *et al.* [168] compared particle uptake in Type I and Type II cells for both positively and negatively charged particles. The cell dependent parameter k_c for AT1 and AT2 has been estimated using *in vitro* results from Kemp *et al.* [168]. Original NPs and NPs bound to surfactant would have different adhesion with cells. Ruge *et al.* [169] reported that the surface zeta potential of NPs after binding with PL and SP-A is -39.2mV. Endocytosis and phagocytosis processes are modeled by Michaelis-Menten kinetics. Michaelis-Menten parameters for NP endocytosis by AT1 and AT2 were estimated from Chithrani *et al.* [170] where endocytosis of gold NPs by HeLa cells is reported. NP phagocytosis rate parameters were estimated from Beduneau *et al.* [171]. The uptake of NPs by cells is given by:

$$\frac{dN}{dt} = -R_{AT1} - R_{AT2} - R_{Mph} \tag{IV.16}$$

$$\text{where, } R_{AT1,AT2} = k_{f,n} \frac{V_c N}{K_c + N}; R_{Mph} = k_{f,m} \frac{V_m N}{K_m + N} \tag{IV.17}$$

$$\text{and, } k_{f,i} = k_i \frac{(1-\epsilon)}{\epsilon d_c} \eta_o \eta_e, \text{ where, } \eta_o = f(d_p), \eta_e = f(\zeta) \tag{IV.18}$$

Table IV.2: Parameter values for estimating cellular uptake for various alveolar cells [145]

Parameter	AT1 cells	AT2 cells	Mph
Cell porosity, ϵ*	0.04	0.97	0.99
Cell diameter, d_c (µm)	75**	10**	11.2†

* Values estimated from Clegg *et al.* [172]
** From Chen *et al.* [173]
† From Morgan and Talbot [174]

IV.2.4 Cellular immune response

One major aspect of cellular interactions with particulate matter is cellular immune response due to the entry of the xenobiotic [175]. The inflammatory response system in mammals consists of a series of cascading events facilitated by several types of cells and protein mediators such as cytokines and chemokines [176]. The major types of lung cells involved in the inflammatory response system are macrophages (Mph), dendritic cells, alveolar epithelial type I and type II (AT1 and AT2) cells, and the various inflammatory cells such as poly mono-nuclear neutrophils (PMNs), lymphocytes, eosinophils, etc. [177]. Xenobiotics can trigger cytokine and chemokine production when in the local milieu and once inside the cell. On release, these chemical mediators signal the influx of more macrophages and inflammatory cells into the lung from the blood circulation, inducing further a cascade of events which comprise an inflammatory response, leading to removal of the nanoparticles (NPs) due to phagocytosis and endocytosis by the inflammatory cells [178]. Such a response is expected to restore homeostasis after removal of the xenobiotic chemical and replenishment of the dead cells. Under normal circumstances, an inflammatory response is tightly controlled by release of both pro- and anti-inflammatory mediators [179]. However, in some cases, the response might be unable to revert to homeostasis, leading to tissue sepsis [179].

In the early stage of inflammation, elimination of the xenobiotic (e.g. NPs) by phagocytosis is the priority of the response system [180]. Macrophages (Mph) play a major role in the phagocytic removal of NPs, after which they migrate to the lymph glands through the lymphatic and blood circulation system, or may be transferred

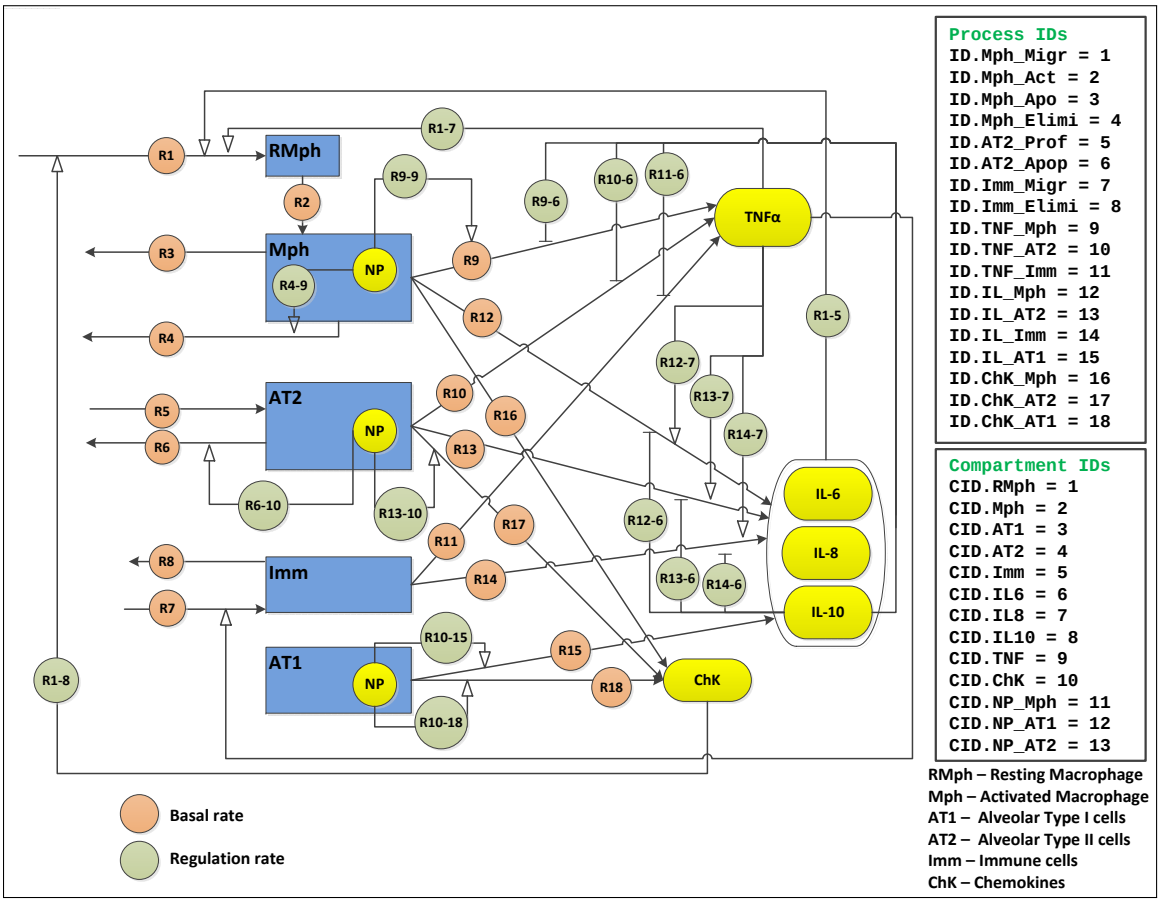

Figure IV.4: Cellular interaction, migration, and cytokine secretion of four cell types in the pulmonary alveolar sub-system for a proposed *in vivo* toxicodynamic model - macrophages, alveolar type I and type II cells, and immune cells, including cell-cell regulatory and signaling pathways. R1, R2, etc. are the basal kinetic rates of the various cellular processes; Ri-j is the rate of regulation of process Ri by the cell or chemical in CID j. All process and compartment IDs are listed on the right. [The diagram follows the standards of the Systems Biology Graphical Notation (SBGN); see *www.sbgn.org*] (Reproduced from Mukherjee *et al.* [44] under Creative Commons Attribution License)

to the throat via the mucociliary clearance system and swallowed or expectorated. NPs are also endocytosed by other cells of the alveolar region. Inside the cells, large quantities of reactive intermediates (reactive oxygen and nitrogen) are produced in the early stage to set up an appropriate response and neutralize the xenobiotics [181]. However, production of excess of reactive intermediates also triggers secondary mechanisms which might lead to cellular apoptosis [178]. As mentioned earlier, the presence of NPs signals the influx of more phagocytic cells to the alveolar region for removal of NPs, partly involving release of cytokines and chemokines, which are produced by cells such as Mph, immune cells (Imm), comprising neutrophils, and lymphocytes in varying amounts [182]. As inflammation progresses, there is an increase in the cell count of the system due to influx of Mph and Imm and also an increase in concentration of the chemical mediators. Inflammatory chemical mediators can be pro-inflammatory or anti-inflammatory or both, depending on their concentration [183]. In essence, pro-inflammatory mediators (such as TNF-α and IL-6) upregulate and anti-inflammatory mediators (IL-10) downregulate the inflammatory response. In ideal cases, after the NPs have been removed from the system, the anti-inflammatory response is expected to help restore the system to homeostasis [183]. This is accompanied by removal of apoptotic cells, reduction in concentrations of pro-inflammatory cytokines, and clearance of immune cells from the tissue by migration or apoptosis [179]. Figure IV.4 summarizes the signaling effects mediated by the various alveolar cells in response to xenobiotic exposure. Table IV.3 summarizes the important cell-NP interactions and the cellular dynamic processes as described in a comprehensive mathematical framework.

Alveolar macrophages play a critical role in phagocytosis and immune response due to inhaled NPs [171]. Consequently, NP interaction with these cells is of crucial importance. Module III of the overall toxicodynamic model which concerns NP-cell interaction, has been improved by utilizing *in vitro* measurements from cultures of rat alveolar macrophages (AMs) and human monocyte-derived macrophages (MDMs). A

Table IV.3: Equations constituting the mathematical framework for a proposed *in vivo* cellular scale inflammatory pathway model

Resting macrophages:	$\frac{dN_{\mathrm{RMph}}}{dt} = R_{\mathrm{Mig,RMph}} - R_{\mathrm{Act}}$
Active macrophages:	$\frac{dN_{\mathrm{Mph}}}{dt} = R_{\mathrm{Act}} - R_{\mathrm{Elim,Mph}} - R_{\mathrm{Apo,Mph}}$
Type I cells:	$\frac{dN_{\mathrm{AT1}}}{dt} = R_{\mathrm{Pro,AT1}} - R_{\mathrm{Apo,AT1}}$
Type II cells:	$\frac{dN_{\mathrm{AT2}}}{dt} = R_{\mathrm{Pro,AT2}} - R_{\mathrm{Apo,AT2}}$
Immune cells:	$\frac{dN_{\mathrm{Imm}}}{dt} = R_{\mathrm{Mig,Imm}} - R_{\mathrm{Elim,Imm}}$
NP uptake by Mph:	$\frac{dN_{\mathrm{NP,Mph}}}{dt} = k_{\mathrm{f,Mph}} \cdot \frac{V_{\mathrm{Mph}} N_{\mathrm{NP}}}{K_{\mathrm{Mph}} + N_{\mathrm{NP}}}$
NP uptake by AT1:	$\frac{dN_{\mathrm{NP,AT1}}}{dt} = k_{\mathrm{f,AT1}} \cdot \frac{V_{\mathrm{AT1}} N_{\mathrm{NP}}}{K_{\mathrm{AT1}} + N_{\mathrm{NP}}}$
NP uptake by AT2:	$\frac{dN_{\mathrm{NP,AT2}}}{dt} = k_{\mathrm{f,AT2}} \cdot \frac{V_{\mathrm{AT2}} N_{\mathrm{NP}}}{K_{\mathrm{AT2}} + N_{\mathrm{NP}}}$
TNF-α secretion:	$\frac{dM_{\mathrm{TNF}}}{dt} = R_{\mathrm{TNF,Mph}} + R_{\mathrm{TNF,AT2}} + R_{\mathrm{TNF,Imm}}$
IL-6 secretion:	$\frac{dM_{\mathrm{IL6}}}{dt} = R_{\mathrm{IL6,Mph}} + R_{\mathrm{IL6,AT1}} + R_{\mathrm{IL6,AT2}} + R_{\mathrm{IL6,Imm}}$
IL-8 secretion:	$\frac{dM_{\mathrm{IL8}}}{dt} = R_{\mathrm{IL8,Mph}} + R_{\mathrm{IL8,AT1}} + R_{\mathrm{IL8,AT2}} + R_{\mathrm{IL8,Imm}}$
IL-10 secretion:	$\frac{dM_{\mathrm{IL10}}}{dt} = R_{\mathrm{IL10,Mph}} + R_{\mathrm{IL10,AT1}} + R_{\mathrm{IL10,AT2}} + R_{\mathrm{IL10,Imm}}$
Chemokine secretion:	$\frac{dM_{\mathrm{ChK}}}{dt} = R_{\mathrm{ChK,Mph}} + R_{\mathrm{ChK,AT1}} + R_{\mathrm{ChK,AT2}}$
NP balance:	$\frac{dN_{\mathrm{NP}}}{dt} = R_{\mathrm{NP,alv}} - R_{\mathrm{NP,Mph}} - R_{\mathrm{NP,AT1}} - R_{\mathrm{NP,AT2}} - R_{\mathrm{Elim}}$

separate immune response model is developed and implemented for *in vitro* cultures which is parameterized using *in vitro* measurements from collaborators (Drs. Stephan Schwander and Srijata Sarkar, Rutgers School of Public Health and Drs. Teresa Tetley and Andrew Thorley, Imperial College, London). Mathematical modeling of cellular responses to xenobiotics requires estimation of a large number of parameters for the particular cell types under consideration. *In vitro* toxicological studies of the cellular response to xenobiotics allow for a simplified system that excludes confounding factors

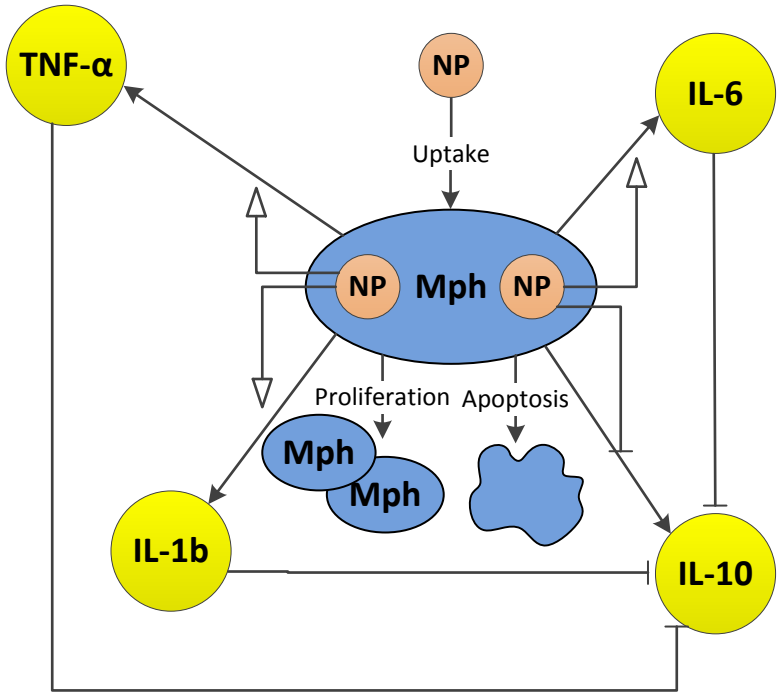

Figure IV.5: Schematic representation of macrophage dynamics involving proliferation, apoptosis, and cytokine secretion *in vitro*. [The diagram follows the standards of the Systems Biology Graphical Notation (SBGN); see sbgn.org] (Reproduced from Mukherjee *et al.* [44] under Creative Commons Attribution License)

introduced by other cells and processes involved in tissue dosimetry. Derivation of parameters for such studies can be facilitated by modeling first the *in vitro* case, in conjunction with parameter optimization based on results of *in vitro* experiments. This information can provide a foundation for subsequent *in vivo* modeling of cellular responses in animal systems, which is beyond the scope of this thesis.

Immune response model for alveolar macrophages

Mathematical modeling of cellular dynamics has been accomplished mechanistically utilizing systems of ordinary differential equations (ODEs)to simulate cellular processes [184, 185]. The model developed here has been implemented for macrophages comprising *in vitro* cultures. Figure IV.5 shows the effects considered in the model for macrophages (Mph). The model considers macrophage proliferation and apoptosis and the production of four key cytokines in response to uptake of nAg from

the culture media. For the *in vitro* model, the process is designed to start from the initial number of cells used in each sample medium. The cell count is modulated due to apoptosis and proliferation. Proliferation of cells is assumed not to be limited by the presence of nutrients in the medium. These processes can be represented by the equations below:

$$\frac{dN}{dt} = R_{\mathrm{Pro}} - R_{\mathrm{Apo}}, \tag{IV.19}$$

where, R_{Pro} is the rate of cellular proliferation, and R_{Apo} is the rate of cellular apoptosis.

Cytokines TNF, IL-6, IL-1b, and IL-10 are considered to be secreted by the cell in the *in vitro* culture at a basal rate R_{i} and to degrade at a rate $k_{\mathrm{d,i}}$. The production of cytokines by cells is influenced by xenobiotics or cytokines present in the environment. The regulation is modeled using Hill-type kinetics. It is assumed here that the regulation is uniform over each cell type.

$$\frac{dC_{\mathrm{i}}}{dt} = R_{\mathrm{i}}(1 + f_{\mathrm{reg,i}}) - k_{\mathrm{d,i}}C_{\mathrm{i}}, \tag{IV.20}$$

$$f_{\mathrm{reg,i}} = \prod_{i,j} f_{\mathrm{i\text{-}j}}, \tag{IV.21}$$

where $f_{\mathrm{i\text{-}j}}$ denotes the regulation effect of cytokine j on cytokine i. The regulation effects are modeled via Hill-type equations as follows:

$$f_{\mathrm{i\text{-}j}} = \frac{C_{\mathrm{j}}^{\mathrm{n}}}{x_{\mathrm{i\text{-}j}} + C_{\mathrm{j}}^{\mathrm{n}}}, \text{for upregulation} \tag{IV.22}$$

$$f_{\mathrm{i\text{-}j}} = \frac{x_{\mathrm{i\text{-}j}}}{x_{\mathrm{i\text{-}j}} + C_{\mathrm{j}}}, \text{for downregulation} \tag{IV.23}$$

The power n controls the strength of the regulation effect.

In vitro cell model results

Further details of the model implementation including description of the *in vitro* cell cultures can be obtained in the corresponding published article (Mukherjee *et al.* [44]). Cell viability was measured *in vitro* for human alveolar macrophages using MTS assays. Figure IV.6 shows comparisons between model predictions and measured values for four doses of 20 and 110 nm citrate-coated nAg. There is good agreement between model predictions and measured values, except for the dose of 6.25 μg/ml of 110nm nAg for which the measurement shows an unusually high value but also a correspondingly high error. Figure IV.7 shows a comparison between model predictions and measured values for pro-inflammatory cytokine (IL-1b, TNF-α, IL-6) levels in the cell culture medium. Cytokine mRNA levels were measured in cell culture medium with human MDMs 4 hours after incubation with 20 and 50 nm citrate-coated nAg. Model predictions and measured values seem to agree well for IL-1b and TNF-α, however the model seems to consistently underestimate the level of IL-6 cytokine. Figure IV.8 shows the same comparison for the anti-inflammatory cytokine IL-10. Model predictions agree well with measured values, except for the highest dose of 20nm nAg, where the measured value shows a high degree of uncertainty. The estimated final parameter values have been summarized in Table IV.4.

Table IV.4: Optimized values of parameters for MDM *in vitro* cultures (with reference for initial estimate)

Proliferative index	0.23	[186]
Apoptotive index	0.11	[186]
TNF production rate*	2.671×10^{-10} nmol/min	[182]
IL-6 production rate*	7.0962×10^{-10} nmol/min	[182]
IL-8 production rate*	4.34×10^{-8} nmol/min	[182]
IL-10 production rate*	9.458×10^{-10} nmol/min	[187]

*Cytokine production rates represent the rate for 10^6 cells

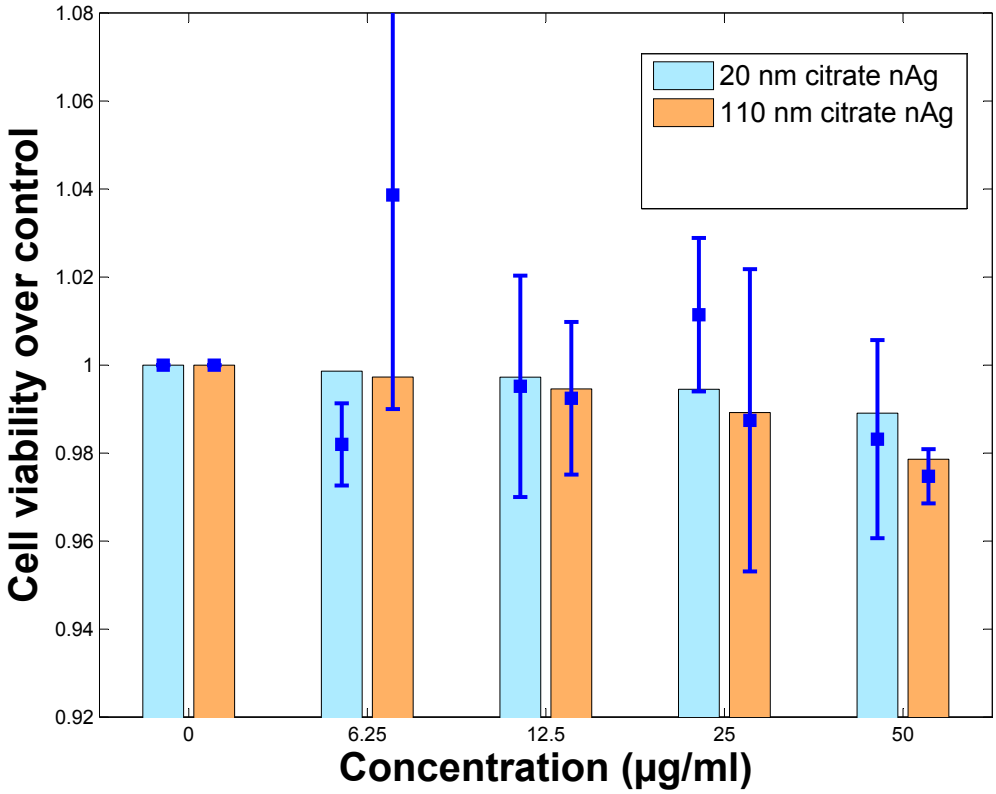

Figure IV.6: Comparison between model prediction and *in vitro* measurement for human alveolar macrophage cell viability, 24 hours after incubation. Bars represent model predictions and squares and error bars represent *in vitro* measurements. (Figure reproduced from Mukherjee *et al.* [44] under Creative Commons Attribution License)

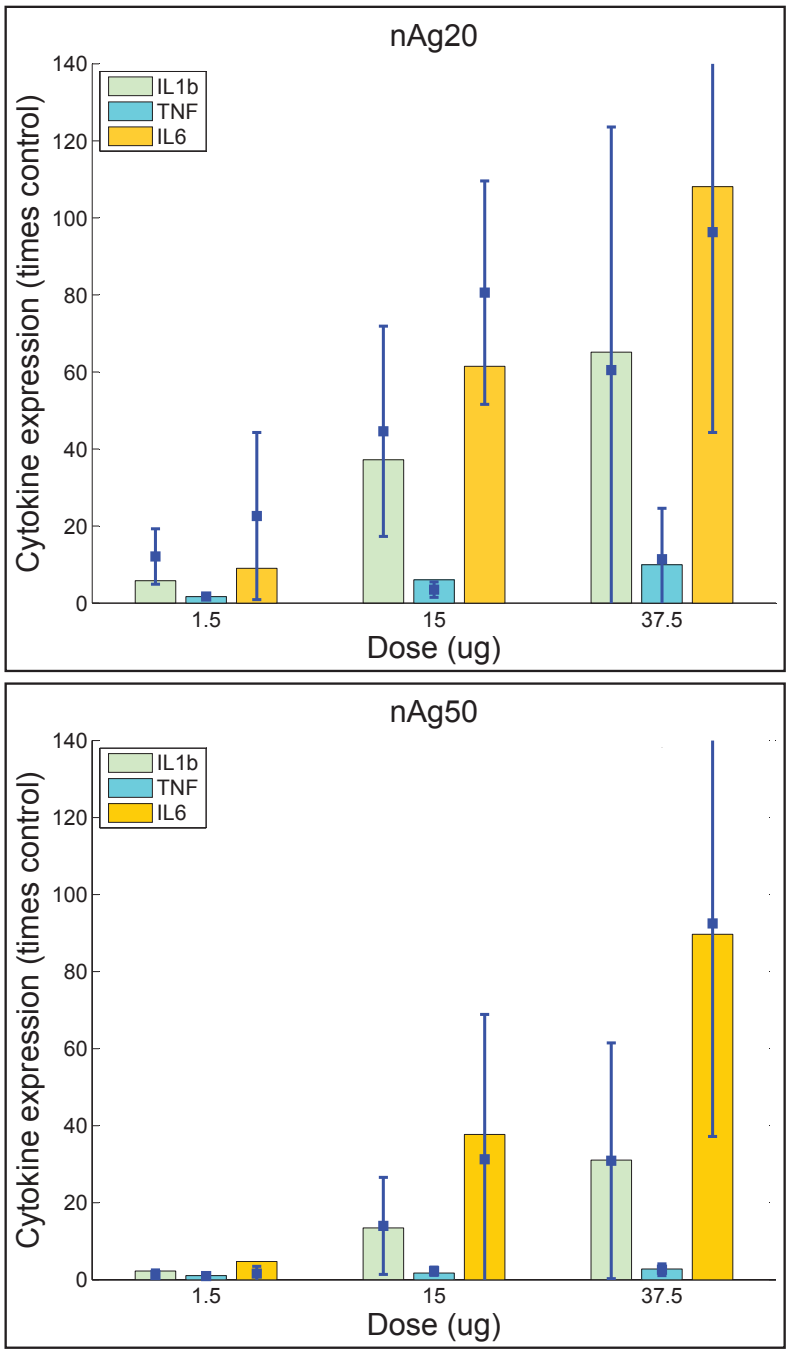

Figure IV.7: Comparison of model predictions and measured values of pro-inflammatory cytokine levels in culture medium after 4 hours for human MDMs with different doses of 20nm (top) and 50nm (bottom) nAg *in vitro*. Bars represent model predictions and squares and error bars represent *in vitro* measurements. (Figure reproduced from Mukherjee *et al.* [44] under Creative Commons Attribution License)

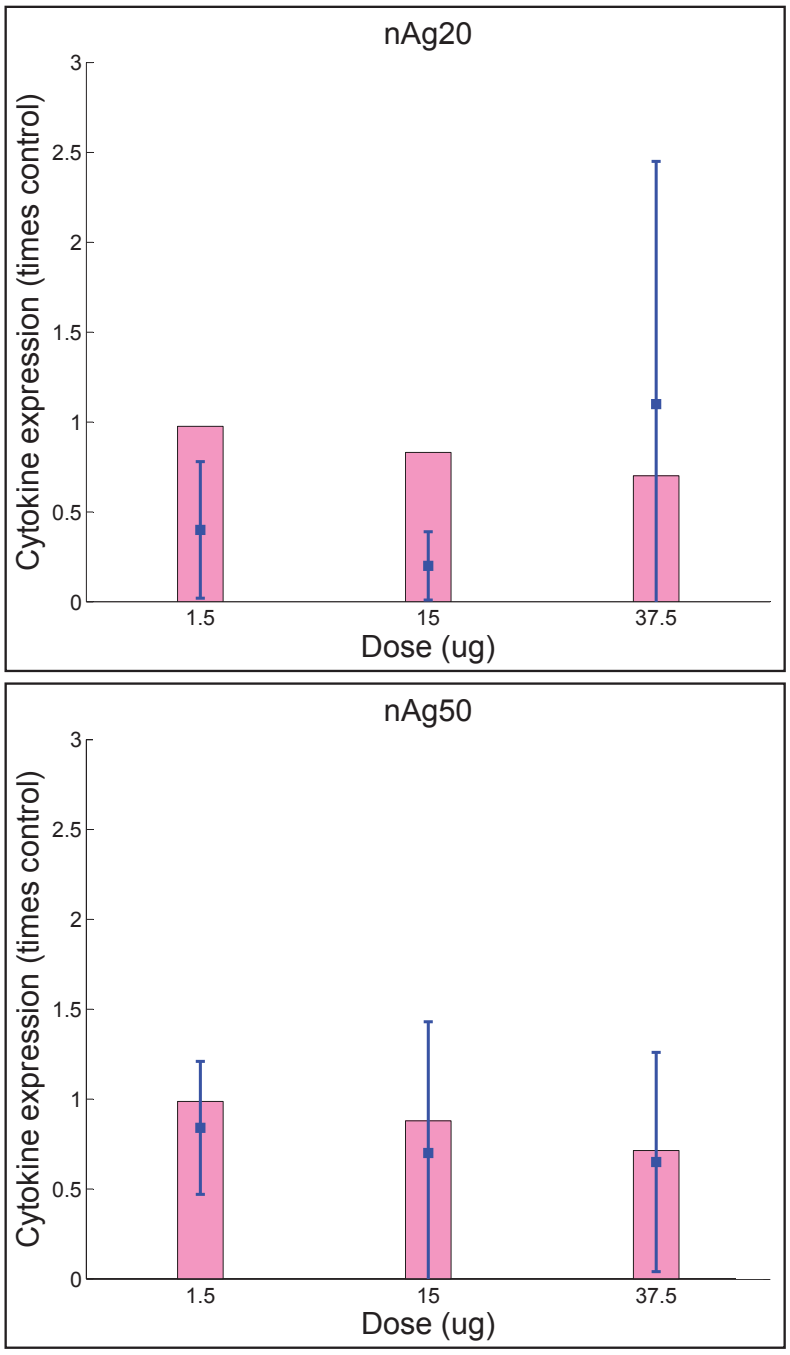

Figure IV.8: Comparison of model predictions and measured values of anti-inflammatory cytokine (IL-10) levels in culture medium after 4 hours for human MDMs with different doses of 20nm (top) and 50nm (bottom) nAg *in vitro*. Bars represent model predictions and squares and error bars represent *in vitro* measurements. (Figure reproduced from Mukherjee *et al.* [44] under Creative Commons Attribution License)

IV.2.5 Elimination of nanoparticles

Elimination of NPs from the alveolar region can involve 3 major routes [33]:

- Elimination of particles through the tracheobroncheal tree along with mucus into the gastro-intestinal system
- Elimination of particles by macrophages via phagocytosis or translocation into lymph nodes
- Diffusion of particles into blood circulation

Deposition of inhaled particles in the airway has been studied in multiple species. Raabe *et al.* [72] studied fractional deposition of ultrafine particles in mice. The results were extrapolated to get fractional deposition for 15 nm particles. Based on the observations from Raabe *et al.* [72], 40.26% of inhaled particles of 15nm size can be predicted to reach the alveoli. The fractions deposited in the trachea, bronchi and alveoli were added to constitute the mass entering the pulmonary system during intratracheal (IT) instillation, which is 52.18% of the IT dose. In the absence of exact elimination fractions for each elimination pathway, the overall elimination estimated by Takenaka *et al.* [33] after IT dosing of 4-10 nm silver ultrafine particles in rats was used. Using the value of 52.18% of an IT dose reaching the alveoli, and the overall daily elimination estimated by Takenaka *et al.*, the elimination rate, K_{el}, can be estimated to be 3.511×10^{-4} per min.

IV.3 Results of toxicodynamic model implementation in mice

IV.3.1 Surfactant components

The model described before was executed with a time-span of 1, 3, & 7 days after dosing of nanoparticles to simulate the condition of mice which were subjected to forced oscillation 1, 3, & 7 days after nanoparticle instillation. Figure IV.9 shows the

total phospholipid (PL) levels over 1, 3, & 7 days and the kinetics of total PL over 7 days in mice (red for nAg and black for carbon black). The model simulation was initiated at a time-point corresponding to 10 days prior to dosing of nanoparticles, to allow the systems to reach steady state. So the 1, 3, & 7 days are depicted as 11, 13, & 17 days respectively. Total PL refers to free PL on the alveolar interface as well as PL bound to nanoparticles and inside lamellar bodies. Despite binding to NPs and decrease in available free PL on the alveolar interface, the amount of total PL increases due to the presence of nanoparticles. The model captures the increase in PL adequately. However, the clearance of PL bound to NPs from the alveolar region due to the phagocytic clearance of NPs and the return of PL levels to homeostatic levels is not captured adequately by the model. This will require a coupling of the cellular modules of the model to simulate macrophage mediated particle clearance from the alveolar space. More detailed results have been included in the publication - Mukherjee *et al., PLOS One,* 2013 [145].

IV.3.2 Cellular interactions

Figure IV.10(a) shows the kinetics of nAg in the alveolar fluid over 24 hours. The NP dose is assumed to be given at 10 days at which time the model reaches steady-state with respect to the surfactant levels. Accordingly, the figure shows the kinetics from 10 to 17 days for 2 different doses (1 µg/ml and 10 µg/ml). The smaller dose shows a much faster clearance through the alveolar region than the higher dose. Figure IV.10 (b-d) shows NP uptake per cell of every type where macrophages dominate because on a per cell basis, macrophages are more efficient in the uptake of NPs than Type I or Type II cells.

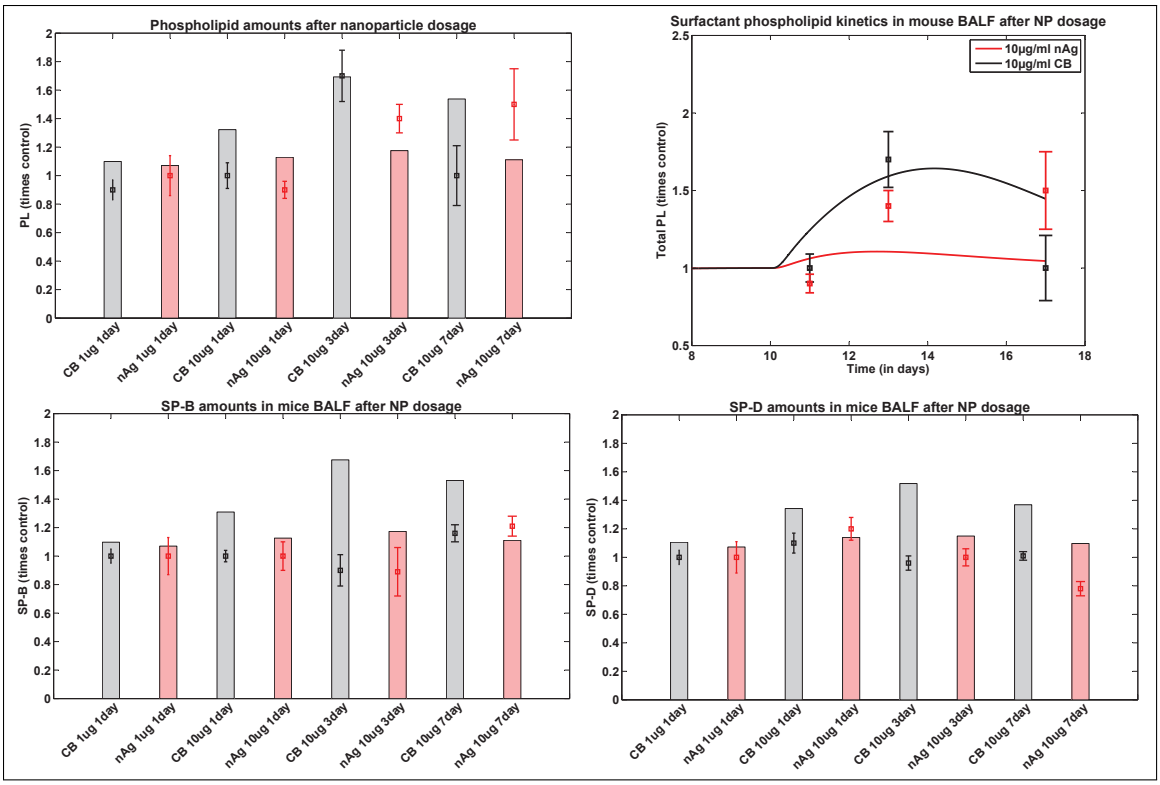

Figure IV.9: Comparison of predicted and measured values of total PL in mouse BALF 1, 3, and 7 days post-instillation of 10μg of nAg and CB. (in top figure bars represent model predictions and squares with error bars represent measured values. In the bottom graph the lines represent model predictions and the squares with error bars represent measured values - nAg shown in red and CB in black) (Figure reproduced from Mukherjee *et al.*, 2013 [145] under Creative Commons Attribution License)

IV.4 Extension and cross-species extrapolation

The alveolar toxicodynamic model developed in modular fashion in the previous sections has been implemented in mice. Model predictions were compared with *in vivo* measurements from mouse lung lavage post dosing with nAg and CB via intratracheal instillation. However, the model still has the following shortcomings:

- Model results are apparently not sensitive to NP type, as seen in Figure IV.9.
- The model has been implemented for intratracheal instillation dosage in mice, whereas realistic particulate matter exposure takes place via inhalation.

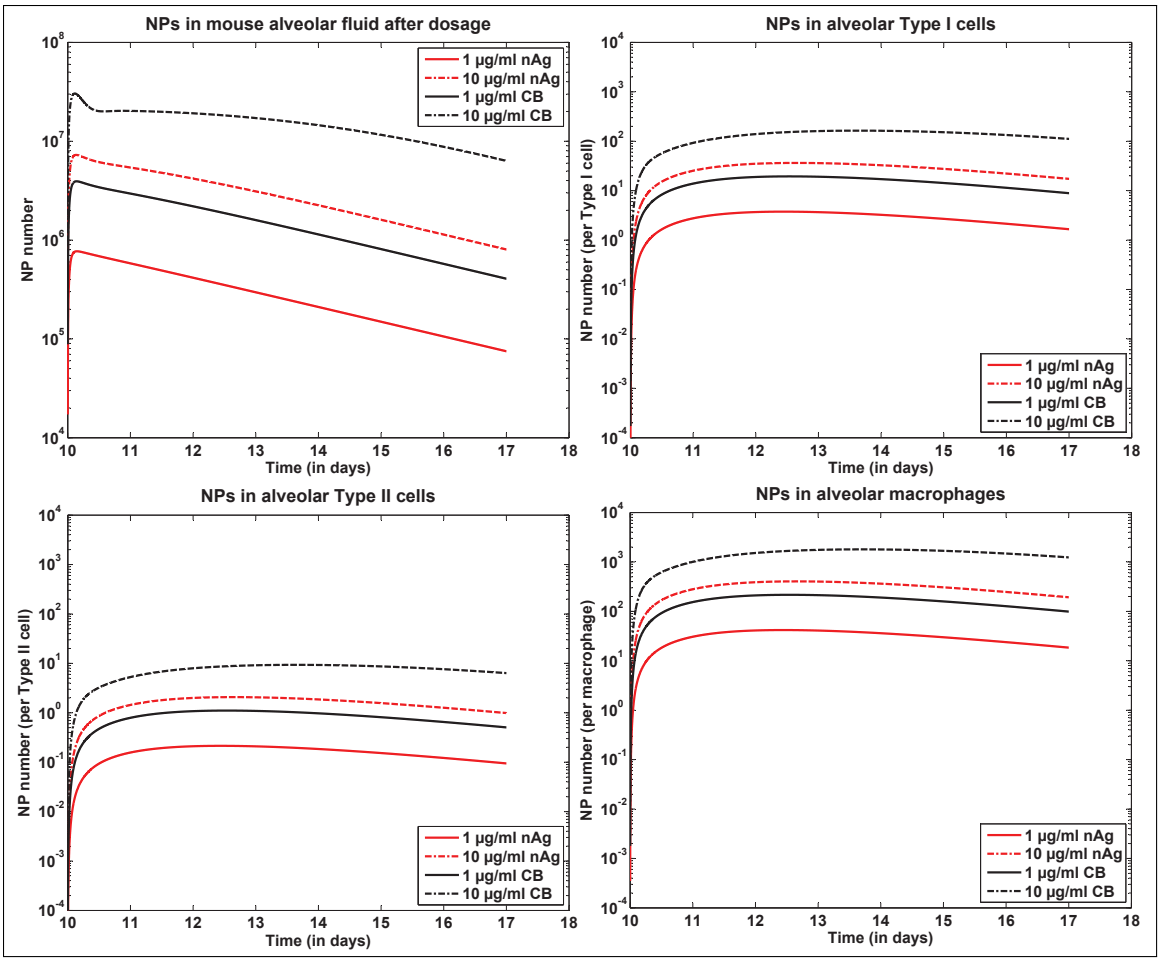

Figure IV.10: Model predictions for kinetics of nAg and CB in the alveolar region; (a) NP kinetics in the alveolar fluid post dosing; (b-d) NP uptake by various alveolar cells representing uptake per each type of cell (Figure reproduced from Mukherjee *et al.*, 2013 [145] under Creative Commons Attribution License)

- Model needs to be extrapolated to humans for it to be utilized as a risk assessment tool for inhalation exposure to ENMs.

- The toxicodynamic endpoints obtained from the model should ideally be related to one or more observable endpoints at the organism level.

The first three concerns will be addressed in this section, while the last one will be addressed in the next chapter. In this section, the toxicodynamic model developed before will be extended and extrapolated to rats and then to humans. To achieve these objectives, the following steps were taken:

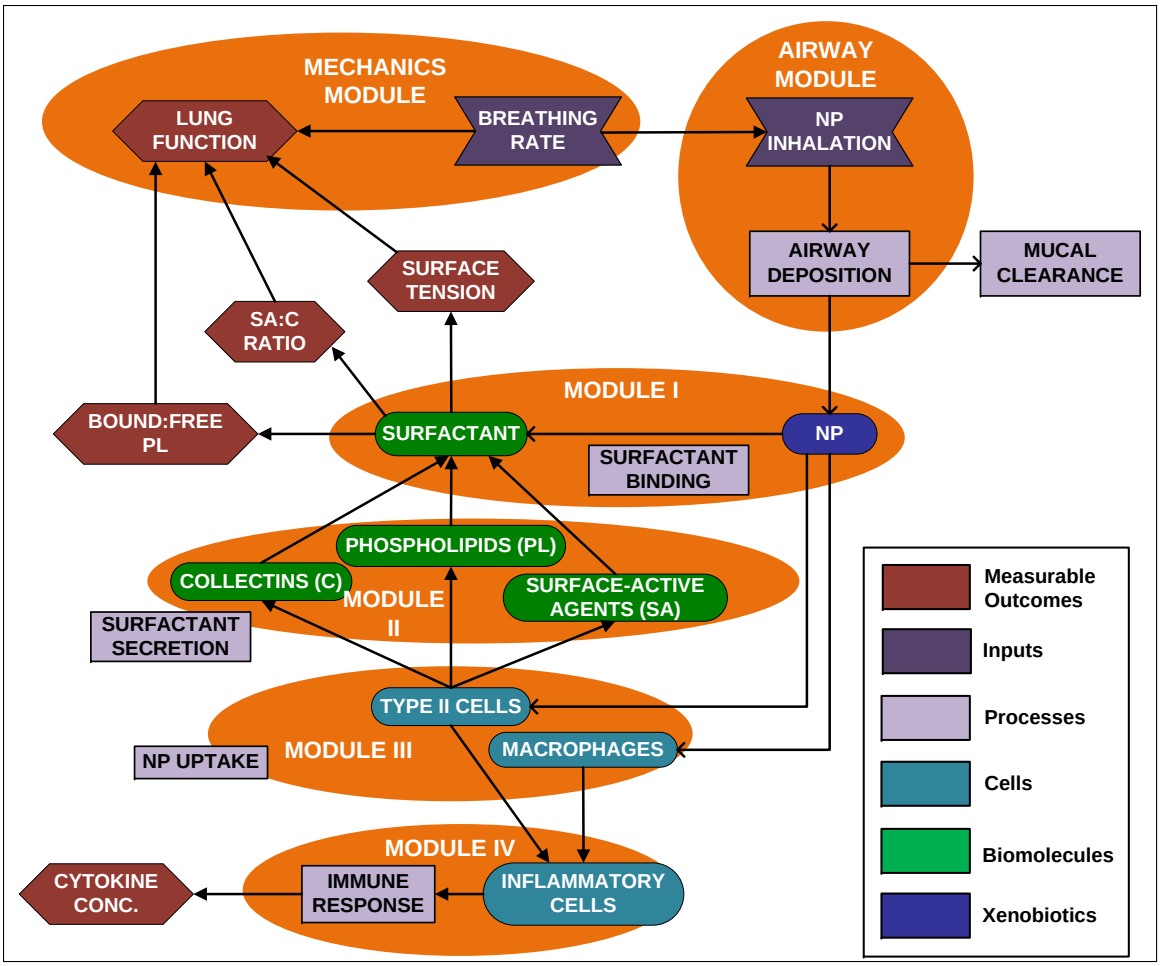

Figure IV.11: Modular decomposition of alveolar toxicodynamic processes with additional pulmonary dosimetry module

- Addition of a pulmonary dosimetry module to the three existing modules based on respiratory dosimetry assessed in Chapter II (shown in Figure IV.11)

- Incorporation of nano scale particokinetic estimates obtained from the ADSRM implementation as described in Chapter III

- Consideration of additional mechanisms such as digestion of adsorbed PL inside alveolar cells by intracellular phospholipases and dissolution of NPs in both intracellular and extracellular media

IV.4.1 Inhalation vs instillation

Inhalation (IH) exposure is realized in the laboratory using a nose-breathing apparatus, where the subject is allowed to breathe an aerosolized formulation. Intratracheal (IT) instillation on the other hand is done by injecting a liquid solution of the NPs (in water, saline or in commercial surfactant) via a syringe into the trachea of the subject [188, 189]. For both of these exposure routes, pulmonary dosimetry needs to be considered in detail. To address this issue a pulmonary dosimetry module was added to the five existing modules (shown earlier in Figure IV.1) of the toxicodynamic model. Pulmonary dosimetry was discussed in detail in Chapter II. Oberdorster *et al.* [188] showed that airway clearance (or short-term clearance) of particles shows almost no difference between nose inhalation and intratracheal instillation. However, it was also observed from their studies that intratracheal instillation produces a comparatively larger alveolar dose, and that the alveolar clearance (or long-term clearance) is slower than that for inhalation exposures. An IT dose is more conducive for toxicological studies because it allows one to study alveolar toxic responses with a comparatively smaller dose and with lesser amount of particles lost to mucal clearance. Model implementations simulating IT doses are also important in order to mechanistically model key alveolar toxicodynamic processes in a simpler framework without having to consider airway dosimetry or breathing rates of the subject. From the point of view of the modeling framework, IT dose was implemented in the model to match the conditions of the experiment. However, in this section IH dose is also being implemented for extension of the model ultimately to humans for which IH dosimetry is essential.

Airway Module

Pulmonary dosimetry for mice can be assessed using results by Raabe *et al.* [72] and Mendez *et al.* [68]. Airway dosimetry for rats and humans has been assessed

using MPPD [71]. Further details of the dosimetry calculations have been included in Chapter II, as it falls under estimation of organism level particle distribution. Table IV.5 summarizes the average percentage deposition for 10-50 nm NPs for different species. It can be seen that for larger species, the effective alveolar dose from the same number dose of NPs is lesser than that in mice. This produces an additional defensive mechanism in larger animals from inhalation exposure to ultrafine particulate matter. The percentage deposition values summarized in Table IV.5 are used to estimate the appropriate alveolar dose for an IT or an IH dose in any species.

Table IV.5: Percentage deposition for ultrafine particles (10-50 nm diameter) in different species

Pulmonary section	Mouse [72]	Rat [71]	Human [71]
Pharynx	9.08	16.4	11.19
Trachea	0.68	4.72	3.03
Bronchi	19.91	20.5	13.17
Alveoli	64.58	31.82	35.33

IV.4.2 Nanoscale particokinetics

The earlier version of the toxicodynamic model consisted of most of the NP-specific parameters to be estimated from various literature sources. In many instances, appropriate parameters were not available for nAg and parameters specific to other types of NPs were used. However, due to their small size and high surface-volume ratio, nano scale properties such as diameter, surface zeta potential, coating chemistry can have significant effects on the ultimate toxicodynamics [43, 40, 190]. NP-specific nano scale particokinetic parameters were estimated using the ADSRM framework as described in Chapter III. These parameter values were appropriately used in the extended and improved toxicodynamic model.

IV.4.3 Intracellular digestion

NP removal from the alveolar regions has been considered only in the case of phagocytic removal. However, NPs also suffer digestion and dissolution inside cells. Subsequent to endocytosis and phagocytosis, NPs are localized inside lysosomal fluid within cytoplasmic vacuoles [191]. It has been shown that the process of lysosomal digestion consists of two distinct steps: digestion of the adsorbed phospholipid on the NP and then the digestion of the NP. Consideration of both distinct steps in necessary for modeling immune response due to NPs [191]. Kinetic data for the process has been provided in Wallace *et al.* [192]. An exponential model was fit to the kinetic data of fraction DPPC remaining on the NPs with time, which results in a linear ordinary differential equation as follows:

$$\frac{df_{\mathrm{PL}}}{dt} = -k_{\mathrm{PLase}}.f_{\mathrm{PL}}, \tag{IV.24}$$

where k_{PLase} is the rate constant for PL digestion due to phospholipases, and f_{PL} is the fraction of adsorbed PL remaining on the NPs. Subsequent to digestion of the adsorbed PL, the NP suffers dissolution leading to release of Ag ions within the cell. Rate of dissolution has been modeled using the rate constants estimated in Chapter III for the different types of NPs. It was shown in Chapter III that dissolution is significantly influenced by the pH of the media. It is also known that extracellular media has a pH of 7 while lysosomal media is more acidic and has a pH of 5 [39]. Accordingly, intracellular and extracellular dissolution rates were separately estimated in Chapter III corresponding to pH of 5 and 7 respectively.

IV.5 Results of toxicodynamic model in multiple species

The toxicodynamic model for silver nanoparticles was implemented for C57BL/6J mice, Sprague-Dawley (SD) rats, Brown-Norway (BN) rats, and also in humans. The

appropriate biological parameters are summarized in Table IV.6. Both instillation and inhalation doses were implemented as described in Section IV.4.1 using appropriate models of pulmonary airway dosimetry. The toxicodynamic model is run for 14 days prior to NP dosage to allow the surfactant components to reach their biological homeostatic value. Actual values of the NP dose are summarized in Table IV.7. The instillation dose amounts in mice and rats were selected based on the animal *in vivo* study conducted by collaborators from which measurements were used to compare with model prediction. Two different inhalation doses were implemented in rats: a low dose (LD) comprising a single 3 hour inhalation dose and a high dose (HD) comprising four 3 hour doses on four consecutive days. The corresponding exposure concentrations and breathing rates are summarized in Table IV.7.

Table IV.6: Physiological parameters across species for pulmonary toxicodynamic model implementation

Parameter	Mouse	Rat	Human
Body weight (BW) (g)	140 [193]	303;200*	70000**
Lung volume (ml/kg BW)	10 [194]	29.2 [195]	12.91 [196]
Lung mass (g/kg BW)	3.07 [193]	11.3 [197]	12 [198]
No. of AT1 (per g lung)	1.32×10^{7}†	4.43×10^{6} [199]	1.55×10^{7} [200]
No. of AT2 (per g lung)	9.13×10^{7} [156]	3.07×10^{7} [195]	2.98×10^{7} [200]
No. of Mph (per animal)	1.66×10^{5} [201]	1×10^{7} [202]	2.6×10^{10} [200]
Alveolar thickness (µm)	0.2	0.2	0.2
Alveolar surface area (cm^2/ml)	273 [203]	377.36 [195]	774 [204]

* Based on average body weights of Sprague-Dawley and Brown-Norway rats used for *in vivo* measurements
** Based on adult male human
† Scaled from the rat using body weight and the relative number of AT2 cells in the two species

IV.5.1 Model predictions in mice and rats

Subsequent to alveolar deposition, NPs are immersed in the alveolar fluid (AF) during which they get coated with surfactant phospholipids (PL). Surfactant proteins (SP) also get adsorbed on to the NPs. NPs also get taken up by alveolar cells and are also removed by dissolution into Ag ions. Figure IV.12 compares predictions for time

Table IV.7: Summary of NP doses for instillation and inhalation studies in different species

	Mouse	BN Rat	SD rat	Human
Exposure conc. (μg/L)	0.092 (LD), 0.077 (HD)	0.791 (LD), 0.617 (HD)	0.801 (LD), 0.67 (HD)	0.65 (LD), 0.544 (HD)
Exposure duration (min)	180 (LD), 720* (HD)	180 (LD), 720* (HD)	180 (LD), 720* (HD)	180 (LD), 720* (HD)
Breathing rate (L/min)	0.06	0.06	0.06	20
Cumulative dose (μg/m^2/day)	-	25.9 (LD), 21.66 (HD)	25.58 (LD), 19.95 (HD)	-
Instillation dose (μg/g BW)	0.05	0.1	0.1	-

* 3 hours of exposure each day for four consecutive days

Exposure concentrations for mice and human were estimated based on an equal cumulative dose per unit alveolar surface area as for rats

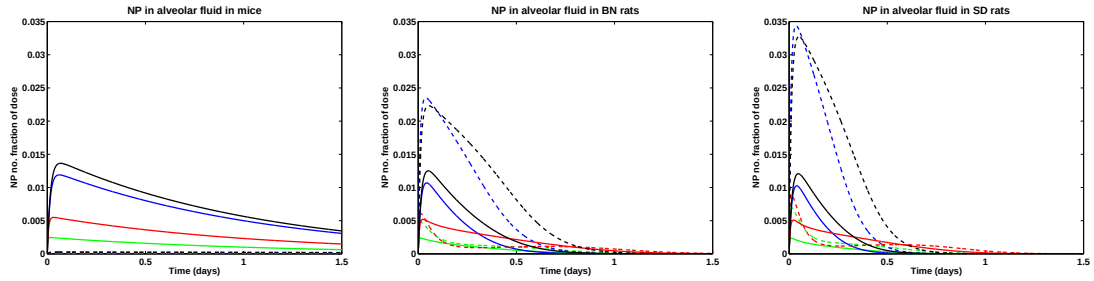

(a) Mouse (b) BN rat (c) SD rat

— C20, - - PL-coated C20, — C110, - - PL-coated C110, — P20, - - PL-coated P20, — P110, - - PL-coated P110

Figure IV.12: Model predictions of time dynamics of NPs and PL-coated NPs in the alveolar fluid in three different species.

dynamics of the number fraction of dosed NPs in the alveolar fluid of the animals. It can be observed that bigger NPs (C110, P110) have a longer residence time in the alveolar fluid, while smaller particles are removed much faster probably due to a combination of dissolution and uptake. An interesting observation is that surfactant-coated NPs are produced in larger numbers in rats than in mice, where uncoated NPs are much higher. This phenomenon is most probably due to the fact that the mouse being a much smaller animal, has a lower capacity of surfactant production and hence suffers an early deficiency in surfactant amounts due to the NP dose. This fact is also supported by other results shown later. Figures IV.13 - IV.15 show NP

uptake by various alveolar cells in the three animals. The NP number shown in the figures have been normalized by the total number of cells of that type in the animal. It can be seen that on a per cell basis, Type I cells take up more NPs than Type II cells. This is because of the higher surface area presented by Type I cells in the alveolar sub-phase than Type II cells which are present only intermittently at the alveolar air-exchange surface. Alveolar macrophages take up much more NPs (about 2-3 orders higher) than the other cell types, which is an expected observation and is due to their higher rate of phagocytosis.

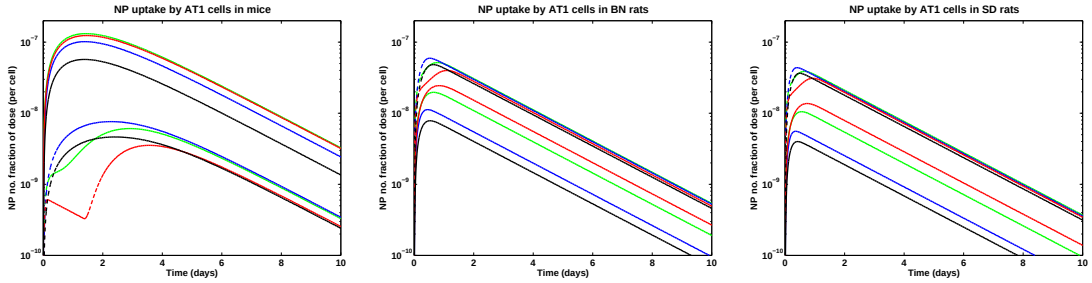

(a) Mouse (b) BN rat (c) SD rat

— C20, - - PL-coated C20, — C110, - - PL-coated C110, — P20, - - PL-coated P20, — P110, - - PL-coated P110

Figure IV.13: Model predictions of uptake of NPs and PL-coated NPs by alveolar Type I cells in three different species

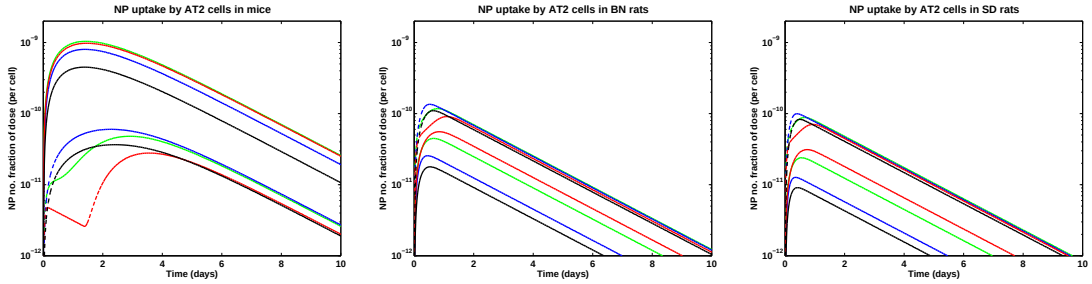

(a) Mouse (b) BN rat (c) SD rat

— C20, - - PL-coated C20, — C110, - - PL-coated C110, — P20, - - PL-coated P20, — P110, - - PL-coated P110

Figure IV.14: Model predictions of uptake of NPs and PL-coated NPs by alveolar Type II cells in three different species

Figure IV.16 compares free PL amounts in the alveolar fluid in the three species.

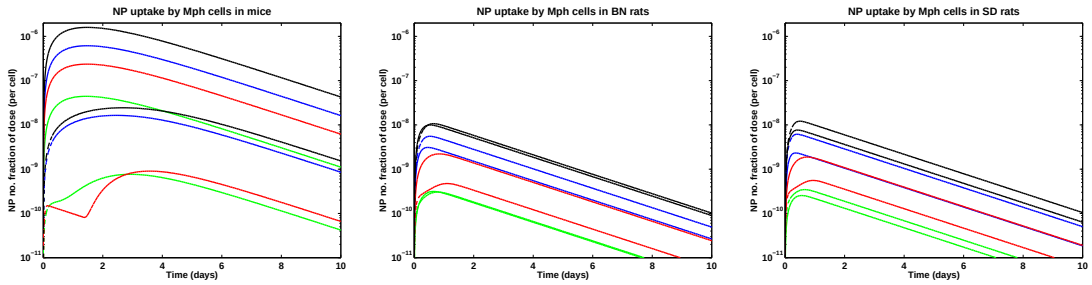

(a) Mouse (b) BN rat (c) SD rat

C20, PL-coated C20, C110, PL-coated C110, P20, PL-coated P20, P110, PL-coated P110

Figure IV.15: Model predictions of uptake of NPs and PL-coated NPs by alveolar macrophages in three different species

It can be observed that mice suffer the biggest loss of free PL due to NP dosage compared to rats. The loss in PL also takes longer to be alleviated to normal levels in mice. It is also observed that smaller NPs (C20, P20) have a much larger effect on free surfactants. This might be due to the fact that the same mass dose has a larger number of smaller NPs than bigger NPs and the larger number causes greater binding of PLs. The effect of a single instillation dose seems to be alleviated by 3-4 days in mice, while it only takes about 2 days in rats. Figure IV.17 shows the time dynamics of surfactant proteins (SA & C) in the alveolar fluid post NP instillation. Surface-active proteins (SA) which comprise SP-B and SP-C are significantly lowered due to adsorption to NPs. They are also lowered due to negative surfactant regulation. As described in Section IV.2.1, collectins are known to be upregulated due to presence of xenobiotics in the alveolar fluid and they in turn inhibit PL and SA formation by reducing exocytosis of lamellar bodies and also increasing PL recycle. This can be observed in Figure IV.17 which shows a decrease in SA accompanied by an increase in C, both of which go back to normal levels in about 3-4 days. Mice are seen to be more susceptible to these changes than rats. The SA:C ratio which is often used as a alveolar biomarker for immune response is shown in Figure IV.18. Smaller NPs are found to cause more significant changes in the SA:C ratio than larger NPs.

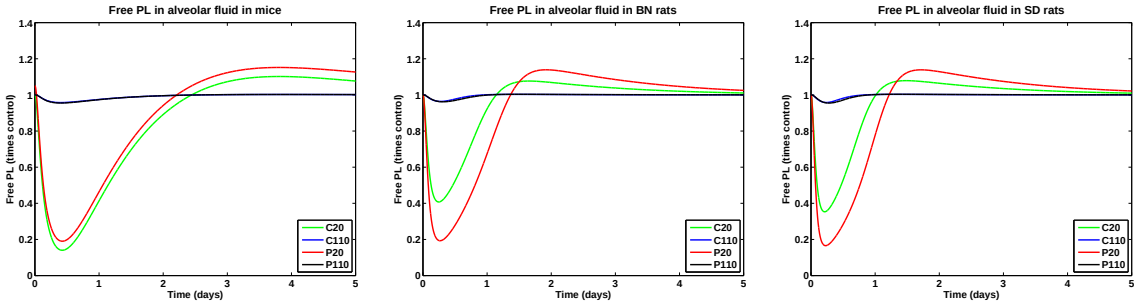

(a) Mouse (b) BN rat (c) SD rat

Figure IV.16: Model predictions of free phospholipid in the alveolar fluid of three different species after instillation dose of four types of NPs.

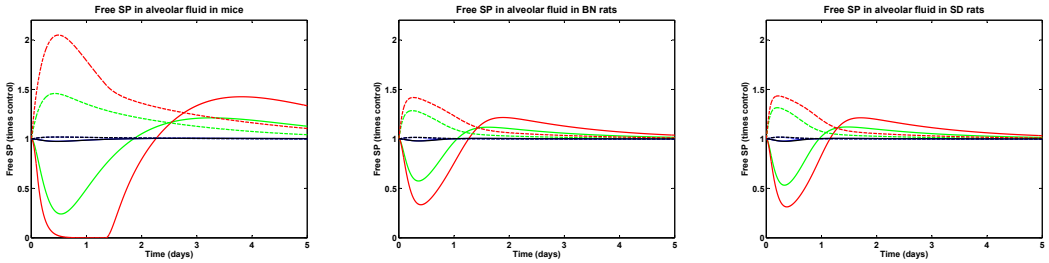

(a) Mouse (b) BN rat (c) SD rat

—SA(C20), - -C(C20), —SA(C110), - -C(C110), —SA(P20), - -C(P20), —SA(P110), - -C(P110)

Figure IV.17: Model predictions of surfactant proteins in the alveolar fluid of three different species after instillation dose of four types of NPs.

Figures IV.19-IV.21 show comparisons for ratios of bound to free surfactant components. Smaller NPs lead to an instantaneous increase in the ratio for both PL and SA. However, for collectins (Figure IV.21), the ratio first suffers a small decrease before going back up. The initial decrease is due to increase in direct secretion of free collectins due to the presence of xenobiotics in the alveolar fluid.

Figure IV.22 shows comparisons for ionic concentrations of Ag in the alveolar fluid due to dissolution of NPs. The ionic concentration increases and rapidly reaches a steady value due to removal of NPs from the alveolar fluid. Mice are found to have a higher concentration of ionic Ag in the alveolar fluid due to the smaller volume of tissue fluid. An interesting observation in these results is that size and coating chemistry appear to have opposite effects on dissolution. Among citrate-coated NPs

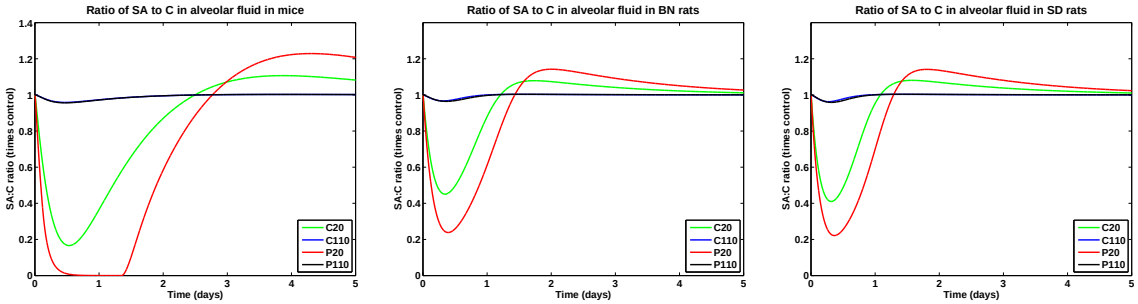

(a) Mouse (b) BN rat (c) SD rat

Figure IV.18: Model predictions of SA:C ratio in the alveolar fluid of three different species after instillation dose of four types of NPs.

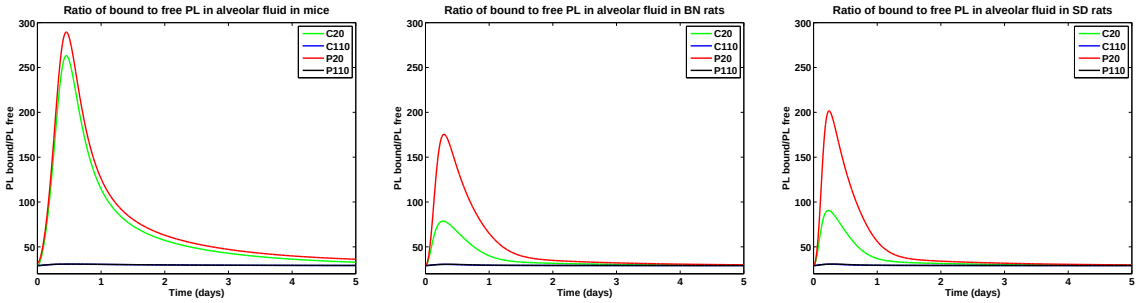

(a) Mouse (b) BN rat (c) SD rat

Figure IV.19: Model predictions of ratio of bound to free phospholipids in the alveolar fluid of three different species after instillation dose of four types of NPs.

(C20, C110), larger NPs have a higer rate of dissolution because larger NPs have a larger residence time in the alveolar fluid (Figure IV.12). However, between NPs of the same size (C20, P20), citrate-coated NPs have a higher rate of dissolution due to the citrate-coating which is oxidized relatively easily, whereas PVP coating offers better stabilization.

IV.5.2 Model predictions for inhalation dosage in rodents

Inhalation dosage allows one to assess more realistic exposure scenarios. From the point of view of pulmonary toxicodynamics, an inhalation dose produces a more sustained effect than a single instillation dose. Results are presented for low dose (LD) and high dose (HD) scenarios. LD comprises a single 3 hour period of continuous

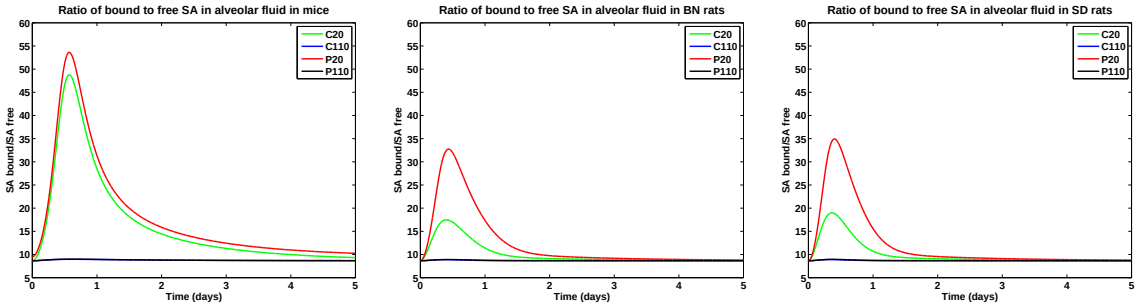

(a) Mouse (b) BN rat (c) SD rat

Figure IV.20: Model predictions of ratio of bound to free surface-active proteins in the alveolar fluid of three different species after instillation dose of four types of NPs.

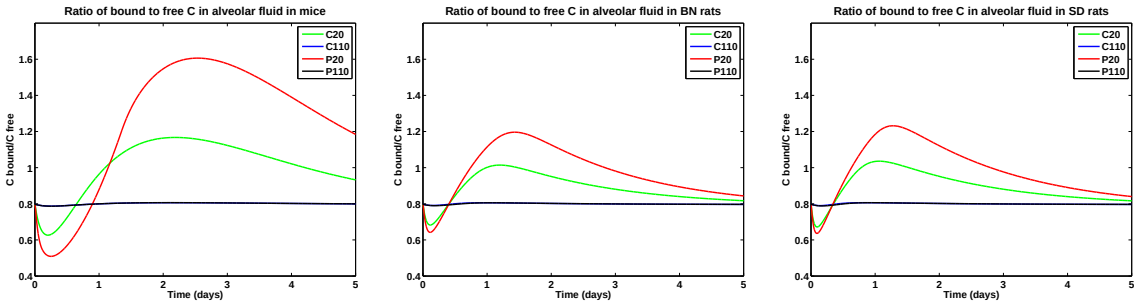

(a) Mouse (b) BN rat (c) SD rat

Figure IV.21: Model predictions of ratio of bound to free collectins in the alveolar fluid of three different species after instillation dose of four types of NPs.

inhalation exposure at a certain constant concentration. HD comprises periods of 3 hour exposures over four consecutive days at a certain concentration. The details of the doses, concentrations, and breathing rates are summarized in Table IV.7. Figure IV.23 compares the presence of NPs and PL-coated NPs (SfNPs) in the alveolar fluid of mice, BN rats, and SD rats. Mice show a comparatively slower rate of NP clearance than the rats. Also, the presence of PL-coated NPs is negligible which is due to absence of free PL as seen in later figures. Between BN and SD rats, SD rats show faster clearance of NPs but not SfNPs which are produced in larger numbers in SD rats due to more available free PL.

Figures IV.24 - IV.26 show the uptake of NPs and SfNPs by various alveolar cells lining the alveolar region. Alveolar macrophages show comparatively more prolific

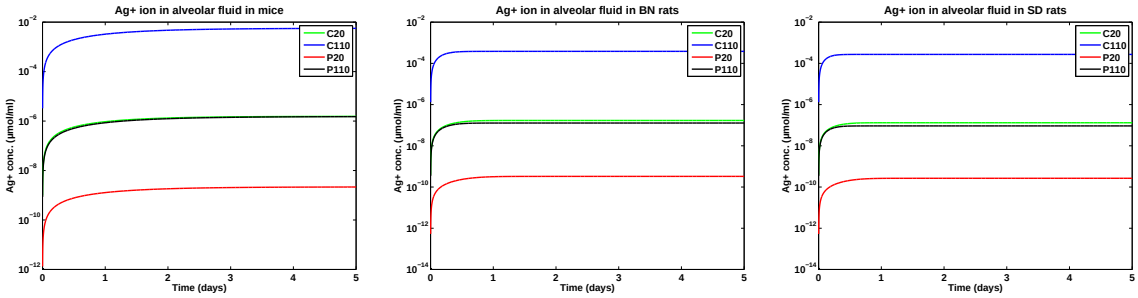

(a) Mouse (b) BN rat (c) SD rat

Figure IV.22: Model predictions of Ag ion concentration in the alveolar fluid of three different species after instillation dose of four types of NPs.

uptake for mice as compared to other alveolar cells. This phenomenon was also observed for instillation doses. Figure IV.27 compares time dynamics of surfactant components - PL, SA, and C for both dosage scenarios in 3 different species. The results show depletion in free PL and free SA while the amounts of C are increased over control values. This also results in an decrease in the SA:C ratio, which is a key biomarker for immune response.

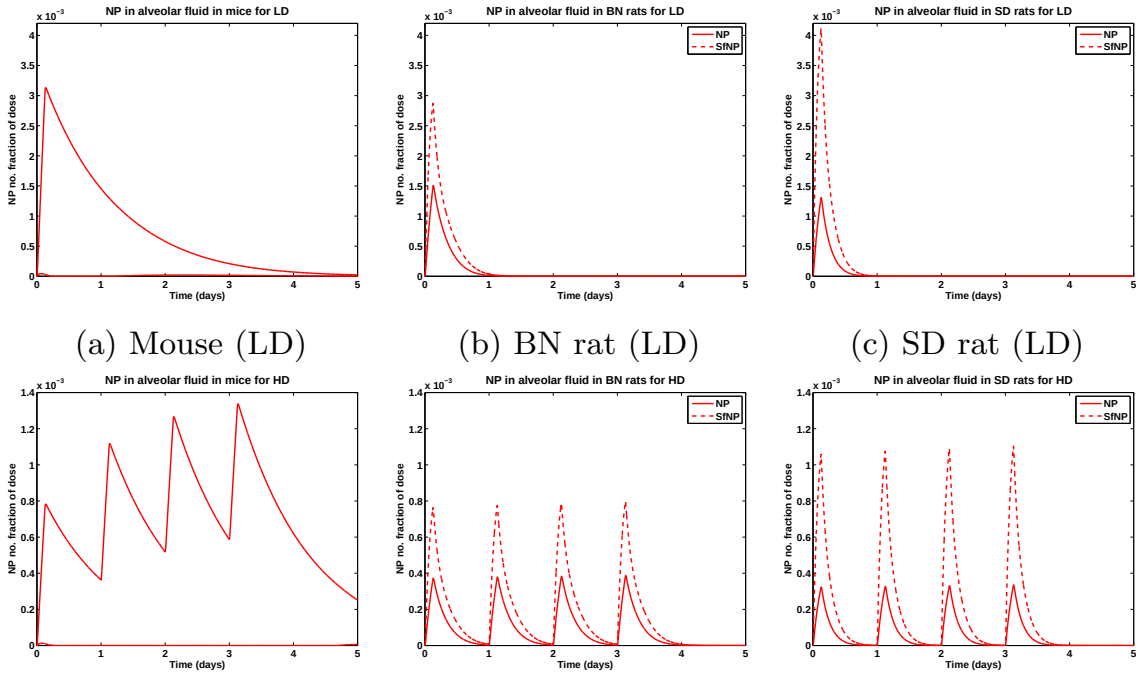

(a) Mouse (LD) (b) BN rat (LD) (c) SD rat (LD)

(d) Mouse (HD) (e) BN rat (HD) (f) SD rat (HD)

Figure IV.23: Model predictions of time dynamics of NPs and PL-coated NPs in the alveolar fluid in three different species for two different dosage scenarios - low dose (LD) (top panel), and high dose (HD) (bottom panel).(Details of the dosage scenarios summarized in Table IV.7

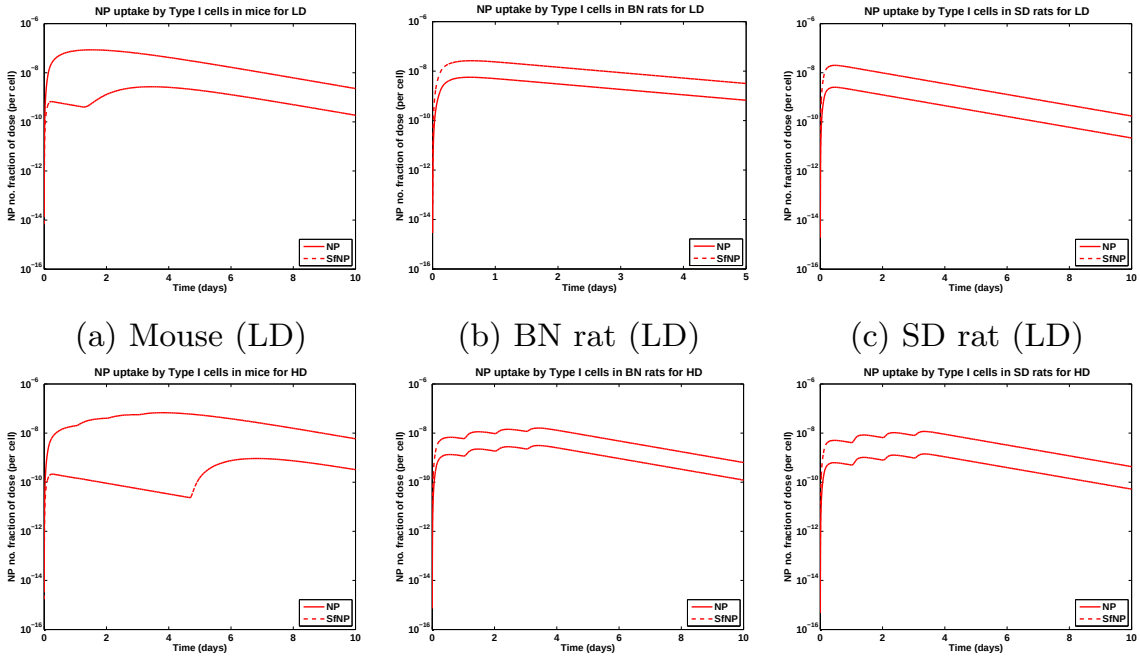

(a) Mouse (LD) (b) BN rat (LD) (c) SD rat (LD)

(d) Mouse (HD) (e) BN rat (HD) (f) SD rat (HD)

Figure IV.24: Model predictions of time dynamics of uptake of NPs and PL-coated NPs by alveolar Type I cells in three different species for two different dosage scenarios - low dose (LD) (top panel), and high dose (HD) (bottom panel).(Details of the dosage scenarios summarized in Table IV.7)

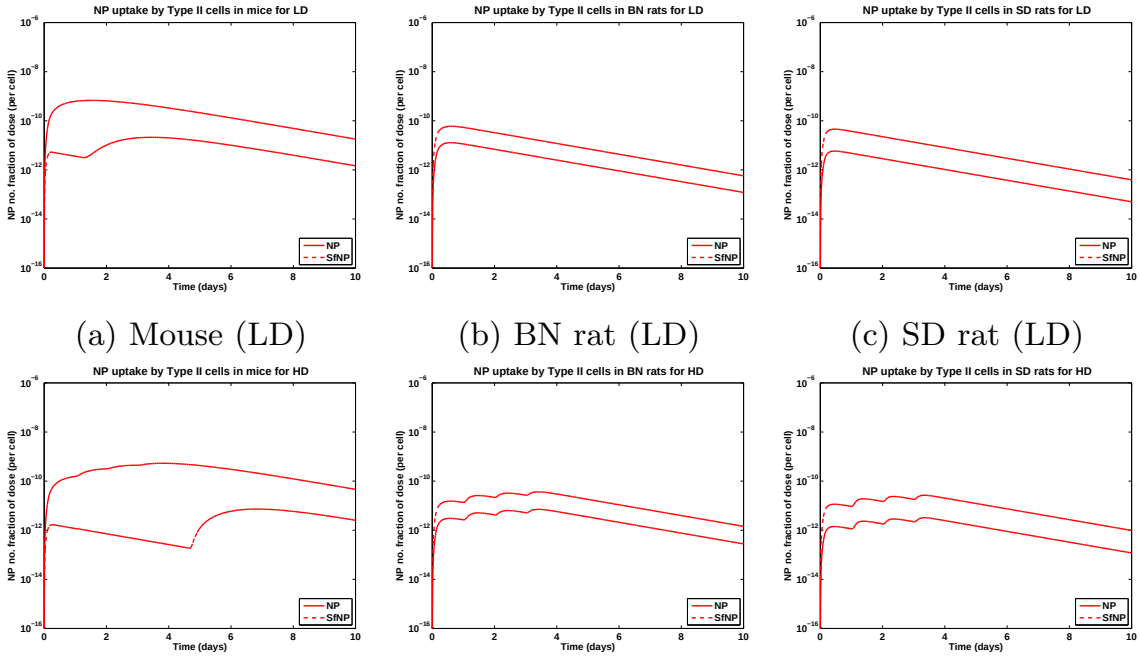

(a) Mouse (LD) (b) BN rat (LD) (c) SD rat (LD)

(d) Mouse (HD) (e) BN rat (HD) (f) SD rat (HD)

Figure IV.25: Model predictions of time dynamics of uptake of NPs and PL-coated NPs by alveolar Type II cells in three different species for two different dosage scenarios - low dose (LD) (top panel), and high dose (HD) (bottom panel).(Details of the dosage scenarios summarized in Table IV.7)

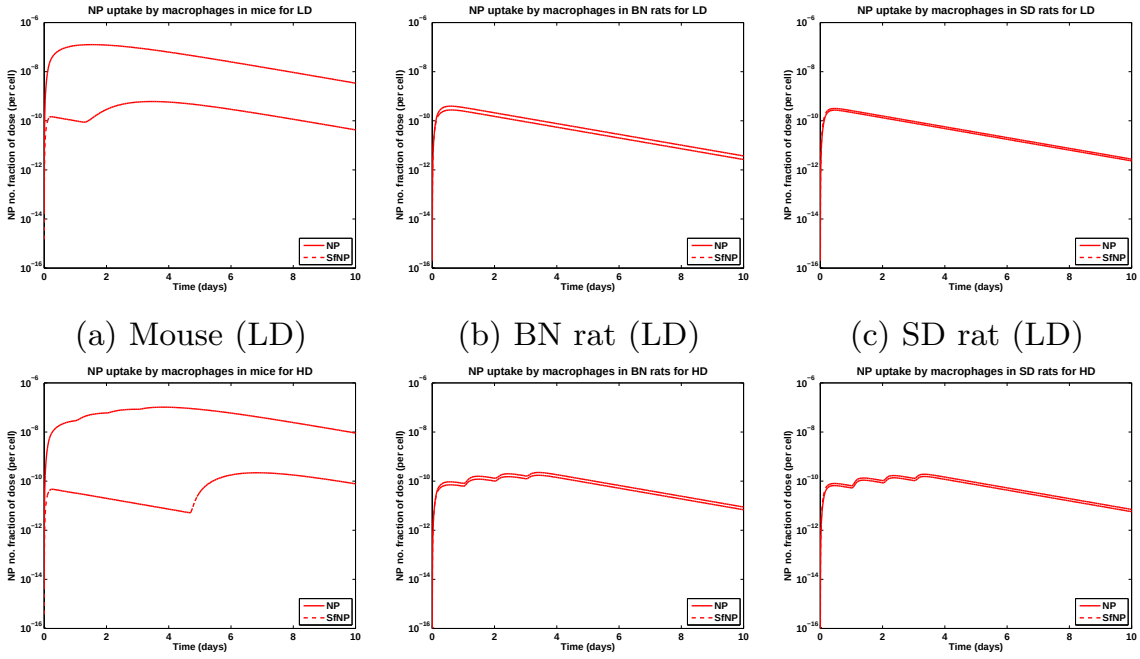

(a) Mouse (LD) (b) BN rat (LD) (c) SD rat (LD)

(d) Mouse (HD) (e) BN rat (HD) (f) SD rat (HD)

Figure IV.26: Model predictions of time dynamics of uptake of NPs and PL-coated NPs by alveolar macrophages in three different species for two different dosage scenarios - low dose (LD) (top panel), and high dose (HD) (bottom panel).(Details of the dosage scenarios summarized in Table IV.7)

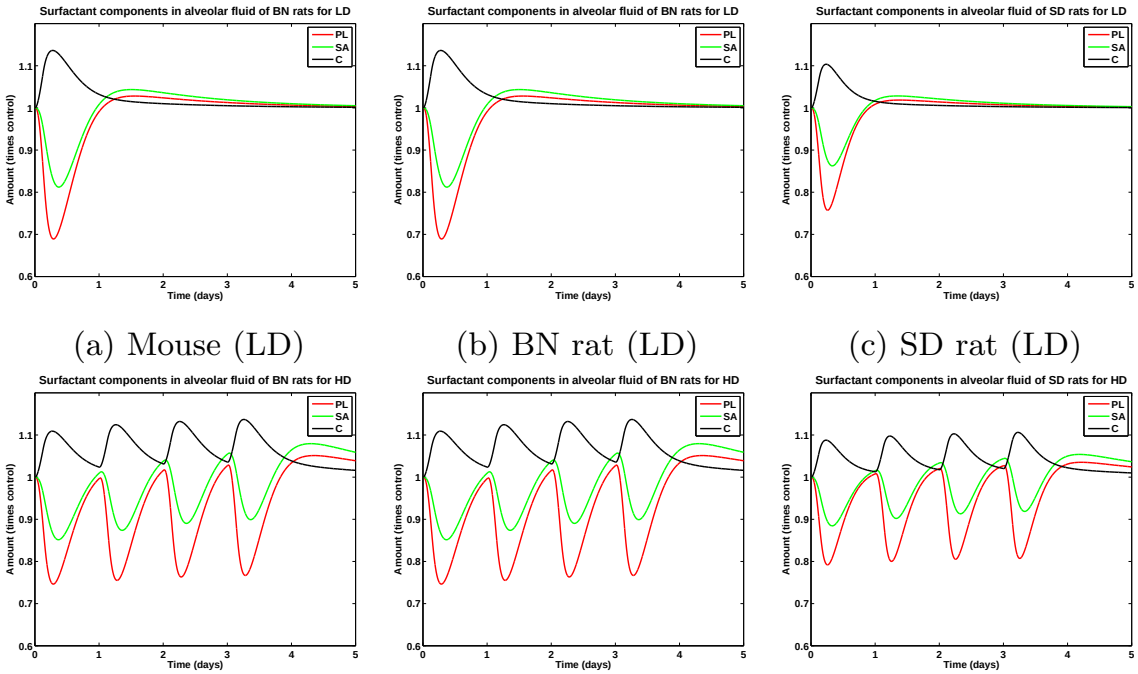

(a) Mouse (LD) (b) BN rat (LD) (c) SD rat (LD)

(d) Mouse (HD) (e) BN rat (HD) (f) SD rat (HD)

Figure IV.27: Model predictions of time dynamics of surfactant PL, SA, and C in three different species for two different dosage scenarios - low dose (LD) (top panel), and high dose (HD) (bottom panel).(Details of the dosage scenarios summarized in Table IV.7)

IV.5.3 Model predictions for human

The pulmonary toxicodynamic model for NPs was implemented for an adult human (21 years old, 70 kg body weight) using appropriate physiological parameters from the NHANES database [196]. Physiological parameters of the respiratory system were obtained from literature and are summarized in Table IV.6. Human exposure dose was estimated by scaling the inhalation dose in rats to humans using identical NP number per unit alveolar surface area. This method of scaling doses to compare alveolar toxicity has been employed by Wang *et al.* [43]. Airway dosimetry for humans has been estimated by the MPPD software [71] as described in detail in Chapter II. Comparative airway dosimetry estimates of other species including human are also summarized in Table IV.7. The dose scaling by the method of Wang *et al.* [43], however, does not take into account the differences in airway dosimetry between species. This results in a comparatively smaller delivered dose to the alveoli in human. Figure IV.28 shows the time dynamics of the NPs (both uncoated and PL-coated) in the alveolar fluid for both low-dose (LD) and high-dose (HD) scenarios. The NPs are removed from the AF much more rapidly as compared to rodents and are almost gone in a few hours after exposure.

Figure IV.29 compares model predictions of NP uptake by the different alveolar cells for single dose (LD) and multiple doses (HD). Unlike in rodents, where alveolar macrophages show the highest uptake of NPs, in human, alveolar type I cells show a predicted higher uptake than either Type II cells or macrophages. This might be due to the comparatively higher number of macrophages per unit body weight in smaller animals.

Figure IV.30 compares time dynamics of phospholipids (PL), surface-active proteins (SA), and collectins (C) in human alveolar fluid post inhalation exposure. The top panel (Figure IV.30(a) and IV.30(b)) shows plots of the individual components (times change over values before dosage), while the bottom panel (Figure IV.30(c)

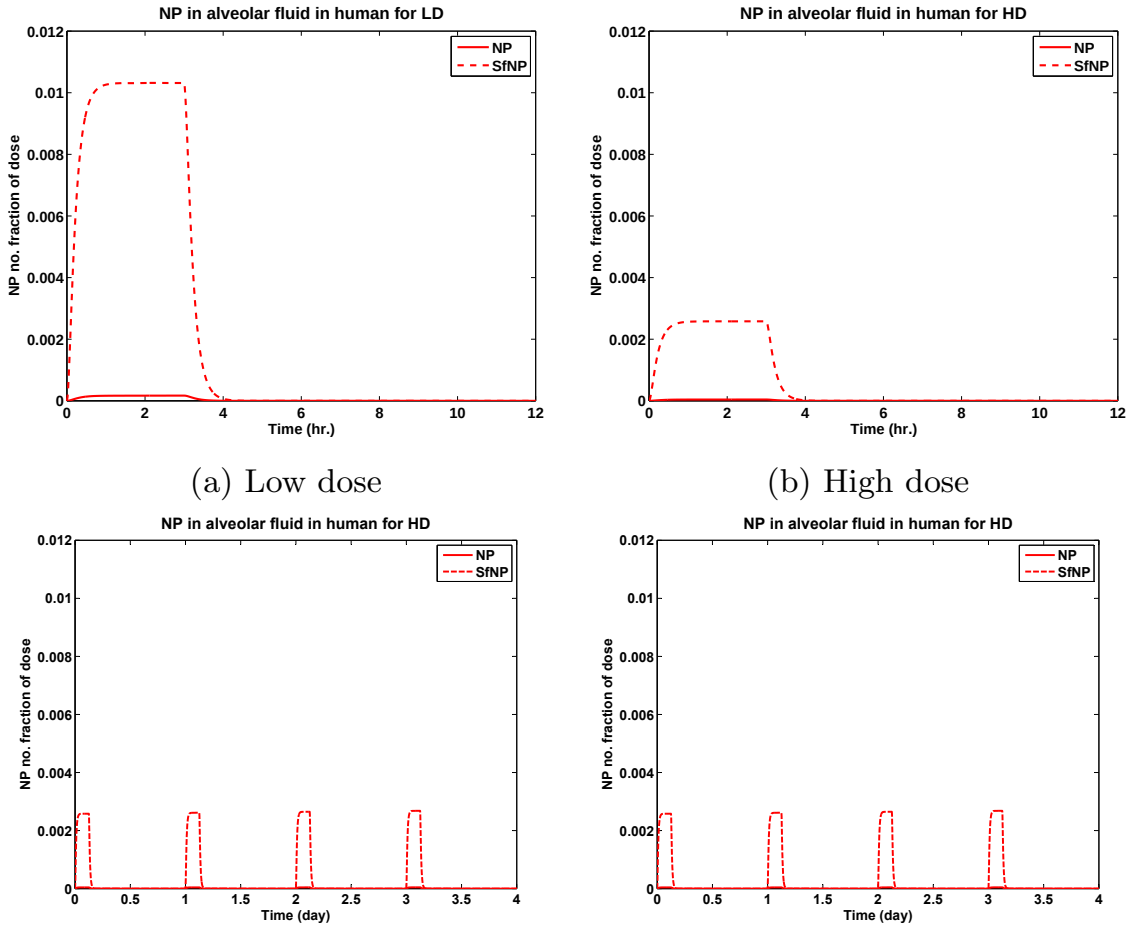

(a) Low dose

(b) High dose

(c) Low dose

(d) High dose

Figure IV.28: Model predictions of SparkAg NPs and surfactant-coated NPs in human alveolar fluid after inhalation exposure; LD represents 3 hour inhalation exposure while HD represents four consecutive exposures over four days; Top panel shows the time dynamics after the first exposure and bottom panel shows the dynamics over a longer span of time.

and IV.30(c)) presents comparisons for the ratio of SA to C for the two doses.

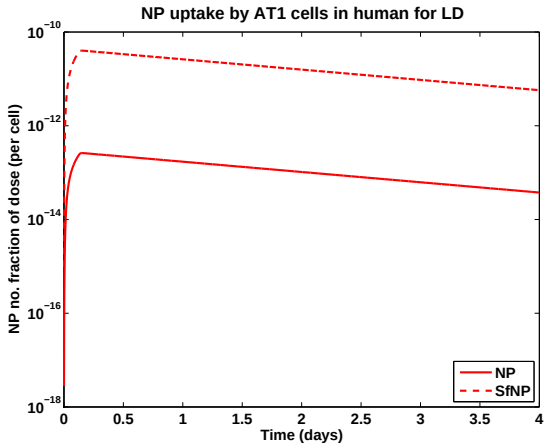

(a) Type I cells (Low dose)

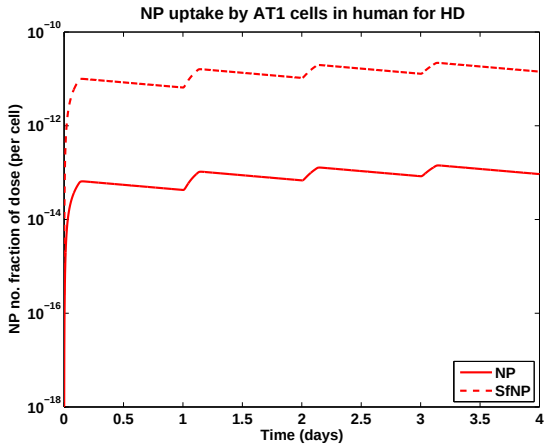

(b) Type I cells (High dose)

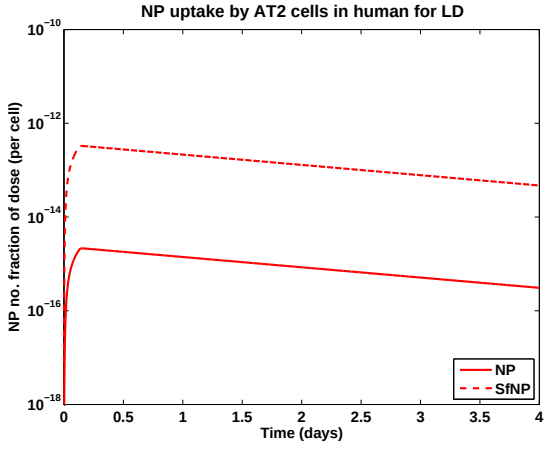

(c) Type II cells (Low dose)

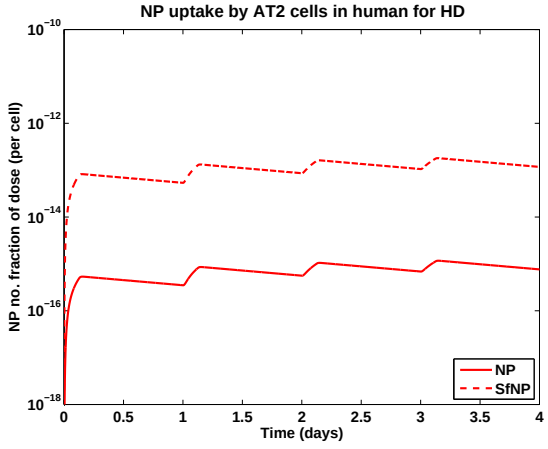

(d) Type II cells (High dose)

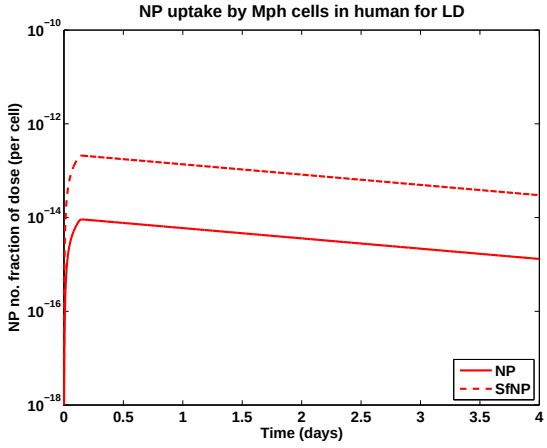

(e) Mph (Low dose)

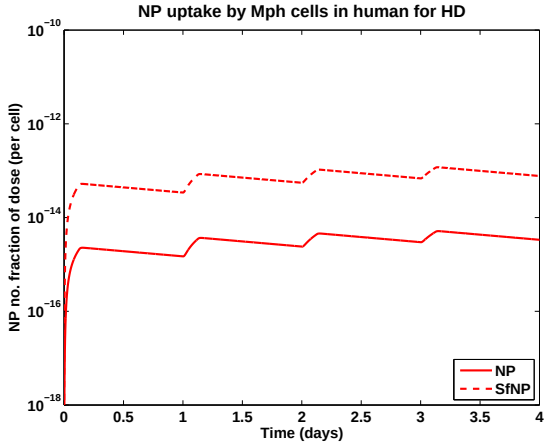

(f) Mph (High dose)

Figure IV.29: Model predictions of SparkAg NPs and surfactant-coated NPs in human alveolar cells after inhalation exposure; LD represents 3 hour inhalation exposure while HD represents four consecutive exposures over four days

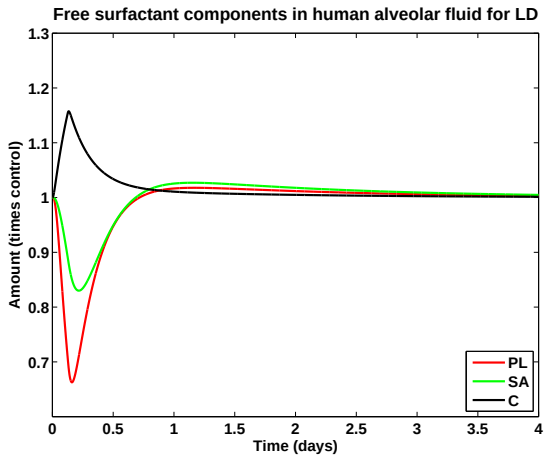

(a) Low dose

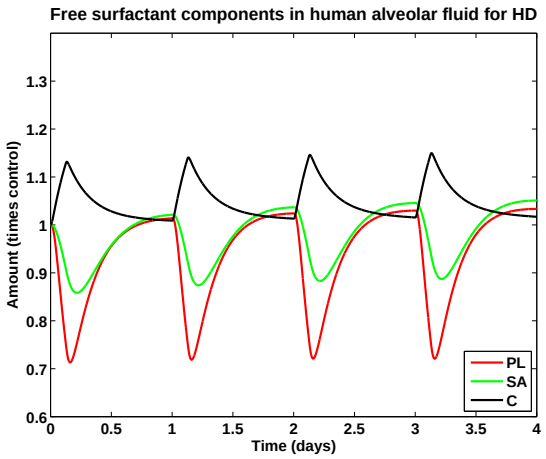

(b) High dose

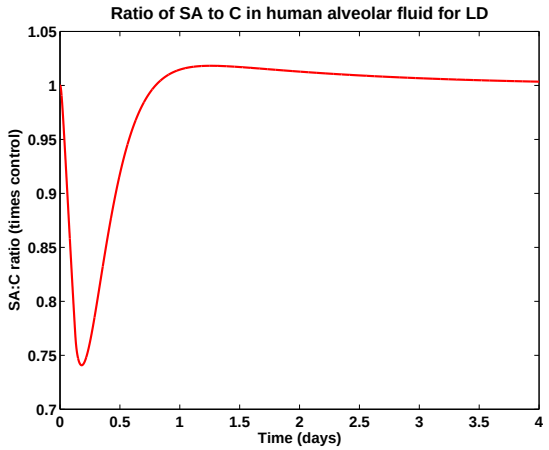

(c) Low dose

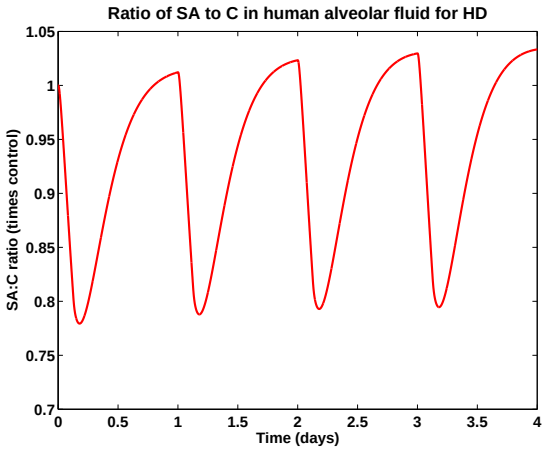

(d) High dose

Figure IV.30: Model predictions of PL, SA, and C in human alveolar fluid after inhalation exposure; LD represents 3 hour inhalation exposure while HD represents four consecutive exposures over four days

Chapter V

Multiscale Pulmonary Mechanics

V.1 Background

This chapter describes the linking of various aspects of the pulmonary toxicodynamic model to organism scale pulmonary mechanics or lung function. The cell and tissue level effects caused by NP inhalation were described in detail in previous chapters. The integration of various biological scales considered in this thesis is schematically presented in Figure V.1 from a physiological viewpoint of the human respiratory system. Physiome level changes in lung function over time represents one of the significant observable changes to particulate matter exposure [205, 206]. Changes in pulmonary function due to chemical exposure has been studied extensively in laboratory animals including dogs [207], cats [208], mice [147], and rats [209]. However, there has been no attempt at linking tissue level toxicodynamic changes due to particle inhalation to observable changes in pulmonary function from a mechanistic point of view. The mathematical model described here simulates the mechanical operation of the lung involving its cyclic expansion and compression and links pulmonary tissue resistance and elastance to surfactant dynamics in the alveolar hypophase and the dynamic surface tension of the alveolar air-liquid interface.

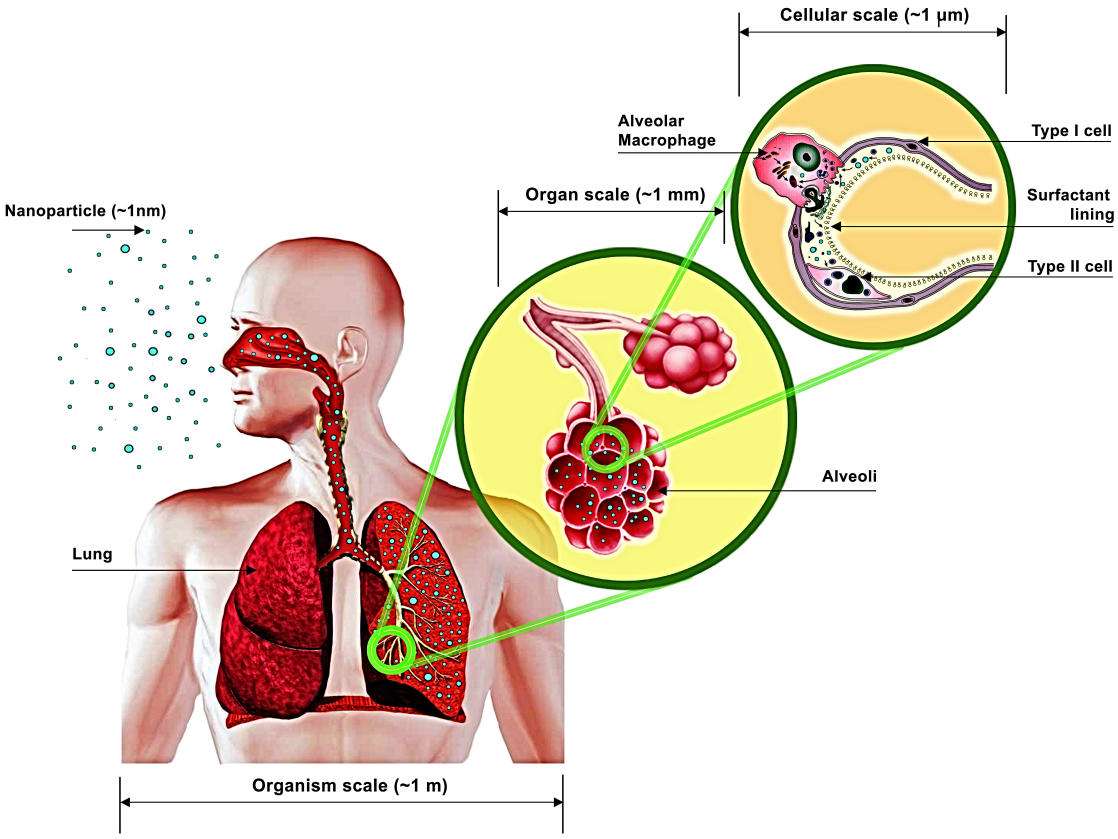

Figure V.1: Diagram showing the various scales in the mammalian respiratory system which have been separately modeled in this framework

V.1.1 Bronchoalveolar factors affecting pulmonary mechanics

It is well known that lung function is a complex aspect and is affected by a number of quantities of the alveolar fluid and the alveolar air-liquid interface. The most important and critical variable which is known to affect pulmonary function is surface tension (γ) of the alveolar air-liquid interface [159, 210, 211]. The primary motive of surfactant phospholipids (PL) and surfactant proteins (SP) is to reduce γ to make the work of breathing easier. A physiologically normal value of γ also prevents closure of the alveoli and the smaller airways thus promoting efficient gaseous exchange [210].

Based on previous research in this field, a set of bronchoalveolar factors (BAFs) have been identified, which could be dynamically quantified based on the alveolar

toxicodynamic model described in Chapter IV. The values of the BAFs for some select time points for mice and rats, are compared here to identify potential effects on surfactant dysfunction.

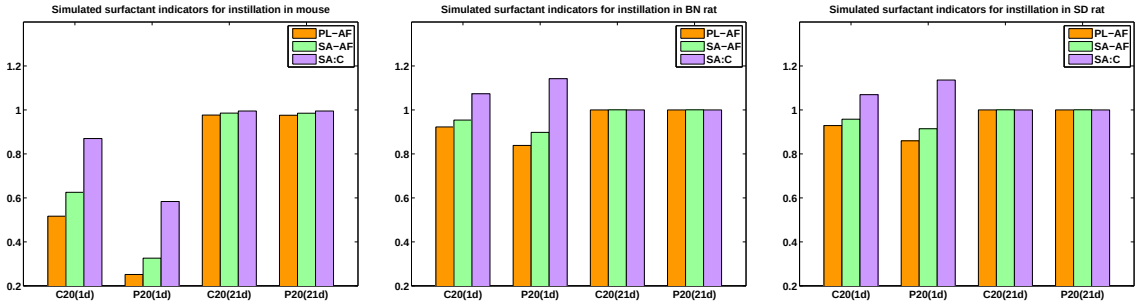

(a) Mouse (b) BN rat (c) SD rat

Figure V.2: Comparison of bronchoalveolar factors at 1, 3, and 7 days post NP instillation in various species (PL-AF represents free PL in alveolar fluid, SA-AF represents free SA in alveolar fluid, and SA:C represents the ratio of SA to C in the alveolar fluid)

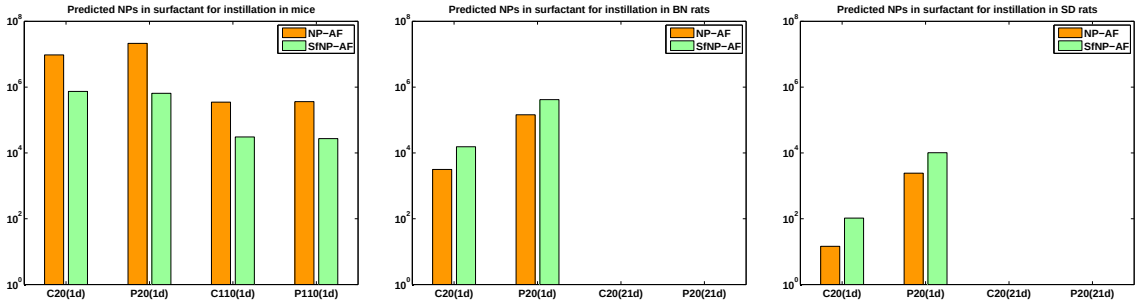

(a) Mouse (b) BN rat (c) SD rat

Figure V.3: Comparison of bronchoalveolar factors at 1, 3, and 7 days post NP instillation doses in various species (NP-AF represents NPs in alveolar fluid and SfNP-AF represents surfactant coated NPs in alveolar fluid)

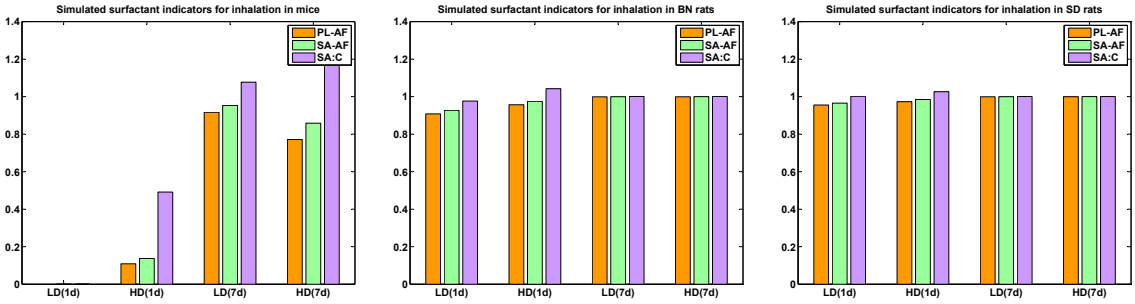

(a) Mouse (b) BN rat (c) SD rat

Figure V.4: Comparison of bronchoalveolar factors at 1 and 7 days post NP inhalation doses in various species (PL-AF represents free PL in alveolar fluid, SA-AF represents free SA in alveolar fluid, and SA:C represents the ratio of SA to C in the alveolar fluid)

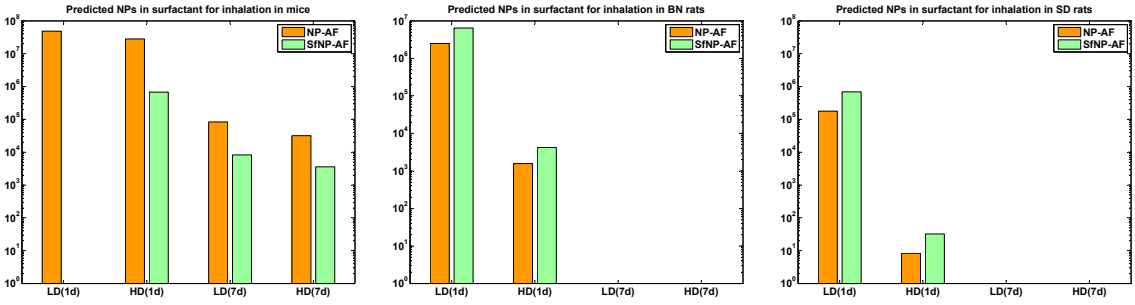

(a) Mouse (b) BN rat (c) SD rat

Figure V.5: Comparison of bronchoalveolar factors at 1 and 7 days post NP inhalation doses in various species (NP-AF represents NPs in alveolar fluid and SfNP-AF represents surfactant coated NPs in alveolar fluid)

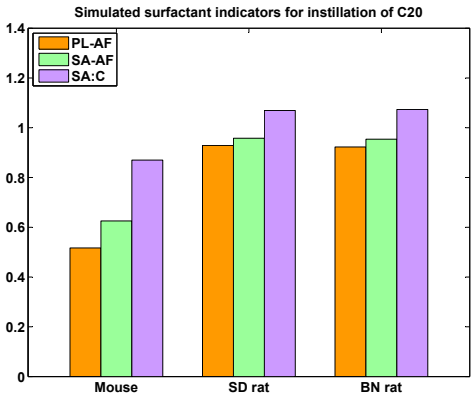

(a) C20

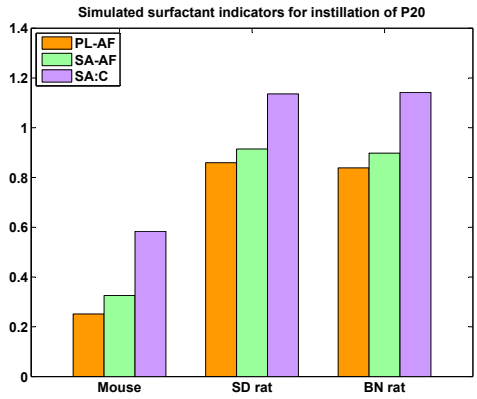

(b) P20

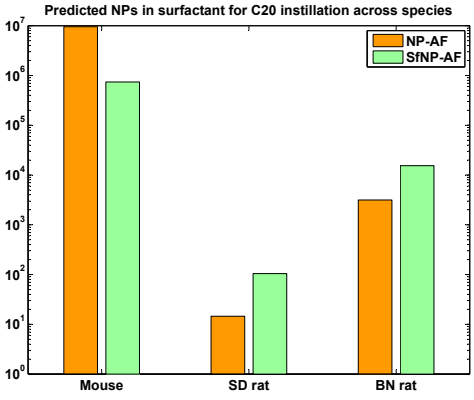

(c) C20

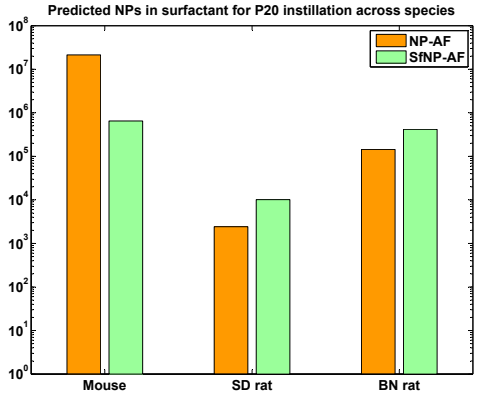

(d) P20

Figure V.6: Comparison of bronchoalveolar factors at 1, 3, and 7 days post NP instillation doses in various species for C20 and P20 NPs (PL-AF represents free PL in alveolar fluid, SA-AF represents free SA in alveolar fluid, SA:C represents the ratio of SA to C in the alveolar fluid, NP-AF represents NPs in alveolar fluid and SfNP-AF represents surfactant coated NPs in alveolar fluid)

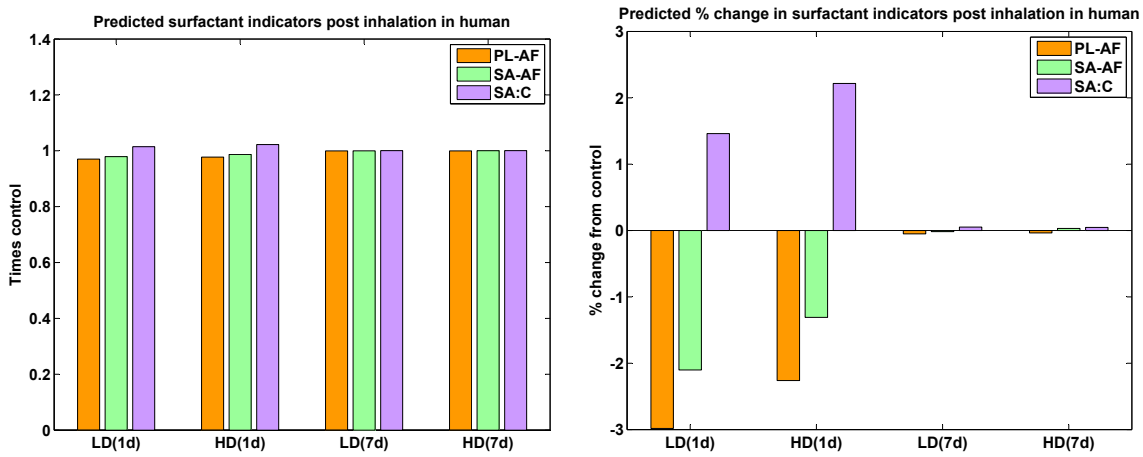

(a) (b)

Figure V.7: (a)Comparison of model predicted bronchoalveolar factors at 1 and 7 days post NP inhalation doses in human; (b) Percent changes in BAFs over control (PL-AF represents free PL in alveolar fluid, SA-AF represents free SA in alveolar fluid, and SA:C represents the ratio of SA to C in the alveolar fluid)

V.2 Pulmonary pressure-volume relationships

The following definitions associated with a normally functioning lung are required to characterize the pulmonary mechanics of air-breathing mammals:

Tidal volume: Tidal volume, V_{T} is the normal volume of air displaced between inspiration and expiration during unstressed breathing

Minute volume: Minute volume, V_{m} is the total volume of air entering the lungs in 1 minute

Expiratory Reserve Volume: Expiratory reserve volume, ERV is the maximum extra volume that can be used in stress compressions

Inspiratory Reserve Volume: Inspiratory reserve volume, IRV is the maximum extra volume that can be used in stress expansions

Residual Volume: Residual volume, RV is the extra volume in lungs that is normally not used during breathing

Total Lung Capacity: Total lung capacity, $TLC = V_{\mathrm{T}} + IRV + ERV + RV$

Alveolar Volume: Alveolar volume, V_{alv} is the total volume of the alveoli in the lungs

Dead Volume: Dead volume, V_{D} is the total volume in the bronchioles and smaller branches of the trachea where some air is stored during breathing

Volume expansion of the lung caused by air flow is a cyclical process and can be expressed as a sinusoidally varying signal as:

$$V = V_{\text{amp}}[1 + sin(\omega t)] + V_{\text{min}}, \tag{V.1}$$

where V_{amp} is the amplitude of the volume variation and during tidal breathing, $V_{\text{amp}} = V_{\text{T}}/2$. V_{min} is the residual volume of air at the end of expiration and would depend on the value of PEEP (Positive End Expiratory Pressure). For normal tidal breathing, $V_{\text{min}} = ERV + RV$. Consequently, the air flow rate through the lungs can be expressed as:

$$\dot{V} = \frac{dV}{dt} = V_{\text{amp}}\omega cos(\omega t) = V_{\text{amp}}\omega sin(\omega t + \pi/2) \tag{V.2}$$

Here ω is the angular frequency of breathing, related to the frequency, f, as $\omega = 2\pi f$. The functional volume, V can be related to the actual alveolar volume, V_{alv} as: $V_{\text{alv}} = V - V_{\text{D}}$, where V_{D} is the dead volume defined before.

The total transpulmonary pressure, P follows the same breathing cycle but is shifted in phase from both V and $\dot{V}$, the exact phase difference depending on mechanical parameters of the airway and alveoli.

$$P = P_{\text{m}} sin(\omega t + \phi) \tag{V.3}$$

Pressure (P) and volume (V) is also often related using empirical equations such as the Salazar-Knowles equation [212] which is expressed as:

$$V = A - Be^{\text{-kP}}, \tag{V.4}$$

where A, B, and k are intrinsic parameters of the lung.

V.3 Modeling pulmonary impedance

Pulmonary impedance can be described as the opposition to the flow of air into the lungs, and like electrical impedance, is defined as the ratio of the driving force causing the flow (in this case, pressure) and the rate of flow (in this case, air flow rate, $\dot{V}$). The relation between pressure and volume of air in lungs has been modeled since Otis *et al.*, 1956 [213], using the analogy of an electric R-C circuit, with pressure and flow rate analogous to voltage and electric current respectively. Hence, P and V can be related as $P = \dot{V}Z$, where Z is the pulmonary impedance. Pulmonary impedance is intrinsically dependent on lung viscoelasticity. Various formulations have been developed over the years to relate various frequency dependent and independent lung parameters with impedance. Hildebrandt [208] first showed in 1970, by his experiments with cat lungs, that the viscoelastic modulus of this system varies linearly with the logarithm of time. Hantos and co-workers [207, 214] made modifications to Hildebrandt's original theory with their Constant-Phase Model (CPM), where they decomposed the complex pulmonary impedance into components due to airway resistance (R_{aw}), inertance (I), tissue-damping (G), and tissue elastance (H). Based on an understanding of mechanics, air flow rate, $\dot{V}$ and pulmonary impedance, Z can be expressed as:

$$\dot{V(t)} = \frac{dV(t)}{dt} \tag{V.5}$$

$$Z(t) = \frac{P(t)}{\dot{V(t)}} \tag{V.6}$$

$$Z(\omega) = \frac{P(\omega)}{i\omega V(\omega)}, \text{ (Taking Fourier transform of both sides)} \tag{V.7}$$

The mechanics equation which relates pulmonary air flow to pressure can be considered to have components due to inertial effects, airway resistance and the elastic forces in the lung [204]. Accordingly the force balance for flow into and out of the

lung can be written as a differential equation in time domain as:

$$P(t) = P_{\circ} + I\frac{d^2V(t)}{dt^2} + R\frac{dV(t)}{dt} + b_{\mathrm{k}}\frac{d^{\mathrm{k}}V(t)}{dt^{\mathrm{k}}}, \tag{V.8}$$

where I is the gas inertance responsible for inertial forces, R is the airway resistance, and k is a dimensionless number representing the dimensionality of the pulmonary elastic forces. Fourier transformation of each component in Equation V.8 helps transform the quantities from time (t) domain to frequency (ω) domain and makes the analysis more mathematically amenable by utilizing the theory of complex numbers. Fourier transformation of each term in Equation V.8, with subsequent addition, produces real and imaginary parts of complex impedance in frequency domain, $Z(\omega)$, as:

$$Z(\omega) = (R + \frac{G}{\omega^{\alpha}}) + i(I\omega - \frac{H}{\omega^{\alpha}}) \tag{V.9}$$

where, $G = (P_{\circ}\sqrt{\frac{2}{\pi}})\Gamma(1-k)\cos[(1-k)\pi/2]$, $H = (P_{\circ}\sqrt{\frac{2}{\pi}})\Gamma(1-k)\sin[(1-k)\pi/2]$, and $\alpha = 1 - k = (2/\pi)\tan^{-1}(H/G)$. This is the form of the Constant Phase Model (CPM), the name arising out of the fact that the phase difference between the real and imaginary components of the equation is independent of frequency, ω [204]. The CPM has been widely used to characterize pulmonary mechanics in mammals because of its apparent simplicity, elegance and the fact that it can be readily separated into dissipative and capacitive effects of the lung [204, 215, 206].

Physically, the real part of pulmonary impedance, Z_{Re} captures the dissipative effects of pulmonary mechanics, and represents the physical impedance to airflow and energy loss due to impedance. The imaginary part of impedance, Z_{Im} captures the capacitive effects and represents energy storage due to the recoil forces in the lung.

They can be separately written as:

$$Z_{\mathrm{Re}} = R + \frac{G}{\omega^{\alpha}} \tag{V.10}$$

$$Z_{\mathrm{Im}} = I\omega - \frac{H}{\omega^{\alpha}} \tag{V.11}$$

Here, the parameters R, I, G, and H represent airway resistance, tissue inertance, tissue resistance, and tissue elastance respectively. Following the analogy of an R-C circuit, the magnitude of impedance $|Z|$ can be expressed as $|Z| = \sqrt{Z_{\mathrm{Re}}^2 + Z_{\mathrm{Im}}^2}$ and the phase angle as $\phi = \tan^{-1}\left(\frac{Z_{\mathrm{Im}}}{Z_{\mathrm{Re}}}\right)$.

V.3.1 Relating impedance to alveolar properties

Despite numerous research efforts to model pulmonary impedance in animals, a comprehensive model relating the parameters of the Constant Phase Model to alveolar properties has been seriously lacking. Researchers have identified various alveolar properties with possible effects on various aspects of lung function but there is till date no mechanistic model relating surfactant concentrations or surface tension to pulmonary tissue elastance or resistance. Mukherjee *et al.* [145] have quantified changes in surfactant concentrations at the alveolar level in mice due to NP instillation and linked alveolar concentrations of surfactant to pulmonary resistance and elastance via an empirical model. In this section, a more mechanistic description is attempted on the basis of changes in alveolar recruitment due to NP-induced changes in surfactant profiles.

In the CPM equations, R is known to represent airway resistance [204, 216]. Inertance I is also a parameter of the airways and is expected to vary between animals but is not expected to change due to tissue-level changes in surfactant dynamics. The real part of pulmonary impedance is generally considered to be composed of two resistances - airway resistance (R_{AW}) and pulmonary tissue resistance (R_{T})

[204, 206]. However, for some animals there is another resistive component - chest-wall impedance (R_{CH}). For mice, which are "open-chested" [204], R_{CH} is very small but might be significant for bigger mammals. Crosfill and Widdicombe [217] studied eight different species of mammals and found chest wall compliance (inverse of impedance) to be significantly higher for smaller mammals such as mouse, rat, guinea-pig, and rabbit, than that in bigger mammals such as cats, dogs, and human. The real part of impedance, Z_{Re}, thus can be written as composed of three different resistive components as:

$$Z_{\mathrm{Re}} = R_{\mathrm{AW}} + R_{\mathrm{CH}} + R_{\mathrm{T}} \tag{V.12}$$

Comparing Equations V.9 and V.12, we have the pulmonary tissue resistance as:

$$R_{\mathrm{T}} = \frac{G}{\omega^{\alpha}} \tag{V.13}$$

Similarly, the pulmonary tissue elastance, E_{T} can be expressed as:

$$E_{\mathrm{T}} = \frac{H}{\omega^{\alpha}} \tag{V.14}$$

The variables R_{T} and E_{T} are expected to depend on pulmonary tissue properties including surfactant profiles. It should be pointed out here that the CPM parameters G and H, which represent pulmonary tissue resistance and elastance do not change independent of each other, and are in fact related. The ratio $\eta = H/G$ is known as tissue hysteresivity and remains fairly unchanged in a particular subject, unless there is a very high extent of lung injury [218]. η has been measured in a number of mammalian species and was found to be in the range 0.1-0.2 [204, chap. 10]. Thus a model which is able to predict pulmonary tissue elastance (H) under various conditions, is sufficiently equipped to predict overall pulmonary function under conditions of limited lung injury. In the following sections an alveolar recruitment model has been proposed to link pulmonary tissue properties to pulmonary tissue elastance, H,

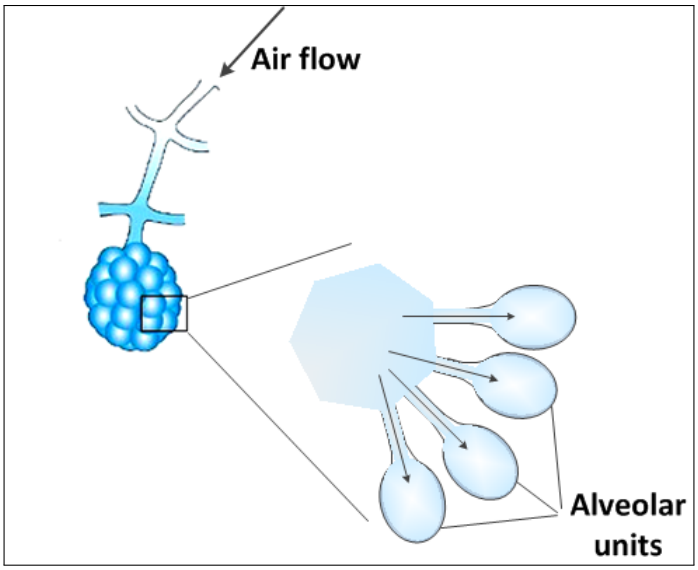

(a)

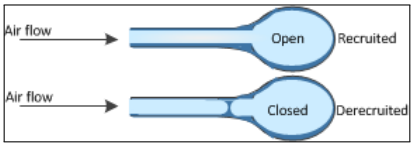

(b)

Figure V.8: Schematic representation of the alveolar recruitment model based on Massa *et al.* [147] showing (a) integration of alveolar units at the terminus of an airway and (b) opening and closing of individual airways due to surfactant dynamics

with the tissue properties being represented by the bronchoalveolar factors (BAFs) which have been described before.

V.3.2 Alveolar recruitment model

Alveolar recruitment is a key mechanism in the process of breathing by mammals. Recruitment refers to the opening of alveolar air spaces so that air can flow into these spaces. During normal breathing process (tidal breathing), most of the alveoli remain recruited (or open) and they only expand and contract during inspiration and expiration. Recruitment and derecruitment (R/D) changes substantially during lung injury [219] and is also a significant factor during normal tidal breathing [220]. Small airway and alveolar closure is known to occur at low lung volumes in normal lungs and may exist even at larger lung volumes in subjects with lung obstruction [210].

Alveolar R/D has been shown to modulate pulmonary tissue resistance and elastance [147] in mice with acute lung injury (ALI). Increase in alveolar surface tension has been known to cause derecruitment of alveolar units leading to an increase in both G and H [204, chap. 10], which represent pulmonary tissue resistance and elastance respectively (Equations V.13 and V.14). More severe pulmonary injury which leads to remodeling of the lung tissue can independently increase G, without an associated increase in H. The alveolar recruitment model described here predicts the fractional alveolar recruitment and its effect on tissue elastance, H. The alveolar R/D model follows the model developed by Bates *et al.* [221] and Massa *et al.* [147]. Figure V.8 shows a graphical representation of the model. The model simulates alveolar R/D based on a pressure signal using the following key alveolar parameters - critical opening pressure (P_{O}), critical closing pressure (P_{C}), rate of opening (S_{O}), and rate of closing (S_{C}). Opening and closing of alveolar units and the smallest airways are dependent on a number of surfactant and airway properties. Gaver *et al.* [210] and Halpern and Grotberg [222] studied surfactant effects in liquid-lined flexible tubes which were used as models of the small airways in the lung. The effects of surfactant properties on the four alveolar properties are discussed in detail in Section V.3.3. The model considers a set of N individual alveolar units and models their opening and closing as well as expansion/contraction due to a selected air flow. A variable x is defined such that $0 < x < 1$ which determines if an alveolar unit is open or closed with $x = 0$ representing a closed state and $x = 1$ representing the open state. The variable x_{i} for the ith airway follows the differential equation:

$$\frac{dx_{\mathrm{i}}}{dt} = \begin{cases} S_{\mathrm{Oi}}(P - P_{\mathrm{Oi}}) & \text{if } P > P_{\mathrm{Oi}} \\ S_{\mathrm{Ci}}(P - P_{\mathrm{Ci}}) & \text{if } P < P_{\mathrm{Ci}} \\ 0 & \text{otherwise} \end{cases} \tag{V.15}$$

Here, P represents the external applied pressure which is provided as a sinusoidal function as $P = P_{\mathrm{m}} sin(\omega t)$, where P_{m} is the pressure amplitude determined by the actual tidal volume of the species and ω is the frequency of breathing. Tissue resistance R_{T} and tissue elastance E_{T} depend upon the fraction of alveolar units open (f_{open}) at any point of time as:

$$R_{\mathrm{T}} = \frac{R_{\mathrm{i}}}{f_{\mathrm{open}}} \tag{V.16}$$

$$E_{\mathrm{T}} = \frac{E_{\mathrm{i}}}{f_{\mathrm{open}}} \tag{V.17}$$

Here, R_{i} and E_{i} are the individual unit resistance and elastance for the ith alveolar unit. They are assumed to be identical for all units and are determined from the control values of G and H for the particular species under consideration. Lung tissue heterogeneity is taken into account by considering the values of the four parameters as distributions rather than as single values. The opening and closing pressures, P_{Oi} and P_{Ci} for the ith alveolar unit are randomly selected from normal distributions as:

$$P_{\mathrm{O}} \quad \epsilon \quad \mathcal{N}(\mu_{\mathrm{Po}}, \sigma_{\mathrm{Po}}) \tag{V.18}$$

$$P_{\mathrm{C}} \quad \epsilon \quad \mathcal{N}(\mu_{\mathrm{Pc}}, \sigma_{\mathrm{Pc}}) \tag{V.19}$$

Here, $\mathcal{N}(\mu, \sigma)$ is a normal distribution with mean μ and standard deviation σ. Rate of opening (S_{o}) and rate of closing (S_{c}) are selected from hyperbolic distributions as described below [147]:

$$S_{\mathrm{O}} \quad \epsilon \quad \frac{\beta_{\mathrm{O}}}{\mathrm{unif}[0,1]} \tag{V.20}$$

$$S_{\mathrm{C}} \quad \epsilon \quad \frac{\beta_{\mathrm{C}}}{\mathrm{unif}[0,1]} \tag{V.21}$$

Here, unif[0,1] is a uniform distribution between 0 and 1, and β_{O}, β_{C} are scaling parameters for the rate of opening and closing respectively. In the subsequent sections,

the effect of NP dosing on these key parameters (μ_{Po}, μ_{Pc}, β_{O}, β_{C}) has been investigated. σ_{Po} and σ_{Pc} essentially reflect the extent of heterogeneity in the alveoli and is assumed to be unchanged due to NP inhalation.

Table V.1: Respiratory parameters for breathing in different species (in ml)

Parameter	Mouse (in µL)	SD rat (in mL) [197]	BN rat (in mL) [197]	Human (in mL) [196]
V_{T}	165**	2.2	1.44	500
TLC	1175*	14.9	9.72	6800
V_{D}	200*	2.53	1.65	150
FRC	341*	6.18	3.91	2200

* Reinhard *et al.* [223]

** Based on correlation from Stahl [197]

V.3.3 Alveolar surface tension

Pulmonary surfactant is composed of 3 main constituents: Surface-active agents (SA), collectins (C) and phospholipids (PL). Lipoproteins A and D make up the collectins and are associated with protection and immune response. Lipoproteins B and C make up the surface-active agents which are responsible for regulating the surface properties of the air-liquid interface of the alveoli. However, PL constitutes 90% of pulmonary surfactant and hence, surface tension is largely controlled by the lipid concentration at the alveolar surface. The functional form was derived using data from Walters *et al.* [158], (details in Appendix D). The surface tension γ_{PL} which is dependent on the concentration of PL in the alveolar lining can be expressed using the following equation:

$$\gamma_{\text{PL}} = \gamma_{\max}\left(1 - \frac{C_{\text{s}}^{n}}{K + C_{\text{s}}^{n}}\right), \tag{V.22}$$

where, C_{s} is the surface concentration of free PL at the alveolar interface and K and n are Hill-type coefficients.

Effect of surfactant proteins

Surface tension γ is also known to depend on the presence of SA (SP-B and SP-C) in the alveolar lining. These hydrophobic surfactant proteins have a striking impact in improving adsorption and dynamic surface activity of PL [115, Chap. 8]. During the process of breathing, PL bilayers are repeatedly squeezed out from dynamically compressed surface films and suffer respreading during expansion [150]. The ability of PL bilayers to function repeatedly in this fashion is significantly dependent on the presence of SA in close association to the PL bilayers [224]. Wang *et al.* [225] measured the surface tension produced by various surfactant formulations and showed that the minimum surface tension produced by natural calf lung surfactant extract was about 50% lower than PL by itself. The surface tension γ_{PL} given by Equation V.22 is based solely on the surface concentration of free PL. However, the actual

surface tension γ of the alveolar interface is a result of PL adsorption to the interface, composition of bilayers, and spreading of the PL bilayers which requires the presence of SA. To take this into account, the effective surface tension γ was modified by a surface-active factor f_{SA} as:

$$\gamma = \gamma_{\mathrm{PL}}.f_{\mathrm{SA}}, \tag{V.23}$$

where, f_{SA} is estimated by $f_{\mathrm{SA}} = k_{\mathrm{surf,SA}}(1 - C_{\mathrm{SA}})$, C_{SA} being the fractional concentration (by weight) of SA in surfactant and $k_{\mathrm{surf,SA}}$ is a constant quantifying the effect of SA on γ. The value of $k_{\mathrm{surf,SA}}$ is estimated using measurements from Wang *et al.* [225] (Details of estimation procedure included in Appendix D).

Effect of NPs within phospholipid bilayers

Although there has been considerable research [210, 222, 226] regarding the effect of various surfactant lipids and proteins on the final surfactant function, the effect of NP-interaction with surfactant lipids and proteins has not been researched sufficiently from the point-of-view of pulmonary function. The effect of NPs embedded within lipid bilayers has been studied in the field of drug delivery and biomedical imaging for the use of lipids as stabilizing agents or functional ligands for drug-carrier NPs [227, 228]. Presence of NPs within lipid bilayers can lead to changes in lipid packing and can result in changes in the degree of lipid ordering and bilayer viscosity [229], all of which are known to affect interfacial surface tension in lungs [159, 230]. Bothun [228] studied hydrophobic silver NPs embedded within bilayers of DPPC (1,2 - depalmitoyl -glycero -3-phosphocholine) and quantified the changes in DPPC bilayer anisotropy caused by presence of AgNPs. Lipid bilayer anisotropy is is a measure of lipid ordering and bilayer microviscosity [228]. Gel phase bilayers exhibit high anisotropy and associated high viscosity, which is desirable for surfactant action. Presence of NPs was found to decrease anisotropy and promote gel-to-fluid transition in a dose-dependent manner [228]. The relative change in anisotropy at 30°C due to increasing weight fraction of

NPs from measurements conducted by Bothun [228] was used to estimated the relative change in viscosity of surfactant PL in the lungs (Details of estimation procedure included in Appendix D).

Effect of NPs on alveolar recruitment

The alveolar R/D model described in Section V.3.2 contains four key alveolar parameters - mean critical opening pressure (μ_{Po}), mean critical closing pressure (μ_{Pc}), scaling parameter for rate of opening (β_{O}), and scaling parameter for rate of closing (β_{C}). All of these parameters are expected to be affected by changes in the surfactant profile caused by NP inhalation. Gaver *et al.* [210] found airway opening pressures to be affected by the airway radius, axial wall tension, surface tension (γ), and viscosity of the lining fluid (μ). In this model implementation, heterogeneity in airway radii across the lung has not been considered due to simplicity. Gaver *et al.* [210] also found airway opening pressures to be increased by an increase in γ. Accordingly, the value of μ_{Po} was modulated with respect to the control value, $\mu_{\mathrm{Po}}*$ as:

$$\mu_{\mathrm{Po}} = \mu^{*}_{\mathrm{Po}}.\left(\frac{\gamma}{\gamma*}\right), \tag{V.24}$$

where, $\gamma*$ is the control value of surface tension in alveolar fluid and μ^{*}_{Po} is the value obtained for normal mice [147]. Gaver *et al.* [210] also found that once the applied pressure exceeds the critical opening pressure, the mechanics of airway opening depend on the relative magnitudes of viscous forces and surface tension, as reflected in the dimensionless Capillary Number, $Ca = \mu S/\gamma$, where S is the speed of airway opening, μ is the viscosity of surfactant, and γ is the surface tension. Unless there is a complete change in the flow pattern of the surfactant, Ca is assumed to remain fairly unchanged and so the value of β_{O} can be modeled as:

$$\beta_{\mathrm{O}} = \beta^{*}_{\mathrm{O}}.\left(\frac{\mu^{*}}{\mu}\right).\left(\frac{\gamma^{*}}{\gamma}\right), \tag{V.25}$$

Change in viscosity, μ, and the resultant change in alveolar opening rate, β_o was modeled based on measurements of surfactant bilayer anisotropy from Bothun [228] for AgNPs as discussed in Section V.3.3.

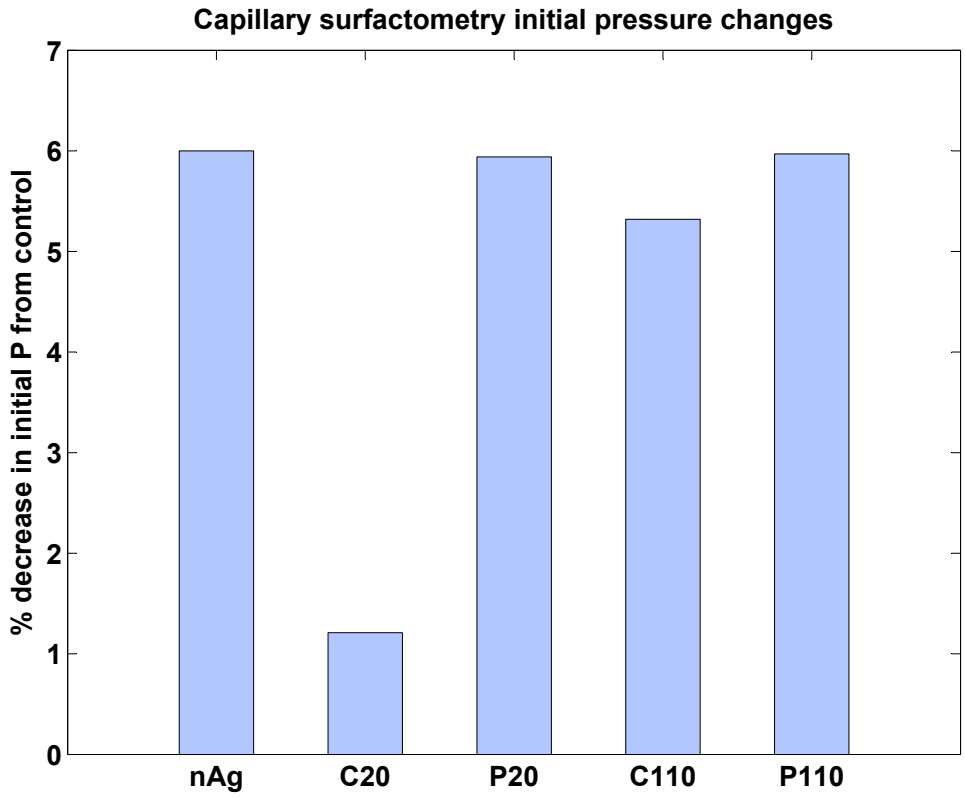

Figure V.9: Comparison of measured percentage changes in initial pressure from capillary surfactometry of large aggregate fraction of bronchoalveolar lavage 1 day after dosing with various NPs. (Data from Danielle Botelho and Dr. Andrew Gow, School of Pharmacy, Rutgers University)

V.3.4 In vivo measurements of lung function

In vivo measurements of nanoparticle effects were done in experiments involving nine-week old C57-BL6 Jackson wild-type male mice. The animals (average body weight 24.82 g) were intra-tracheally dosed with 1 and 10 μg/ml per g body weight of silver nanoparticles (nAg) and carbon black (CB). Additional details regarding the protocols for the *in vivo* measurements in mice are included in Mukherjee *et al.* [145]. The dosed

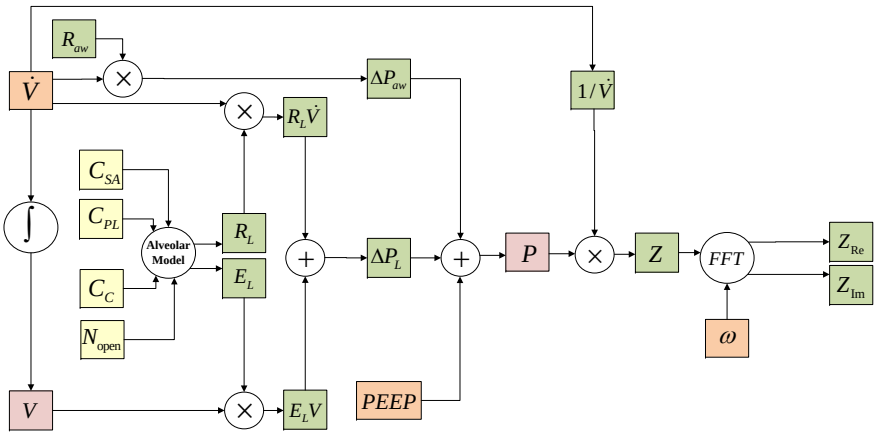

Figure V.10: Schematic describing variables and parameters comprising the model for pulmonary mechanics.

mice were rested for 1 day, 3 days and 7 days and then anesthetized and subjected to forced oscillatory breathing manoeuvres on a Flexivent (SCIREQ, Montreal, Canada) system for a spectrum of frequencies at different positive end expiratory pressures, which consists of measurements of overall pulmonary resistance (R_{L}) and elastance (E_{L}) which are related to the real and imaginary parts of impedance as: $R_{\mathrm{L}} = Z_{\mathrm{Re}}$ and $E_{\mathrm{L}} = \omega|Z_{\mathrm{Im}}|$. The lung function measurements in the BN and SD rats were conducted using a computer-controlled ventilator (eSpira, EMMS, UK) [148]. Further details regarding the measurement protocols are included in Seiffert *et al.* [148].

V.4 Comparison of model predictions with in vivo measurements

Model predictions of tissue elastance, H were compared with values of H from *in vivo* lung function measurements in mice and in rats. As stated earlier, only the measurements corresponding to a PEEP of 3 were used. Figure V.13 shows the comparisons model predictions and *in vivo* measurements of tissue elastance, H. Model predictions of H were obtained from the alveolar R/D model as discussed in Section V.3.2 using modulations in surface tension and viscosity of surfactant based on various published models. Model predictions seem to capture the overall changes in H very well. However, it seems to over predict the value of H in some cases, especially for

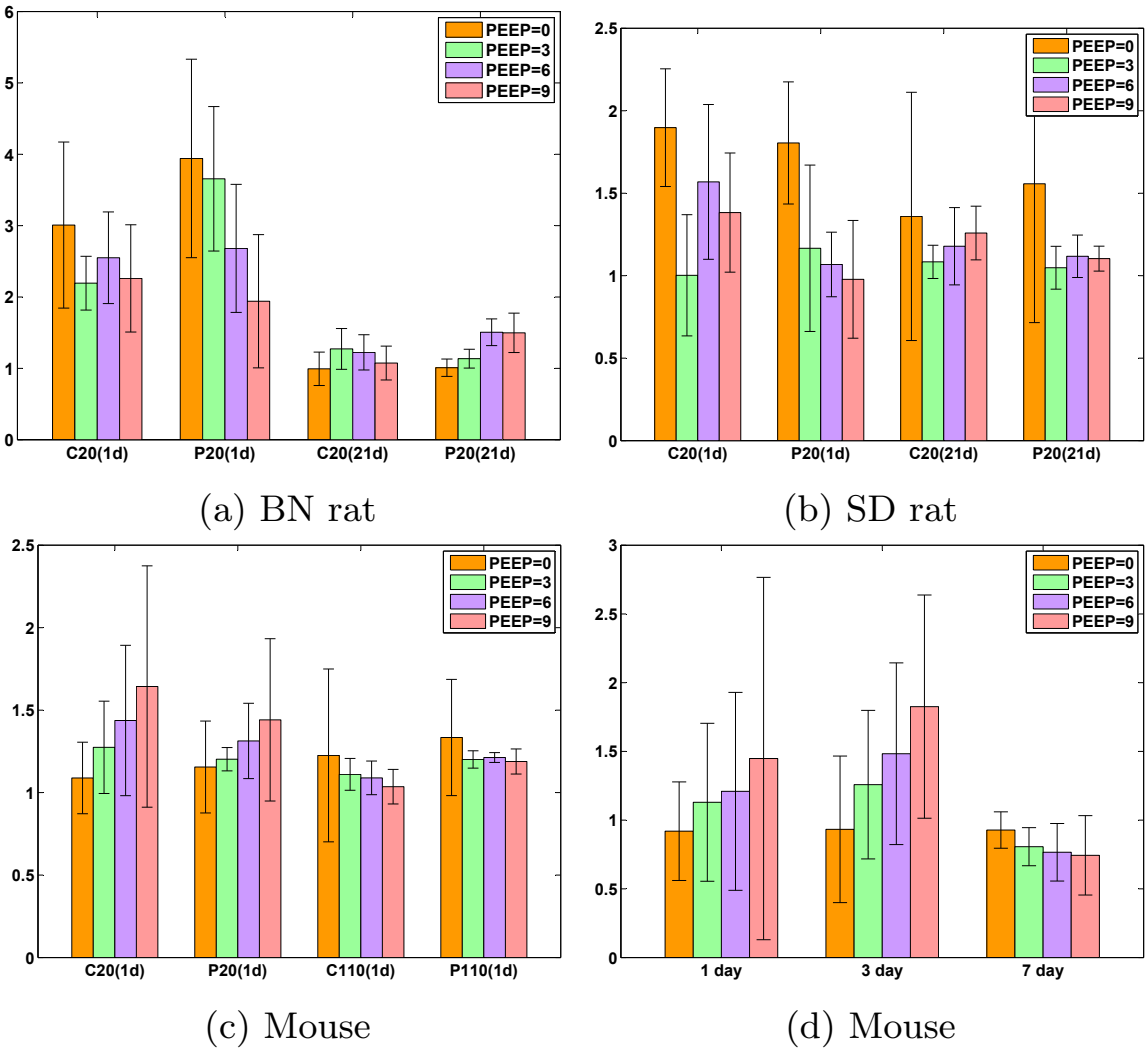

Figure V.11: Comparison of measured lung elastance (H), in mice, BN rats, and SD rats post NP instillation at different values of PEEP. (Bars represent mean values while error bars represent standard deviations about the mean value; measurements in mice from Danielle Botelho, Rutgers School of Pharmacy and measurements in rats from Joanna Seiffert, Imperial College London [148])

SD rats (Figure V.13(b)) and under predict the value for BN rats (Figure V.13(a)). The intrinsic sensitivity of species was already considered in the model using control measurements in respective species. However, it appears there might still be some species-specific differences which is not captured by the model. This might be due to immune responses elicited by NP exposure, which has not been considered in this implementation of the model. Immune response due to NPs (discussed in detail

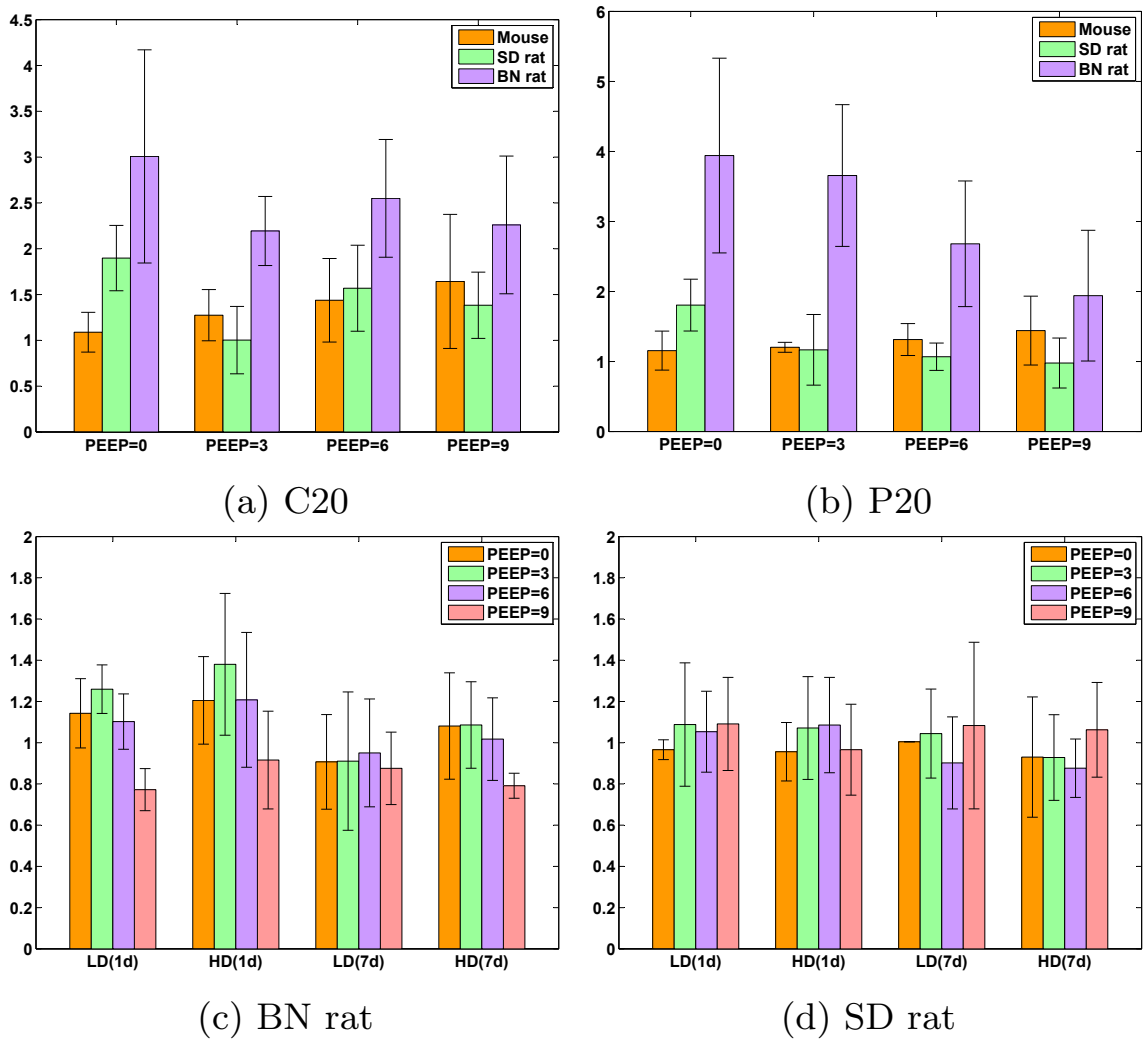

Figure V.12: Comparison of measured lung elastance (H), in mice, BN rats, and SD rats post NP instillation and inhalation at different values of PEEP. (Bars represent mean values while error bars represent standard deviations about the mean value; measurements in mice from Danielle Botelho, Rutgers School of Pharmacy and measurements in rats from Joanna Seiffert, Imperial College London [148])

in Chapter IV) is not expected to become a significant factor unless the subject is exposed to a very large amount of NPs, might still have some effect on surfactant dysfunction. Intratracheal instillation, which involves dosing into the trachea of the animal using a cannula, is an invasive procedure and is liable to produce some immune response in the subject [189]. The model was also implemented for an adult human (21 years, 70 kg body weight) to estimate the changes in pulmonary function

as a result of the stated doses of Spark-Ag at a PEEP of 3. Figure V.14 shows the percent changes in pulmonary tissue elastance, H from control for the various two dosage scenarios at 1 day and 7 day. The model predicts a 1% increase in H for the LD dose scenario and a 0.3% increase for the HD dose scenario.

Table V.2: Physiological parameters of respiratory system of species involved

	Mouse	SD rat	BN rat	Human
Lung volume (ml/kg BW)	10 [194]	29.2 [195]	29.2	12.91 [196]
Lung mass (g/kg BW)	3.07 [193]	11.3 [197]	11.3	12 [198]
Alv. surface area (cm^2/ml)	273 [203]	377.36 [195]	377.36	1000 [231]
Alv. thickness (μm)	0.2	0.2	0.2	0.2
No. of LB (per AT2 cell)	150	150	150 [195]	150
No. of AT1 cells (per g lung)	4.43×10^6	4.43×10^6 [199]	4.43×10^6	1.55×10^7 [200]
No. of AT2 cells (per g lung)	9.13×10^7 [156]	3.07×10^7 [195]	3.07×10^7	2.98×10^7 [200]
No. of Mph (per animal)	1.66×10^5 [201]	1×10^7 [202]	1×10^7	2.6×10^{10} [200]

Values without literature references are scaled from other species by body weight or lung size.

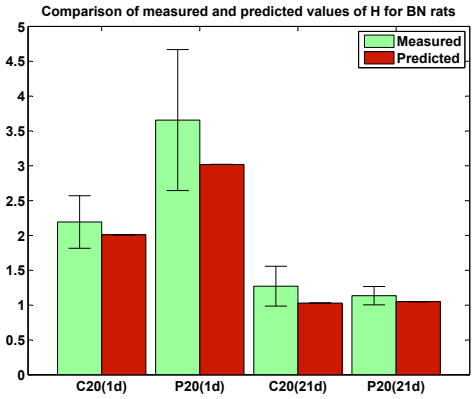

(a) BN rat (instillation)

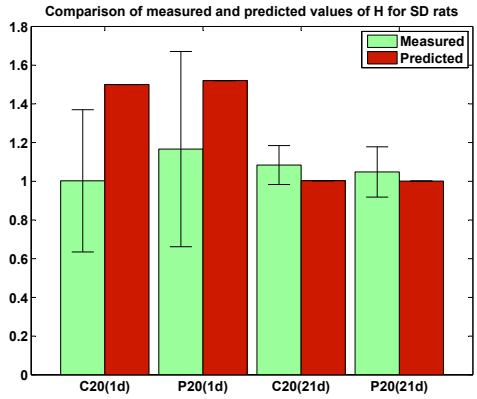

(b) SD rat (instillation)

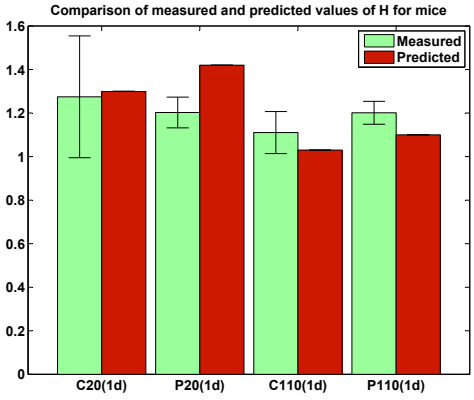

(c) Mouse (instillation)

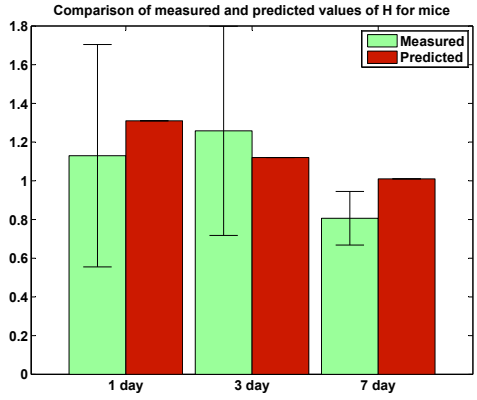

(d) Mouse (instillation)

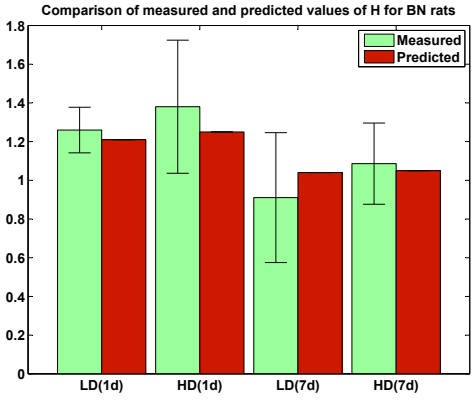

(e) BN rat (inhalation)

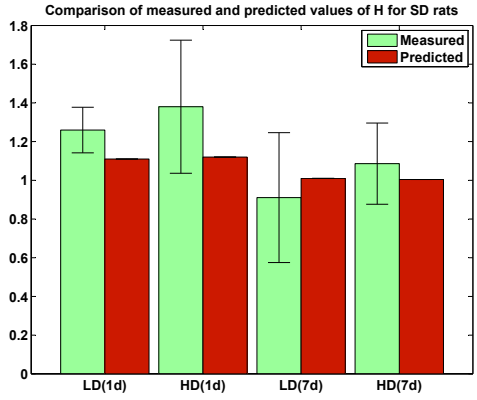

(f) SD rat (inhalation)

Figure V.13: Comparison of measured and model predicted lung tissue elastance (H), in mice, BN rats, and SD rats post NP instillation and inhalation at PEEP = 3. (Bars represent mean values while error bars represent standard deviations about the mean value; measurements in mice from Danielle Botelho, Rutgers School of Pharmacy and measurements in rats from Joanna Seiffert, Imperial College London [148])

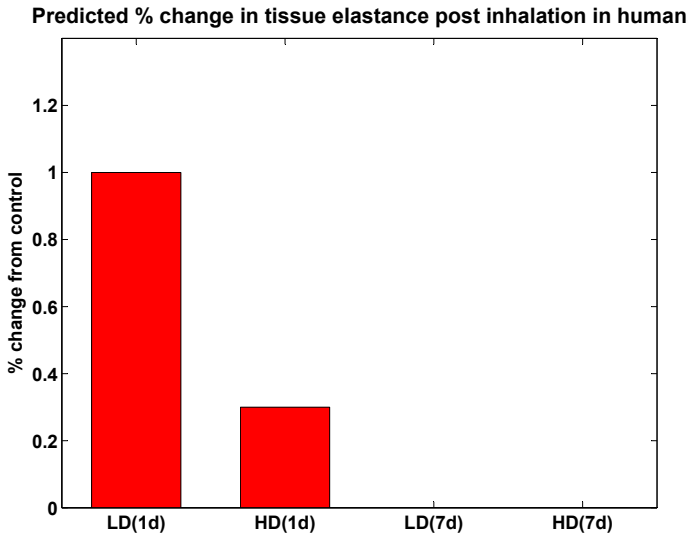

Figure V.14: Model predicted percent change in values of tissue elastance (H), in adult human subjects post inhalation exposure to SparkAg at PEEP = 3.

Chapter VI

Summary and Conclusions

VI.1 Major outcomes and findings

The multiscale toxicodynamic model developed in this dissertation has successfully simulated NP-biosystem interactions at multiple scales, while considering key biological mechanisms in an integrated, modular framework, that represents a substantial and novel accomplishment. Furthermore, the model provides a platform for analyzing animal-xenobiotic interactions in a toxicodynamic framework using multidisciplinary tools and multiple, heterogenous sources of information. As shown in Figure I.5, this Thesis has utilized both *in vitro* and *in vivo* measurements to extract mechanistic information relevant to the various modules described in this work.

VI.1.1 Nanoparticle distribution in the organism

As a first step towards quantifying nanoparticle risks in the context of human biology, a physiologically-based toxickinetic model was developed for a rodent system and was parameterized and tested using measurements from the scientific literature. Novel features of the PBTK model include: (a) nano scale particle uptake processes in cells, (b) particle margination in blood flow, (c) lymphatic drainage from interstitial spaces, and (d) consideration of particle and ionic silver simultaneously. The model was

developed by incorporating multiple scales and multiple transport processes instead of simplifying the transport using a single partition-coefficient based formulation.

VI.1.2 Nanoscale particle transformation

Physico-chemical transformation of ENMs has been modeled using the ADSRM (Agglomeration - Diffusion - Sedimentation - Reaction Modeling) module, developed through the present research effort, which considers key transformation processes affected by a variety of conditions (pH, ionic strength, height of liquid, nature of coating, etc.). The ADSRM module has been implemented for *in vitro* systems and then extended to the biological microenvironment of the alveolar lining layer to estimate key kinetic rates that affect overall toxicodynamics in the pulmonary system.

VI.1.3 Tissue scale toxicodynamics

Following the characterization of NP distribution and dosimetry, attention was focussed on the respiratory system, which is critical for assessing inhalation exposures to nanoparticles. Specifically, a set of operational computational modules was developed, linking multiple biological scales, that provide quantitative estimates of the impact of nAg exposures on biological response. Particular focus was on inhalation exposures and corresponding impact on lung function: modular dosimetric and toxicodynamic models for the mouse lung were completed, compiled, and evaluated, using *in vivo* measurements from collaborating research groups. The model was subsequently extended to Brown-Norway and Sprague-Dawley rats and model predictions were compared with *in vivo* measurements for both instillation and inhalation dose scenarios. The model was also implemented for an adult human and corresponding model predictions were developed for changes in alveolar surfactant composition with time.

VI.1.4 Organ scale pulmonary mechanics

Finally, the estimates and predictions from the multiple modules spanning the range of multiple biological scales were integrated and used to predict changes in organism-level pulmonary function for rats and human using an alveolar recruitment model. The alveolar recruitment/derecruitment model uses various bronchoalveolar factors (BAFs) estimated by the modules of the toxicodynamic model and computes resultant fractional recruitment of alveoli, as a result of changes in surfactant profiles at the alveolar lining. The model considers changes in surface-tension and viscosity of alveolar surfactant and predicts changes in pulmonary tissue resistance and elastance.

VI.2 Major contributions

Based on the entire plan of research outlined in Chapter I, all of the stated objectives have been accomplished. The major scientific contributions accomplished in this thesis can be summarized as follows:

VI.2.1 Pulmonary dynamics

In silico models of tissue systems are valuable tools for testing and implementing various scenarios concerning biological impact of xenobiotics. Among these tissue systems, the hepatic, dermal, and pulmonary systems are of major concern as they form the first line of defense against chemical, physical, and biological agents entering the body. Mechanisms of transport and reactions of chemicals within these organ systems are critical determinants of the fate and impact of a particular toxicant in the biological system. Among these systems, the pulmonary system is particularly unique in its structure and function, due to the fact that it is the only system incorporating both blood and air flow. Hepatic systems are often modeled as networks of well-mixed reactors, with individual hepatocytes contributing as individual mini-reactors. The dermal system has been modeled as a series of parallel layers of tissue with molecules

being transported across them. However, the pulmonary system has an air-liquid interface at the alveolar region, in addition to the conventional capillary endothelial barrier. The pulmonary system presents unique pressure-driven mechanical changes in addition to chemical interactions in the tissue fluid, which increases the complexity of the mechanistic description of the system. There have been various attempts at describing parts of this system using computational models; however, this thesis presents for the first time a multiscale model linking the cellular level chemical changes to the organ-level mechanical changes in the mammalian lung.

VI.2.2 Pulmonary toxicity

Mechanisms of toxicity in the pulmonary tissue system can arise due to a number of reasons. Particulate exposure generally leads to immune response in pulmonary cells [232], characterized by enhanced cell counts in the lavage fluid and increased cell toxicity markers such as LDH and ROS. However, most of these toxicity endpoints have been evaluated through *in vitro* studies or by lavage extracts from exposed animals. The research presented in this thesis demonstrates, for the first time, a link between cellular biochemical changes due to nanoparticle exposure and physiome scale changes in lung function. Persistent and chronic decrease in lung function associated with increase in pulmonary resistance can exacerbate existing pulmonary conditions such as asthma or COPD and can also undermine the quality of life for healthy humans. Inhalation of particulate matter has been associated with an increase in pulmonary resistance and decrease in air flow rate in the lungs [233, Chap. 17]. It is also well known that resistance increase and decrease in flow rate is a consequence of alveolar derecruitment which happens due to surfactant dysfunction in the alveolar region [204]. Unlike traditional definitions of toxicity which focus on various cellular toxicity markers, this thesis deals with pulmonary toxicity from the viewpoint of physiome scale impact on lung function and relates it to critical changes in cellular and tissue scale biochemical changes.

VI.2.3 Linking nanoparticle property to biological impact

Since the emergence of the field of nanotoxicology about a decade ago, one of the major challenges has been to relate the biological effects of nanoparticles to their diverse physicochemical properties [14, 13]. As pointed out in Chapter I, the multiple tunable properties of ENMs, which make their innovative applications possible, also lead to unpredictable scenarios once they enter biological systems. The model developed and applied in this Thesis considers all the important properties of the ENMs explicitly and has expressed various biological and physical mechanisms, including cellular uptake, phagocytosis, surfactant binding, protein adsorption, ENM agglomeration, etc. as functions of key ENM properties such as size, density, surface zeta potential, coating chemistry, etc. Linking nanoparticle properties to potential biological impact, while considering key NP transformation processes, is a major step towards identifying potential hazards and the ensuing development of safe nanotechnologies [19, 22].

Overall, it can be said that the model developed and implemented in this Thesis represents substantial progress in the evolution of tools and methods for high-throughput predictive toxicity assessment of xenobiotics. This paradigm for toxicological risk assessment of chemicals follows the directions provided by the National Research Council (NRC) [45] in the report "Toxicity testing in the 21st century: a vision and a strategy". This approach has also been proposed for the field of nanotoxicology [14], for the purpose of integrating diverse types of mechanistic information collected *in vitro* and *in vivo*, and forms an essential step towards human health risk assessments of these novel materials.

VI.3 Future Research Directions

Ongoing and future work should include development of an inflammatory effects module (as described briefly for alveolar macrophages in Chapter IV) and inclusion of the

module as part of the set of toxicodynamic modules developed for humans to provide estimates of risk for populations exposed to inhaled nanoparticles. In detail, future work should consist of the following items:

Immune response module development and evaluation: One of the major effects of particulate exposure in the lungs is immune response. However, a comprehensive computational model of immune response *in vivo* must involve multiple cell types (macrophages, neutrophils, eosionophils, etc.) and biochemical molecules (cytokines, chemokines, etc.) and also include pathways of interaction among the cell types (shown schematically in Figure IV.4). Inflammatory response was modeled for a single cell type (macrophages) in an *in vitro* system as an example. The model will be extended to the *in vivo* system along with measurements for other cell types and cytokines from collaborative groups. It will involve inter-cellular signalling, and key pro-inflammatory cytokines such as TNF-α, IL-2, IL-6, IL-8 and anti-inflammatory cytokines such as IL-10.

Incorporation of dynamic breathing process modeling function: The model described in this Thesis considered normal breathing maneuvers at a positive end expiratory pressure (PEEP) of 3, which was used as an ideal case. However, realistic scenarios involving ENM inhalation exposure shall include many variations of this idealized scenario. The lung mechanics model should be extended to include dynamic breathing processes and the effect of PEEP in alleviating or exacerbating the impact of ENMs.

Incorporation of new modules for integrative framework: The modules developed and implemented in this Thesis must be incorporated into an exploratory "whole human body" version of the integrative toxicokinetic and toxicodynamic modeling framework for characterization of risks associated with

realistic ENM exposure scenarios, such as usage of consumer products containing ENMs.

VI.4 Translational research

The model developed in this Thesis is not only important for the assessment of nanotoxicological health risks but also represents an important step towards forming a computational description of multiscale human pulmonary dynamics. The pulmonary system is a target for a diverse array of chemicals, both intentionally as well as unintentionally. Inhalation exposures to particulate matter is a reality which has been recognized long before the advent of nanotechnology. Inhalation exposure to smoke, fumes, dust, pollen, and a host of other particulate matter leads to a spectrum of health effects in humans of all ages. The multiscale approach described in this Thesis would be valuable in understanding cell and tissue scale mechanisms associated with various pulmonary diseases such as asthma, COPD, bronchitis, etc. all of which are exacerbated due to inhalation of particulate matter [233]. Most of the observable symptoms associated with these disorders, such as breathlessness, wheezing, emphysema, and coughing, have biochemical origins and are influenced by the presence of inhaled particulate matter [234, Chaps. 9,10,11]. The modeling framework described in this Thesis can be translated to develop predictive models for individuals with specific pathophysiological conditions of the lungs. It can also be used to study the effects of various biochemical parameters at the cellular or tissue scale on the overall pulmonary function under various diseased conditions. The complex relationships between various cellular and tissue parameters, and their relative contribution towards specific disorders, can be unravelled using modeling tools such as the ones described in this thesis.

ENMs are, in general, investigated not only for their potential toxic effects but also for their applicability as drug delivery vehicles [235]. ENMs have led to the

development of the field of "Nanomedicine," which has tried to leverage the multiple tunable properties of ENMs at the nano scale to ensure targeted drug delivery with better efficiency and lower side effects. Biodistribution, clearance, and cellular uptake of ENMs depend on their physico-chemical properties [236]. ENMs can be used for targeted delivery of genes, proteins, and other large biomolecules which cannot be delivered in their native forms. Nanoparticle drug delivery vehicles also make it possible for drugs and biologics to pass certain impenetrable biological barriers like the blood-brain barrier or capillary fenestrations. However, this also requires nano scale modifications of the ENM properties such as size, surface coating, zeta potential, etc., to ensure decreased opsonization and targeting by various phagocytic cells [236]. The model described in this Thesis explicitly considers ENM surface chemistries and their interactions with surfactant proteins, which affect their cellular uptake, and eventually the overall tissue and physiome scale impact. This multiscale approach is necessary in order to understand the effect of nano scale modifications on the ENM-drug delivery devices which could result in better cellular uptake by the target tissue and decreased phagocytosis. ENMs designed for use in consumer products however tend to have an opposite set of requirements: Consumer products require to be safe by design and ENMs to be used for such products must be engineered for faster clearance and enhanced phagocytosis. The computational modules developed in this Thesis can provide unique insights into the design of ENMs for use as pharmaceutics as well as consumer products, to ensure either targeted uptake or minimized health impact, as the case may be.

VI.5 Publications

Articles published

- Mukherjee D., Botelho D., Gow A., Zhang, J., and Georgopoulos P.G. (2013). Computational Toxicodynamic Modeling of Silver and Carbon Nanoparticle Effects on Mouse Lung Function, *PLoS One*, 8(12).

- Mukherjee D., Leo B.F., Royce S.G., Porter A.E., Ryan M.P., Schwander S., Chung K.F., Tetley T.D., Zhang J. and Georgopoulos P.G. (2014). Modeling physicochemical interactions affecting in vitro cellular dosimetry of engineered nanomaterials: application to nanosilver, *Journal of Nanoparticle Research*, 16(10), 2616.

- Mukherjee D., Royce S.G., Sarkar S., Thorley A., Schwander S., Ryan M.P., Porter A.E., Chung K.F., Tetley T.D., Zhang J. and Georgopoulos P.G. (2014). Modeling in vitro cellular responses to silver nanoparticles, *Journal of Toxicology*.

- Royce S.G., Mukherjee D., Cai T., Xu S.S., Alexander J.A., Mi Z., Calderon L., Mainelis G., Lee K., Lioy P.J., Tetley T.D., Chung K.F., Zhang J. and Georgopoulos P.G. (2014). Modeling population exposures to silver nanoparticles present in consumer products, *Journal of Nanoparticle Research*, 16(11), 2724.

Articles under internal review

- Mukherjee D., Porter A.E., Ryan M.P., Schwander S., Chung K.F., Tetley T.D., Zhang J. and Georgopoulos P.G., Modeling In Vivo Interactions of Engineered Nanomaterials in the Pulmonary Alveolar Lining. (under internal review, to be submitted to *Nanomaterials*)

- Mukherjee D., Botelho D., Seiffert, J., Smith, R., Gow A., Porter A.E., Ryan

M.P., Chung K.F., Tetley T.D., Zhang J. and Georgopoulos P.G., Multiscale Computational Modeling of Dynamic Effects of Nanoparticle Exposure on Rodent Pulmonary Dynamics (under internal review, to be submitted to *PLoS One*)

References

[1] ACC. Consideration for a Definition for Engineered Nanomaterials. Technical report, The American Chemistry Council - Nanotechnology Panel, Arlington, VA, 2007.

[2] G. Oberdorster, A. B. Kane, R. D. Klaper, and R. H. Hurt. Nanotoxicology. In C. D. Klaassen, editor, *Casarett and Doull's toxicology: the basic science of poisons*, chapter 28. McGraw-Hill Education, New York, 2013.

[3] ISO. Environmental management - life cycle assessment - requirements and guidelines. International Standardization Organisation (ISO), 2006.

[4] A. Fairbrother and J. R. Fairbrother. Are environmental regulations keeping up with innovation? A case study of the nanotechnology industry. *Ecotoxicology and Environmental Safety*, 72(5):1327–1330, 2009.

[5] K. Aschberger, C. Micheletti, B. Sokull-Klttgen, and F. M. Christensen. Analysis of currently available data for characterising the risk of engineered nanomaterials to the environment and human health Lessons learned from four case studies. *Environment International*, 37(6):1143–1156, 2011.

[6] P. V. AshaRani, G. L. K. Mun, M. P. Hande, and S. Valiyaveettil. Cytotoxicity and Genotoxicity of Silver Nanoparticles in Human Cells. *ACS Nano*, 3(2): 279–290, Feb 2009.

[7] C. Carlson, S. M. Hussain, A. M. Schrand, L. K. Braydich-Stolle, K. L. Hess, R. L. Jones, and J. J. Schlager. Unique cellular interaction of silver nanoparticles: size-dependent generation of reactive oxygen species. *J Phys Chem B*, 112(43):13608–19, Oct 30 2008.

[8] R. Foldbjerg, D. A. Dang, and H. Autrup. Cytotoxicity and genotoxicity of silver nanoparticles in the human lung cancer cell line, A549. *Arch Toxicol*, Apr 29 2010.

[9] H. Johnston, G. Hutchison, F. Christensen, S. Peters, S. Hankin, and V. Stone. A review of the in vivo and in vitro toxicity of silver and gold particulates: Particle attributes and biological mechanisms responsible for the observed toxicity. *Critical Reviews in Toxicology*, 40(4):328–346, 2010.

[10] PEN. The project on emerging nanotechnologies, 2014.

[11] F. Gottschalk, T. Sonderer, R. W. Scholz, and B. Nowack. Modeled Environmental Concentrations of Engineered Nanomaterials (TiO2, ZnO, Ag, CNT, Fullerenes) for Different Regions. *Environmental Science & Technology*, 43(24): 9216–9222, December 2009.

[12] K. Donaldson, V. Stone, C. Tran, W. Kreyling, and P. Borm. Nanotoxicology. *Occupational and Environmental Medicine*, 61(9):727–728, 2004.

[13] G. Oberdorster, A. Maynard, K. Donaldson, V. Castranova, J. Fitzpatrick, K. Ausman, J. Carter, B. Karn, W. Kreyling, D. Lai, S. Olin, N. Monteiro-Riviere, D. Warheit, and H. Yang. Principles for characterizing the potential human health effects from exposure to nanomaterials: elements of a screening strategy. *Part Fibre Toxicol*, 2:8, Oct 6 2005.

[14] A. D. Maynard, R. J. Aitken, T. Butz, V. Colvin, K. Donaldson, G. Oberdorster, M. A. Philbert, J. Ryan, A. Seaton, V. Stone, S. S. Tinkle, L. Tran, N. J. Walker, and D. B. Warheit. Safe handling of nanotechnology. *Nature*, 444 (7117):267–269, 2006.

[15] A. Maynard. Nanotoxicology: Laying a firm foundation for sustainable nanotechnologies. In N. Monteiro-Riviere and C. Tran, editors, *Nanotoxicology - Characterization, Dosing, and Health Effects*, chapter 1. Informa Healthcare, New York, 2007.

[16] V. L. Colvin. The potential environmental impact of engineered nanomaterials. *Nat Biotechnol*, 21(10):1166–70, Oct 2003.

[17] E. S. Money, K. H. Reckhow, and M. R. Wiesner. The use of Bayesian networks for nanoparticle risk forecasting: Model formulation and baseline evaluation. *Science of The Total Environment*, 426(0):436–445, 2012.

[18] A. Praetorius, M. Scheringer, and K. Hungerbuehler. Development of Environmental Fate Models for Engineered NanoparticlesA Case Study of TiO2 Nanoparticles in the Rhine River. *Environmental Science & Technology*, 46 (12):6705–6713, 2012.

[19] S. W. Wijnhoven, W. J. Peijnenburg, C. A. Herberts, W. I. Hagens, A. G. Oomen, E. H. Heugens, B. Roszek, J. Bisschops, I. Gosens, D. Van De Meent, S. Dekkers, W. H. De Jong, M. van Zijverden, A. J. Sips, and R. E. Geertsma. Nano-silver - a review of available data and knowledge gaps in human and environmental risk assessment. *Nanotoxicology*, 3(2):109–138, 2009.

[20] C. O. Hendren, X. Mesnard, J. Droge, and M. R. Wiesner. Estimating Production Data for Five Engineered Nanomaterials As a Basis for Exposure Assessment. *Environmental Science & Technology*, 45(7):2562–2569, 2011.

[21] RCEP. Novel materials in the environment: The case of nanotechnology, 2008.

[22] USEPA. U.s. environmental protection agency - nanotechnology white paper, 2007.

[23] E. Commission. Nanosciences and nanotechnologies: An action plan for europe 2005-2009. European Communities, 2005.

[24] X. Li, J. J. Lenhart, and H. W. Walker. Dissolution-Accompanied Aggregation Kinetics of Silver Nanoparticles. *Langmuir*, 26(22):16690–16698, 2010.

[25] T. Benn and P. Westerhoff. Nanoparticle Silver Released into Water from Commercially Available Sock Fabrics. *Environmental Science & Technology*, 42(11): 4133–4139, 2008.

[26] M. E. Quadros and L. C. Marr. Silver Nanoparticles and Total Aerosols Emitted by Nanotechnology-Related Consumer Spray Products. *Environmental Science & Technology*, 45(24):10713–10719, 2011.

[27] Y. Nazarenko, T. W. Han, P. J. Lioy, and G. Mainelis. Potential for exposure to engineered nanoparticles from nanotechnology-based consumer spray products. *Journal of Exposure Science and Environmental Epidemiology*, 21(5):515–28, Sep-Oct 2011.

[28] S. Royce, D. Mukherjee, T. Cai, S. Xu, J. Alexander, Z. Mi, L. Calderon, G. Mainelis, K. Lee, P. Lioy, T. Tetley, K. Chung, J. Zhang, and P. Georgopoulos. Modeling population exposures to silver nanoparticles present in consumer products. *Journal of Nanoparticle Research*, 16(11):1–25, 2014.

[29] P. Georgopoulos. A Multiscale Approach for Assessing the Interactions of Environmental and Biological Systems in a Holistic Health Risk Assessment Framework. *Water, Air, & Soil Pollution: Focus*, 8(1):3–21, 2008.

[30] Y. Song, X. Li, and X. Du. Exposure to nanoparticles is related to pleural effusion, pulmonary fibrosis and granuloma. *Eur Respir J*, 34(3):559–67, Sep 2009.

[31] C. Schleh, C. Muhlfeld, K. Pulskamp, A. Schmiedl, and Others. The effect of titanium dioxide nanoparticles on pulmonary surfactant function and ultrastructure. *Respiratory Research*, 10(90):1–11, 2009.

[32] C. Salvador-Morales, P. Townsend, E. Flahaut, C. Venien-Bryan, A. Vlandas, M. L. H. Green, and R. B. Sim. Binding of pulmonary surfactant proteins to carbon nanotubes; potential for damage to lung immune defense mechanisms. *Carbon*, 45(3):607–617, Mar 2007.

[33] S. Takenaka, E. Karg, C. Roth, H. Schulz, and Others. Pulmonary and Systemic Distribution of Inhaled Ultrafine Silver Particles in Rats. *Environmental Health Perspectives*, 109(suppl. 4), 2001.

[34] L. MacCalman, C. Tran, and E. Kuempel. Development of a bio-mathematical model in rats to describe clearance, retention and translocation of inhaled nano particles throughout the body. *Journal of Physics: Conference Series*, 151: 1–10, 2009.

[35] M. L. Shelley, A. J. Wagner, S. M. Hussain, and C. Bleckmann. Modeling the In Vivo Case with In Vitro Nanotoxicity Data. *International Journal of Toxicology*, 27(5):359–367, 2008.

[36] E. Frohlich and S. Salar-Behzadi. Toxicological assessment of inhaled nanoparticles: role of in vivo, ex vivo, in vitro, and in silico studies. *Int J Mol Sci*, 15 (3):4795–822, 2014.

[37] S. Sarkar, Y. Song, H. M. Kipen, R. J. Laumbach, J. Zhang, P. A. Strickland, C. R. Gardner, and S. Schwander. Suppression of the NF-kappaB pathway by diesel exhaust particles impairs human antimycobacterial immunity. *J Immunol*, 188(6):2778–93, Mar 15 2012.

[38] G. Oberdorster, E. Oberdorster, and J. Oberdorster. Nanotoxicology: an emerging discipline evolving from studies of ultrafine particles. *Environ Health Perspect*, 113(7):823–39, Jul 2005.

[39] B. F. Leo, S. Chen, Y. Kyo, K.-L. Herpoldt, N. J. Terrill, I. E. Dunlop, D. S. McPhail, M. S. Shaffer, S. Schwander, A. Gow, J. Zhang, K. F. Chung, T. D. Tetley, A. E. Porter, and M. P. Ryan. The Stability of Silver Nanoparticles in a Model of Pulmonary Surfactant. *Environmental Science & Technology*, 47(19): 11232–11240, 2013.

[40] M. Tejamaya, I. Romer, R. C. Merrifield, and J. R. Lead. Stability of Citrate, PVP, and PEG Coated Silver Nanoparticles in Ecotoxicology Media. *Environmental Science & Technology*, 2012.

[41] P. M. Hinderliter, K. R. Minard, G. Orr, W. B. Chrisler, B. D. Thrall, J. G. Pounds, and J. G. Teeguarden. ISDD: A computational model of particle sedimentation, diffusion and target cell dosimetry for in vitro toxicity studies. *Part Fibre Toxicol*, 7(1):36, 2010.

[42] D. Mukherjee, B. Leo, S. Royce, A. Porter, M. Ryan, S. Schwander, K. Chung, T. Tetley, J. Zhang, and P. Georgopoulos. Modeling physicochemical interactions affecting in vitro cellular dosimetry of engineered nanomaterials: application to nanosilver. *Journal of Nanoparticle Research*, 16(10):1–16, 2014.

[43] X. Wang, Z. Ji, C. H. Chang, H. Zhang, M. Wang, Y.-P. Liao, S. Lin, H. Meng, R. Li, B. Sun, L. V. Winkle, K. E. Pinkerton, J. I. Zink, T. Xia, and A. E. Nel. Use of Coated Silver Nanoparticles to Understand the Relationship of Particle Dissolution and Bioavailability to Cell and Lung Toxicological Potential. *Small*, 10(2):385–398, 2014.

[44] D. Mukherjee, S. G. Royce, S. Sarkar, A. Thorley, S. Schwander, M. P. Ryan, A. E. Porter, K. F. Chung, T. D. Tetley, J. Zhang, and P. G. Georgopoulos. Modeling In Vitro Cellular Responses to Silver Nanoparticles. *Journal of Toxicology*, 2014:13, 2014.

[45] NRC. Toxicity Testing in the 21st Century: A Vision and a Strategy. Technical report, National Research Council, Washington D.C., 2007.

[46] D. M. Moss and M. Siccardi. Optimizing nanomedicine pharmacokinetics using physiologically based pharmacokinetics modelling. *British Journal of Pharmacology*, 171(17):3963–3979, 2014.

[47] D. Lankveld, A. G. Oomen, P. Krystek, *et al.* The kinetics of the tissue distribution of silver nanoparticles of different sizes. *Biomaterials*, 31:8350–8361, 2010.

[48] R. Landsiedel, E. Fabian, L. Ma-Hock, B. van Ravenzwaay, W. Wohlleben, K. Wiench, and F. Oesch. Toxico-/biokinetics of nanomaterials. *Arch Toxicol*, 86(7):1021–60, 2012.

[49] P. Lin, J.-W. Chen, L. W. Chang, J.-P. Wu, *et al.* Computational and Ultrastructural Toxicology of a Nanoparticle, Quantum Dot 705, in Mice. *Environmental Science & Technology*, 42(16):6264–6270, 2008.

[50] H. A. Lee, T. L. Leavens, S. E. Mason, N. A. Monteiro-Riviere, and J. E. Riviere. Comparison of Quantum Dot Biodistribution with a Blood-Flow-Limited Physiologically Based Pharmacokinetic Model. *Nano Letters*, 9(2):794–799, 2009.

[51] A. R. Pery, C. Brochot, P. H. Hoet, A. Nemmar, and F. Y. Bois. Development of a physiologically based kinetic model for 99m-Technetium-labelled carbon nanoparticles inhaled by humans. *Inhal Toxicol*, 21(13):1099–107, Nov 2009.

[52] M. Trop, M. Novak, S. Rodl, B. Hellbom, W. Kroell, and W. Goessler. Silver coated dressing Acticoat caused raised liver enzymes and argyria-like symptoms in burn patient. *Journal of Trauma-Injury Infection and Critical Care*, 60(3): 648–652, Mar 2006.

[53] E. Vlachou, E. Chipp, E. Shale, Y. T. Wilson, R. Papini, and N. S. Moiemen. The safety of nanocrystalline silver dressings on burns: a study of systemic silver absorption. *Burns*, 33(8):979–85, Dec 2007.

[54] A. K. Kohli and H. O. Alpar. Potential use of nanoparticles for transcutaneous vaccine delivery: effect of particle size and charge. *Int J Pharm*, 275(1-2):13–7, May 4 2004.

[55] F. F. Larese, F. D'Agostin, M. Crosera, G. Adami, N. Renzi, M. Bovenzi, and G. Maina. Human skin penetration of silver nanoparticles through intact and damaged skin. *Toxicology*, 255(1-2):33–37, 2009.

[56] M. Schneider, F. Stracke, S. Hansen, and U. F. Schaefer. Nanoparticles and their interactions with the dermal barrier. *Dermatoendocrinol*, 1(4):197–206, Jul 2009.

[57] J. Kreuter, M. Nefzger, E. Liehl, R. Czok, and R. Voges. Distribution and elimination of poly(methyl methacrylate) nanoparticles after subcutaneous administration to rats. *Journal of Pharmaceutical Sciences*, 72(10):1146–1149, 1983.

[58] S. Mirsattari, R. Hammond, M. Sharpe, F. Leung, and G. Young. Myoclonic status epilepticus following repeated oral ingestion of colloidal silver. *Neurology*, 62(8):1408–1410, 2004.

[59] A. L. Chang, V. Khosravi, and B. Egbert. A case of argyria after colloidal silver ingestion. *J Cutan Pathol*, 33(12):809–11, Dec 2006.

[60] Y. S. Kim, J. S. Kim, H. S. Cho, D. S. Rha, J. M. Kim, J. D. Park, B. S. Choi, R. Lim, H. K. Chang, Y. H. Chung, I. H. Kwon, J. Jeong, B. S. Han, and I. J. Yu. Twenty-eight-day oral toxicity, genotoxicity, and gender-related tissue distribution of silver nanoparticles in Sprague-Dawley rats. *Inhal Toxicol*, 20 (6):575–83, Apr 2008.

[61] R. Gibbs. *Silver Colloids: Do They Work?* 1999.

[62] J. F. Hillyer and R. M. Albrecht. Gastrointestinal persorption and tissue distribution of differently sized colloidal gold nanoparticles. *Journal of Pharmaceutical Sciences*, 90(12):1927–1936, 2001.

[63] N. Hussain, V. Jaitley, and A. T. Florence. Recent advances in the understanding of uptake of microparticulates across the gastrointestinal lymphatics. *Advanced Drug Delivery Reviews*, 50(1-2):107–142, 2001.

[64] H. S. Choi, Y. Ashitate, J. H. Lee, S. H. Kim, A. Matsui, N. Insin, M. G. Bawendi, M. Semmler-Behnke, J. V. Frangioni, and A. Tsuda. Rapid translocation of nanoparticles from the lung airspaces to the body. *Nat Biotech*, 28 (12):1300–1303, 2010.

[65] G. Oberdorster. Pulmonary effects of inhaled ultrafine particles. *Int Arch Occup Environ Health*, 74(1):1–8, Jan 2001.

[66] J. H. Ji, J. H. Jung, S. S. Kim, J. U. Yoon, J. D. Park, B. S. Choi, Y. H. Chung, I. H. Kwon, J. Jeong, B. S. Han, J. H. Shin, J. H. Sung, K. S. Song, and I. J. Yu. Twenty-eight-day inhalation toxicity study of silver nanoparticles in Sprague-Dawley rats. *Inhal Toxicol*, 19(10):857–71, 2007.

[67] M. Lazaridis, D. M. Broday, O. Hov, and P. G. Georgopoulos. Integrated exposure and dose modeling and analysis system. 3. Deposition of inhaled particles in the human respiratory tract. *Environ Sci Technol*, 35(18):3727–34, Sep 15 2001.

[68] L. B. Mendez, G. Gookin, and R. F. Phalen. Inhaled aerosol particle dosimetry in mice: A review. *Inhalation Toxicology*, 22(12):1032–1037, 2010.

[69] RIVM. Multiple Path Particle Dosimetry Model (MPPD v 1.0): A Model for Human and Rat Airway Particle Dosimetry. Technical report, National Institute for Public Health and the Environment (RIVM), Bilthoven, The Netherlands, 2002.

[70] I. C. o. R. P. ICRP. Human respiratory tract model for radiological protection. A report of a Task Group of International Commission on Radiological Protection. . *Annals of the ICRP*, 24:1–482, 1995.

[71] CIIT. Multiple path particle dosimetry model (mppd v 2.0): A model for human and rat airway particle dosimetry. CIIT Centers for Health Research, 2006.

[72] O. G. Raabe, M. A. Al-Bayati, S. V. Teague, and A. Rasolt. Regional Deposition of Inhaled Monodisperse Coarse and Fine Aerosol Particles in Small Laboratory Animals. *Annals of Occupational Hygiene*, 32(inhaled particles VI):53–63, 1988.

[73] A. B. Lansdown. Controversies over colloidal silver. *J Wound Care*, 12(3):120, Mar 2003.

[74] L. Stebounova, E. Guio, and V. Grassian. Silver nanoparticles in simulated biological media: a study of aggregation, sedimentation, and dissolution. *Journal of Nanoparticle Research*, 13(1):233–244, 2011.

[75] C.-M. Ho, S. K.-W. Yau, C.-N. Lok, M.-H. So, and C.-M. Che. Oxidative Dissolution of Silver Nanoparticles by Biologically Relevant Oxidants: A Kinetic and Mechanistic Study. *Chemistry An Asian Journal*, 5(2):285–293, 2010.

[76] H. Choi, W. Liu, P. Misra, E. Tanaka, J. P. Zimmer, B. Itty Ipe, M. G. Bawendi, and J. V. Frangioni. Renal clearance of quantum dots. *Nat Biotech*, 25(10): 1165–1170, 2007.

[77] K. Avgoustakis, A. Beletsi, Z. Panagi, P. Klepetsanis, E. Livaniou, G. Evangelatos, and D. S. Ithakissios. Effect of copolymer composition on the physicochemical characteristics, in vitro stability, and biodistribution of PLGA-mPEG nanoparticles. *International Journal of Pharmaceutics*, 259(1-2):115–127, 2003.

[78] K. Furumoto, K.-i. Ogawara, M. Yoshida, Y. Takakura, M. Hashida, K. Higaki, and T. Kimura. Biliary excretion of polystyrene microspheres depends on the type of receptor-mediated uptake in rat liver. *Biochimica et Biophysica Acta (BBA) - General Subjects*, 1526(2):221–226, 2001.

[79] G. Bachler, N. von Goetz, and K. Hungerbuhler. A physiologically based pharmacokinetic model for ionic silver and silver nanoparticles. *Int J Nanomedicine*, 8:3365–82, 2013.

[80] S. Shah. Numerical Simulation of Particle Adhesion Dynamics for Applications in Nanomedicine and Biosensing, 2009.

[81] J. P. Davda, M. Jain, S. K. Batra, P. R. Gwilt, and D. H. Robinson. A physiologically based pharmacokinetic (PBPK) model to characterize and predict the disposition of monoclonal antibody CC49 and its single chain Fv constructs. *International Immunopharmacology*, 8(3):401–413, 2008.

[82] G. Orr, D. J. Panther, J. L. Phillips, B. J. Tarasevich, A. Dohnalkova, D. Hu, J. G. Teeguarden, and J. G. Pounds. Submicrometer and nanoscale inorganic particles exploit the actin machinery to be propelled along microvilli-like structures into alveolar cells. *ACS Nano*, 1(5):463–75, Dec 2007.

[83] D. Su, R. Ma, M. Salloum, and L. Zhu. Multi-scale study of nanoparticle transport and deposition in tissues during an injection process. *Medical & Biological Engineering & Computing*, 48:853–863, 2010.

[84] P. Decuzzi and M. Ferrari. The receptor-mediated endocytosis of nonspherical particles. *Biophys J*, 94(10):3790–7, May 15 2008.

[85] S. D. Conner and S. L. Schmid. Regulated portals of entry into the cell. *Nature*, 422(6927):37–44, 2003.

[86] L. Mullins. An analysis of pore size in excitable membranes. *Journal of General Physiology*, 43:105–117, 1960.

[87] P. Poulin and F. Theil. Prediction of Pharmacokinetics prior to In Vivo studies.II. Generic Physiologically Based Pharmacokinetic Models of Drug Disposition. *Journal of Pharmaceutical Sciences*, 91(5), 2002.

[88] H. Hess and Y. Tseng. Active Intracellular Transport of Nanoparticles: Opportunity or Threat? *ACS Nano*, 1(5):390–392, 2007.

[89] L. K. Limbach, Y. Li, R. N. Grass, T. J. Brunner, M. A. Hintermann, M. Muller, D. Gunther, and W. J. Stark. Oxide nanoparticle uptake in human lung fibroblasts: effects of particle size, agglomeration, and diffusion at low concentrations. *Environ Sci Technol*, 39(23):9370–6, Dec 1 2005.

[90] M. Mason and W. Weaver. The Settling of Small Particles in a Fluid. *Physical Review*, 23(3):412–426, 1924.

[91] D. M. Broday and P. G. Georgopoulos. Growth and Deposition of Hygroscopic Particulate Matter in the Human Lungs. *Aerosol Science and Technology*, 34 (1):144–159, 2001.

[92] H. Zhao, A. Maisels, T. Matsoukas, and C. Zheng. Analysis of four Monte Carlo methods for the solution of population balances in dispersed systems. *Powder Technology*, 173(1):38–50, 2007.

[93] H. H. Liu, S. Surawanvijit, R. Rallo, G. Orkoulas, and Y. Cohen. Analysis of Nanoparticle Agglomeration in Aqueous Suspensions via Constant-Number Monte Carlo Simulation. *Environmental Science & Technology*, 45:9284–9292, 2011.

[94] E.-J. Park, J. Yi, Y. Kim, K. Choi, and K. Park. Silver nanoparticles induce cytotoxicity by a Trojan-horse type mechanism. *Toxicology in Vitro*, 24(3): 872–878, 2010.

[95] Y. Tabata and Y. Ikada. Effect of the size and surface charge of polymer microspheres on their phagocytosis by macrophage. *Biomaterials*, 9(4):356–362, 1988.

[96] R. B. Bird, W. E. Stewart, and E. N. Lightfoot. *Transport Phenomena*. John Wiley and Sons, New York, 1 edition, 1960.

[97] M. Kajihara. Settling Velocity and Porosity of Large Suspended Particle. *Journal of the Oceanographical Society of Japan*, 27(4):158–162, 1971.

[98] M. C. Sterling Jr, J. S. Bonner, A. N. S. Ernest, C. A. Page, and R. L. Autenrieth. Application of fractal flocculation and vertical transport model to aquatic solsediment systems. *Water Research*, 39(9):1818–1830, 2005.

[99] R. J. Hunter. *Foundations of Colloid Science*. Oxford University Press, New York, 2001.

[100] D. N. L. McGown and G. D. Parfitt. Improved Theoretical Calculation of the Stability Ratio for Colloidal Systems. *Journal of Physical Chemistry*, 71(2): 449–450, 1967.

[101] J. Gregory. Approximate Expressions for Retarded van der Waals Interaction. *Journal of Colloid and Interface Science*, 83(1):138–145, 1981.

[102] J. Gregory. Interaction of Unequal Double Layers at Constant Charge. *Journal of Colloid and Interface Science*, 51(1):44–51, 1975.

[103] W. Zhang, Y. Yao, N. Sullivan, and Y. Chen. Modeling the primary size effects of citrate-coated silver nanoparticles on their ion release kinetics. *Environ Sci Technol*, 45(10):4422–8, May 15 2011.

[104] W. Zhang, Y. Yao, K. Li, Y. Huang, and Y. Chen. Influence of dissolved oxygen on aggregation kinetics of citrate-coated silver nanoparticles. *Environmental Pollution*, 159(12):3757–3762, 2011.

[105] H. Fogler. *Elements of Chemical Reaction Engineering*. Prentice Hall, 4 edition, 2005.

[106] F. E. Kruis, A. Maisels, and H. Fissan. Direct simulation Monte Carlo method for particle coagulation and aggregation. *AIChE Journal*, 46(9):1735–1742, 2000.

[107] E. D. Hollander, J. J. Derksen, O. S. L. Bruinsma, H. E. A. van den Akker, and G. M. van Rosmalen. A numerical study on the coupling of hydrodynamics and orthokinetic agglomeration. *Chemical Engineering Science*, 56(7):2531–2541, 2001.

[108] K. A. Huynh and K. L. Chen. Aggregation Kinetics of Citrate and Polyvinylpyrrolidone Coated Silver Nanoparticles in Monovalent and Divalent Electrolyte Solutions. *Environmental Science & Technology*, 45(13):5564–5571, 2011.

[109] M. L. Zheludkevich, A. G. Gusakov, A. G. Voropaev, A. A. Vecher, E. N. Kozyrski, and S. A. Raspopov. Studies of the surface oxidation of silver by atomic oxygen. In J. Kleiman and Z. Iskanderova, editors, *Protection of Materials and Structures from Space Environment*, volume 5 of *Space Technology Proceedings*, chapter 30, pages 351–358. Springer Netherlands, 2003.

[110] M. Delay, T. Dolt, A. Woellhaf, R. Sembritzki, and F. H. Frimmel. Interactions and stability of silver nanoparticles in the aqueous phase: Influence of natural organic matter (NOM) and ionic strength. *J Chromatogr A*, 1218(27):4206–12, Jul 8 2011.

[111] S. Salgin, U. Salgin, and S. Bahadir. Zeta Potentials and Isoelectric Points of Biomolecules: The Effects of Ion Types and Ionic Strengths. *International Journal of Electrochemical Science*, 7:12404–12414, 2012.

[112] M. G. Carneiro-da Cunha, M. A. Cerqueira, B. W. S. Souza, J. A. Teixeira, and A. A. Vicente. Influence of concentration, ionic strength and pH on zeta potential and mean hydrodynamic diameter of edible polysaccharide solutions envisaged for multinanolayered films production. *Carbohydrate Polymers*, 85 (3):522–528, 2011.

[113] Y. Song, J. Thiagarajah, and A. S. Verkman. Sodium and Chloride Concentrations, pH, and Depth of Airway Surface Liquid in Distal Airways. *Journal of General Physiology*, 122:511–519, 2003.

[114] J. Goerke. Pulmonary surfactant: functions and molecular composition. *Biochimica et Biophysica Acta (BBA) - Molecular Basis of Disease*, 1408(2-3):79–89, 1998.

[115] R. H. Notter. *Lung Surfactants: Basic Science and Clinical Applications*, volume 149 of *Lung Biology in Health and Disease*. Marcel Dekker, New York, 2000.

[116] L. A. J. M. Creuwels, L. M. G. van Golde, and H. P. Haagsman. The Pulmonary Surfactant System: Biochemical and Clinical Aspects. *Lung*, 175(1):1–39, 1997.

[117] FIOSH. Dispersion and Retention of Dusts Consisting of Ultrafine Primary Particles in Lungs. Technical report, Federal institute for Occupational Safety and Health, Dortmund, Germany, 2011.

[118] M. Kendall, L. Brown, and K. Trought. Molecular Adsorption at Particle Surfaces: A PM Toxicity Mediation Mechanism. *Inhalation Toxicology*, 16(s1): 99–105, 2004.

[119] I. A. Mudunkotuwa and V. H. Grassian. Citric Acid Adsorption on TiO2 Nanoparticles in Aqueous Suspensions at Acidic and Circumneutral pH: Surface Coverage, Surface Speciation, and Its Impact on Nanoparticle Interactions. *Journal of the American Chemical Society*, 132(42):14986–14994, 2010.

[120] M. Kendall, T. D. Tetley, E. Wigzell, B. Hutton, M. Nieuwenhuijsen, and P. Luckham. *Lung lining liquid modifies PM2.5 in favor of particle aggregation: a protective mechanism*, volume 282. 2002.

[121] F. Blank, B. M. Rothen-Rutishauser, S. Schurch, and P. Gehr. An optimized in vitro model of the respiratory tract wall to study particle cell interactions. *J Aerosol Med*, 19(3):392–405, 2006.

[122] M. S. Bakshi, L. Zhao, R. Smith, F. Possmayer, and N. O. Petersen. Metal nanoparticle pollutants interfere with pulmonary surfactant function in vitro. *Biophys J*, 94(3):855–68, 2008.

[123] C. Schleh and J. M. Hohlfeld. Interaction of nanoparticles with the pulmonary surfactant system. *Inhal Toxicol*, 21 Suppl 1:97–103, 2009.

[124] S. Mornet, O. Lambert, E. Duguet, and A. Brisson. The Formation of Supported Lipid Bilayers on Silica Nanoparticles Revealed by Cryoelectron Microscopy. *Nano Letters*, 5(2):281–285, 2005.

[125] V. P. Zhdanov, C. A. Keller, K. Glasmastar, and B. Kasemo. Simulation of adsorption kinetics of lipid vesicles. *The Journal of Chemical Physics*, 112(2): 900–909, 2000.

[126] V. P. Zhdanov and B. Kasemo. Protein adsorption and desorption on lipid bilayers. *Biophysical Chemistry*, 146(2-3):60, 2009.

[127] D. Stroumpoulis, A. Parra, and M. Tirrell. A Kinetic Study of Vesicle Fusion on Silicon Dioxide Surfaces by Ellipsometry. *AIChE Journal*, 52:2931–2937, 2006.

[128] N. J. Gross and K. R. Narine. *Surfactant subtypes of mice: metabolic relationships and conversion in vitro*, volume 67. 1989.

[129] G. Nordlund, R. Lnneborg, and P. Brzezinski. Formation of Supported Lipid Bilayers on Silica Particles Studied Using Flow Cytometry. *Langmuir*, 25(8): 4601–4606, 2009.

[130] J. H. Shannahan, R. Podila, A. A. Aldossari, H. Emerson, B. A. Powell, P. C. Ke, A. M. Rao, and J. M. Brown. Formation of a Protein Corona on Silver Nanoparticles Mediates Cellular Toxicity via Scavenger Receptors. *Toxicol Sci*, 2014.

[131] I. Lundstrom. Models of protein adsorption on solid surfaces. In B. Lindman, G. Olofsson, and P. Stenius, editors, *Surfactants, Adsorption, Surface Spectroscopy and Disperse Systems*, volume 70 of *Progress in Colloid & Polymer Science*, chapter 12, pages 76–82. Steinkopff, 1985.

[132] V. P. Zhdanov and B. Kasemo. Monte Carlo Simulation of the Kinetics of Protein Adsorption. *Proteins*, 30:177–182, 1998.

[133] T. Heimburg. Monte Carlo simulations of lipid bilayers and lipid protein interactions in the light of recent experiments. *Current Opinion in Colloid & Interface Science*, 5(34):224–231, 2000.

[134] S. Schurch, P. Gehr, V. Im Hof, M. Geiser, and F. Green. Surfactant displaces particles toward the epithelium in airways and alveoli. *Respir Physiol*, 80(1): 17–32, Apr 1990.

[135] S. Damodaran. *Food Proteins and Their Applications*. Food Science and Technology. CRC Press, 1997.

[136] Avanti polar lipids, inc. URL `www.avantilipids.com`.

[137] K. C. Meyer, A. Sharma, R. Brown, M. Weatherly, F. R. Moya, J. Lewandoski, and J. J. Zimmerman. Function and Composition of Pulmonary Surfactant and Surfactant-Derived Fatty Acid Profiles Are Altered in Young Adults With Cystic Fibrosis*. *Chest*, 118(1):164–174, 2000.

[138] P. Wilhelm and D. Stephan. On-line tracking of the coating of nanoscaled silica with titania nanoparticles via zeta-potential measurements. *Journal of Colloid and Interface Science*, 293(1):88–92, 2006.

[139] ARA. Multiple-path particle dosimetry model (mppd v 2.11) a model for human and rat airway particle dosimetry. Applied Research Associates, 2014.

[140] S. A. Shelley, M. V. L'Heureux, and J. U. Balis. Characterization of lung surfactant: factors promoting formation of artifactual lipid-protein complexes. *J Lipid Res*, 16(3):224–34, May 1975.

[141] A. C. Woodka, P. D. Butler, L. Porcar, B. Farago, and M. Nagao. Lipid Bilayers and Membrane Dynamics: Insight into Thickness Fluctuations. *Physical Review Letters*, 109(058102), 2012.

[142] J. Bastacky, C. Y. Lee, J. Goerke, H. Koushafar, D. Yager, L. Kenaga, T. P. Speed, Y. Chen, and J. A. Clements. Alveolar lining layer is thin and continuous: low-temperature scanning electron microscopy of rat lung. *J Appl Physiol*, 79 (5):1615–28, Nov 1995.

[143] H. Fischer, I. Polikarpov, and A. Craievich. Average protein density is a molecular-weight-dependent function. *Protein Science*, 13:2825–2828, 2004.

[144] M. E. Young, P. A. Carroad, and R. L. Bell. Estimation of diffusion coefficients of proteins. *Biotechnology and Bioengineering*, 22(5):947–955, 1980.

[145] D. Mukherjee, D. Botelho, A. J. Gow, J. Zhang, and P. G. Georgopoulos. Computational Multiscale Toxicodynamic Modeling of Silver and Carbon Nanoparticle Effects on Mouse Lung Function. *PLoS ONE*, 8(12):e80917, 2013.

[146] E. D. Kuempel, C.-L. Tran, R. J. Smith, and A. J. Bailer. A Biomathematical Model of Particle Clearance and Retention in the Lungs of Coal Miners: II. Evaluation of Variability and Uncertainty. *Regulatory Toxicology and Pharmacology*, 34(1):88–101, 2001.

[147] C. B. Massa, G. B. Allen, and J. H. Bates. Modeling the dynamics of recruitment and derecruitment in mice with acute lung injury. *J Appl Physiol*, 105(6): 1813–21, Dec 2008.

[148] J. Seiffert, F. Hussain, C. Wiegman, F. Li, L. Bey, W. Baker, A. Porter, M. P. Ryan, Y. Chang, A. Gow, J. Zhang, J. Zhu, T. D. Tetley, and K. F. Chung. Pulmonary Toxicity of Instilled Silver Nanoparticles: Influence of Size, Coating and Rat Strain. *PLoS ONE*, 10(3):e0119726, 2015.

[149] S. A. Rooney, S. L. Young, and C. R. Mendelson. Molecular and cellular processing of lung surfactant. *FASEB J*, 8(12):957–67, Sep 1994.

[150] J. Archie. A mathematical model for pulmonary mechanics: The alveolar surface contribution. *International Journal of Engineering Science*, 11(6):659–671, 1973.

[151] W. Z. Martini, D. L. Chinkes, R. E. Barrow, E. D. Murphey, and R. R. Wolfe. Lung surfactant kinetics in conscious pigs. *American Journal of Physiology - Endocrinology And Metabolism*, 277(1):E187–E195, July 1999.

[152] D. Froh, L. W. Gonzales, and P. L. Ballard. Secretion of Surfactant Protein A and Phosphatidylcholine from Type II Cells of Human Fetal Lung. *American Journal of Respiratory Cell and Molecular Biology*, 8(5):556–561, 1993.

[153] A. B. Fisher, C. Dodia, P. Ruckert, J. Q. Tao, and S. R. Bates. Pathway to lamellar bodies for surfactant protein A. *American Journal of Physiology - Lung Cellular and Molecular Physiology*, 299:L51–L58, 2010.

[154] B. Robertson, L. M. G. Van Golde, and J. J. Batenburg, editors. *Pulmonary Surfactant: From Molecular Biology to Clinical Practice*. Elsevier Science Publishers, Amsterdam, 1992.

[155] J. R. Wright and L. G. Dobbs. Regulation of Pulmonary Surfactant Secretion and Clearance. *Annual Review of Physiology*, 53(1):395–414, 1991.

[156] O. Gurel, M. Ikegami, Z. C. Chroneos, and A. H. Jobe. Macrophage and type II cell catabolism of SP-A and saturated phosphatidylcholine in mouse lungs. *American Journal of Physiology - Lung Cellular and Molecular Physiology*, 280: L1266–L1272, 2001.

[157] A. Pettenazzo, A. Jobe, J. Humme, S. Seidner, and M. Ikegami. Clearance of surfactant phosphatidylcholine via the upper airways in rabbits. *J Appl Physiol*, 65(5):2151–5, 1988.

[158] R. W. Walters, R. R. Jenq, and S. B. Hall. Distinct Steps in the Adsorption of Pulmonary Surfactant to an Air-Liquid Interface. *Biophysical Journal*, 78(1): 257–266, 2000.

[159] J. P. Archie. An Analytic Evaluation of a Mathematical Model for the Effect of Pulmonary Surfactant on Respiratory Mechanics. *Diseases of the Chest*, 53 (6):759–764, 1968.

[160] Y. Suzuki, Y. Fujita, and K. Kogishi. Reconstitution of tubular myelin from synthetic lipids and proteins associated with pig pulmonary surfactant. *American Review of Respiratory Diseases*, 140:75–81, 1989.

[161] S. Hawgood and K. Shiffer. Structure and properties of the surfactant-associated proteins. *Annual Review of Physiology*, 53:375–394, 1991.

[162] J. Bourbon, editor. *Pulmonary surfacxtant: biochemical, functional, regulatory, and clinical concepts*. CRC Press, Florida, 1991.

[163] F. Possmayer, K. Nag, K. Rodriguez, R. Qanbar, and S. Schurch. Surface activity in vitro: role of surfactant proteins. *Comp Biochem Physiol A Mol Integr Physiol*, 129(1):209–20, 2001.

[164] M. Oosterlaken-Dijksterhuis, M. Van Eijk, B. Van Buel, L. M. G. Van Golde, and H. P. Haagsman. Surfactant protein composition of lamellar bodies isolated from rat lung. *Biochemical Journal*, 274:115–119, 1991.

[165] Y. Lai, P. Chiang, J. Blom, N. Li, and Others. Comparison of In vitro Nanoparticles Uptake in Various Cell Lines and In vivo Pulmonary Cellular Transport in Intratracheally Dosed Rat Model. *Nanoscale Research Letters*, 3:321–329, 2008.

[166] O. Harush-Frenkel, N. Debotton, S. Benita, and Y. Altschuler. Targeting of nanoparticles to the clathrin-mediated endocytic pathway. *Biochem Biophys Res Commun*, 353(1):26–32, Feb 2 2007.

[167] D. Simionescu and M. Simionescu. Differentiated distribution of the cell surface charge on the alveolar-capillary unit. Characteristic paucity of anionic sites on the air-blood barrier. *Microvasc Res*, 25(1):85–100, Jan 1983.

[168] S. Kemp, A. Thorley, J. Gorelik, M. Seckl, and Others. Immortalization of Human Alveolar Epithelial Cells to Investigate Nanoparticle Uptake. *American Journal of Respiratory Cell and Molecular Biology*, 39:591–597, 2008.

[169] C. A. Ruge, J. Kirch, O. Caadas, M. Schneider, J. Perez-Gil, U. F. Schaefer, C. Casals, and C.-M. Lehr. Uptake of nanoparticles by alveolar macrophages is triggered by surfactant protein A. *Nanomedicine: Nanotechnology, Biology and Medicine*, 7(6):690–693, 2011.

[170] B. D. Chithrani, A. A. Ghazani, and W. C. W. Chan. Determining the Size and Shape Dependence of Gold Nanoparticle Uptake into Mammalian Cells. *Nano Letters*, 6(4):662–668, 2006.

[171] A. Beduneau, Z. Ma, C. Grotepas, A. Kabanov, and B. Rabinow. Facilitated Monocyte-Macrophage Uptake and Tissue Distribution of Superparamagnetic Iron-Oxide Nanoparticles. *PLoS ONE*, 4(2):e4343, 2009.

[172] G. R. Clegg, C. Tyrrell, S. R. McKechnie, M. F. Beers, D. Harrison, and M. C. McElroy. Coexpression of RTI40 with alveolar epithelial type II cell proteins in lungs following injury: identification of alveolar intermediate cell types. *American Journal of Physiology - Lung Cellular and Molecular Physiology*, 289(3): L382–L390, 2005.

[173] J. Chen, Z. Chen, T. Narasaraju, N. Jin, and L. Liu. Isolation of highly pure alveolar epithelial type I and type II cells from rat lungs. *Laboratory Investigation*, 84:727–735, 2004.

[174] A. Morgan and R. J. Talbot. Effects of inhaled alpha-emitting actinides on mouse alveolar macrophages. *Environ Health Perspect*, 97:177–84, Jul 1992.

[175] S. Arora, J. Jain, J. Rajwade, and K. Paknikar. Cellular responses induced by silver nanoparticles: In vitro studies. *Toxicology Letters*, 179:93–100, 2008.

[176] D. L. Laskin, V. R. Sunil, C. R. Gardner, and J. D. Laskin. Macrophages and tissue injury: Agents of defense or destruction? In A. K. Cho, editor, *Annual Review of Pharmacology and Toxicology, Vol 51, 2011*, volume 51 of *Annual Review of Pharmacology and Toxicology*, pages 267–288. 2011.

[177] R. N. Johnatty, D. D. Taub, S. P. Reeder, S. M. Turcovski-Corrales, D. W. Cottam, T. J. Stephenson, and R. C. Rees. Cytokine and chemokine regulation of proMMP-9 and TIMP-1 production by human peripheral blood lymphocytes. *J Immunol*, 158(5):2327–33, Mar 1 1997.

[178] D. H. Bowden and I. Y. Adamson. The alveolar macrophage delivery system. Kinetic studies in cultured explants of murine lung. *Am J Pathol*, 83(1):123–34, April 1976.

[179] I. Adamson and D. Bowden. Chemotactic and Mitogenic Components of the Alveolar Macrophage response to Particles and Neutrophil Chemoattractant. *American Journal of Physiology*, 109(1):71–77, 1982.

[180] B. A. Katsnelson and L. I. Privalova. Recruitment of phagocytizing cells into the respiratory tract as a response to the cytotoxic action of deposited particles. *Environ Health Perspect*, 55:313–25, Apr 1984.

[181] L. Muller, M. Riediker, P. Wick, M. Mohr, P. Gehr, and B. Rothen-Rutishauser. Oxidative stress and inflammation response after nanoparticle exposure: differences between human lung cell monocultures and an advanced three-dimensional model of the human epithelial airways. *J R Soc Interface*, 7 Suppl 1:S27–40, Feb 6 2010.

[182] S. Becker, J. Quay, and J. Soukup. Cytokine (tumor necrosis factor, IL-6, and IL-8) production by respiratory syncytial virus-infected human alveolar macrophages. *The Journal of Immunology*, 147(12):4307–4312, December 15 1991.

[183] D. L. Laskin. Macrophages and inflammatory mediators in chemical toxicity: a battle of forces. *Chem Res Toxicol*, 22(8):1376–85, Aug 2009.

[184] B. B. Aldridge, J. M. Burke, D. A. Lauffenburger, and P. K. Sorger. Physicochemical modelling of cell signalling pathways. *Nat Cell Biol*, 8(11):1195–1203, 2006.

[185] R. Samaga and S. Klamt. Modeling approaches for qualitative and semi-quantitative analysis of cellular signaling networks. *Cell Commun Signal*, 11 (1):43, 2013.

[186] M. J. Evans, L. J. Cabral, R. J. Stephens, and G. Freeman. Cell division of alveolar macrophages in rat lung following exposure to NO2. *Am J Pathol*, 70 (2):199–208, Feb 1973.

[187] S. Wang, R. Young, N. Sun, and M. Witten. In vitro cytokine release from rat type II penumocytes and alveolar macrophages following exposure to JP-8 jet fuel in co-culture. *Toxicology*, 173:211–219, 2002.

[188] G. Oberdorster, C. Cox, and R. Gelein. Intratracheal instillation versus intratracheal-inhalation of tracer particles for measuring lung clearance function. *Exp Lung Res*, 23(1):17–34, Jan-Feb 1997.

[189] K. E. Driscoll, D. L. Costa, G. Hatch, R. Henderson, G. Oberdorster, H. Salem, and R. B. Schlesinger. Intratracheal Instillation as an Exposure Technique for the Evaluation of Respiratory Tract Toxicity: Uses and Limitations. *Toxicological Sciences*, 55(1):24–35, May 1, 2000 2000.

[190] G. Oberdorster. Safety assessment for nanotechnology and nanomedicine: concepts of nanotoxicology. *J Intern Med*, 267:89–105, 2010.

[191] W. Wallace, M. Keane, D. Murray, W. Chisholm, A. Maynard, and T.-m. Ong. Phospholipid lung surfactant and nanoparticle surface toxicity: Lessons from diesel soots and silicate dusts. *Journal of Nanoparticle Research*, 9(1):23–38, 2007.

[192] W. E. Wallace, M. J. Keane, J. C. Harrison, J. W. Stephens, P. S. Brower, G. R. L., V. Vallyathan, and M. D. Attfield. *Cellular and Molecular Effects of Mineral and Syntheitc Dusts and Fibres*, volume 85 of *NATO ASI Series*. 1994.

[193] L. Wu, G. Zhang, Q. Luo, and Q. Liu. An image-based rat model for Monte Carlo organ dose calculations. *Medical Physics*, 35(8):3759–3764, 2008.

[194] D. O. Kuethe, V. C. Behr, and S. Begay. Volume of rat lungs measured throughout the respiratory cycle using 19F NMR of the inert gas SF6. *Magnetic Resonance in Medicine*, 48(3):547–549, 2002.

[195] S. L. Young, S. A. Kremers, J. S. Apple, J. D. Crapo, and G. W. Brumley. Rat lung surfactant kinetics biochemical and morphometric correlation. *Journal of Applied Physiology*, 51(2):248–253, August 1, 1981 1981.

[196] NHANES. National health and nutrition examination survey, 2011.

[197] W. R. Stahl. Scaling of respiratory variables in mammals. *J Appl Physiol*, 22 (3):453–60, Mar 1967.

[198] D. K. Molina and V. J. DiMaio. Normal organ weights in men: part II-the brain, lungs, liver, spleen, and kidneys. *Am J Forensic Med Pathol*, 33(4): 368–72, Dec 2012.

[199] N. K. Weller and M. J. Karnovsky. Isolation of pulmonary alveolar type I cells from adult rats. *Am J Pathol*, 124(3):448–56, Sep 1986.

[200] J. D. Crapo, E. Barry, B, P. Gehr, M. Bachofen, and E. R. Weibel. Cell Number and Cell Characteristics of the Normal Human Lung. *American Review of Respiratory Diseases*, 125:332–337, 1982.

[201] Y. Kubota, Y. Iwasaki, H. Harada, I. Yokomura, M. Ueda, S. Hashimoto, and M. Nakagawa. Depletion of alveolar macrophages by treatment with 2-chloroadenosine aerosol. *Clin Diagn Lab Immunol*, 6(4):452–6, Jul 1999.

[202] B. Rehn, J. Bruch, T. Zou, and G. Hobusch. Recovery of Rat Alveolar Macrophages by Bronchoalveolar Lavage under Normal and Activated Conditions. *Environmental Health Perspectives*, 97:11–16, 1992.

[203] J. Knust, M. Ochs, H. J. Gundersen, and J. R. Nyengaard. Stereological estimates of alveolar number and size and capillary length and surface area in mice lungs. *Anat Rec (Hoboken)*, 292(1):113–22, Jan 2009.

[204] J. H. Bates. *Lung Mechanics - An Inverse Modeling Approach*. Cambridge University Press, Cambridge, UK, 2009.

[205] S. R. Bates, J. Q. Tao, K. Notarfrancesco, K. DeBolt, H. Shuman, and A. B. Fisher. Effect of surfactant protein A on granular pneumocyte surfactant secretion in vitro. *American Journal of Physiology Lung Cell Molecular Physiology*, 285:L1055–L1065, 2003.

[206] C. G. Irvin and J. H. Bates. Measuring the lung function in the mouse: the challenge of size. *Respir Res*, 4:4, 2003.

[207] Z. Hantos, B. Daroczy, B. Suki, S. Nagy, and J. J. Fredberg. Input impedance and peripheral inhomogeneity of dog lungs. *Journal of Applied Physiology*, 72 (1):168–178, 1992.

[208] J. Hildebrandt. Pressure-volume data of cat lung interpreted by a plastoelastic, linear viscoelastic model. *Journal of Applied Physiology*, 28(3):365–372, 1970.

[209] E. Bermudez, J. B. Mangum, B. A. Wong, B. Asgharian, P. M. Hext, D. B. Warheit, and J. I. Everitt. Pulmonary responses of mice, rats, and hamsters to subchronic inhalation of ultrafine titanium dioxide particles. *Toxicological Sciences*, 77(2):347–357, Feb 2004.

[210] D. P. Gaver, R. W. Samsel, and J. Solway. Effects of surface tension and viscosity on airway reopening. *Journal of Applied Physiology*, 69(1):74–85, 1990.

[211] A. V. Andreeva, M. A. Kutuzov, and T. A. Voyno-Yasenetskaya. Regulation of surfactant secretion in alveolar type II cells. *American Journal of Physiology - Lung Cellular and Molecular Physiology*, 293(2):L259–L271, August 1, 2007 2007.

[212] R. Harris. Pressure-Volume Curves of the Respiratory System. *Respiratory Care*, 50(1):78–99, 2005.

[213] A. B. Otis, C. B. McKerrow, R. A. Bartlett, J. Mead, M. B. McIlroy, N. J. Selverstone, and E. P. Radford. Mechanical Factors in Distribution of Pulmonary Ventilation. *Journal of Applied Physiology*, 8(4):427–443, 1956.

[214] C. Thamrin, T. Janosi, R. Collins, P. Sly, and Z. Hantos. Sensitivity analysis of Respiratory Parameter Estimates in the Constant-Phase Model. *Annals of Biomedical Engineering*, 32(6):815–822, 2004.

[215] Z. Hantos, B. Suki, T. Csendes, and B. Daroczy. Constant-Phase Modelling of Pulmonary Tissue Impedance. *Clinical Respiratory Physiology*, 23:325s, 1987.

[216] M. S. Ludwig, I. Dreshaj, J. Solway, A. Munoz, and R. H. Ingram. *Partitioning of pulmonary resistance during constriction in the dog: effects of volume history*, volume 62. 1987.

[217] M. L. Crosfill and J. G. Widdicombe. Physical characteristics of the chest and lungs and the work of breathing in different mammalian species. *J Physiol*, 158 (1):1–14, 1961.

[218] B. Suki, F. Petak, A. Adamicza, Z. Hantos, and K. R. Lutchen. Partitioning of airway and lung tissue properties: comparison of in situ and open-chest conditions. *Journal of Applied Physiology*, 79(3):861–869, 1995.

[219] W. Cheng, D. S. DeLong, G. N. Franz, E. L. Petsonk, and D. G. Frazer. Contribution of opening and closing of lung units to lung hysteresis. *Respir Physiol*, 102(2-3):205–15, Dec 1995.

[220] L. Brancazio, G. N. Franz, E. L. Petsonk, and D. G. Frazer. Lung Area-Volume Models in Relation to the Recruitment-Derecruitment of Individual Lung Units. *Annals of Biomedical Engineering*, 29(3):252–262, 2001.

[221] J. H. Bates and C. G. Irvin. Time dependence of recruitment and derecruitment in the lung: a theoretical model. *J Appl Physiol*, 93(2):705–13, Aug 2002.

[222] D. Halpern and J. B. Grotberg. Surfactant effects on fluid-elastic instabilities of liquid-lined flexible tubes: a model of airway closure. *J Biomech Eng*, 115 (3):271–7, Aug 1993.

[223] C. Reinhard, G. Eder, H. Fuchs, A. Ziesenis, J. Heyder, and H. Schulz. Inbred strain variation in lung function. *Mammalian Genome*, 13(8):429–437, 2002.

[224] S. G. Taneva and K. M. W. Keough. Dynamic Surface Properties of Pulmonary Surfactant Proteins SP-B and SP-C and Their Mixtures with Dipalmitoylphosphatidylcholine. *Biochemistry*, 33(49):14660–14670, 1994.

[225] Z. Wang, S. B. Hall, and R. H. Notter. Dynamic surface activity of films of lung surfactant phospholipids, hydrophobic proteins, and neutral lipids. *Journal of Lipid Research*, 36(6):1283–93, 1995.

[226] T. J. Gregory, W. J. Longmore, M. A. Moxley, J. A. Whitsett, C. R. Reed, r. Fowler, A. A., L. D. Hudson, R. J. Maunder, C. Crim, and T. M. Hyers. Surfactant chemical composition and biophysical activity in acute respiratory distress syndrome. *J Clin Invest*, 88(6):1976–81, Dec 1991.

[227] L. Zhang, X. Sun, Y. Song, X. Jiang, S. Dong, and E. Wang. Didodecyldimethylammonium Bromide Lipid Bilayer-Protected Gold Nanoparticles: Synthesis, Characterization, and Self-Assembly. *Langmuir*, 22(6):2838–2843, 2006.

[228] G. Bothun. Hydrophobic silver nanoparticles trapped in lipid bilayers: Size distribution, bilayer phase behavior, and optical properties. *Journal of Nanobiotechnology*, 6(13), 2008.

[229] S.-H. Park, S.-G. Oh, J.-Y. Mun, and S.-S. Han. Effects of silver nanoparticles on the fluidity of bilayer in phospholipid liposome. *Colloids and Surfaces B: Biointerfaces*, 44(23):117–122, 2005.

[230] R. Pattle. The Relation Between Surface Tension and Area in the Alveolar Lining Film. *Journal of Physiology*, 269:591–604, 1977.

[231] B. M. Wiebe and H. Laursen. Human Lung Volume, Alveolar Surface Area, and Capillary Length. *Microscopy Research and Technique*, 32:255–262, 1995.

[232] K. Donaldson, V. Stone, P. S. Gilmour, D. M. Brown, and W. MacNee. *Ultrafine particles: mechanisms of lung injury*, volume 358. 2000.

[233] D. V. Bates, P. T. Macklem, and R. V. Christie. *Respiratory Function in Disease*. W.B. Saunders and Co., 1971.

[234] Q. Hamid, J. Shannon, and J. Martin. *Physiological Basis of Respiratory Disease*. PMPH USA, 2005.

[235] M. C. Garnett. Biodistribution of nanoparticles - insights from drug delivery. In N. Monteiro-Riviere and C. Tran, editors, *Nanotoxicology - Characterization, Dosing, and Health Effects*. Informa Healthcare, New York, 2007.

[236] S. M. Moghimi, A. C. Hunter, and J. C. Murray. Nanomedicine: current status and future prospects. *FASEB J*, 19(3):311–30, Mar 2005.

[237] C. C. Michel. Transport of macromolecules through microvascular walls. *Cardiovasc Res*, 32(4):644–53, Oct 1996.

[238] G. M. L. Meno-Tetang, H. Li, S. Mis, N. Pyszczynski, P. Heining, P. Lowe, and W. J. Jusko. Physiologically Based Pharmacokinetic Modeling of FTY720 (2-Amino-2[2-(-4-octylphenyl)ethyl]propane-1,3-diol hydrochloride) in Rats After Oral and Intravenous Doses. *Drug Metabolism and Disposition*, 34(9):1480–1487, 2006.

[239] J. Hay and B. Hobbs. The Flow of Blood to Lymph Nodes and its relation to Lymphocyte Traffic and the Immune Response. *The Journal of Experimental Medicine*, 145:31–44, 1977.

[240] L. Baxter, H. Zhu, D. Mackensen, and R. Jain. Physiologically Based Pharmacokinetic Model for Specific and Nonspecific Monoclonal Antibodies and Fragments in Normal tissues and Human Tumor Xenografts in Nude Mice. *Cancer Research*, 54(6):1517–1528, 1994.

[241] J. M. Bryan. The effect of hydrogen-ion concentration on the rate of oxidation of solutions of ferrous citrate. *Transactions of the Faraday Society*, 29(140): 830–833, 1933.

[242] I. Siriwardane. *Adsorption of citric acid on cerium oxide nanoparticles (nanoceria): effects of pH, surface charge and aggregation.* PhD thesis, Masters Thesis, University of Iowa, 2012.

[243] X. Zeng, B. Zhou, Y. Gao, C. Wang, S. Li, C. Y. Yeung, and W. Wen. Structural dependence of silver nanowires on polyvinyl pyrrolidone (PVP) chain length. *Nanotechnology*, 25, 2014.

[244] A. Apelblat and E. Manzurola. Apparent Molar Volumes of Organic Acids and Salts in Water at 298.15K. *Fluid Phase Equilibria*, 60:157–171, 1990.

[245] A. A. Allam, M. E. Sadat, S. J. Potter, D. B. Mast, D. F. Mohamed, F. S. Habib, and G. M. Pauletti. Stability and magnetically induced heating behavior of lipid-coated Fe3O4 nanoparticles. *Nanoscale Res Lett*, 8(1):426, 2013.

[246] S. Hawgood, B. J. Benson, and R. L. Hamilton. Effects of a Surfactant-Associated Protein and Calcium ions on the Structure and Surface Activity of Lung Surfactant Lipids. *Biochemistry*, 24:184–190, 1985.

[247] B. Muller, H. Garn, and R. Hochscheid. Impaired recycling of surfactant-like liposomes in type II pneumocytes from injured lungs. *Thorax*, 58:127–134, 2003.

[248] A. C. Moessinger, R. Harding, T. M. Adamson, M. Singh, and G. T. Kiu. Role of lung fluid volume in growth and maturation of the fetal sheep lung. *J Clin Invest*, 86(4):1270–7, 1990.

[249] M. Rudiger, S. Wendt, L. Kothe, W. Burkhardt, R. R. Wauer, and M. Ochs. Alterations of alveolar type II cells and intraalveolar surfactant after bronchoalveolar lavage and perfluorocarbon ventilation. An electron microscopical and stereological study in the rat lung. *Respiratory Research*, 8(40):1–9, 2007.

Appendix A

Toxicokinetic Model Calculations

A.1 Model Formulation

The rate of particle transfer from the vascular space (capillaries) to the interstitial space is modeled as follows:

$$\begin{aligned} V_i\frac{dC_i}{dt} &= Q_L(1-\sigma_L)C_V + PS_L(C_V - \frac{C_i}{P})\frac{Pe_L}{e^{Pe_L}-1} \\ &+ Q_S(1-\sigma_S)C_V + PS_S(C_V - \frac{C_i}{P})\frac{Pe_S}{e^{Pe_S}-1}, \end{aligned} \tag{A.1}$$

where, C_V is the vascular concentration, C_i is the interstitial concentration, PS_L,PS_S are the permeability-surface area products for the 2 pore types, P is partition coefficient, Pe_L,Pe_S are the Peclet Nos. for the 2 pore types calculated as $Pe = Q(1-\sigma)/PS$, Q_L & Q_S are the flow rates through the large and small pores respectively, given by $Q_L = Q_{iso} + \alpha_L L$, and $Q_S = Q_{iso} + \alpha_S L$.

Here, L is the local tissue lymph flow rate, Q_{iso} is the recirculation rate due to osmosis between the blood and interstitium, and α_L,α_S are the vasculo-lymphatic conductivities.

σ, the osmotic reflection coefficient is estimated using data from Michel *et al.*, 1996 [237] as:

$\sigma = (0.0542)\log(d_p) + 0.7843$, where d_p is the particle diameter in nm.

The values for all parameters are summarized in Table.

The process of particle uptake from the interstitial space to the cells is modeled via two processes: the adhesion of particles onto the cell surface and the actual endocytosis of the particles into the cells. The rate of particle adhesion onto the cellular surface is modeled by a probability of deposition on the cell surface, given by [83]:

$$k_f = \frac{3(1-\epsilon)}{2\epsilon d_c}\eta_s u, \tag{A.2}$$

where, ϵ is the porosity of the tissue, d_c is the diameter of each cell, u is the local flow velocity and η_s is the collector efficiency of the particle. The collector efficiency is assumed to be composed of 2 independent factors, η_o (dependent on particle size) and η_e (dependent on surface zeta potential) related as $\eta_s = \eta_o \times \eta_e$, where, $\eta_o = f(d_p)$ and $\eta_e = f(\psi_p, \psi_c)$

Here, d_p is the diameter of nanoparticles and ψ_c,ψ_p are the surface potentials on the cell and on the particle respectively.

η_o is related to d_p(in nm) using data from Su *et al.* [83] as: $\eta_o = 2.4481(d_p)^{-0.693}$

Using data from the same source, η_e is related to the particle and cell surface potentials (for anionic particles)as: $\eta_e = 214966(\psi_{pr})^{-2.605}$, where ψ_{pr} is the product of the magnitudes of ψ_p and ψ_c.

Using data from HarushFrenkel *et al.*, [166] we find the relation for cationic particles as: $\eta_e = 215.486(\psi_{pr})^{-2.605}$

The scaling factor k depends on the nature of the particles and is parametrized using measurements for silver nanoparticles.

The process of actual endocytosis (or phagocytosis) into the cells is modeled by the Michaelis-Menten equation based on the concentration of particles adhered to the cell surface.

$$\frac{dN_s}{dt} = -\frac{V_m N_s}{K_m + N_s}, \tag{A.3}$$

where, N_s is the number of particles adhered to the surface of a single cell, V_m and

K_m are the Michaelis-Menten constants. The number concentration (no. per vol.) of particles inside the cell, C_c can be related to N_s by the equation: $C_c.V_c = N_s^o - N_s$
The Michaelis-Menten parameters for phagocytosis were obtained from Beduneau *et al.* [171] for FeO NPs as: $V_{\rm m} = 2.217 \times 10^2$ per cell per min, and $K_{\rm m} = 5.502 \times 10^6$ per cell per min.
The Michaelis-Menten parameters for endocytosis were obtained from Chithrani *et al.* [170] for gold NPs as: $V_{\rm m} = 47.68$ per cell per min, and $K_{\rm m} = 3.652 \times 10^3$ per cell per min.

A.1.1 Vascular space

$$V_{\rm V,T}\frac{dC_{\rm V,T}}{dt} = Q_{\rm C,T}(C_{\rm a} - C_{\rm V,T}) - m_{\rm vi,T}, (\text{for T = all tissues except lung, liver, kidney}), \tag{A.4}$$

$$V_{\rm V,L}\frac{dC_{\rm V,L}}{dt} = Q_{\rm C}(C_{\rm ven} - C_{\rm V,L}) - m_{\rm vi,L}, (\text{for lungs}), \tag{A.5}$$

$$V_{\rm V,k}\frac{dC_{\rm V,k}}{dt} = Q_{\rm C,k}(C_a - C_{\rm V,T}) - k_{\rm f}C_{\rm V,k}V_{\rm V,k} - m_{\rm vi,k}, (\text{for kidney}), \tag{A.6}$$

$$V_{\rm V,liv}\frac{dC_{\rm V,liv}}{dt} = Q_{\rm hep}C_a + H - Q_{\rm liv}C_{\rm V,liv} - m_{\rm vi,liv}(\text{for liver}), \tag{A.7}$$

where, $Q_{\rm hep} = Q_{\rm C,liv} - Q_{\rm C,spl} - Q_{\rm C,sto} - Q_{\rm C,g}$ and $H = C_{\rm V,spl}Q_{\rm C,spl} + C_{\rm V,sto}Q_{\rm C,sto} + C_{\rm V,g}Q_{\rm C,g}$

A.1.2 Vasculo-Interstitial transfer

$$\begin{aligned} m_{\rm vi,T} &= Q_{\rm L}(1-\sigma_{\rm L})C_{\rm V,T} + PS_{\rm L}(C_{\rm V,T} - \frac{C_{\rm I,T}}{P})\frac{Pe_{\rm L}}{e^{Pe_{\rm L}}-1} \\ &+ Q_{\rm S}(1-\sigma_{\rm S})C_{\rm V,T} + PS_{\rm S}(C_{\rm V,T} - \frac{C_{\rm I,T}}{P})\frac{Pe_{\rm S}}{e^{Pe_{\rm S}}-1}, \end{aligned} \tag{A.8}$$

where, $C_{\rm V}$ is the vascular concentration, $C_{\rm I}$ is the interstitial concentration, $PS_{\rm L}$,$PS_{\rm S}$

are the permeability-surface area products for the 2 pore types, P is partition coefficient, Pe_{L},Pe_{S} are the Peclet Nos. for the 2 pore types calculated as $Pe = Q(1-\sigma)/PS$, Q_{L} & Q_{S} are the flow rates through the large and small pores respectively, given by $Q_{\mathrm{L}} = Q_{\mathrm{iso}} + \alpha_{\mathrm{L}} L$, and $Q_{\mathrm{S}} = Q_{\mathrm{iso}} + \alpha_{\mathrm{S}} L$.

Here, L is the local tissue lymph flow rate, Q_{iso} is the recirculation rate due to osmosis between the blood and interstitium, σ is the osmotic reflection coefficient, and α_{L},α_{L} are the vasculo-lymphatic conductivities.

A.1.3 Interstitial space

$$V_{\mathrm{I,T}} \frac{dC_{\mathrm{I,T}}}{dt} = -Q_{\mathrm{ly,T}} C_{\mathrm{I,T}} + m_{\mathrm{vi,T}} - m_{\mathrm{ic,T}} - m_{\mathrm{im,T}} \tag{A.9}$$

$$V_{\mathrm{I,LG}} \frac{dC_{\mathrm{I,LG}}}{dt} = Q_{\mathrm{ly}} (C_{\mathrm{ly}} - C_{\mathrm{I,LG}}) + m_{\mathrm{vi,LG}} - m_{\mathrm{ic,LG}} - m_{\mathrm{im,LG}} \tag{A.10}$$

Here, the first equation represents the mass balance for all tissues, T except the lymph glands, while the other equations is for lymph glands.

A.1.4 Interstitial-Cellular transfer

The amount of particles $m_{\mathrm{s,T}}$ adhered to the cellular surface is given by:

$$m_{\mathrm{s,T}} = k_{\mathrm{s}} C_{\mathrm{I,T}} V_{\mathrm{I,T}}, \tag{A.11}$$

where, k_{s} is the probabilistic rate of particle adhesion to cell surfaces given by the following equation.

$$k_{\mathrm{s}} = \frac{3(1-\epsilon)}{2\epsilon d_c} \eta_s u, \tag{A.12}$$

where, ϵ is the porosity of the tissue, d_c is the diameter of each cell, u is the local flow velocity and η_s is the collector efficiency of the particle.

The collector efficiency is assumed to be composed of 2 independent factors, η_o (dependent on particle size) and η_e (dependent on surface zeta potential) related as

$\eta_s = \eta_o \times \eta_e$, where, $\eta_o = f(d_p)$ and $\eta_e = f(\psi_p, \psi_c)$

d_p is the diameter of nanoparticles and ψ_c,ψ_p are the surface potentials on the cell and on the particle respectively.

The number of particles on each cell $N_{\mathrm{sc,T}}$ is given by: $N_{\mathrm{sc,T}} = m_{\mathrm{s,T}} N_{\mathrm{Av}} / N_{\mathrm{cell,T}}$. The no. of particles on each macrophage $N_{\mathrm{sm,T}}$ is given by: $N_{\mathrm{sm,T}} = m_{\mathrm{s,T}} N_{\mathrm{Av}} / N_{\mathrm{mac,T}}$.

$N_{\mathrm{cell,T}}$, $N_{\mathrm{mac,T}}$ are the nos. of cells and macrophages in tissue T and N_{Av} is the Avogadro's no.

Particle uptake from the cellular surface into the cell (both for cells and macrophages) is modeled using Michaelis-Menten kinetics.

$$\frac{dN_{\mathrm{sc,T}}}{dt} = -\frac{V_{\mathrm{mc}} N_{\mathrm{sc,T}}}{K_{\mathrm{mc}} + N_{\mathrm{sc,T}}}, \tag{A.13}$$

$$\frac{dN_{\mathrm{sm,T}}}{dt} = -\frac{V_{\mathrm{mm}} N_{\mathrm{sm,T}}}{K_{\mathrm{mm}} + N_{\mathrm{sm,T}}}, \tag{A.14}$$

where, $V_{\mathrm{mc}}, V_{\mathrm{mm}}$ and $K_{\mathrm{mc}}, K_{\mathrm{mm}}$ are the Michaelis-Menten parameters respectively for cells and macrophages.

Amount of particles transferred into the cell, $m_{\mathrm{ic,T}}$ and $m_{\mathrm{im,T}}$ can be related to $N_{\mathrm{sc,T}}$ and $N_{\mathrm{sm,T}}$ by the equations:

$$m_{\mathrm{ic,T}} = -\frac{dN_{\mathrm{sc,T}}}{dt} \times \frac{N_{\mathrm{cell,T}}}{N_{\mathrm{Av}}}, \tag{A.15}$$

$$m_{\mathrm{im,T}} = -\frac{dN_{\mathrm{sm,T}}}{dt} \times \frac{N_{\mathrm{mac,T}}}{N_{\mathrm{Av}}}, \tag{A.16}$$

A.1.5 Cellular space (cells and macrophages)

$$V_{\mathrm{C,T}} \frac{dC_{\mathrm{C,T}}}{dt} = m_{\mathrm{ic,T}} - R_{\mathrm{C,T}} \text{ (for T = all tissues except liver)}, \tag{A.17}$$

$$V_{\mathrm{C,liv}} \frac{dC_{\mathrm{C,liv}}}{dt} = m_{\mathrm{ic,liv}} - R_{\mathrm{C,liv}} - k_{\mathrm{b}} C_{\mathrm{C,liv}} Q_{\mathrm{b}} \text{ (for liver)}, \tag{A.18}$$

$$V_{\mathrm{M,T}} \frac{dC_{\mathrm{M,T}}}{dt} = m_{\mathrm{im,T}} - R_{\mathrm{M,T}} \text{ (for macrophages in T = all tissues)}, \tag{A.19}$$

A.1.6 Body fluids

$$V_{\text{ven}}\frac{dC_{\text{ven}}}{dt} = Q_{\text{car}}(C_{\text{v,mix}} - C_{\text{ven}}) - m_{\text{adh,v}} \text{ (for vein)}, \quad \text{where, } C_{\text{v,mix}} = \sum_T C_{\text{V,T}}Q_{\text{C,T}}/Q_{\text{car}} \tag{A.20}$$

$$V_{\text{ar}}\frac{dC_{\text{ar}}}{dt} = Q_{\text{car}}C_{\text{V,L}} - B_{\text{inf}} - m_{\text{adh,a}} \text{ (for artery)}, \quad \text{where, } B_{\text{inf}} = (\sum_T Q_{\text{C,T}} + Q_{\text{hep}})C_{\text{ar}} \tag{A.21}$$

$$V_{\text{ly}}\frac{dC_{\text{ly}}}{dt} = Q_{\text{ly}}(C_{\text{ly,mix}} - C_{\text{ly}}) \text{ (for lymph)}, \quad \text{where, } C_{\text{ly,mix}} = \sum_T C_{\text{I,T}}Q_{\text{ly,T}}/Q_{\text{ly}} \tag{A.22}$$

$$V_{\text{b}}\frac{dC_{\text{b}}}{dt} = k_{\text{b}}C_{\text{C,liv}}Q_{\text{b}} \text{ (for bile)}, \tag{A.23}$$

$$V_{\text{u}}\frac{dC_{\text{u}}}{dt} = k_{\text{f}}C_{\text{V,k}}V_{\text{V,k}} \text{ (for urine)}, \tag{A.24}$$

List of subscripts:

ar : Arterial, **ven** : Venous, **b** : Bile, **u** : Urine

car : cardiac, **ly** : Lymph

vi : Vascular-to-Interstitial, **ic** : Interstitial-to-Cellular, **im** : Interstitial-to-Macrophage

mac : Macrophage

car : Cardiac

A.2 Physiological Parameters

Table A.1: Tissue volumes in different species (in ml)

	Mouse (0.025 kg)	**Rat (0.25 kg)**	**Human (72.35 kg)**
Fat	2.13	17.5	22400
Brain	0.51	1.3	1340
Gut	2.9	6.5	888
Stomach	0.56	3.16	222
Heart	0.14	1.1	344
Kidneys	0.38	2.3	280
Liver	1.35	9	1414
Lung	0.17	1.3	965
Muscle	10.75	122	28660
Spleen	0.12	0.6	198
Plasma	1.06	10.55	3220
Lymph Glands	0.28	1.6	112

Values for rat (250g) and mouse (25g) are from Simcyp* Animal v12; Values for human are from P3M** (White male, aged 27 years, body weight: 72.35 kg; Stomach volumes for rat and mouse are scaled by body weight factor from human; Human stomach and gut (small intestine) volume are calculated as 20% and 80% respectively of the total volume of GI organs). Volume of lymph glands from Meno-Tetang *et al.* [238]

* Simcyp Animal and Simcyp Simulator v12 are trademarks of Simcyp Ltd., Sheffield, UK
** P3M (Physiological Parameters for PBPK Modeling) v1.3 is a trademark of the Lifeline Group

Table A.2: Blood flow rates in various species (% cardiac output)

	Mouse	Rat	Human	
			Male	Female
Fat	7	5.9	5	8.5
Brain	3.31	1.4	12	12
Stomach	0.43	1.7	1	1
Gut	7.19	6.2	10	11
Heart	5.7	4	4	5
Kidneys	13.55	14.5	19	17
Liver	22.51	24.2	25.5	27.5
Lung	100	100	100	100
Muscle	11.6	23.7	17	12
Spleen	0.71	1.1	2	3
Lymph Glands	0.012	0.012	0.012	0.012
Cardiac output(ml/min)	14.01	80	5100	

Values for rat (250g) and mouse (25g) from Simcyp v12 Animal; Human blood flow rates are from SimCYP v12 Simulator (using a population of body weight 70 kg, and aged between 18 and 65 years); Total cardiac output is from P3M for white male, 27 years old, body weight 72.35 kg; Flow to lymph glands based on [239] for rats; Hematocrit taken as 0.467 for all species.

Table A.3: Lymphatic flow parameters for different tissues

	Lymph flow (10^{-4} ml/min/g tissue wt.)	Lymph recirculation (10^{-4} ml/min/g tissue wt.)	Hydraulic conductivity
Fat	0.093	0	0.1
Brain	0.093	0	0.1
Stomach	0.433	0.018	0.2
Gut	1.397	0.003	0.2
Heart	0.75	4.21	0.5
Kidneys	5.7	18.8	0.3
Liver	2.1	4.84	0.25
Lung	5.2	15.7	0.1
Muscle	0.76	0.006	0.23
Spleen	0.2	3.0	0.65
Lymph glands	93.3		0.6

Lymph flow rates to tissues and lymph recirculation rates from [240]; Lymph flow rate to stomach and gut estimated by considering the same percentage distribution of lymph as of blood between stomach and gut in mice; Brain and Fat have no lymphatics so a nominal value of 0.1% of total lymph flow rate assumed; Hydraulic conductivities are from [81].

Table A.4: Fractional distribution of tissue volumes between vascular, interstitial, and cellular fractions

	Vascular fraction	Interstitial fraction	Cellular fraction
Fat	0.01	0.102	0.888
Brain	0.12	0.351	0.529
Stomach	0.029	0.174	0.797
Gut	0.029	0.174	0.797
Heart	0.053	0.143	0.804
Kidneys	0.1	0.339	0.561
Liver	0.1	0.199	0.701
Lung	0.1	0.298	0.602
Muscle	0.019	0.13	0.851
Spleen	0.1	0.2	0.7
Lymph Glands	0.009	0.15	0.841

Values from [81].

Appendix B

Parameter Estimation for Nanoscale Transformation

B.1 Zeta potential (ζ) variation with ionic strength (I) and pH

Figure B.1 (reproduced from Liu *et al.* [93]) shows the logistic nature of the curves for variation of ζ with pH and the isoelectric point (IEP). The IEP is the value of pH at which the surface zeta potential of particles dispersed in a medium becomes zero.

Table B.1: Reported zeta potential measurements (from Leo *et al.* [39]) corresponding to *in vitro* measurements compared with model predictions.

pH = 3	pH = 5	pH = 7
ζ = -18.2 mV	ζ = -22.5 mV	ζ = -32.5 mV

The values of ζ in Table B.1 were used to fit a logistic curve as:

$$\zeta = \beta \left(\frac{1 - e^{\lambda}}{1 + e^{\lambda}} \right), \tag{B.1}$$

where, $\lambda = pH - pI$. Here, pI = IEP = 1.75 and $\beta = 37$. β is the half of the range of the y-axis, i.e., the maximum value of ζ. Figure B.2 shows data from Salgin *et al.* [111] for NaCl and KCl for two different ionic strengths 0.001M and 0.1M. Increase in ionic strength consistently reduces the range of zeta potentials, i.e. reduces the parameter

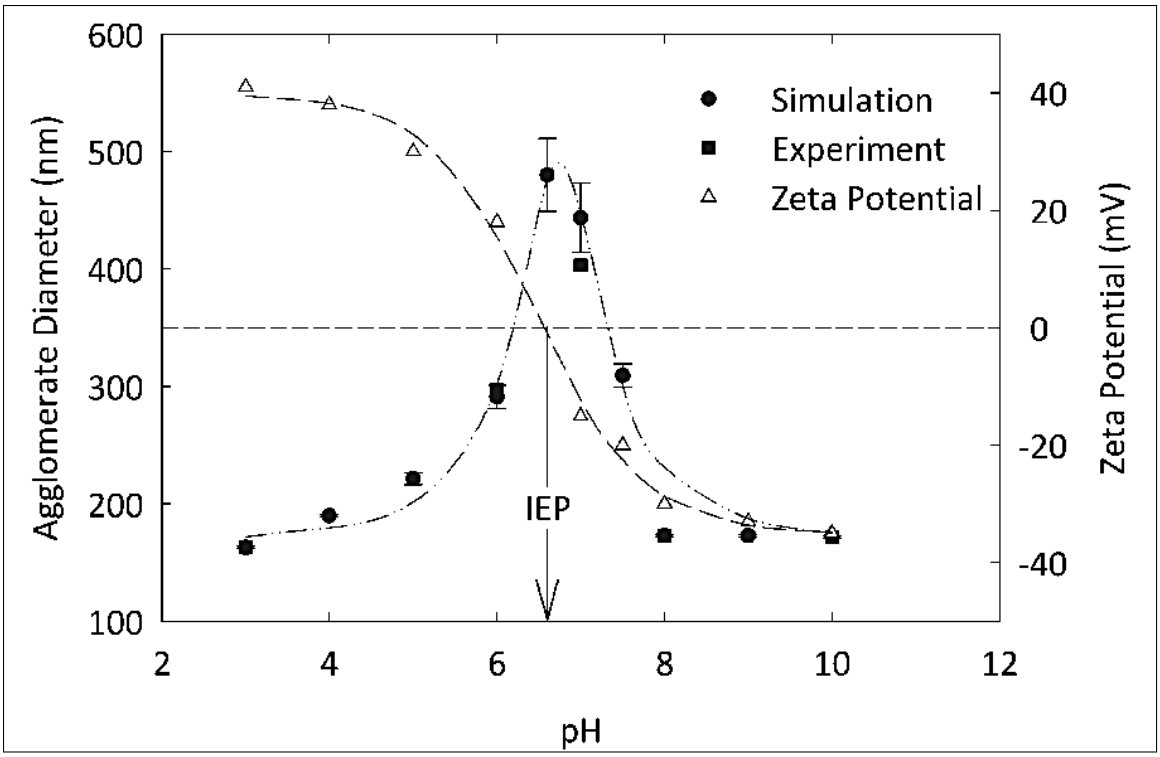

Figure B.1: Logistic nature of the curves for variation of ζ with pH and the isoelectric point (IEP). (Figure reprinted with permission from Liu *et al.* [93]. Copyright 2011 American Chemical Society)

β. Additional data in Salgin *et al.* [111] also point to the same fact. Equation B.1 was fitted to the data in the Figure B.2, and the values of β estimated are shown in Table B.2.

Table B.2: Estimated parameter values for variation of zeta potential with ionic strength

	KCl	NaCl	KCl	NaCl
I	0.001M	0.001M	0.1M	0.1M
$\log_{10} I$	-3	-3	-1	-1
β	42.46	35.64	20.02	16.37

Let the value of β at $I = 0.1$ be β_0. Then we can express β as $\beta = -\beta_0(1+\log_{10} I)$. The data in Table B.2 was fitted to Equation B.1 to obtain, $\beta_0 = 37$ (since the value of I for this set of experiments was close to 0.1M as shown in the next section). So

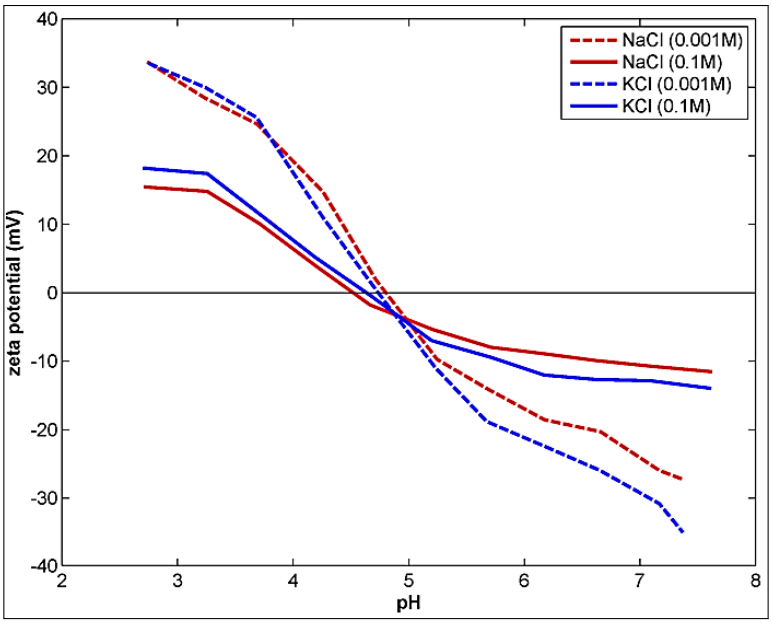

Figure B.2: Data from Salgin *et al.* [111] for NaCl and KCl for two different ionic strengths of 0.001M and 0.1M

we can express the final expression as:

$$\zeta = -\beta_0(1 + \log_{10} I)\left(\frac{1 - e^{\lambda}}{1 + e^{\lambda}}\right), \tag{B.2}$$

where, $\beta_0 = 37$ for the present set of NPs and incubation medium.

B.2 Estimation of electric potentials

The attractive van der Waals interaction potential is given by the expression proposed by Gregory [102] that accounts for the electromagnetic retardation effect:

$$\phi_{\mathrm{A}}(h) = -\frac{A r_{\mathrm{i}} r_{\mathrm{j}}}{6h(r_{\mathrm{i}} + r_{\mathrm{j}})} \cdot \left[1 - \frac{bh}{\lambda}\log\left(1 + \frac{\lambda}{bh}\right)\right], \tag{B.3}$$

Here, h is the distance between the surfaces of the agglomerates, A is known as the Hamaker constant with a value of 37×10^{-21} (for nAg), b is a constant with a value of 5.32, and λ is the characteristic wavelength for the reaction = 100 nm. The repulsive interaction potential between the agglomerates can be expressed via the

electric double layer (EDL) interaction potential equation that was developed using the Linear Superposition Principle by Gregory [101] as:

$$\phi_{\mathrm{R}}(h) = 128\epsilon\pi \left(\frac{k_{\mathrm{B}}T}{Ze}\right)^{2} . \left(\frac{r_{\mathrm{i}} r_{\mathrm{j}}}{r_{\mathrm{i}} + r_{\mathrm{j}}}\right) \gamma^{2} \exp(-\kappa h) \tag{B.4}$$

Here, ϵ is the permittivity of the medium, Z is the valence of ions in the medium, e is the elementary charge, k_{B} is the Boltzmanns constant, κ is the Debye-Hückel parameter, and γ is the reduced surface potential which is a function of the surface zeta potential ζ of the particles and is given by:

$$\gamma = \tanh\left(\frac{Ze\zeta}{4k_{\mathrm{B}}T}\right) \tag{B.5}$$

The Debye-Hückel parameter, κ is expressed in terms of the ionic strength, I of the medium as:

$$\kappa = \sqrt{\frac{2N_{\mathrm{A}}Ie^{2}}{\epsilon k_{\mathrm{B}}T}} \tag{B.6}$$

where, N_{A} is the Avogadros number.

B.3 Estimation of citrate oxidation

Figure B.7 (adapted from Bryan [241]) plots rate of citrate oxidation as a function of pH. The kinetic rate constants (% per hr.) for citrate oxidation are estimated and summarized in Table B.3.

Table B.3: Estimated kinetic rate constants (% per hr.) for citrate oxidation

pH = 3.31	pH = 4.56	pH = 5.35	pH = 5.71
k = 12	k = 35	k = 45	k = 50

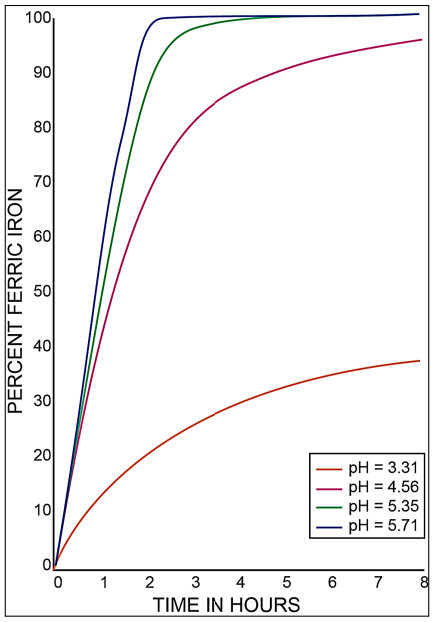

Figure B.3: The effect of hydrogen-ion concentration on the rate of oxidation of solutions of ferrous citrate. (Figure adapted from Bryan [241] with permission from The Royal Society of Chemistry.)

B.3.1 Ionic Strength Estimation

Ionic strength is affected by all ions present in a solution and depends on the methods of preparation of a solution. Ionic strength, I is defined as: $I = (1/2)\Sigma c_i z_i^2$, where c_i is the concentration of the ith ionic species and z_i is the charge of that ion. Based on charge conservation, the total concentrations of positive and negative ions should be equal. The positive ions present in the solution are $[H^+]$ and $[Na^+]$, while the negative charges are $[ClO_4^-]$, $[OH^-]$, $[H_2C^-]$, $[HC^{2-}]$, and $[C^{3-}]$. So we have:

$$[H^+] + [Na^+] = [ClO_4^-] + [OH^-] + [C^{3-}] + [HC^{2-}] + [H_2C^-] \tag{B.7}$$

For the citrate-stabilized nAg incubation study [39] that has been used to evaluate the model, the incubation solutions were prepared with 0.1M $NaClO_4$ solutions (pH = 6) and then titrated with 0.1M $HClO_4$ solution (pH = 1) for reaching pH values of 3 and 5 and titrated with 0.1M NaOH solution (pH = 12) for reaching a pH of 7. The ions from the citrate coating are considered in the next section. The ionic

concentrations of all medium ions are summarized in Table B.4.

Table B.4: Ionic concentrations (M) of all ions in the medium used by Leo *et al.* [39]

	pH = 3	pH = 5	pH = 7
H^+	1×10^{-3}	1×10^{-5}	1×10^{-7}
Na^+	0.0999	0.1	0.09989
$[ClO_4^-]$	0.1	0.1	0.099
$[OH^-]$	1×10^{-11}	1×10^{-9}	1×10^{-7}

Table B.5: Ionic concentrations (M) of all ions in the medium used by Tejamaya *et al.* [40]

Salts	Conc. (mg/L)	Mol. wt.	Molarity (mmol/L)(c_i)	$c_i z_i^2$	Ionic strength (mol/L) ($\Sigma c_i z_i^2$)
			CM-1		
$CaCl_2 \cdot 2H_2O$	294	147	2	12	
$MgSO_4 \cdot 7H_2O$	123.25	246	0.501	4.008	
$NaHCO_3$	64.75	84	0.771	1.542	0.0178
KNO_3	5.75	74.5	0.077	0.154	
Na_2SeO_3	2	173	0.012	0.072	
			NM-1		
$CaNO3_2 \cdot 4H_2O$	472.25	236	2.001	12.006	
$MgSO_4 \cdot 7H_2O$	123.25	246	0.501	4.008	
$NaHCO_3$	64.75	84	0.771	1.542	0.0178
KNO_3	7.5	101	0.074	0.148	
Na_2SeO_3	2	173	0.012	0.072	
			SM-1		
$CaSO_4$	271.75	136	1.998	15.984	
$MgSO_4 \cdot 7H_2O$	123.25	246	0.501	4.008	
$NaHCO_3$	64.75	84	0.771	1.542	0.0218
K_2SO_4	6.75	174	0.039	0.234	
Na_2SeO_3	2	173	0.012	0.072	

CM-10, NM-10, and SM-10 media were obtained by 10-fold dilution of the above media.

B.4 Protonation of Citrate Ions

Protonation of citrate ions is a process controlled by ionic equilibria. The equilibrium of various citrate species is shown below:

$$[C^{3-}] + 3[H^+] \overset{pKa_3}{\rightleftharpoons} [HC^{2-}] + 2[H^+] \overset{pKa_2}{\rightleftharpoons} [HC^{2-}] + [H^+] \overset{pKa_1}{\rightleftharpoons} [H_3C] \qquad \text{(B.8)}$$

Here, C denotes the citrate ion and so H_3C is citric acid and H_2C and HC are citrate ionic species at different extents of protonation. The three pKa values for citric acid are: pKa1 = 3.13, pKa2 = 4.76, pKa3 = 6.4. Based on the Henderson-Hasselbach equation, we can write the following equations:

$$\mathrm{pH} = \mathrm{pKa}_1 + \log\left(\frac{\mathrm{H_2C^-}}{\mathrm{H_3C}}\right), \tag{B.9}$$

$$\mathrm{pH} = \mathrm{pKa}_2 + \log\left(\frac{\mathrm{HC^{2-}}}{\mathrm{H_2C^-}}\right), \tag{B.10}$$

$$\mathrm{pH} = \mathrm{pKa}_3 + \log\left(\frac{\mathrm{C^{3-}}}{\mathrm{HC^{2-}}}\right), \tag{B.11}$$

The ionic concentrations of $[H^+]$, $[Na^+]$, $[ClO_4^-]$, and $[OH^-]$ are estimated in the previous section. So the total concentration of citrate ions, [Cit], is given by:

$$[\mathrm{Cit}] = [\mathrm{C^{3-}}] + [\mathrm{HC^{2-}}] + [\mathrm{H_2C^-}] = [\mathrm{H^+}] + [\mathrm{Na^+}] - [\mathrm{ClO_4^-}] - [\mathrm{OH^-}] \tag{B.12}$$

So based on Henderson-Hasselbach equation, we can write:

$$\frac{\mathrm{Cit}}{[\mathrm{H_3C}]} = \frac{[\mathrm{C^{3-}}]}{[\mathrm{H_3C}]} + \frac{[\mathrm{HC^{2-}}]}{[\mathrm{H_3C}]} + \frac{[\mathrm{H_2C^-}]}{[\mathrm{H_3C}]} \tag{B.13}$$

$$= \frac{[\mathrm{C^{3-}}]}{[\mathrm{HC^{2-}}]}.\frac{[\mathrm{HC^{2-}}]}{[\mathrm{H_2C^-}]}.\frac{[\mathrm{H_2C^-}]}{[\mathrm{H_3C}]} + \frac{[\mathrm{HC^{2-}}]}{[\mathrm{H_2C^-}]}.\frac{[\mathrm{H_2C^-}]}{[\mathrm{H_3C}]} + \frac{[\mathrm{H_2C^-}]}{[\mathrm{H_3C}]} \tag{B.14}$$

$$= 10^{\text{pH-pKa1}}.(1 + 10^{\text{pH-pKa2}}.(1 + 10^{\text{pH-pKa3}})) \tag{B.15}$$

The value of [Cit] is calculated in the previous section. The value of $[H_3C]$ can be calculated from Equation B.15. Then, the values of $[H_2C]$, [HC], and $[C^{3-}]$ can be calculated as:

$$[\mathrm{H_2C^-}] = [\mathrm{H_3C}].10^{\text{pH - pKa1}} \tag{B.16}$$

$$[\mathrm{HC}^{2-}] = [\mathrm{H_2C}^{-}].10^{\mathrm{pH\ -\ pKa2}} \tag{B.17}$$

$$[\mathrm{C}^{3-}] = [\mathrm{HC}^{2-}].10^{\mathrm{pH\ -\ pKa3}} \tag{B.18}$$

Thus the ionic strength, I, can be calculated once we have the concentrations of all ions in solution using the formula: $I = (1/2)\Sigma c_{\mathrm{i}} z_{\mathrm{i}}^2$.

B.5 Nanoparticle surface coverage

Initial fraction of NP surface area coated, f_{Ao} would be given by:

$$f_{\mathrm{Ao}} = \frac{N_{\mathrm{C}} N_{\mathrm{A}} (\pi r^2)}{SA_{\mathrm{T}}}, \tag{B.19}$$

where, N_{C} is the total moles of citrate present, N_{A} is the Avogadro No., r is the radius of a citrate ion, and SA_{T} is the total surface area of the NPs.

Fraction of SA that is dynamically available for reaction can be estimated as:

$$f_{\mathrm{A}} = f_{\mathrm{Ao}} \frac{C_{\mathrm{Cit}}/SA_{\mathrm{T}}}{C^{\mathrm{o}}_{\mathrm{Cit}}/SA^{\mathrm{o}}_{\mathrm{T}}} = f_{\mathrm{Ao}} \frac{C_{\mathrm{Cit}}/SA_{\mathrm{T}}}{.} \frac{1}{F^{\mathrm{o}}_{\mathrm{coat}}}, \tag{B.20}$$

where, C_{cit} is the concentration of citrate ions in the medium and F_{coat} is the parameter quantifying the extent of surface protection as defined in the main body of the article as:

$$F_{\mathrm{coat}} = \frac{\text{Total Models citrate adhered to NPs}}{\text{Total SA of NPs in medium}} = \frac{n_{\mathrm{Cit}}}{SA_{\mathrm{T}}} \tag{B.21}$$

Data obtained from Siriwardane [242] (summarized in Table B.6) is used to estimate the functional variation of f with d and pH. The value of f is approximately linear with d for every value of pH (Figure). The best-fit lines are summarized in

Table B.6: Data for nanoparticle surface coverage for citrate coating from Siriwardane [242]

pH	NP diameter, d (nm)	Surface coverage, f ($\times 10^{14}$) (molecules/cm^2
2	4	3.7
4	4	2.9
5.5	4	2.2
7.5	4	0.92
2	9	5.9
4	9	3.7
5.5	9	2.7
2	39	51.9
4	39	18.5
5.5	39	17.2

Table B.7. So the variation of slope, m with pH (Figure S6) is:

$$m = (63.53).\exp(-2.083\text{pH}) + 0.447 \tag{B.22}$$

Table B.7: Best-fit equations for variation of f with diameter, d

pH	Best-fit line	Slope, m
2	f = (1.432)d - 4.315	1.432
4	f = (0.4623)d + 0.353	0.4623
5	f = (0.4477)d - 0.393	0.4477

Based on Figure, the effective ionic diameter of the citrate ion was assumed to be $\tilde{3}$ A$^{\circ}$. The intercept is very close to zero (Figure S4) for higher values of pH. So for pH = 7, we can select the intercept as zero. So $f = 0.447d$. So the values of f for citrate-stabilized nAg can be estimated and are summarized in Table B.8.

Table B.8: Final estimated values of f for citrate-stabilized nAg

NP	Mean dia. (nm)	f
Ag20	20	8.94
Ag50	50	22.35
C20	20	8.94
C110	110	49.17

B.6 Nanoparticle Surface Coverage for PVP

For PVP coated nAg, we have the PVP/Ag mass ratio from nanoComposix (www.nanoComposix.com)

As an example, the estimation for P20 is shown below:

Material conc. $= 2.1 \times 10^{13} \times (\pi/6)(20)^3 \times 10^{-21} \times 10.87$ g/mL $= 0.956$ mg/mL

PVP conc. $= 0.956 \times 20 = 19.12$ mg/mL

No. of PVP molecules per mL $= (19.12 \times 10^{-3}/10000) \times 6.023 \times 10^{23} = 1.15 \times 10^{18}$

PVP molecules per NP $= (1.15 \times 10^{18})/(2.1 \times 10^{13}) = 5.48 \times 10^{4}$

PVP molecules per cm^2 $= (5.48 \times 10^{4})/(400\pi \times 10^{-14}) = 43.58 \times 10^{14}$

Table B.9: Final estimated values of f for PVP-stabilized nAg

NP	NP density (g/cm^3)	PVP/Ag mass ratio	PVP MW	NP conc. (NP/ml)	$f(\times 10^{14})$ (molecules/cm^2)
P20	10.87	20:1	10 kD	2.1×10^{13}	43.58
P110	10.49	10:1	40 kD	1.9×10^{11}	28.96

B.7 Size distribution of lipid vesicles

Size distribution of lipid vesicles is constructed based on available information regarding vesicular size in mammalian alveolar fluid. There are generally 3 broad types of vesicles based on size - small unilamellar vesicles (SUVs), large unilamellar vesicles (LUVs), and giant unilamellar vesicles (GUVs). The available information has been summarized in Table B.10. The upper and lower limits of the size ranges (Table B.10) are taken as the 95th and 5th percentile values of a log-normal distribution for vesicular size. Then the subsequent mean and standard deviation for each type of vesicle are estimated. The measures for the respective log-normal distributions and combined with the respective percent compositions to construct an overall population of vesicles having SUVs, LUVs, and GUVs with a size distribution representative of mammalian alveolar fluid. Figure B.4 shows the overall size distribution of lipid

vesicles.

Table B.10: Properties of lipid vesicles in alveolar surfactant

Vesicle type	Percent composition [114]	Size range [115]	Mean, SD (nm)
SUV	43%	20-50 nm	35, 7.5
LUV	48%	50-500 nm	275, 112.5
GUV	9%	$>$ 1000 nm	1000, 0

SUV: Small Unilamellar Vesicles, LUV: Large Unilamellar Vesicles, GUV: Giant Unilamellar Vesicles

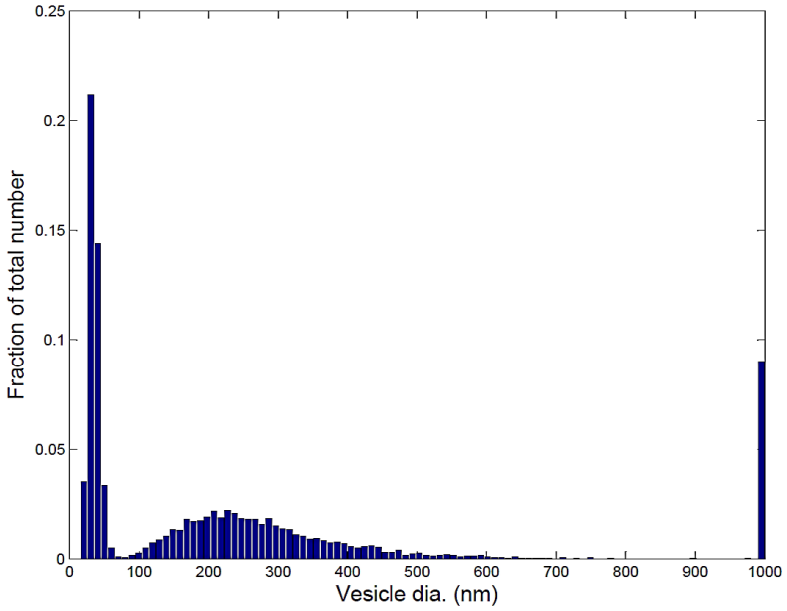

Figure B.4: Lipid vesicle size distribution involving SUVs, LUVs, and GUVs.

B.8 Size distribution of lipid vesicles

Steric effects have been considered for coating molecules using the method shown by Damodaran [135, chap. 3], who used the following equation to estimate the repulsive energy due to steric effects:

$$E_{\mathrm{st}} = (k_{\mathrm{B}} T n_{\mathrm{m}} L/s).\left[(2L/d)^{2.25} - (2L/d)^{0.75}\right], \tag{B.23}$$

where, k_B is the Boltzmanns constant, T is the absolute temperature, n_m is the number of coating molecules per unit surface area of the ENM, L is the chain length of the coating molecule, s is the mean distance between coating molecules, and d is the mean distance between interacting ENMs. Here, the mean distance between coating molecules, s is given by: $s = \sqrt{1/n_m}$. The distance between interacting ENMs, d varies as two ENMs approach each other, and hence the total interaction energy is estimated by integrating over the entire distance as was done by Mukherjee *et al.* [42] for attractive and repulsive electrical potentials.

Parameters L and n_m in Equation B.23, for citrate and PVP molecules are summarized in Table B.11. Number of coating molecules per unit ENM surface area (n_m) is generally known to vary with ENM size. The values of n_m for various sizes of ENMs have been estimated by Mukherjee *et al.* [42]. The molecular lengths of citrate and PVP molecules are taken from the literature (PVP from Zeng *et al.* [243] and citrate from Apelblat and Manzurola [244]).

Table B.11: Molecular properties of citrate and PVP coatings

Parameters	C20	C110	P20	P110
L (nm)	0.673*	0.673*	16**	16**
n_m(molecules/m^2)	8.94×10^{18}	4.92×10^{19}	4.36×10^{19}	2.9×10^{19}

* based on an apparent molar volume of 96.24 cm^3/mol for trisodium citrate from Apelblat and Manzurola [244]
** based on 10 kDa and 40 kDa PVP chain length from Zeng *et al.* [243]

The steric repulsive potential estimated from Equation B.23 is normalized by the steric potential created by an uncoated Ag ENM. The molar volume of Ag is 10.335 cm^3 per mole. Considering an Avogadro number of molecules making up that volume, and assuming an Ag atom as roughly spherical, the mean radius of the Ag atom, r_{Ag} can be estimated as 1.6 A°. Empirical and calculated values of the atomic radius of Ag are also reported to be around 160 pm or 1.6 A° [*www.webelements.com/silver/atom$_s$izes.html*]. Number of Ag atoms present on the surface of an uncoated Ag ENM can be estimated as $n_m = 1/\pi r_{Ag}^2$. So using $L = 3.2A^\circ$, and $n_m = 1.24 \times 10^{19}$ atoms/m^2, we can get from Equation B.23, the value

of E_{Ag}. The steric effect is quantified as:

$$\lambda = \frac{|E_{\mathrm{Ag}}|}{|E_{\mathrm{coat}}|} \tag{B.24}$$

Mutual interaction of ENMs consists of an attractive van der Waals interaction potential and a repulsive interaction potential. Detailed expressions for these interaction potentials are provided Equations B.3 and B.4. The effective repulsive potential, ϕ_{e} is obtained by adjusting the electric repulsive potential ϕ_{R} by the steric effect represented by λ_{ST} as:

$$\phi_{\mathrm{e}}(h) = \phi_{\mathrm{R}}(h).\lambda_{\mathrm{ST}}(h) \tag{B.25}$$

B.9 Estimation of zeta potentials

Zeta potential of lipid-adsorbed ENMs has been estimated using a weighed function as:

$$\zeta = \zeta_{\mathrm{L}}\theta + \zeta_0(1-\theta), \tag{B.26}$$

where, ζ_0 is the zeta potential of the ENM without lipid adsorption, ζ_{L} is the reduced zeta potential due to lipid adsorption, and θ is the fractional surface coverage of the ENM by lipids. Allam *et al.* [245] measured zeta potentials of nanoparticles, with and without the presence of lipids. The measurements are shown in Table B.12. From these measurements, the average value of $\zeta_{\mathrm{L}}/\zeta_0$ was estimated as 0.34. Zeta potentials of various types of uncoated ENMs are summarized in Chapter III.

Table B.12: Measured values of ζ (in mV) for NPs with and without coated lipids from Allam *et al.* [245]

ζ (uncoated NPs)	-32.4	-40.7	-47.1	-11.2	-12.3	-23.3	-10.3	-10.8	-22.5
ζ (lipid coated NPs)	-11.9	-15.6	-19.1	-4.5	-5.5	-7.4	-2.2	-3.4	-5.2

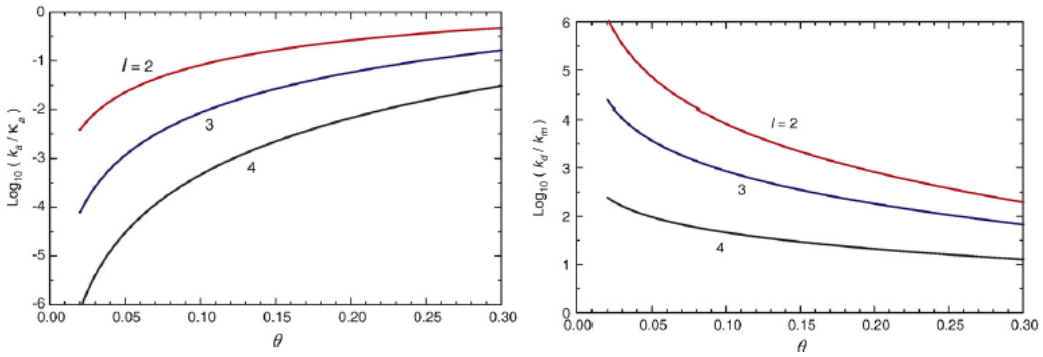

(a) Adsorption (b) Desorption

Figure B.5: Figures from Zhdanov and Kasemo [126], showing variation of adsorption and desorption rates (k_a,k_d) for proteins with change in lipid surface coverage.(Reprinted from *Biophysical Chemistry*, Vol. 146(2-3), Zhdanov V.P. & Kasemo B., 60, Copyright(2009), with permission from Elsevier)

B.10 Protein adsorption and desorption

Zhdanov and Kasemo [126] modeled protein adsorption and desorption on lipid bilayers and how the adsorption and desorption rates (k_a&k_d) varied with lipid surface coverage. The measurements shown in Figure B.5 were used to fit a function for k_a and k_d as follows:

$$k_a = k_a^0.(1 + \beta_a \theta^{n_a}) \tag{B.27}$$

$$k_d = k_d^0.(1 + \beta_d \theta^{n_d}) \tag{B.28}$$

Here, k_a^0 and k_d^0 are the values of k_a and k_d obtained by extrapolation of the data shown above for $\theta = 0$. Without the presence of lipids ($\theta = 0$), there would be no preference for any of the proteins regarding adsorption and hence the values of k_a^0 and k_d^0 would be the same. The exact values do not matter here as they are normalized in the model and used as relative probabilities. The values of the fitted parameters for the four surfactant proteins are shown in Table B.13.

Table B.13: Estimated parameters for the four surfactant proteins

Protein	L	k_a^0	k_d^0	β_a	β_d	k_a	k_d
SP-A	2	3.16×10^{-4}	2×10^7	1.5×10^4	2.5×10^{-7}	1.79	-3.2
SP-B	4	3.16×10^{-4}	2×10^7	4.58×10^7	2.3×10^{-3}	3.92	-1.09
SP-C	4	3.16×10^{-4}	2×10^7	4.58×10^7	2.3×10^{-3}	3.92	-1.09
SP-D	2	3.16×10^{-4}	2×10^7	1.5×10^4	2.5×10^{-7}	1.79	-3.2

B.11 Estimation of diffusion coefficients for proteins

Estimation of diffusion coefficients of proteins involve multiple parameters such as the molecular weight M, partial specific volume $\bar{V}$, and the sedimentation coefficient, s, which are related by the Svedberg equation [144] shown below:

$$D = \frac{RTs}{M(1-\nu\rho)}, \tag{B.29}$$

Young *et al.* [144] used the Svedberg equation to derive an empirical correlation for proteins, which can be written as:

$$D = 7.51 \times 10^{-8}.(T\bar{V}^{-1/3}/\eta), \tag{B.30}$$

where, $\bar{V}$ is the partial specific volume of the protein under consideration, η is the viscosity of the medium, and T is the absolute temperature.

Appendix C

Toxicodynamic Model Calculations

C.1 Estimation of surfactant kinetics

Kinetic parameters corresponding to kinetics of various surfactant components discussed in Chapter IV have been estimated using measurements from various published *in vivo* studies.

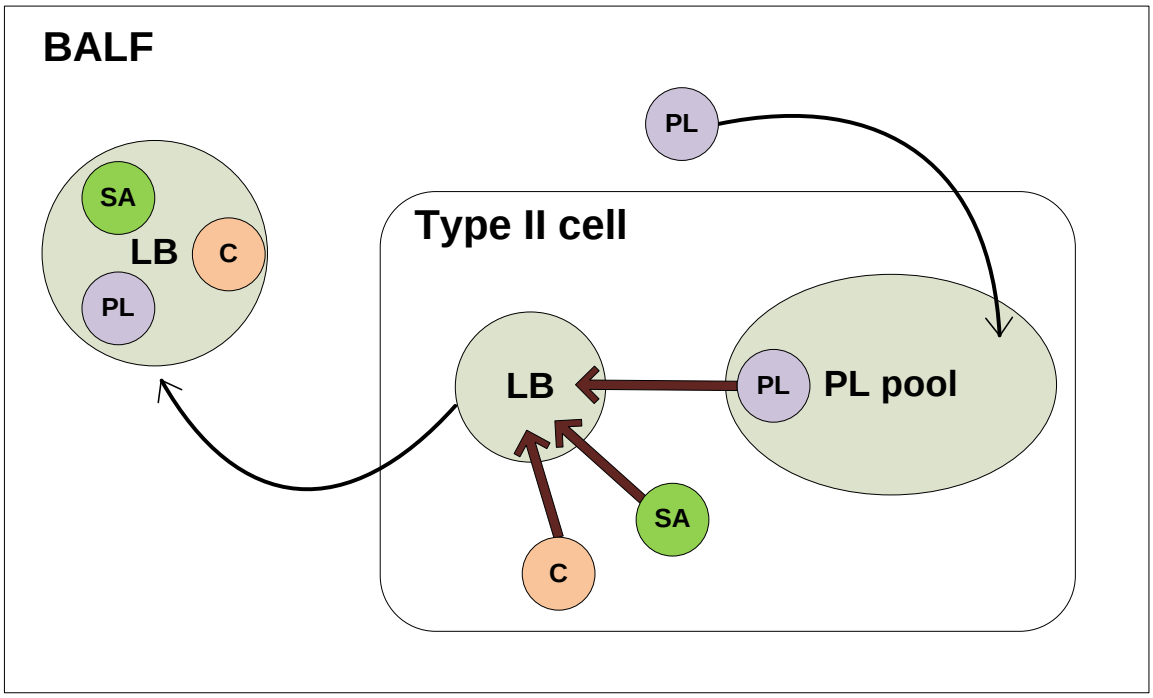

Figure C.1: Schematic representation of alveolar surfactant component kinetics within alveolar lavage fluid.

Based on data from Martini *et al.* [151], we have the following:

PL secretion into LB: 2.1 + 20.9 = 23 nmol/h/g lung

LB secretion outside the cell: 239 nmol/h/g lung

PL recycling: 215.9 nmol/h/g lung

PC pool size in LB: 1.14 µmol/g lung

PC pool size in surface: 1.46 µmol/g lung

PC pool size in tissue: 12.6 µmol/g lung

So, PC pool size in type II cells = 12.6 - 1.46 - 1.14 = 10 µmol/g lung = 10000 nmol/g lung

Based on data from Young *et al.* [195], we have the following:

No. of LB per type II cell = 150

No. of type II cells per lung = 126×10^6

Based on data from Oosterlaken-Dijksterhuis *et al.* [164], we have the following:

nmol SP-A/mol PL in LB = 0.006

nmol SP-B/mol PL in LB = 5.5

nmol SP-C/mol PL in LB = 12

Based on data from Bourbon [162]:

Half-life of SA = 12 hr. (Based on SP-B)

Rate constant for transfer of PL from pool to LB = 23/10000 hr^{-1} = 3.833×10^{-5} min^{-1}. Rate constants for SA and C are assumed to be same as that of PL, since the "unpackaging" of all surfactant components from LB to the alveolar fluid happens at the same time.

Rate of LB release out of the cell (for entire lung):

Rate of PL transport by LB out of the cell = 239 nmol/h/g lung (Martini *et al.* [151])
Rate of LB exocytosis (dividing by amount of PL in LB) = 239/1140 hr^{-1} = 239/1140/60 min^{-1} = 0.0035 min^{-1}.
Rate of PL recycling back into the cell = 215.9 nmol/h/g lung
Rate constant for the transfer (for the whole lung) = 215.9/1460 h^{-1} = 215.9/1460/60 min^{-1} = 0.0025 min^{-1}
Rate constant for SA recycling = 0.0025 min^{-1} (assumed same)
Rate constant for C recycling = -log(1/2) / $t_{1/2}$ = 0.0578 h^{-1} = 9.627×10^{-4} min^{-1} (based on half-life from Martini *et al.* [151]).

C.1.1 Surfactant uptake by alveolar macrophages

Gurel *et al.* [156] studied surfactant uptake by alveolar macrophages. Based on the data [156], considering the first data point (at 15 minutes after start of incubation), the DPPC uptake can be estimated as: 15 dpm per 10^3 cells. Based on the specific activity of DPPC of 2.3 nCi/µL, and 1 Ci = 2.22×10^{12} dpm, the uptake rate of PL by macrophages can be estimated as: $15/(2.3 \times 2.22 \times 10^3)$ µL per 10^3 cells per 15 mins = 1.958×10^{-4} µL per 10^3 cells per min.
The 60 µL dose is approximately 10% of the alveolar pool [156].
Alveolar pool = (1.14 + 1.46)µmol/g lung = 2.6 µmol/g lung = 2.6 × 0.43 µmol (mice) = 1.118 µmol.
So, uptake rate of PL = $1.958 \times 10^{-4} \times 0.112/60$ µmol per 10^3 cells per min = 3.655×10^{-7} µmol per 10^3 cells per min = 6.067×10^{-5} µmol per min (1.66×10^5 macrophages per lung) = 6.067×10^{-5} µmol per min/(0.0818 × 0.43 µmol) (previously estimated amount in the alveolar fluid) = 1.725×10^{-3} per min.

Gurel *et al.* [156] also measured SP-A uptake by cells as 5 dpm per 10^3 cells. Based on a specific activity of SP-A = 0.011 µCi/µg protein and the fact that 1 Ci = 2.22×10^{12} dpm, the uptake rate of SA = $5/(0.011 \times 2.22 \times 10^6$ µg per 10^3 cells per 15 min =

1.365×10^{-5} µg per 10^3 cells per min = 5.25×10^{-10} µmol per 10^3 cells per min = 8.715×10^{-8} µmol per min (1.66×10^5 macrophages per lung) = 8.715×10^{-8} µmol per min/(0.0146×0.43 µmol) (previously estimated amount in the alveolar fluid) = 1.388×10^{-5} **per min**.

C.2 Estimation of regulatory parameters

Surfactant proteins exert critical regulatory effects on alveolar processing of PL. These effects have been estimated using *in vitro* measurements from multiple published studies.

C.2.1 Effect of Surfactant Proteins on PL adsorption

Hawgood *et al.* [246] compared changes in surface tension due to change in amounts of surfactant proteins in a PL mixture. The slopes of the surface pressure - time curves were compared for cases A and B (Figure 6 in Hawgood *et al.* [246]) which is a good indicator of the different rates of PL adsorption on to the air-liquid interface.

Table C.1: Parameters for surfactant regulation by surfactant proteins estimated using measurements from Hawgood *et al.* [246]

	Case A	Case B
Slope, m	5.58	1.63
SP conc., C	2 μg/ml	0.5 μg/ml
m/C	2.79	3.26
Mean	3.025	

Based on these results, we can say the effect of surfactant proteins on PL adsorption can be quantified as 3.025 per unit conc. (μg/ml) of surfactant proteins present in the lavage fluid.

C.2.2 Effect of SP-A on PL secretion

Measurements from Bates *et al.* [205] were used to estimate the percentage change in PL secretion with change in concentration of SP-A. The mean slope estimated (Figure 1 from citetBates2003) is -6.6783. So the decrease in secretion rate can be estimated to be 6.67 % per μg/ml of SP-A.

C.2.3 Effect of SP-A on PL recycling

Measurements from Muller *et al.* [247] were used to estimate the effect of SP-A on PL recycling. Based on Figure 1 from Muller *et al.* [247], the control values with and without SP-A were considered. Considering the initial slope, the initial slope for the case without SP-A was 0.0924, while that for the case with SP-A was 0.6393. So it was evident that the recycling rate of DPPC increased increased (0.6393/0.0924), i.e. 6.92 times for an increase of 5 μg/ml of SP-A. So it could be assumed that the increase in recycling rate per μg/ml of SP-A = 1.384.

Table C.2: Morphological parameters of the pulmonary system used in the model

Parameter	**Value**	**Reference**
Total lung volume	1.43 ml	Measured in mice by Wu *et al.* [193]
Total lung mass	0.43 g	Measured in mice by Wu *et al.* [193]
Volume of alveolar fluid	10 ml/kg BW	Reported in sheep by Moessinger *et al.* [248]
Alveolar surface	0.072 m^2	Scaled by lung volume from alveolar surface in Wistar rats reported by Rudiger *et al.* [249]
Thickness of alveolar interface	0.2 μm	Reported in rats by Bastacky *et al.* [142]
Volume of single Type II cell	385.7 μm^3	Number weighted mean in rats [249]
No. of Type II cells	9.13×10^7	Reported in mice by Gurel *et al.* [156]
Volume of LB per Type II cell	61.3 μm^3	Reported in rats by Rudiger *et al.* [249]
No. of LB per Type II cell	150	Estimated in rats by Young *et al.* [195]

Table C.3: Initial (literature) estimates of parameters for surfactant kinetics

Parameter	**Description**	**Value** (in min^{-1},except where mentioned)	**Reference**
K_{LB}	Rate constant for LB exocytosis	0.0035	Martini *et al.* [151]
K_{Re}	Rate constant for surfactant recycling	0.0025(PL,SA); 9.63×10^{-4} (C)	Martini *et al.* [151]
K_{Ad}	Rate constant for surfactant adsorption	1.649 ml/μmol.min	Walters *et al.* [158]
K_{Dep}	Rate constant for surfactant depletion	1.649	Walters *et al.* [158]
K_{Mph}	Rate constant for macrophage uptake	1.725×10^{-3}(PL,SA); 1.388×10^{-5} (C)	Gurel *et al.* [156]
K_{AW}	Rate constant for airway loss of surfactant	2.083×10^{-5}	Pettenazzo *et al.* [157]
K_{Sec}	Rate constant for surfactant secretion into LB	3.833×10^{-5}	Martini *et al.* [151]

Table C.4: Values of parameters for surfactant regulation

Parameter	**Description**	**Literature value**	**Reference**
$k_{\mathrm{Ad}}^{\mathrm{SA}}$	Parameter for activation of surfactant adsorption by SA	3.025 per μg/ml of SA	Hawgood *et al.* [246]
$k_{\mathrm{Ad}}^{\mathrm{C}}$	Parameter for activation of surfactant adsorption by C	3.025 per μg/ml of C	Hawgood *et al.* [246]
$k_{\mathrm{LB}}^{\mathrm{C}}$	Parameter for inhibition of surfactant secretion by C	0.0668 per μg/ml of C	Bates *et al.* [205]
$k_{\mathrm{Re}}^{\mathrm{C}}$	Parameter for activation of surfactant recycling by C	1.384 per μg/ml of C	Muller *et al.* [247]

Table C.5: Optimized values of parameters for surfactant kinetics (in min^{-1})

Parameter	**PL**	**SA**	**C**
K_{Sec}	3.99×10^{-4}	3.99×10^{-4}	1.33×10^{-8}
K_{Re}	4.88×10^{-2}	1.995×10^{-2}	9.78×10^{-6}
K_{Dep}	0.0924	0.1917	1.594

Parameters K_{LB}, & K_{Ad} are considered to have the same values for all components. For other parameters K_{Mph}, & K_{AW}, the literature obtained values are considered. K_{CSec} is considered to be 6 times that of K_{Sec} for collectins in the absence of definitive data on the relative contributions of either pathways.

C.3 Intracellular digestion of surfactant lipids

Wallace *et al.* [192] measured digestion of PL which was adsorbed on nanoparticles by cells. Figure C.2 shows measurements of fraction of PL, f remaining with time.

Table C.6: Summary of nanoparticles used in the analysis

Particle Designation	Nanomaterial	Hydrodynamic diameter (nm)	Core diameter (nm)	Ag conc. (mg/g)	Zeta Potential in BEGM (mV)
nAg	15 nm citrate stabilized nAg	15	12	1	-9.6
CB	15 nm citrate stabilized CB	15	12	1	-9.6

Table C.7: Michaelis-Menten parameters for surfactant adsorption

	V_{A}(mg/ml)	K_{A}(m^2/ml)
Oxidized surface	5.1×10^{-3}	1.03×10^{-2}
Non-oxidized surface	3.581×10^{-3}	1.131×10^{-2}

The fraction f can be fitted to an exponential function given by:

$$f = K_{\mathrm{PLase}}.\exp(-kt) \tag{C.1}$$

So f can be expressed as a differential equations as:

$$\frac{df}{dt} = a.\exp(-k_{\mathrm{PL}}t), \tag{C.2}$$

where, $a = 1$, and k_{PL} was estimated to be 0.13 hr^{-1}.

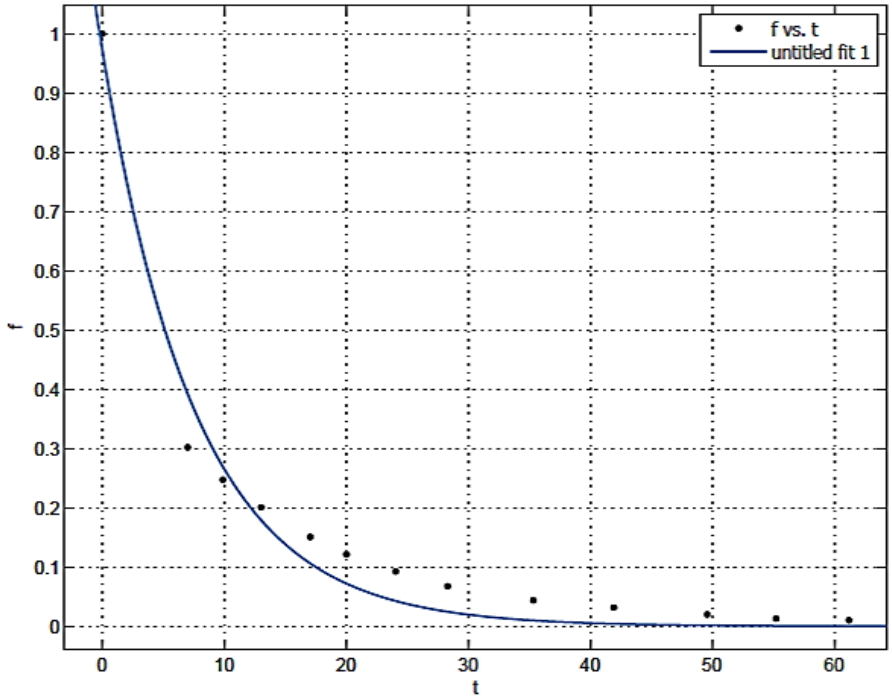

Figure C.2: Data points from Wallace *et al.* [192] for fraction f, of PL digested and a best-fit exponential function for the data.

Appendix D

Estimations for lung mechanics

D.1 Effect of surfactant concentration on surface tension

Surface tension at the alveolar interface is a function of surfactant concentration in the hypophase. The relationship was investigated by Walters *et al.* [158]. Using data from Walters *et al.* [158], the following relationship was developed:

$$\gamma = \gamma_{\max}. \left[1 - \frac{C_{\mathrm{S}}^{\mathrm{n}}}{K + C_{\mathrm{S}}^{\mathrm{n}}}\right], \tag{D.1}$$

where, C_{S} is the surface concentration of PL, $\gamma_{\max}$ is the maximum surface tension of the alveolar interface estimated to be 28.1 mN/m, and K, n are parameters with values estimated to be 18.647 and 2.81 respectively. So the relation between γ_{PL} the surface tension due to PL and $\gamma_{\mathrm{PL}}*$, the surface tension in control conditions can be obtained as:

$$\gamma_{\mathrm{PL}}/\gamma_{\mathrm{PL}}* = \frac{K + C_{\mathrm{S}}^{\mathrm{n}^*}}{K + C_{\mathrm{S}}^{\mathrm{n}}}, \tag{D.2}$$

D.2 Effect of SA on surface tension

The effective surface tension, γ is given as:

$$\gamma = \gamma_{\mathrm{PL}}.f_{\mathrm{SA}} \tag{D.3}$$

Here, f_{SA} is related to the surface concentration of SA as $f_{\mathrm{SA}} = k_{\mathrm{surf,SA}}.(1 - C_{\mathrm{SA}})$.

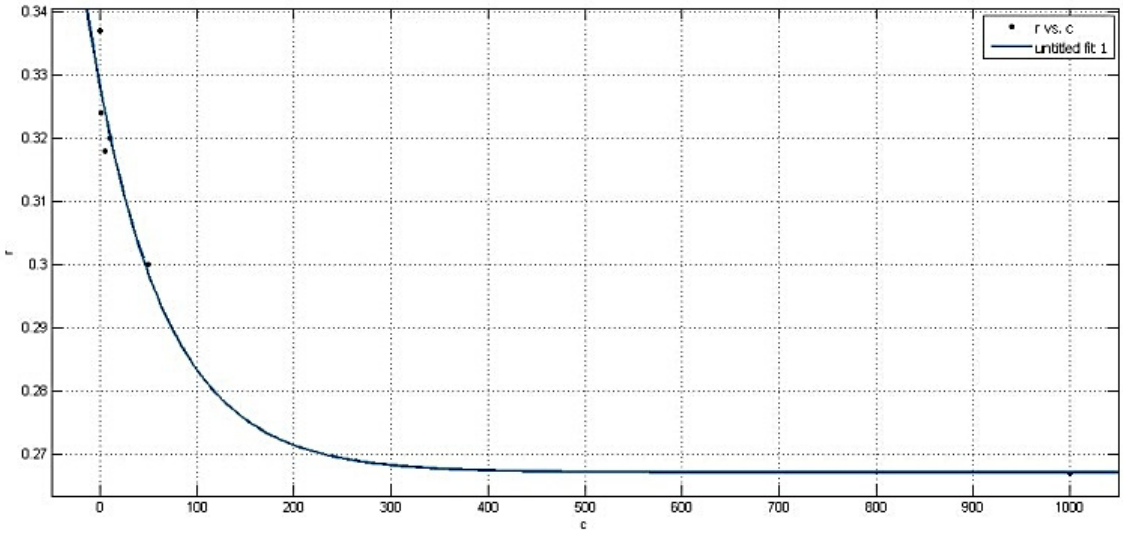

Figure D.1: Data points for lipid layer anisotropy vs AgNP concentration in surfactant lipids and fitted curve based on an exponential model (data from Bothun [228].

D.3 Effect of NP on surfactant viscosity

Surfactant viscosity, μ can be related to lipid layer anisotropy, $< r >$ as:

$$\mu = \mu_0.\left(\frac{< r >}{< r_0 >}\right), \tag{D.4}$$

where, μ_0 and $< r_0 >$ are values in the absence of any NPs.

Lipid bilayer anisotropy, $< r >$ was related to AgNP concentration, c, based on

data from Bothun [228]:

$$< r >= (0.061).\exp(-0.013c) + 0.2672 \tag{D.5}$$

Table D.1: Data for changes in lipid bilayer anisotropy from Bothun [228]

AgNP conc. (mg/L)	$< r >$ at 30°C
0	0.337
1	0.324
5	0.318
10	0.320
50	0.3
500	0.292
1000	0.267